

University of Nottingham
UK | CHINA | MALAYSIA

Design and study on fault tolerant permanent magnet starter-generator for more electric aircraft application

Bo Wang, B.Sc, M.Sc.

Thesis submitted to the University of Nottingham

for the degree of Doctor of Philosophy

September 2023

Abstract

The implementation of a permanent magnet electrical machine is a very attractive candidate for aircraft industry, especially which applications need high power density and high efficiency. Besides, achieving such objectives while pursuing high reliability is very challenging and requires an optimal machine design with robust solutions for fault tolerance. To address these aspects, this thesis aims to utilize a novel fault tolerant topology through detailed comparisons, verifying fundamental performance and fault tolerance.

To achieve this goal, the first stage of the project involves the comprehensive review in aircraft electrification and the state-of-art fault tolerant approaches for permanent magnet synchronous machine. The second stage has shown the initial design of the feasible candidates, with multiple objective optimization design process and validation of fault tolerance. The third stage consists of thermal management, mechanical design and final electromagnetic design. All the details of this optimal candidate are sorted out. A prototype machine based on the optimal candidate of this project is manufactured and experimentally tested. The main contribution of this work is the investigation and verification of a feasible design process and novel topology for safety-critical application applied on aircraft due to 1) multiple objective and multiple discipline design process 2) the proposed novel topology for the improvement of fault tolerance.

This knowledge is then used to inform future machine designers on how to take these aspects into consideration during the design of electrical machines.

Acknowledgements

Returning to university for a PhD program was not an easy decision, especially after five years of industry work. However, looking back now, I am grateful that I made this choice, despite the challenges posed by the Covid-19 pandemic. The PhD journey is a long and uncertain one, full of both difficulties and opportunities. Through hard work over the past four years, I have grown tremendously as an individual and researcher.

I would like to express my gratitude to the China Scholarship Council (CSC) for their generous financial support.

My supervisors, Dr. Tao Yang and Dr. Gaurang Vakil, have been instrumental in guiding and supporting my research work. I am deeply grateful for their dedication and regular guidance, which have been crucial to my successful completion of the PhD program. I would also like to thank my internal examiner, Dr. Adam Walker, for his valuable feedback and examination each year, which helped me improve my research work.

I am grateful to NEMA, UK, for their support in prototype manufacturing. I would also like to thank the technicians in the PEMC Research Group, including John Hinchliffe, Daniel Bathgate, Guy Thompson, Chris Varley, and Paul Girling, for their support in setting up the test rig whenever I needed it.

My thanks go to Prof. Chris Gerada, Dr. Tianjie Zou, and Dr. Antonino La Rocca for their guidance and valuable support on research activities, such as general discussion and thermal analysis. I would also like to thank Dr. Mi Tang, Dr. Mohammad Ilkhani, Dr. Yuzheng Chen, and Dr. Seang Yeoh for their contributions to the development of the motor test rig and control drive platform.

I am deeply grateful to all the people, including friends and colleagues, that I met during these years within or outside of the PEMC Research group. My PhD journey

would not have been as wonderful without you.

Last but not least, I must thank my family: my wife Ruomeng Li, my son Hanzhang Wang (Yuanbao), and my parents. Their endless love and understanding have been my source of strength throughout this long journey. I dedicate this thesis to them.

Contents

Abstract I

Acknowledgements III

Contents VI

Acronyms XI

Symbols XIII

List of Figures XVI

List of Tables XXIV

Chapter 1 Introduction 1

1.1 Background 1

1.2 Aims and objectives 1

1.3 Thesis outline 2

1.4 Scientific contribution and list of related publications 4

Chapter 2 Electrical machines for aircraft electrification 6

2.1 Introduction 6

2.2 Aircraft electrification 6

2.3 Distribution of electrical machines on aircraft 7

2.3.1 Flight control system 8

2.3.2 Engine control 11

2.3.3 Landing gear system 12

2.3.4 Fuel system 14

2.3.5 Environmental control system 15

2.3.6 Electric tail rotor system 16

2.3.7 Electric power generation 17
2.4 The state-of-the-art of electrical machines on MEA 20
2.5 Chapter conclusion 24
Chapter 3 The state-of-the-art fault tolerant PMSM design for aircraft application 25
3.1 Introduction 25
3.2 Electrical machine faults 25
3.2.1 Electrical faults 26
3.2.2 Thermal faults 28
3.2.3 Mechanical faults 31
3.3 Fault tolerant design of PMSM 33
3.3.1 SC current 34
3.3.2 Fault isolation 35
3.3.3 Innovation of topology 37
3.4 Discussion 40
3.5 Conclusion 42
Chapter 4 Initial design of the permanent magnet starter-generator 43
4.1 Introduction 43
4.2 Requirements capture 44
4.2.1 Specification 44
4.2.2 Reliability 46
4.2.3 Interface 46
4.3 Initial definition 47
4.3.1 Machine type 47
4.3.2 Slot/pole selection 47
4.3.3 Material 48
4.4 Machine design process 49
4.4.1 Multiple-objective and multiple-discipline optimization design 49
4.4.2 Objectives and constraints 51
4.4.3 Search space 51

4.4.4 Exploration of the solution space 52
4.4.5 Evaluation and rank 53
4.5 Conclusion 58
Chapter 5 Fault tolerance improvement of PMSM candidate 59
5.1 Winding design 59
5.2 Topology Feasibility of multiple three-phase 59
5.2.1 Dual three-phase layout 60
5.2.2 Triple three-phase layout 71
5.2.3 Multiple three-phase (Phases>9) 72
5.2.4 Conclusion of suggested selection 76
5.3 Validation of topology 76
5.3.1 Dual three-phase 76
5.3.2 Triple three-phase 87
5.4 Improvement of fault tolerance 92
5.4.1 Splits in stator teeth 92
5.4.2 Modular design 99
5.5 Comprehensive evaluation 105
5.5.1 Iterated optimization process. 106
5.5.2 Validation of FT topology 108
5.5.3 FEA simulation 109
5.5.4 Faulty scenarios 113
5.6 Conclusion 118
Chapter 6 Thermal management and machine losses 119
6.1 Thermal management 119
6.2 Limitation and selection of materials 120
6.3 Loss modelling 120
6.3.1 Copper loss 120
6.3.2 Magnetic circuit loss 123
6.4 Cooling methods 125

6.4.1 Slot cooling 126
6.4.2 Housing jacket cooling 127
6.4.3 Enhanced cooling 129
6.5 Analysis and results 130
6.5.1. Methods 130
6.5.2. Results 131
6.5.3. Effect of thermal isolation 135
6.6 Discussion 135
Chapter 7 Prototype design and performance analysis 137
7.1 Introduction 137
7.2 Fault monitoring design 137
7.2.1 Search coils 137
7.2.2 Thermal sensors 142
7.3 Mechanical analysis 143
7.3.1. Rotor stress 143
7.3.2. Modal analysis 147
7.4 Electromagnetic force 149
7.4.1 On-load electromagnetic force 150
7.4.2 Rotor force under faulty modes 150
7.5 Mechanical design 151
7.5.1 Assembly of segment 151
7.5.2 Cooling structure 152
7.6 Interface design 152
7.6.1 Mechanical interface 153
7.6.2 Electrical interface 153
7.6.3 Cooling interface 157
7.7 Conclusion 157
Chapter 8 Prototyping and experimental validation 159
8.1 Introduction 159

8.2 Manufacturing and Assembly 159
8.2.1 Stator assembly 159
8.2.2 Rotor assembly 160
8.2.3 Housing 161
8.2.4 Overall structure and assembly 161
8.3 Static measurement 162
8.3.1 Resistance and inductance of per phase 162
8.3.2 D-axis and Q-axis Measurement 164
8.4 Dynamic test 174
8.4.1 Setup of test-rig 174
8.4.2 Commissioning 179
8.5 On-load test 189
8.5.1 On 270 VDC 191
8.5.2 On 540 VDC 194
8.6 Faulty scenarios 197
8.6.1 Open-circuit (OC) fault 197
8.6.2 Short-circuit (SC) fault 205
8.7 Conclusion 209
Chapter 9 Conclusion and future work 210
9.1 General conclusion 210
9.2 Future work 212
Bibliography 214

Acronyms

AC	Alternating current
AEA	All Electric Aircraft
AlNiCo	Aluminium nickel cobalt
APU	Auxiliary Power Units
CFD	Computational Fluid Dynamics
CSCF	Constant speed constant frequency
D-axis, *d*	Direct-axis
DC	Direct current
DL	Double-layer
DTC	Direct torque control
DW	Distributed winding
ECS	Environmental Control System
EHA	Electro-hydrostatic Actuator
EMA	Electromechanical Actuator
EMF	Electromotive force
EMI	Electromagnetic Interference
EV	Electric Vehicle
EBHA	Electrical backup hydraulic actuator
EHA	Electro-hydraulic actuators
eVTOL	Electric vertical take-off and landing
FEM	Finite element Method
FFT	Fast Fourier Transform
FSCW	Fractional slot concentrated winding
FT	Fault tolerant
HA	Hydraulic actuators
HESM	Hybrid excitation synchronous machines

HTS	High temperature superconducting
HVDC	High-voltage direct current
IPMSM	Interior permanent magnet synchronous machine
LPTN	Lumped parameter thermal network
MBSE	Model-based system engineering
MCDM	Multiple criterion decision making
ME	Main exciter
MEA	More-electric aircraft
MG	Main generator
MTBF	Mean time between Failures
NdFeB	Neodymium iron boron
N&H	Noise and vibration
NSGA	Nondominated sorting genetic algorithm
OBIGGS	On-board inert gas generation system
OC	Open circuit
PE	Pre-exciter
PM	Permanent magnet
PMSM	Permanent magnet synchronous machine
PMASRM	PM-assisted synchronous reluctance motor
Q-axis, *q*	Quadrature-axis
RAT	Ram Air Turbine
RTD	Resistance temperature detectors
SC	Short circuit
SCADA	Supervisory control and data acquisition
SG	Starter-generator
SL	Single layer
SmCo	Samarium cobalt
SPM	Surface mounted machine
SRM	Switched reluctance machine
VSCF	Variable speed constant frequency
VSVF	Variable speed variable frequency
WBG	Wide bandgap
WFSM	Wound field synchronous machine

Symbols

A	Total conductor area, mm^2
A_e	Effective conductor area, mm^2
ABC	Phases in three-phase
$A^{'}B^{'}C^{'}$	2nd three-phase in dual three-phase layout
B	Magnitude of the flux density, T
B_m	Magnetic induction in calculating Ferrite loss, T
B_r	Remanence, T
B_{rotor}	Flux density in rotor back iron, T
d_c	Diameter of the conductors, m
D_b	Diameter of stator bore, mm
D_s	Depth of slot, mm
D_t	Depth of tooth tip, mm
E_1, E_2, E_3	Elastic module in three directions, GPa
f	Operation frequency, Hz
H	Magnetic field intensity, A/m
I	Current, A
I_r, I_f	Rising edge current trailing edge current, A
I_s	RMS phase current, A
I_{SC}	Short-circuit current, A
K_e	Back-EMF constant
K_t	Torque constant
L_s, L_m	Self and mutual inductance of phases, μH
l_a	Active length of conductor, m
L_d, L_q	Inductance of d-axis and q-axis, μH
N	Turns of winding
N_{ph}	Number of phases
p	Number of poles

P_{AC}	AC loss, W
$P_{_in}$, $P_{_out}$	Input/output power of in parametric analysis, W
P_H	Hysteresis losses per unit mass, W/kg
P_{out}	Output power, kW
P_V	Eddy current loss, W
Q	Number of slots
R	Resistance, $m\Omega$
r	The conductor radius, mm
R_{ac}^{Tcal}	AC resistance per phase at the reference temperature, $m\Omega$
R_{dc}^{Tcal}	DC resistance per phase at the reference temperature, mΩ
R_{dc}^{Tref}	Calculated or measured at the reference temperature, mΩ
R_{ph}	Resistance of per phase, mΩ
T	Winding temperature, ℃
T_0	Reference temperature, ℃
T_{calc}	Average winding temperature, ℃
T_{drag}	Drag torque in SC fault, Nm
T_m	Thickness of magnet, mm
T_{ref}	The average winding temperature, ℃
$T_{winding}$	Temperature of winding, ℃
η	Efficiency
U_{ll}	Line-line voltage, V
W	Weight of active parts, kg
W_{cu}	Copper loss, W
W_s	Slot opening of slot, mm
W_t	Width of tooth, mm
α	Temperature coefficient of resistivity at 20℃
α_m	Angle of central magnet, degree
α_t	Angle of tooth tip, degree
ω	Electrical angular speed, rpm
σ	Electrical conductivity of the conductor material
$\sigma_1, \sigma_2, \sigma_2$	Mechanical stress in three directions, MPa
σ_r, σ_θ	Mechanical stress in radial and circumferential directions, MPa
ε	Mechanical strain.
σ_H	The ratio of the specific mass

σ_V	The coefficient of proportionality
δ	The skin depth, mm
ρ	Density, $\mathrm{kg/m^3}$
τ	Time constant, s

List of Figures

Fig. 2.1 Comparison of electrification between conventional (B737) and some pioneering MEAs [21]. 7
Fig. 2.2 Electrical power generating capacity of aircraft [21]. 8
Fig. 2.3 Flight control surfaces on aircraft [22]. 9
Fig. 2.4 Classification of different flight control EMA types [25]. 10
Fig. 2.5 Electrical dual-redundant structure [33]. 11
Fig. 2.6 Main landing gear assembly (hydraulic) on a Boeing 777 [38]. 12
Fig. 2.7 Comparison of engine and electric taxiing [43]. 13
Fig. 2.8 The green taxiing (GT) motor prototype [44]. 13
Fig. 2.9 Prototype nose wheel steering actuator (left–right: functional schematic and illustration) [45]. 14
Fig. 2.10 A fault tolerant PMSM (4-phase, 100kW) for fuel pump [8]. 15
Fig. 2.11 (a) ECS with bleed air. (b) Electric ECS with no bleed air [8]. 16
Fig. 2.12 Axial-flux and radial-flux electrical machine topologies considered. (a)Double air gap axial-flux topology, 4 rotor discs (b) 4 x 3-phase phase modular wound radial-flux topology. 17
Fig. 2.13 Electrical power system structure of B787 [51]. 19
Fig. 2.14 Schematic of an aircraft generator. (a) Three-stage aircraft generator. (b) Two-stage aircraft generator with the three-phase ac exciter [52]. 20
Fig. 2.15 Power density of advanced electrical machines applied on aircraft applications. 22
Fig. 2.16 High-power (>100 kw) PMSM for AEA/MEA applications. 22
Fig. 3.1 Schematic diagram of (a) axial flux and (b) radial flux PMSM. 26
Fig. 3.2 Classification of PMSM. 26
Fig. 3.3 Schematic classification of PMSM faults. 26

Fig. 3.4 Failure tree analysis of PMSM electrical faults. 27
Fig. 3.5 Equivalent circuit under varied scenarios (a) Healthy. (b) Open-circuit. (c) Symmetrical short-circuit. (d) Turn-to-turn short-circuit of Phase C. 28
Fig. 3.6 Failure tree analysis of PMSM magnetic faults. 28
Fig. 3.7 B-H Curve of the Arnold Magnetic Technologies SmCo magnet, blue lines: PM intrinsic demagnetization curve, orange lines: normal demagnetization curves [91]. 30
Fig. 3.8 Magnet collapse during the high-speed operation. 31
Fig. 3.9 Failure tree analysis of PMSM eccentricity faults. 31
Fig. 3.10 Schematic diagram of mixed eccentricity in radial flux [97] and axial flux [98] PMSM. 32
Fig. 3.11 Example of the damaged rotor due to the contact between stator and rotor. 32
Fig. 3.12 Topology configuration of single phase drive. 35
Fig. 3.13 Stator with concentrated coils in (a) axial flux PMSM [110] (b) radial flux PMSM [1]. 36
Fig. 3.14 Topology configuration of (a) Schematic of modular multiple three-phase. (b) Example of modular multiple three-phase [13]. (c) 6-phase axial flux PMSM [1]. 38
Fig. 3.15 Proposed machine topology of (a) doubly-salient flux controllable out-rotor motor [16] and (b) ISNCW [15]. 39
Fig. 4.1 Design process of main phases and tasks. 43
Fig. 4.2 Schematic of (a)space limitation and (b) torque-speed characteristics. 45
Fig. 4.3 Block process of optimization. 50
Fig. 4.4 Schematic of the motor assembly. 52
Fig. 4.5 The optimization model of PMSM. 53
Fig. 4.6 Weight (kg) of the optimal combinations. 54
Fig. 4.7 Short circuit current (A) of the optimal combinations. 54
Fig. 4.8 Efficiency of the optimal combinations. 54
Fig. 4.9 Visualization results of feasible design in 18 slot/12 pole combination 55
Fig. 5.1 Double layer three-phase based on selected slot/pole combinations. 67
Fig. 5.2 Single layer three-phase based on selected slot/pole combinations. 69
Fig. 5.3 Feasible topology of triple three-phase. 75
Fig. 5.4 (a) Sextuple three-phase 18/12. (b) Quadruple three-phase 24/8. (c) Sextuple

three-phase 36/12. 75
Fig. 5.5 Potential candidates for dual three-phase. 77
Fig. 5.6 Dual three-phase, 18slot/12pole in ANSYS Maxwell: (a) topology Model; (b) meshing plots. 78
Fig. 5.7 The waveform of (a) no-load line-line back EMF, (b) analysis of harmonics and (c) efficiency map. 79
Fig. 5.8 The SC behaviour: (a) SC current in the fault phases (b) output torque. 82
Fig. 5.9 Illustration and comparison of inductance of candidates. 83
Fig. 5.10 Comparison of output torque of candidates under difference operation. .. 84
Fig. 5.11 Comparison of torque ripple of candidates under difference operation. ... 85
Fig. 5.12 Comparison of axial force of candidates under difference operation. 86
Fig. 5.13 Comparison of line-line current of candidates under difference operation. 87
Fig. 5.14 Topology of triple three-phase (a) Winding arrangement. (b) Diagram of phasor. 88
Fig. 5.15 Model of triple three-phase 18/12. 88
Fig. 5.16 Diagram of back-EMF and output torque. 89
Fig. 5.17 Schematic diagram of potential location of winding faults. (a) OC in M3. (b) SC in M3. 90
Fig. 5.18 Comparison of torque under open circuit scenarios 91
Fig. 5.19 Current in the M3 and brake torque. 92
Fig. 5.20 Position of the ducts. 93
Fig. 5.21 Size of the duct 93
Fig. 5.22 Sensitivity analysis of split size and output power. 94
Fig. 5.23 Dual three-phase 18/12 DL-1with (a) centre duct (b) inside ducts (c) outside ducts in stator. 96
Fig. 5.24 Dual three-phase 12/10 DL with (a) centre duct (b) inside ducts (c) outside ducts in stator. 97
Fig. 5.25 Comparison of power and inductance ratio with the different ducts in 18/12. 98
Fig. 5.26 Comparison of power and inductance ratio with the different ducts in 18/12. 99
Fig. 5.27 Schematic of windings and splits, and asymmetrical back-emf in 18/12. .. 99
Fig. 5.28 Output torque of triple three-phase machine with varied splits. 101

Fig. 5.29 Effects of slits on output torque and inductance ratio. 101
Fig. 5.30 Torque ripple of triple three-phase with varied split. 102
Fig. 5.31 Out circuit of phase-to-phase SC in one module. 103
Fig. 5.32 Fluctuations of faulty current in the SC phases. 103
Fig. 5.33 Varied sizes of splits with (a) torque and (b) current of post-fault. 104
Fig. 5.34 Triple three-phase with 9 slits in stator. (a) 1-mm slits. (b) 2-mm slits. .. 105
Fig. 5.35 The iterated model for optimization based on proposed model. 106
Fig. 5.36 Bubble chart of weight (kg), short-circuit current (A) and efficiency (%). 107
Fig. 5.37 Schematic topology of optimal candidate. 107
Fig. 5.38 Schematic diagram of phasor. 108
Fig. 5.39 Matrix diagram of self-inductance and mutual inductance. 109
Fig. 5.40 Flux plot distributions under open-circuit in (a) conventional topology (b) modular segments. 110
Fig. 5.41 The fluctuation of flux density in the airgap based on varied rotor position and time. 111
Fig. 5.42 Air gap flux density versus rotor position. 111
Fig. 5.43 FEA results of three-phase. (a) single modular back-EMF voltage @ 11000 rpm. (b) Spectra. 112
Fig. 5.44 Output torque verse rotor position. 113
Fig. 5.45 The radial force on rotor under the on-load operation. 113
Fig. 5.46 Output of the machine under three-phase short-current. (a) Phase current plots. (b) Fluctuation of radial force and torque. 116
Fig. 5.47 Schematic diagram of SC winding and healthy winding of Phase 9 in the module 3 (M3). 117
Fig. 5.48 The output torque under the turn-to-turn SC fault in Phase 9. 117
Fig. 5.49 Flux density distribution on permanent magnets and the demagnetization coefficient. 118
Fig. 6.1 AC copper loss with varied stands of winding. 123
Fig. 6.2 Core loss and its components: eddy current loss and hysteresis loss. 125
Fig. 6.3 Efficiency map of the whole speed range 125
Fig. 6.4 Section of flow direction with slot cooling. 127
Fig. 6.5 Exploded view of a high speed machine with an oil sleeve. 127
Fig. 6.6 Section of flow direction with water jacket cooling. 128

Fig. 6.7 Exploded view of a high speed machine with housing water jacket...... 128
Fig. 6.8 The (a) main process and (b) schematic of potting in the end-winding. 130
Fig. 6.9 Overview of Lumped parameter thermal network applied on this machine. 131
Fig. 6.10 Model created for CFD analysis. 131
Fig. 6.11 Illustration of velocity streamline of coolant in one segment...... 132
Fig. 6.12 The result of temperature rises with varied segment gap size and filling. 132
Fig. 6.13 Temperature distribution of components based on housing water jacket. 133
Fig. 6.14 Comparison of temperature rise in stator (a) Temperature distribution in 3D model. (b) Axial section of segment. 134
Fig. 6.15 Illustration of the potting improvement. 134
Fig. 6.16 Validation of thermal isolation...... 135
Fig. 7.1 The arrangement of search coil for the prototype machine. 138
Fig. 7.2 Induced voltage in search coils with electrical machine speed at 11000 rpm. 138
Fig. 7.3 Voltage of search coils (a) No-load at varied rotor speed (b) Varied load at 11000 rpm. 139
Fig. 7.4 The induced voltage in the varied faults (a) Eccentricity. (b) Winding faults in Module 3: open-circuit, phase-to-phase SC and turn-to-turn SC...... 141
Fig. 7.5 Peak value of induced voltage in search coil (a) clockwise (b) anticlockwise. 142
Fig. 7.6 Schematic of hotspot in the windings. 143
Fig. 7.7 Schematic of orthotropic of carbon fibre. 144
Fig. 7.8 Rotor assembly of surface mounted PMSM...... 144
Fig. 7.9 Model created for mechanical analysis...... 146
Fig. 7.10 FEA results at 20000 rpm. (a) Deformation. (b) Equivalent stress. (c) Equivalent elastic strain...... 147
Fig. 7.11 Model created for mechanical analysis...... 148
Fig. 7.12 Results of modal analysis. 148
Fig. 7.13 Campbell diagram of first four critical speeds...... 149
Fig. 7.14 Electromagnetic force on rotor at initial position. (a) Radial force on rotor. (b) Tangential force on rotor. 150
Fig. 7.15 Radial force under faulty operation. 151
Fig. 7.16 Steel sleeve for assembling the segments. 152

Fig. 7.17 Structure of housing for water jacket. 152
Fig. 7.18 Schematic of testbed and flange. 153
Fig. 7.19 Candidates of feasible layout of receptacles for phase and sensor connector. 157
Fig. 7.20 Interface of inlet and outlet for machine cooling. 157
Fig. 8.1 Schematic of search coils and resistance temperature detectors (RTDs) in (a) segments and (b) Stator assembly. 160
Fig. 8.2 Distribution of temperature sensors in the prototype machine. 160
Fig. 8.3 Rotor shaft and rotor assembly 161
Fig. 8.4 Assembly of stator and housing. 161
Fig. 8.5 Prototype machine. 162
Fig. 8.6 The (a) schematic diagram of resistance measurement and (b) example of measurement. 162
Fig. 8.7 Comparison of measured phase resistance DC and AC (varied frequency). 163
Fig. 8.8 Comparison of phase resistance at DC and AC power supply (at 2k Hz). . 164
Fig. 8.9 Comparison of phase inductance at 1.2 kHz and 2 kHz power supply. 164
Fig. 8.10 The schematic position of d-/q-axis alignment. 166
Fig. 8.11 The connection for measuring inductance (a) d-axis alignment (b) q-axis alignment. 166
Fig. 8.12 (a) RC circuit test (b)Waveform of current of the RC circuit test. 167
Fig. 8.13 The connections for measuring inductances. 168
Fig. 8.14 Example of measured inductance of connection of AB with rotor position (a) at 1200 Hz. (b) at 2000 Hz. 171
Fig. 8.15 Fluctuation of measured resistance and inductance with different connection in three modules (M1, M2 and M3). 173
Fig. 8.16 The schematic of setup for machine test. 175
Fig. 8.17 Setup of testbed connection. 175
Fig. 8.18 Vibration sensors on the test rig. 175
Fig. 8.19 AC/DC power converters for IGNITE machine (a) single unit. (b) three modules assembly. 176
Fig. 8.20 Layout of cooling system for IGNITE machine test. 177
Fig. 8.21 Cooling pipe for the electrical machine test. 177
Fig. 8.22 Stepped speed curve. 180

Fig. 8.23 Measured vibration of electrical machine from standstill to 16500 rpm (Stepped). 181
Fig. 8.24 Vibration acceleration of IGNITE machine in the stepped speed test. 182
Fig. 8.25 FFT spectrum of vibration at 10500 rpm. 182
Fig. 8.26 Test procedure for continuous run-up test. 183
Fig. 8.27 Measured vibration of electrical machine from standstill to 20000 rpm (continuous). 183
Fig. 8.28 Measured induced voltage in the search coils at 2000rpm. 184
Fig. 8.29 Radar map of the measured peak values in the 9 search coils at varied speed (500 ~ 2000 rpm). 184
Fig. 8.30 Waveform of line-line back-EMF (a) at 11000 rpm (b) Comparison with FEA results. 186
Fig. 8.31 Measured back-EMF line-line voltage results in three modules. 187
Fig. 8.32 FFT spectrum of measured line-line back-EMF in three modules (at 12000rpm). 188
Fig. 8.33. Comparison of line-line back-EMF voltage between measured results in module 1 (M1) and FEA results (fundamental results). 188
Fig. 8.34 Temperature rises during the commissioning. 189
Fig. 8.35 Three converters and control box. 190
Fig. 8.36 Operation points of on-load in the test procedures. 190
Fig. 8.37 Measured current vs. torque under 270 VDC. 192
Fig. 8.38 Measured current vs. output power under 270 VDC. 192
Fig. 8.39 Comparison of measured and simulated current vs. efficiency on 270 VDC under varied speeds (5000 rpm, 6000 rpm and 7000 rpm). 193
Fig. 8.40 Measured output torque curve (a) raw data. (b)Filtered data. 194
Fig. 8.41 Transient temperature rise of 7000 rpm with 24.5 Nm output. 194
Fig. 8.42 Comparison of measured and simulated current vs. efficiency under 540 VDC. 195
Fig. 8.43 Comparison of measured and simulated current vs. efficiency under 540 VDC. 196
Fig. 8.44 Measured current vs. output power under 540 VDC. 196
Fig. 8.45 Raw data of measured voltage output from torque sensor. 196
Fig. 8.46 Transient temperature rise of 11000 rpm under 540 VDC. 197
Fig. 8.47 Circuit breaker for open-circuit test. 197

Fig. 8.48 Schematic of OC occurred in phase or sectors. (a) One sector OC. (b) Two sectors OC. 198
Fig. 8.49 Transient response of output torque. 198
Fig. 8.50 Response of vibration speed of OC test. 199
Fig. 8.51 Measured vibration response of post OC fault at varied speed at 1000 rpm. 201
Fig. 8.52 Measured vibration response of post OC fault at 5000 rpm (a) velocity (b) acceleration. 201
Fig. 8.53 Vibration response of post OC fault at 6000 rpm. 202
Fig. 8.54 Waveform of phase current under varied scenarios. (a) Healthy. (b) OC in one module. (c) OC in two modules. 204
Fig. 8.55 Measure temperature curves in combined test of speed (1000, 5000 and 6000 rpm), load (0, 10 or 20 A) and healthy/faulty M2 (solid lines). 205
Fig. 8.56 Measured temperature fluctuation of M1 and M2 under 6000 rpm with 20 A phase current. 205
Fig. 8.57 Fault current during the EMI issue. 206
Fig. 8.58 Waveform of fault current during the EMI issue. 207
Fig. 8.59 Example of unexpected temperature rise in phase winding during the machine test. 207
Fig. 8.60 Temperature record of critical failure. 208

List of Tables

Table 2.1The location, power, type, quantity of electrical actuators on A380 flight control system [22, 24]. 9
Table 2.2 Capacity comparison of power supply on the MEA. 18
Table 2.3 Information of advanced electrical machine on aircraft. 21
Table 3.1 Configuration and evaluation of FT approaches. 40
Table 3.2 PMSM application on aircraft and the approaches for improving reliability. 41
Table 4.1 The Specification of candidate PMSG. 45
Table 4.2 The winding factor of varied slot/pole combination. 48
Table 4.3 Classifications of slot/pole combinations. 48
Table 4.4 Linear MCDM values of 18/12 candidate 57
Table 4.5 The comprehensive rank of feasible combination. 57
Table 5.1 The feasibility of multiple three-phase topology. 60
Table 5.2 The FT evaluation of dual three-phase winding. 70
Table 5.3 Feasible slot/pole combination for triple three phase. 71
Table 5.4 Feasible slot/pole combination for quadruple and sextuple three-phase. 72
Table 5.5 The FT Evaluation of Dual three-phase winding. 82
Table 5.6 Faults combination of triple three-phase topology. 90
Table 5.7 The comparison of output under varied scenarios. 91
Table 5.8 The range of variables in duct. 93
Table 5.9 Evaluation of fault tolerance of 18/12 slot/pole combination. 100
Table 5.10 Comparisons of currents in varied topologies 103
Table 5.11 Average and torque ripple in varied splits and size. 105
Table 5.12 Differences of iterated model and previous model. 106
Table 5.13 Parameters of optimal design and output performance. 107
Table 5.14 Angle of windings. 108
Table 5.15 Potential failure modes and fault's location. 114

Table 5.16 Output comparison under varied scenarios. 115
Table 6.1 Loss distribution. 125
Table 6.2 Property of the coolant: oil and water. 126
Table 7.1 Properties of selected carbon fibre. 146
Table 7.2 Frequency and critical speed. 149
Table 7.3 Definition of electrical interface of windings. 154
Table 7.4 Definition of electrical interface of embedded sensors. 154
Table 8.1 Results of Ld and Lq. 167
Table 8.2 Calculated Ld and Lq at 1100 Hz. 174
Table 8.3 Calculated Ld and Lq at 2000 Hz. 174
Table 8.4 List of setup for electrical machine test. 178
Table 8.5 Classification of rotating machinery in ISO 10816. 179
Table 8.6 Velocity range limits and machine classes. 180
Table 8.7 Measured back-EMF constant and torque constant. 192
Table 8.8 Comparison of measured post-fault output. 199
Table 8.9 The status of the vibration test with random OC fault. 200
Table 8.10 Static measurement after converter damaged. 208

Chapter 1 Introduction

In this chapter, the aims and objectives of this thesis will be explained, including the overall intention of the project and specific steps involved.

1.1 Background

The aviation industry is under the pressure to decarbonize and achieve net zero emission. For example, conventional aircraft would make the first step towards electrification as more-electric aircraft (MEA). The background of this thesis is aviation electrification. The main focus of this thesis is the implementation of a product-oriented design and study of a permanent magnet starter-generator for use in MEA.

Besides, the requirements for the final prototype were provided by the IGNITE project, which is funded by the Clean Sky 2 Joint Undertaking under the Horizon 2020 research and innovation program, grant agreement number 820913. It aims to develop a high-performance test rig for testing and demonstrating high-voltage direct current (HVDC) power generation channels. This involves the achievement of electrical machines, drive integration and testing, as well as the design of a test rig, supervisory control and data acquisition (SCADA), test rig integration of high-performance electrical generation systems, test rig commissioning, and test planning and management.

1.2 Aims and objectives

The objective of this thesis is to design and develop an innovative aircraft starter/generator that is both fault tolerant and high in power density. The aim is to create a fault tolerant starter/generator that is efficient, reliable, compact, and lightweight, contributing to higher performance and efficiency.

To achieve this goal, the research will focus on meeting the following potential requirements:

(1) To identify the system design specifications and requirements in terms of torque-speed performance, weight, reliability and power density with the aim of developing an innovative device.

(2) To design and develop a novel permanent magnet starter/generator (structure/topology), high power density and fault tolerant with high robustness and mechanical strength, that can be easily integrated and manufactured. The machine will be developed with innovative magnetic, electrical, mechanical and thermal materials to achieve the high efficiency, reliability and mechanical strength while minimizing the overall cost, size, weight and cooling effort.

(3) To perform a set of trade-off studies and conceptual designs in order to identify the best combination of electrical machines, power electronic converters to achieve maximum power density and optimized.

(4) To evaluate an innovative and integrated cooling loop for the device with focus on efficiency and minimization of system weight and size.

(5) To manufacture and test the devices. The prototype will be tested initially to validate the design and then will be delivered, integrated and tested.

(6) To perform extensive functional tests of the mechatronic system. The functional tests will include motoring, generation, and fault tolerant test, electromagnetic conduction as well as mechanical vibration and heat generations.

(7) To develop functional and behavioural dynamic models of electrical machine and their interface with the mechatronic system to support the system design. The developed dynamic models will also be used to provide the ability to design and tune control laws in the future.

1.3 Thesis outline

This thesis will follow a formalized methodology known as model-based systems engineering (MBSE) to support the requirements, design, analysis, verification, and validation associated with the development of complex systems. The design process

will be carried out in accordance with this methodology.

Chapter 2 will give a comprehensive review of electrical machines for aircraft electrification and elicit the general requirements from specific application.

Based on the requirements for electrical machine applied on aircraft, Chapter 3 will present the state-of-the-art techniques for fault tolerant permanent magnet synchronous machine design and control methods for aircraft applications.

In Chapter 4, the initial design of the permanent magnet starter-generator will be carried out based on specifications, initial definitions, and a multiple-objective, multiple-discipline machine design process.

To meet the requirements of fault tolerance, a detailed topology design of multiple three-phase will be compared and evaluated in Chapter 5. The finite element analysis method will support this design process. A novel topology is proposed and investigated for fault tolerance, and the optimal candidate under faulty scenarios will be researched.

Chapter 6 will focus on thermal management and machine losses. Loss modelling and cooling methods will be introduced, and two different methods of thermal management, Lumped parameter thermal network (LPTN) and computational fluid dynamics (CFD), will be utilized to quantify the performance of cooling.

Chapter 7 will provide the final design, including fault monitoring, mechanical and interface design. Extra sensors, such as search coils and thermal sensors, will be embedded in the winding to monitor potential faults. Modal analysis and rotor stress analysis will verify the safety under high-speed operation, and details of the interface will also be designed.

In Chapter 8, the comprehensive prototype process will be exhibited, from critical parts to assembly design. Static measurement will be the first test, followed by dynamic testing. Commissioning and on-load testing will be the basis for the following test of faulty scenarios. The performance of the prototype machine will validate its requirements.

Based on the experience gained during the development of the prototype, general

conclusions and future work will be discussed in Chapter 9.

1.4 Scientific contribution and list of related publications

This thesis provides the-state-of-the-art reviews about permanent magnet electrical machines applied on current aircraft, as well as the solutions of fault tolerant. Based on these conclusions, a novel topology of permanent magnet start-generator was proposed, optimized, prototyped and experimental validated, given consideration to the requirements of fault tolerance and high power density

The final conclusion proves the permanent magnet electrical machine with innovative topology is capable of safety-critical application on aircraft, such as starter-generator. These conclusions can move forward to higher level of aviation electrification.

International conferences

B. Wang, Y. Liu, G. Vakil, T. Yang and Z. Zhang, "Feasibility of Permanent Magnet Fault Tolerant Machines for Aircraft Starter/Generator Systems," 2020 International Conference on Electrical Machines (ICEM), Gothenburg, Sweden, 2020, pp. 2104-2110, doi: 10.1109/ICEM49940.2020.9270965.

Wang, B., Rocca, A., Vakil, G., Yang, T. et al., "Design Optimization of Modular Permanent Magnet Machine with Triple Three-Phase for Aircraft Starter Generator," SAE Technical Paper 2022-01-0055, 2022, https://doi.org/10.4271/2022-01-0055.

Journals

Wang, Bo, Gaurang Vakil, Ye Liu, Tao Yang, Zhuoran Zhang, and Chris Gerada. 2021. "Optimization and Analysis of a High Power Density and Fault Tolerant Starter–Generator for Aircraft Application" Energies 14, no. 1: 113. https://doi.org/10.3390/en14010113.

Currently, there are several journal papers are in progress now.

B. Wang, Mi. Tang, G. Vakil, T. Yang, "A Review of Fault tolerant Permanent Magnet Synchronous Machine Design and Control for Future Aircraft Applications".

Status: ***In review***

B. Wang, Mi. Tang, G. Vakil, T. Yang, "Design and validation of Modular Permanent Magnet Machine with Triple Three-phase for Starter-generator of Aircraft Application". Status: ***In review***

Chapter 2 Electrical machines for aircraft electrification

2.1 Introduction

This chapter provides a comprehensive review of the latest advancements in aircraft electrification. Additionally, it will examine the key subsystems that have traditionally been powered by hydraulic or pneumatic systems to determine their suitability for replacement with electrical components. Furthermore, the chapter will present the current state-of-the-art in electrical machines for aircraft applications.

2.2 Aircraft electrification

As the demand for transportation continues to increase, the environmental impact of transportation has become a growing concern. There is a general consensus within the transportation industry about the need for cleaner vehicles. To address this concern, the concept of transportation electrification technology has emerged as an effective approach. Electric vehicles have been at the forefront of this technology, leading the way [18]. Some researchers believe that relief for congested cities may come from the air rather than the roads. The emergence of urban air mobility applications, such as electric vertical take-off and landing (eVTOL) aircraft, has been summarized [19]. These aircraft are being developed as an innovative solution for transportation in urban areas.

Conventional aircraft industries are facing the challenge of addressing climate change and have set challenging targets to reduce CO2 emissions [3]. The most direct approach to achieving aviation electrification is to replace current on-board systems

with electrical counterparts. However, the development of all-electric aircraft (AEA) has faced many challenges and it may be difficult to completely replace conventional aircraft in the short term due to issues such as the energy density of batteries and the requirements for high reliability and power density electrical machines. As a major step forward, the more-electric aircraft (MEA) concept supports the much-needed electrification of aircraft [20].

2.3 Distribution of electrical machines on aircraft

Fig. 2.1 presents a comparison of the electrification levels in important subsystems, between conventional aircraft (B737) and other pioneering MEAs. On the conventional aircraft, all the subsystems are driven by hydraulic or pneumatic systems, which these subsystems are gradually replacing by electrical counterparts.

The adoption of electrical systems, whether in the commercial or military sectors, provides significant benefits. For instance, employing electrical starting for the aeroengine through the engine starter/generator eliminates the need for the engine tower shaft and gears, power take-off shaft, accessory gearboxes, and reduces engine starting power, especially in cold conditions. Additionally, the starter/generator could increase the demand for electricity, as shown in *Fig. 2.2*.

Using a fan shaft generator that allows emergency power extraction under windmill conditions replaces the conventional, inefficient single-shot ram air turbine, which enhances aircraft reliability and survivability under engine-failure conditions. Replacing the engine-bleed system with electric motor-driven pumps reduces complexity and installation costs.

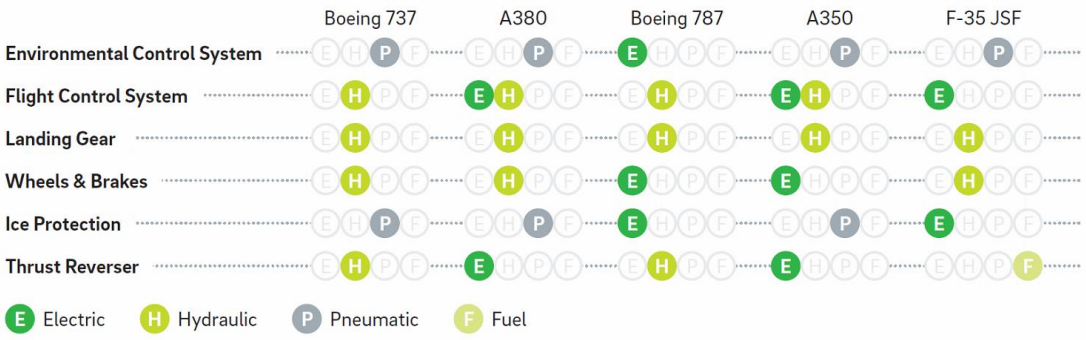


Fig. 2.1 Comparison of electrification between conventional (B737) and some pioneering MEAs [21].

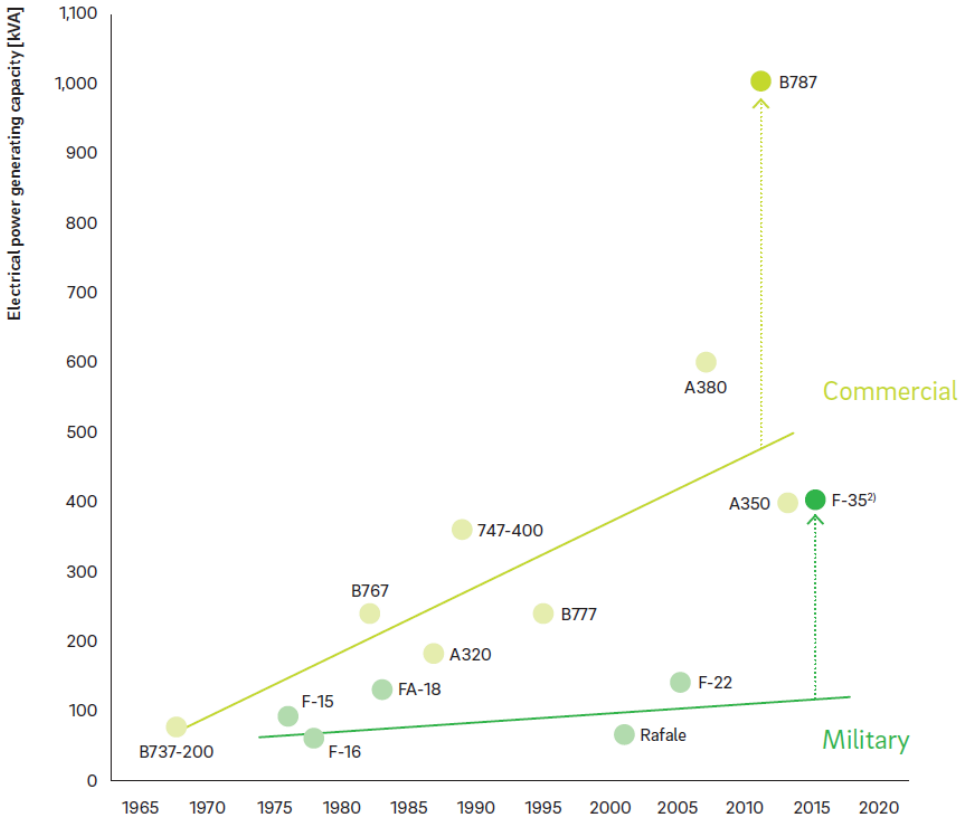


Fig. 2.2 Electrical power generating capacity of aircraft [21].

In summary, it is essential to analyse several key subsystems that could be electrified by utilizing electrical machines and to identify the general requirements for specific applications. This work is highly valuable and can contribute significantly to the development of electrified aircraft.

2.3.1 Flight control system

Typical aircraft flight control surfaces are divided into primary flight surfaces (shown in red in *Fig. 2.3*) and secondary flight surfaces (shown in blue in *Fig. 2.3*). The actuation of primary flight surfaces can control the aircraft trajectory, specifically the three rotational degrees of freedom: the ailerons for roll, the rudder for yaw, and the elevators for pitch. Secondary flight surface actuation is used during takeoff, landing, and braking. Currently, all actuators are driven by hydraulic systems in conventional aircraft architecture.

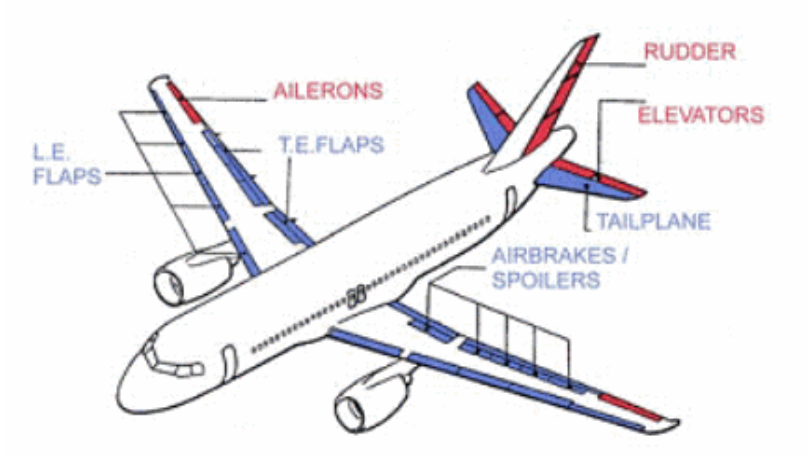


Fig. 2.3 Flight control surfaces on aircraft [22].

When considering replacing hydraulic actuators (HA) with electrical powered actuators, the most obvious options are electromechanical actuators (EMAs) (as shown in *Fig. 2.4*), electro-hydraulic actuators (EHAs), or electrical backup hydraulic actuators (EBHAs). These actuators are already found in in-service aircraft, with EHAs and EMAs becoming increasingly mature and being introduced in recent large commercial transport aircraft, such as EMAs for mid-spoiler surfaces and the trimmable horizontal stabilizer on the Boeing 787 [23]. Table 2.1 lists the location, power, type, and quantity of electrical actuators used for the flight control system on the Airbus A380, although all of them are the alternative actuators of active/back-up work architecture. As a pioneer in military MEA, the Joint Strike Fighter (F-35) has been equipped with EHA-actuated primary flight control systems.

Table 2.1The location, power, type, quantity of electrical actuators on A380 flight control system [22, 24].

No.	Location	Power (kW)	Type	Quantity
1	Aileron	6	EHA	4
2	Spoiler	150	EBHA	4
3	Elevator	10	EHA	4
4	Rudder	10	EBHA	4
5	Horizontal stabilizer	50	EMA	1
6	Flaps	-	EMA	1
7	Slats	-	EMA	1

Continuous advancements in high-performance magnetic materials, miniaturized

and highly efficient power electronics, and gear technology have made electromechanical actuators (EMAs) increasingly competitive compared to hydraulic actuators in terms of power-to-weight ratio, when considering the entire flight control system.

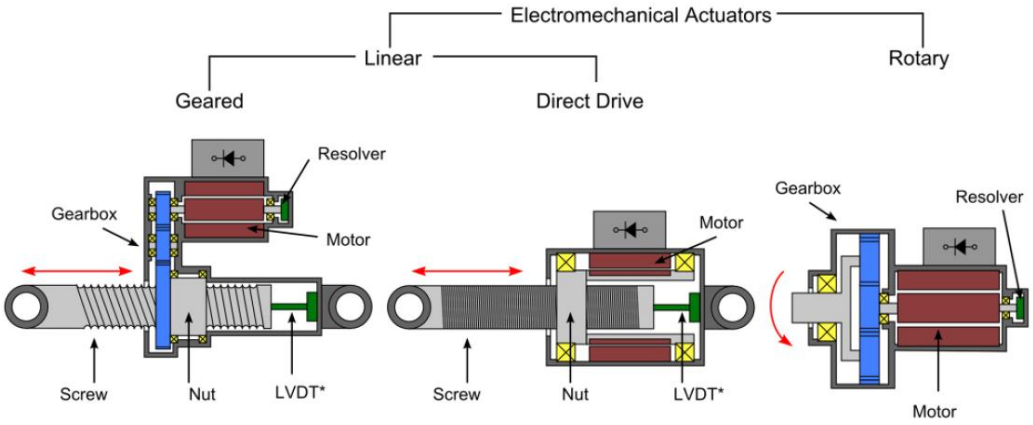


Fig. 2.4 Classification of different flight control EMA types [25].

As a basic form, EMA is susceptible to certain single-point failures that can occur in the permanent magnet synchronous motor (PMSM), gearbox, screw, or other powertrain components, resulting in undesired faults that can complicate flight certification, especially for safety-critical primary flight control surfaces [26].

Fault-tolerance is required for motor-drive high lift system components, such as slats and flaps, and are defined as degraded operating modes [27]. For example, in the case of the EMA for flap application, the first fault (intended as a lack of a phase in the motor or in the power converter) must not affect the rated torque-speed performances (first degraded mode), while the incoming of a second fault implies that the actuation must be guaranteed at the rated torque but at 2/3 speed (second degraded mode).

To decrease the possibility of single-point failure, direct-drive/integrated EMA or redundancy methods have been investigated. An integrated EMA, directly coupled PMSM to a roller screw without any intermediate gearbox, was detailed in [28]. It included a high level of actuator integration in order to minimize weight and volume while ensuring high reliability and fault tolerance. Similar work has been done in [29], aimed at lowering component count and reducing jamming probability. Integrating EMA systems in safety-critical applications implies three main challenges: (a) the detection of all fault cases that could lead to a safety-critical state,

(b) finding measurement parameters capable of detecting faults, and (c) developing algorithms to detect faults under all flight conditions [25].

Compared to complete redundancy and electrical redundancy (as shown in the schematic structure in *Fig. 2.5*), fault tolerant redundancy has significant advantages in terms of volume and mass, good failure isolation, and high utilization level[30]. The work in [31] demonstrated that a sensorless 5-phase permanent magnet brushless motor for aircraft flap actuation can run up to rated torque even when one or two phases were opened. The work in [32] proposed a multipole permanent magnet machine using fractional-slot concentrated winding and the Vernier machine structure which the fault tolerant capability.

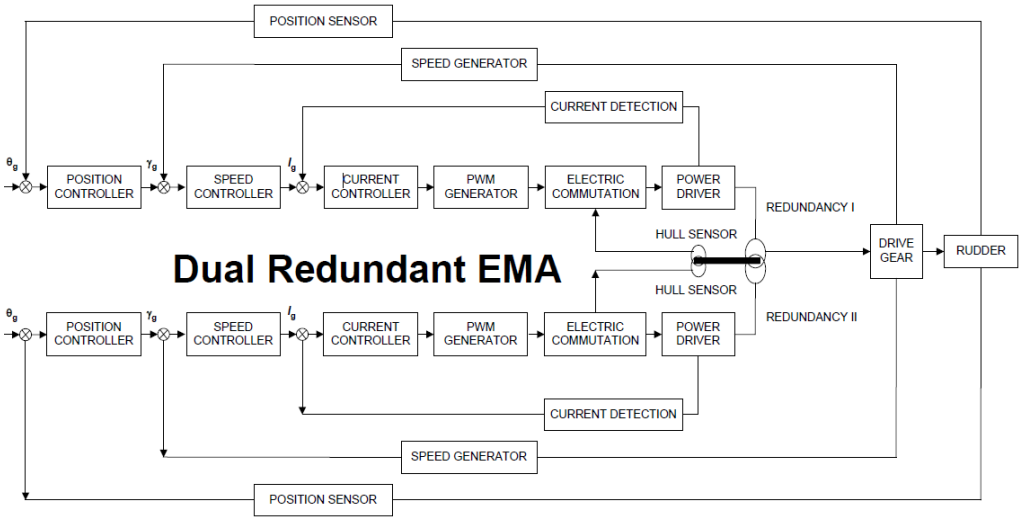


Fig. 2.5 Electrical dual-redundant structure [33].

EMA systems have the added advantage of being able to regenerate electrical power during the 2nd and 4th quadrant of the torque-speed curve, instead of consuming it. This paper investigates two key aspects: the effect of increased DC bus voltage on the management of regenerated energy, and the feasibility of returning energy to the engine inertia [34]. Safety-critical designs of EMA systems for commercial aircraft must also be considered, as discussed in [26]. Further advancements in fault tolerant permanent magnet machines will be addressed in subsequent chapters.

2.3.2 Engine control

The EMAs are also utilized in various control and monitoring functions for MEA engine, including steering of variable stator vanes and variable bleed valves, controlling the thrust reversers, and modifying the geometry of air intakes or nozzles

[35]. These functions often operate under severe environmental conditions, ranging from -50℃ to +125℃. For example, Airbus A380 has implemented EMAs in their Electric Thrust Reverse Actuation System installed on two inboard engines [36].

2.3.3 Landing gear system

The landing gear system is a major consumer of hydraulic power, as it powers the landing gear extension/retraction actuators, braking, and steering using hydraulic pumps. *Fig. 2.6* shows the main landing gear of the B777 aircraft. As MEAs move towards reducing or eliminating hydraulic power for aircraft systems, the electrification of the landing gear system presents additional challenges [37].

However, due to the safety-critical nature and high power output requirements of landing gear systems, EMA systems can easily incorporate active damping, but do not inherently have a simple means of passive (unpowered) damping. Moreover, the electric extension/retraction of landing gear systems is typically only feasible for small aircraft due to certain factors outlined in [38]. Therefore, there has been a concerted effort to develop EHA and EMA solutions for large commercial aircraft [39, 40].



Fig. 2.6 Main landing gear assembly (hydraulic) on a Boeing 777 [38].

Aircraft braking actuators have been integrated into the wheels, with the 787 being the first large commercial aircraft to feature EMA actuated brakes supported by SAFRAN [41]. A trade-off study based on lighter system weight, high availability, low installation and maintenance costs, and comparative performance to hydraulic

actuators, showed that EMA was more beneficial.

In addition, electric taxiing systems can save fuel and reduce engine wear, leading to cost savings for airlines. Similar progress has been made in this topic, with environmental benefits assessed through object-oriented simulation [42]. The aircraft can use electric taxiing supplied by Auxiliary Power Units (APU) instead of the main engines, allowing it to taxi on airport taxiways [43]. Small electric motors fitted inside the wheels of the landing gear enable this capability (*Fig. 2.7*). In [44], the electrical machine (*Fig. 2.8*) was designed using multi-objective optimization, considering power electronics, electromagnetic, thermal, and mechanical constraints due to weight and volumetric budgets. However, the adoption of these systems in commercial aircraft is still limited due to various factors, such as high development and implementation costs, safety and certification concerns, and infrastructure limitations at airports.

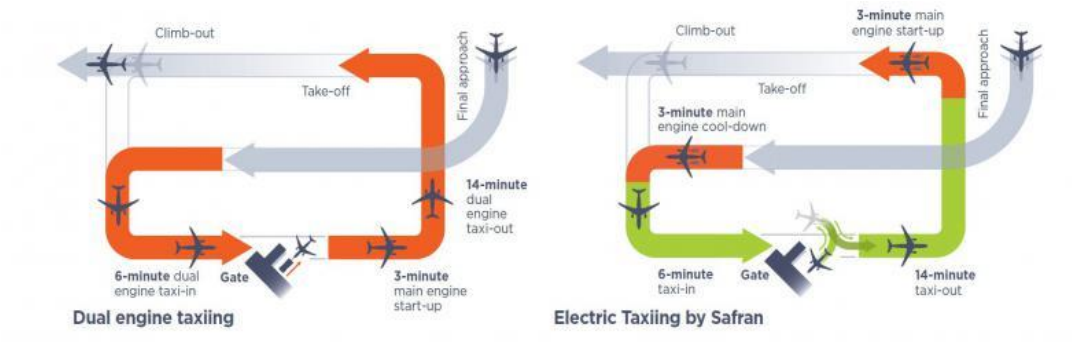


Fig. 2.7 Comparison of engine and electric taxiing [43].

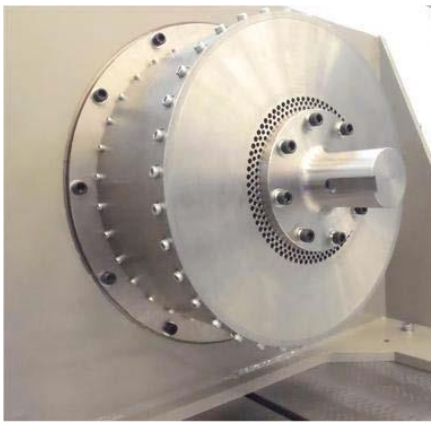


Fig. 2.8 The green taxiing (GT) motor prototype [44].

From a safety standpoint, electric steering is considered less critical than the extension/retraction actuators in the landing gear system, as well as the requirement

for nose-wheel steering. However, nose-wheel steering presents a challenge for conventional EMA actuation due to the periodic high-impact loads caused by runway obstructions. To address this challenge, many existing aircraft use multiple motors to drive electromechanical actuators, which are connected by means of a clutch or speed-summing gearboxes [45] (as shown in *Fig. 2.9*). While these arrangements allow for continued operation after the failure of one motor, there is an additional mass and reliability penalty associated with the gearbox.

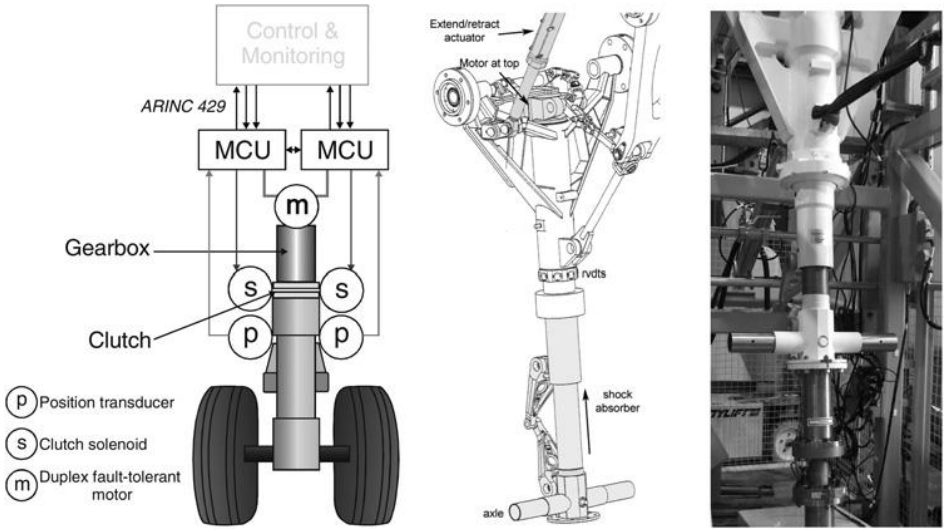


Fig. 2.9 Prototype nose wheel steering actuator (left–right: functional schematic and illustration) [45].

It is important for electrical machines applied in the landing gear system to have similar competences in fault tolerance, high power density, and the ability to withstand demanding environmental conditions, such as landing shock, short-term overload, and high temperature. These competences are similar to those required for the flight control system. This is because the landing gear system plays a crucial role in ensuring the safety of the aircraft during takeoff and landing. Any failure or malfunction in this system can have serious consequences for the aircraft and its passengers. Therefore, the electrical machines used in the landing gear system must be able to operate reliably under these demanding conditions and tolerate faults without compromising safety.

2.3.4 Fuel system

The mechanical power is extracted from the engine shaft and transmitted to the fuel pump via an engine gearbox [46]. Engine fuel pumps consist of low-pressure transfer

pumps (below 5000 psi) and high-pressure fuel pumps (5000 psi or above). Traditionally, the former is electrically driven, and the latter are mechanically (geared) and hydraulically driven. However, it is the latter that are in need of electrification to save space, increase efficiency, and reduce maintenance requirements. Electrically driven fuel pumps provide variable-speed solutions and can dynamically control the fuel flow rate to match the actual demand, thereby reducing fuel consumption, operational costs, and maintenance requirements.

Several studies have investigated the development of fault tolerant fuel pump drives. One study used Halbach magnets and fuel cooling to develop a four-phase, fault tolerant fuel pump drive, which showed excellent performance in full running tests including ride-through performance during an imposed fault in the drive [47]. Another study developed a four-phase, 30 krpm, 100 kW PMSM with electrical fault tolerance that is capable of handling a single electrical fault occurrence [8] (*Fig. 2.10*).

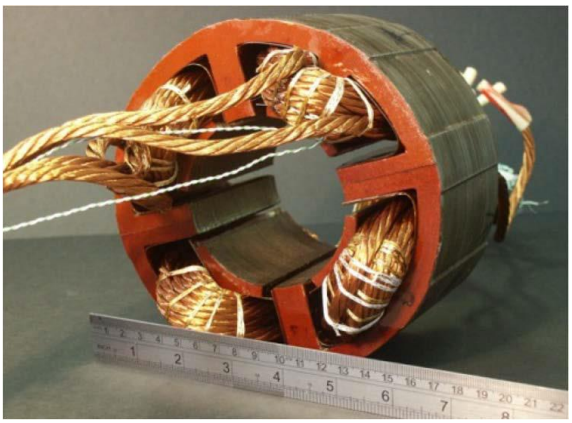


Fig. 2.10 A fault tolerant PMSM (4-phase, 100kW) for fuel pump [8].

An on-board inert gas generation system (OBIGGS) is used to infuse the gas tank of the aircraft with nitrogen to prevent any kind of explosion that might result from a static build-up in the tank, leading to accidental electrical arcing in the various systems in the tank, and causing catastrophic consequences. In conventional architectures, the OBIGGS function has been implemented using a pneumatic system [48]. In modern MEA, it is possible to eliminate the use of bleed air for OBIGGS by implementing a compressor driven by electric motors and power electronic drives. The motor which applied for the fuel system is 270 VDC, 50 kW PMSM.

2.3.5 Environmental control system

The expanding use of electrical systems has led to the elimination of the use of bleed air for the ECS (Environmental Control System) in modern MEA, as shown in *Fig. 2.11* [8]. The ECS is responsible for regulating the cabin temperature and air pressure to achieve passenger comfort. In the Boeing 787, the traditional pneumatic system and air ducts from the engine have been eliminated, and a set of compressors utilizing electric power is used to provide the necessary functions. The largest motors (120 kW, 20000 rpm PMSM) and power electronic converters are used to power these compressors. The design of the total electric power system architecture takes into account reliability and redundancy, which are important considerations for the ECS.

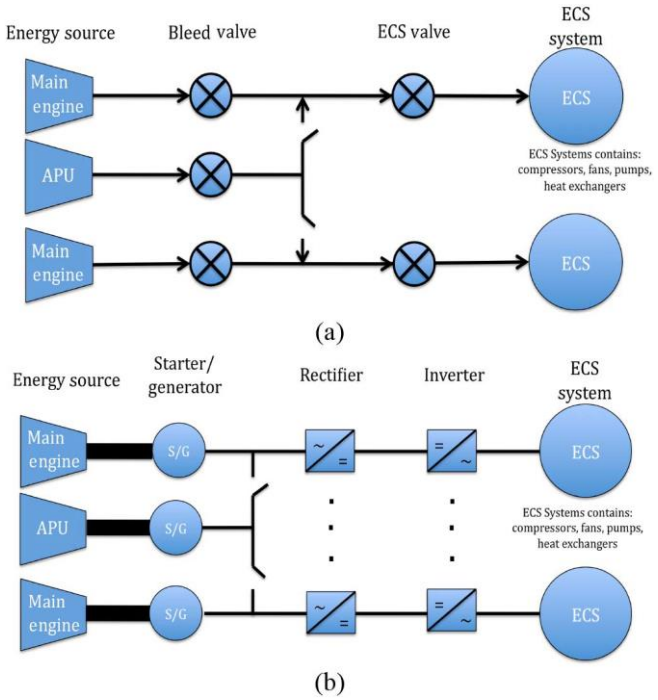
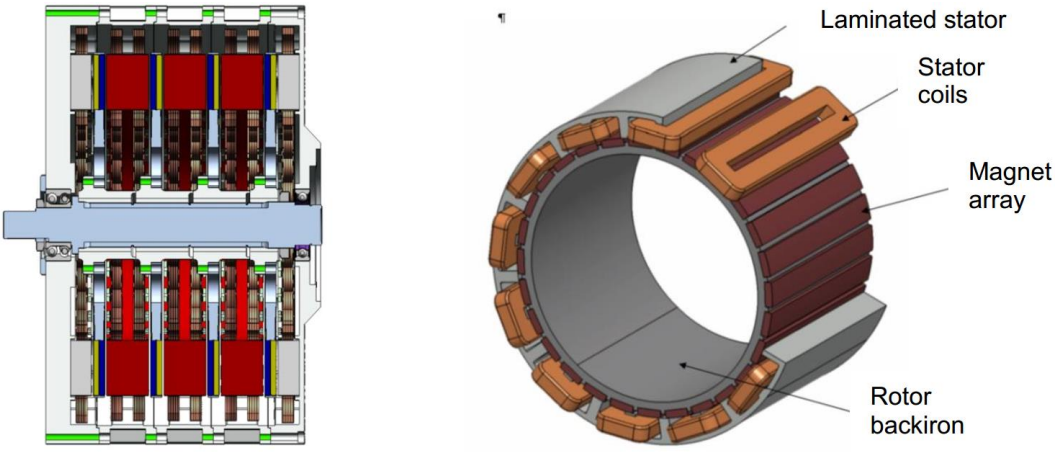


Fig. 2.11 (a) ECS with bleed air. (b) Electric ECS with no bleed air [8].

2.3.6 Electric tail rotor system

The electric tail rotor system also offers improved manoeuvrability and controllability, as well as reduced noise and vibration levels. With electric motors, the torque response is faster and more precise, allowing for more agile and responsive manoeuvres. Additionally, the elimination of mechanical gears and shafts reduces the overall weight and complexity of the system, leading to better fuel efficiency and lower maintenance costs. The use of electric power also allows for more flexible and modular system architecture, making it easier to integrate with other electric systems on the aircraft. Overall, the electric tail rotor system is a promising technology that offers significant benefits for helicopter operations.

The electric tail rotor system has been successfully prototyped and tested, as demonstrated in [49, 50]. *Fig. 2.12* shows the topologies of full-size axial-flux and radial-flux electric tail rotor motors, which have been investigated and achieved peak ratings of up to 340 kW, 2000 Nm, and 4500 rpm. The fault tolerance target was achieved through the use of multiple discs and a modular design in the axial and radial flux topologies, respectively.



(a) (b)

Fig. 2.12 Axial-flux and radial-flux electrical machine topologies considered. (a)Double air gap axial-flux topology, 4 rotor discs (b) 4 x 3-phase phase modular wound radial-flux topology.

The characteristics of the double airgap axial-flux and the modular wound radial-flux topologies have been compared. It was found the axial-flux and radial-flux designs had near identical active weights, and the prototypes exhibited similar continuous output capabilities. However, the radial-flux design proved to be overall more efficient and better suited to the tail rotor drive configuration. To ensure fault tolerance, a multi-phase fault tolerant aircraft propulsion drive has been established, capable of dynamically characterizing electrical drive systems.

2.3.7 Electric power generation

With the continuous advances in high power solid-state static switching technology and corresponding control strategies, the electrical power system has made considerable progress. It started with the twin 28 VDC system and evolved into several types such as constant speed constant frequency (CSCF) system, variable speed constant frequency (VSCF) system, and variable speed variable frequency (VSVF) system. To meet the increasing demand for power capacity and

performance, the use of high voltage systems has obvious merits in terms of reliability, efficiency, and power distribution.

The surging demand for power supply is creating a growing market for aircraft electrification. For commercial aircraft, the generator (main power supply), Auxiliary Power Unit (APU), and Ram Air Turbine (RAT, for emergency) constitute the electric power source [22]. The capacity comparison of power supply of three main MEAs is listed in the Table 2.2.

Table 2.2 Capacity comparison of power supply on the MEA.

Aircraft	Generator	APU	RAT
Boeing 787	250kVA×4	225kVA×2	10kVA
Airbus 380	150kVA×4	120kVA×2	70kVA
F-35	250kVA	-	-

A fault tolerant MEA electrical power system should be capable of providing continuous power to all loads in the event of one failure, mission-critical loads after two failures, and flight-critical loads after three failures. The reliability of an electrical power system is generally evaluated at the system level, with the design philosophy focusing on avoiding single points of failure through redundant systems, standby systems, protective systems, and systems separation. Currently, multiple generators are used for most operations, with the APU and RAT serving as backup in case of emergencies in existing electrical power architectures [33]. The Starter-Generator (SG) is a mature technology that integrates the functions of starter mode and generator mode, with a high power factor and de-excitation ability, and has been applied to several pioneer MEAs, such as the B787 [34]. As shown in the *Fig. 2.13* [35], the electrical power system for the B787 consists of two SGs per engine and the APU, with SGs serving as the main power source for electrical devices during normal operation and the APU serving as emergency backup.

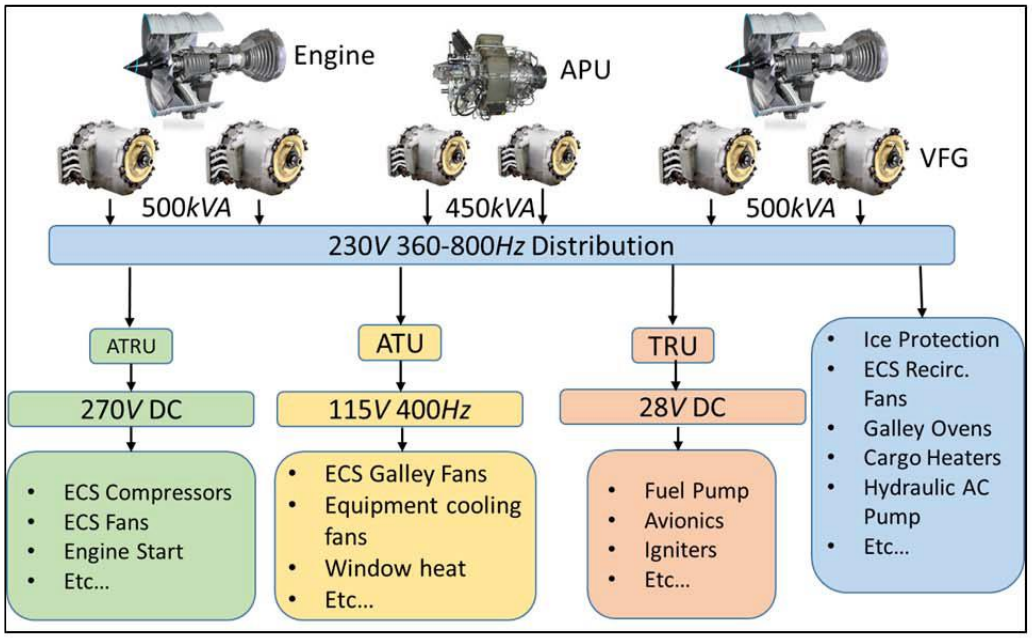


Fig. 2.13 Electrical power system structure of B787 [51].

The mature multi-stage electrical machine is the mainstream candidate for SG even alternative topologies varies. The current generator technology employed on most commercial and military aircraft is the three-stage wound field synchronous generator. These architectures can improve the MTBF (mean time between Failures) and power density. Meanwhile, it is easy to control because of the principle of electrical excitation and demagnetize when faults occurred.

The mature multi-stage electrical machine is the mainstream candidate for SG even alternative topologies varies. As shown in *Fig. 2.14*, the pre-exciter (PE), main exciter (ME) and main generator (MG) are arranged on the rotating shaft, respectively [52]. Two-stage is relatively simpler without PE machine than three-stage. Nonetheless, the complex structure, which power electronics and windings on the rotating ME rotor, has reliability risk at high speed and is difficult in starting control strategy. The Lockheed Martin-led team achieved key accomplishment on development and flight test of a switch reluctance (SR), dual-channel S/G system to provide a fault tolerant, redundant 270 VDC electrical power source for F-35, a single-engine fighter [53]. The research team has adopted the replacement of the original SR machine ES/G with a synchronous generator to accommodate a broader power generation capability.

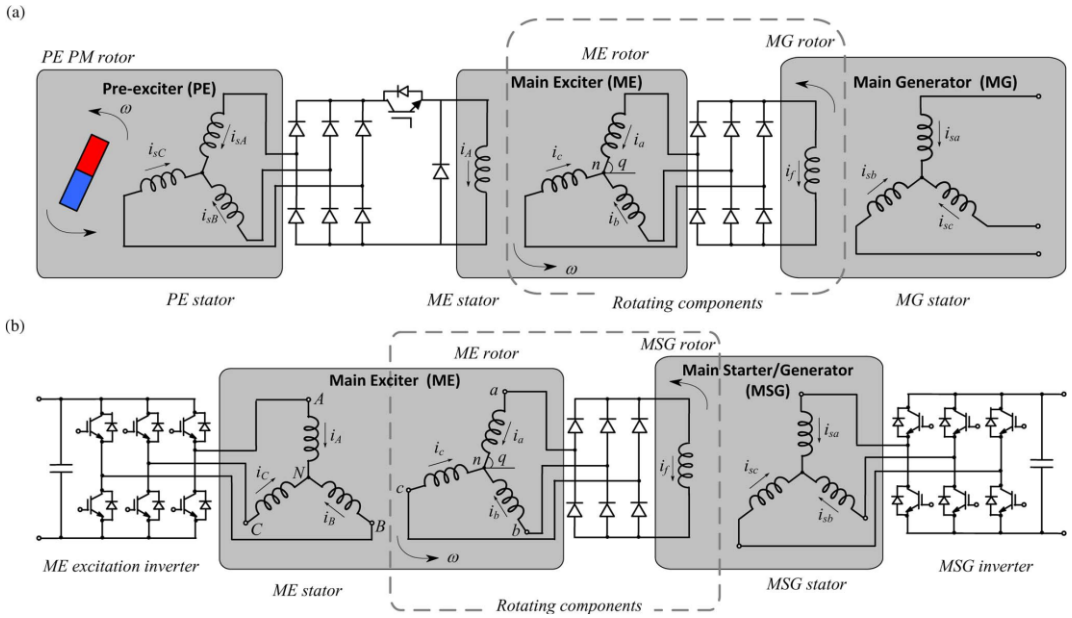


Fig. 2.14 Schematic of an aircraft generator. (a) Three-stage aircraft generator. (b) Two-stage aircraft generator with the three-phase ac exciter [52].

2.4 The state-of-the-art of electrical machines on MEA

Electrical machines, as the core pillar of energy conversion, play a vital role in the transportation electrification [54]. In the electrical machine roadmap, they are expected to achieve better performance with lower cost [55]. Electric Machines, which applied on the more-/hybrid-/turbo-electric aircraft have been reviewed comprehensively [56], such as wound field synchronous machine (WFSM) [57, 58] for generator system, high temperature superconducting (HTS) [59] as strict power density application, switched reluctance machines (SRM) [53] for fault tolerant applications, etc. Due to the merits of high power density and efficiency, PMSMs are the leading selections applied on pioneering MEA, such as actuation of flight control system [22], green taxiing [44], landing gear system [45], fuel pump [47], environment control system [60] and starter-generator [61]. The state-of-the-art of high power density machines for aerospace applications are listed and drawn in the Table 2.3 and *Fig. 2.15* [62].

Additionally, high power PMSMs have been designed as all-/hybrid-electric aircraft propulsion system [63, 64]. The emerging high power PMSMs have been prototyped and applied on AEA/MEA, which low speed suits for propulsion system and high speed for generator, as shown in *Fig. 2.16*.

The e general trends of high power density machines include these aspect:

Table 2.3 Information of advanced electrical machine on aircraft.

Manufacturer	Rated Power (kW)	Rated power density (kW/kg)
ThinGap	4	2.5
Launchpoint	5.22	8.2
KDE Direct	7.2	10.4
Joby motor	8.2	4.6
Yuneee	20	2.4
ACENTISS	32	2.9
Rotex	50	2.5
UoN	59.1	0.5
Siemens	65	5
Siemens	100	7
ENSTROJ	100	4.9
RR-TUOS	100	4.4
Siemens SP200D	260	5.2
Honeywell	1000	7.9

(1) Higher power (>100 kW) electrical machines are utilized in a wide range of applications, including small aircraft (4-seat), regional aircraft (50-seat and more), and large commercial aircraft (such as the Honeywell machine). Electrical machines in the 10-100 kW range predominantly serve smaller planes. For lower power requirements (<10 kW), electrical machines are primarily employed in unmanned aerial vehicles (UAVs) and remote-controlled small planes.

(2) All machines are PM (radial inner rotor, radial outer rotor, and axial flux) electrical machines.

(3) Advanced cooling methods are necessary for high power density application. Higher power machines (≥100 kW) are largely liquid-cooled. Lower power machines (<100 kW) are largely forced air-cooled.

(4) In general, the lower-speed machines lend themselves better to tooth windings (due to the lower frequency, which is typically 10-100 Hz) as well as direct-conductor cooling (due to larger fewer slots). Higher-speed machines (>1 kHz

frequency) lend themselves better to distributed windings as well as indirect-conductor cooling (immersed stator, spray cooling, and cooling jacket).

(5) As previously noted, all the masses are “dry” masses not including the cooling liquid mass. If “wet” masses are included, the gap in specific power between liquid and air-cooling will decrease.

(6) Most of these machines have significantly higher specific power and/or specific torque compared to machines used in the automotive sector.

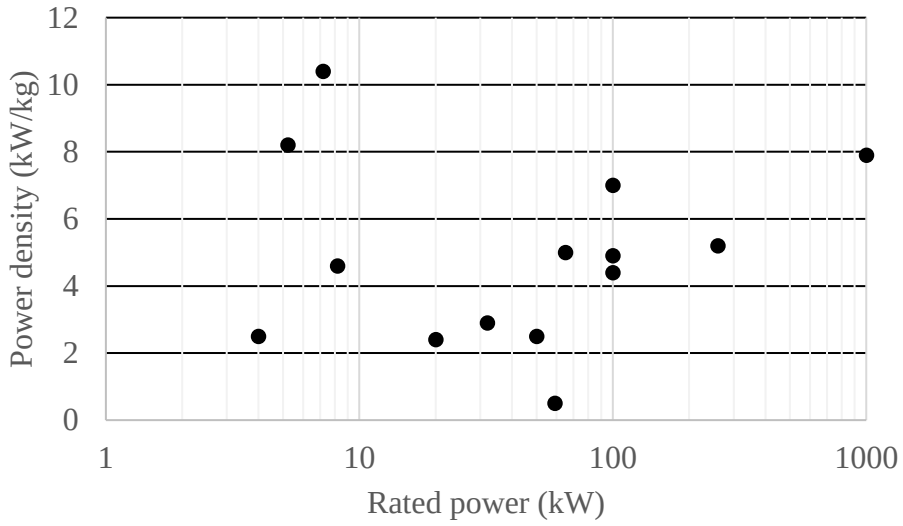


Fig. 2.15 Power density of advanced electrical machines applied on aircraft applications.

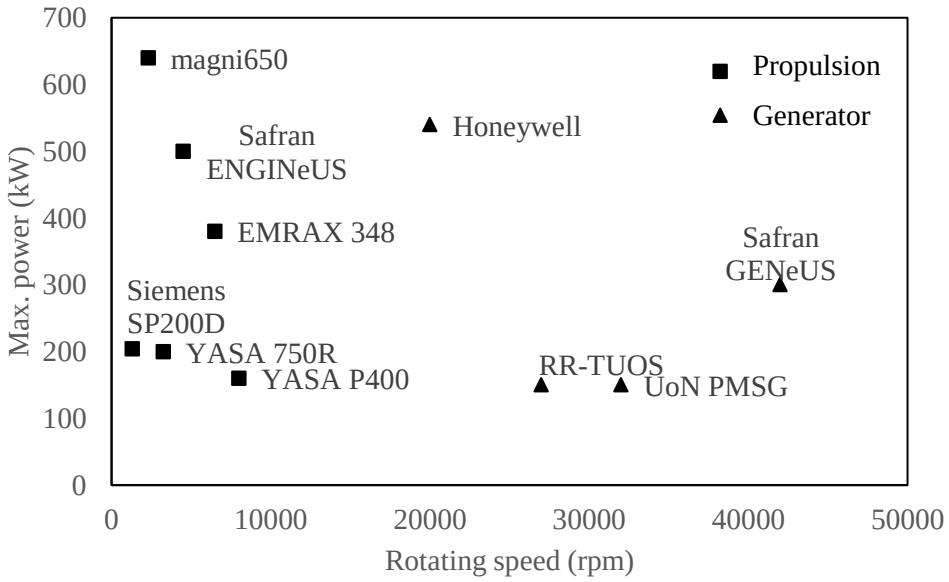


Fig. 2.16 High-power (>100 kw) PMSM for AEA/MEA applications.

One of the prime challenges of electrification for safety-critical subsystems is a gap in the safety and reliability. The corresponding design requirements, fail-safe and fault tolerant, have been defined and practised [65]. These two requirements are determined by the specific application. The fail-safe design means the failure which will not endanger remaining healthy parts. Unlike a fail-safe machine that puts safety ahead of mission, the fault tolerant design is to avoid system-level failure caused by faults at any single point. Generally, redundancy [33, 45] or backup [23] enable the system to maintain operation, potentially with degraded performance as opposed to fail completely. Such as the MEA pioneer B787, reliability of electrical power system is provided by multiple generators for majority operations, APU and RAT as backup for emergencies [51]. These conclusive concepts could be adopted to improve the PMSM, which aims to be utilized on the safety-critical applications.

The main approach consisted of fail-safe and fault tolerant design to improve reliability of PMSM has been widely practiced [2, 3, 60, 66-68]. Electrical machine with multiple three-phase topology is a common fail-safe option, such as dual three-phase Siemens SP200D [69], four three-phase magniX magni650 [70] for aircraft propulsion, dual three-phase starter-generator [71], etc. Multiple phases or multiple three-phases could provide high-level margin for mission reliability but reduce the basic reliability which determined by the number of components. Reversely, the fault tolerant capacity of electric machines can be improved without module duplicated or stacked. The presence of permanent magnet in PMSM may intensify faulty current and affect the adjacent healthy parts. High reactance design is a direct solution to suppress the fault currents, especially the short-circuit (SC) current [72]. Moreover, three-phase current injection provide new method to mitigate SC current [73].

Effective faults diagnosis methods could detect and locate potential faults and perform post-fault operation for mitigating effect and avoiding severe operations [74, 75]. The fault diagnosis of model-based and signal-based methods are the mainstream, while the difference between them is whether a PMSM is needed. Meanwhile, as the emerging method, artificial-intelligence (AI) -based model is a smarter method which does not depend on the relation between faults and signals. For the post-fault control, turn-to-turn short circuit is the most challenging electrical fault for PMSM and few substantial progressions could be found. And, this gap will be a demanding research for PMSM fault diagnosis.

2.5 Chapter conclusion

The ongoing efforts towards aircraft electrification are driving the development of traditional aircraft towards more electric aircraft (MEA). On conventional aircraft, an increasing number of on-board secondary systems such as hydraulic or pneumatic systems are being replaced with their electrical counterparts for energy conversion. Among the various technologies of aircraft electrification, the permanent magnet electrical machine is playing an important role due to its numerous advantages such as high power density and efficiency. The electric power generation system is one of the key pillars supporting this shift towards emerging systems. Consequently, permanent magnet starter-generators (PMSG) have been the focus of current research.

Compared with induction generators and switched reluctance generators, the fault tolerant PMSG is considered to be one of the most attractive options for MEA due to its high power density and efficiency over a wide speed range. However, the main drawback of PM machines is the de-excitation problem in case of a failure, which is a significant issue for aircraft applications. To improve the fault tolerant ability, PM machines with high reactance or multiphase configurations have been utilized. Multi-phase PM generators for large civil aircraft engines have been analysed [76] with the aim of achieving fault tolerance. The trade-off between the limitation of short circuit current and performance has also been demonstrated [77, 78].

To meet the requirements of the fault tolerant starter-generator system, several specific principles should be met, including:

1) Redundancy and partitioning.
2) Fault isolation.
3) Fault detection and annunciation.

Due to its simple and compact structure, high power density, and efficiency, the PMSG is a competitive candidate if its fault-tolerance can be improved to meet the safety-critical requirements of aircraft applications.

Chapter 3 The state-of-the-art fault tolerant PMSM design for aircraft application

3.1 Introduction

As introduced in the Chapter 2, the PMSM exhibits huge potential for applications in transportation electrification due to its high power density and high efficiency. However, there are still concerns of conventional PMSM for safety-critical aircraft system applications. This chapter reviewed the failure modes of PMSM in relation to its electrical, magnetic and mechanical issues. The failure tree analysis is utilized to list a series of independent faults. Moreover, state-of-the-art designs of fault tolerant PMSM are exhibited and suggested. All these efforts can improve the reliability and safety of PMSM for further application in future aircraft applications.

3.2 Electrical machine faults

In general, PMSMs can be divided into two categories, i.e. radial flux PMSMs and axial flux PMSMs, depending on the flux path, as shown in *Fig. 3.1* [79]. The radial-flux PMSMs can be further categorised into surface mounted permanent magnet (SPM) machines and interior permanent magnet (IPM) machines. The types of axial-flux machine are diverse, and its main combinations of rotor and stator include dual-rotor-single-stator and single-rotor-dual-stator types, as shown in *Fig. 3.2*. The main active parts in a PMSM typically include machine windings, permanent magnets, stator back iron and the rotor. During the operation, potential faults may occur in these parts due to electromagnetic, thermal or mechanical issues, as listed in *Fig. 3.3*.

All these potential fault sources are introduced and discussed in the following subsections.

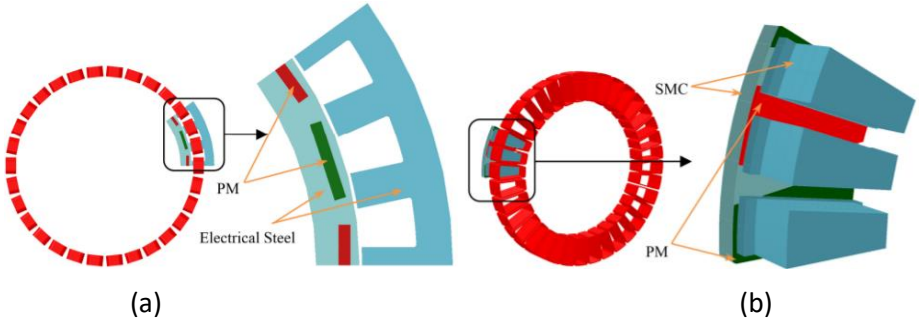


Fig. 3.1 Schematic diagram of (a) axial flux and (b) radial flux PMSM.

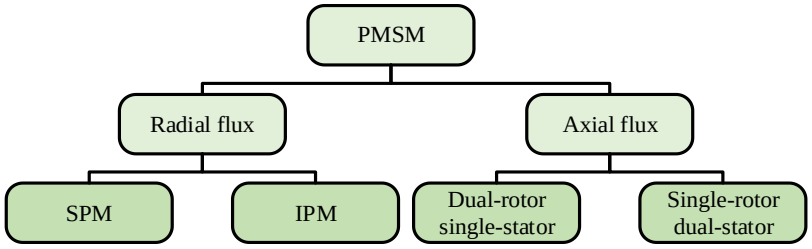


Fig. 3.2 Classification of PMSM.

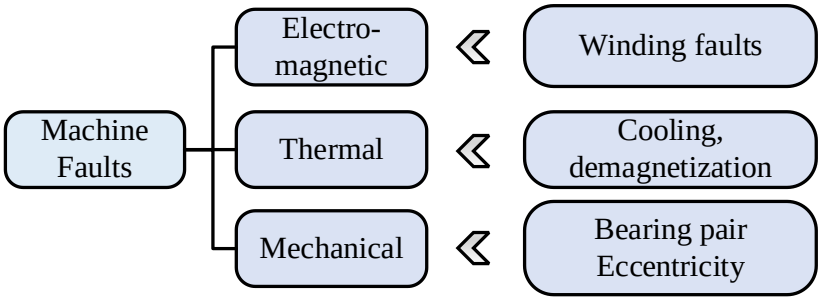


Fig. 3.3 Schematic classification of PMSM faults.

3.2.1 Electrical faults

The electrical machine winding faults consist of open-circuit (OC) faults and short-circuit (SC) faults. The types of OC can be further classified according to the position of fault, such as fault in a single phase or three phases. Several sources can lead to OC faults within an electrical machine, failing of soldering. The cracked winding is the direct cause of the OC fault. For the SC faults, the fundamental reason of these faults is from the failure of winding insulations which can lead to turn-to-turn SC, winding-to-winding, phase-to-phase and phase-to-ground fault. The degradation of insulation is mainly due to the machine operation environment, such as thermal cycles, overheat, partial discharge and ageing. The transient peak surge or overvoltage can also breakdown the winding insulation layers. The

winding friction, which is caused by winding thermal stress or mechanical vibration, could also result in the SC fault. The fault tree analysis in *Fig. 3.4* was adopted to illustrate the electrical faults and potential original sources. The top-down deductive failure analysis, in which electrical fault of PMSM was analysed utilizing Boolean logic to connect lower-level faults.

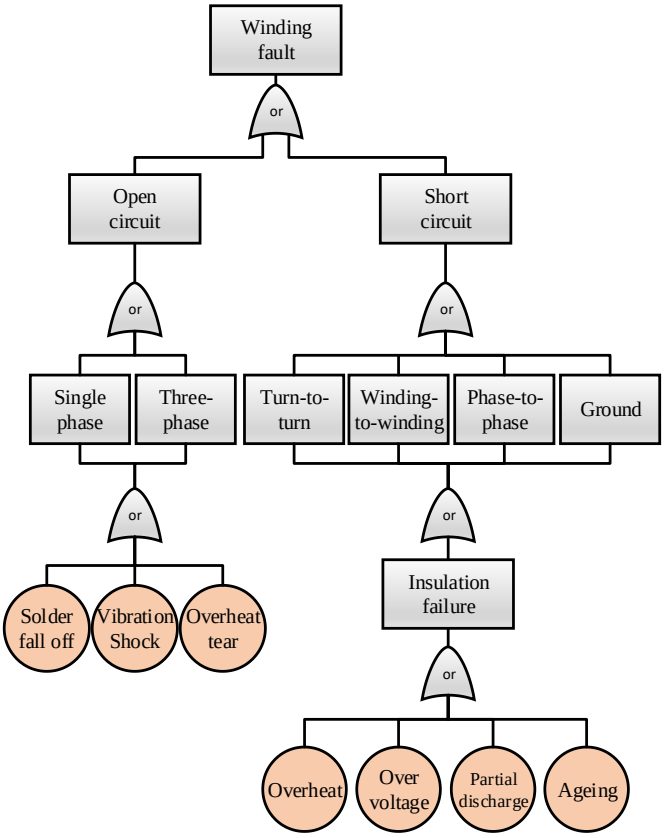


Fig. 3.4 Failure tree analysis of PMSM electrical faults.

Indeed, up to 25% of electrical faults are related to the winding insulation failures [80]. The resulted SC fault can be severe and potentially destroy the entire machine. The phase-to-phase SC and the turn-to-turn SC fault can be found in all kinds of PMSM regardless of slot/pole combination and winding arrangement. To estimate the SC current within a machine and thus predict the heat generated during SC fault condition, equivalent circuits of windings under different scenarios have been developed in various literatures and some of them are shown in *Fig. 3.5*. The simplified external circuit could be modelled to analyse the post-fault performance. The healthy winding condition is illustrated in *Fig. 3.5* (a), where each phase of a PMSM machine is modelled as an ideal voltage source (i.e., back EMF) connected with an RL circuit. The OC fault can be modelled by setting the coil resistance R value to be MΩ such that there is almost no current flow as shown in *Fig. 3.5* (b). For phase-to-phase SC fault, it can be modelled with phase terminals connected

directly or with a very small resistor as shown in *Fig. 3.5* (c). For the turn-to-turn SC fault, an independent circuit is created to represent the faulty windings with an equivalent inductance and resistance dependent on the number of faulty turns as shown in *Fig. 3.5* (d).

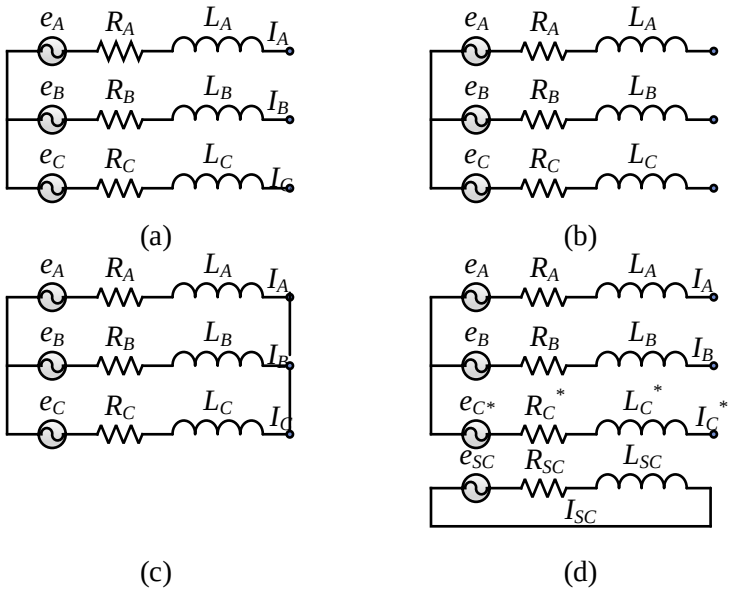


Fig. 3.5 Equivalent circuit under varied scenarios (a) Healthy. (b) Open-circuit. (c) Symmetrical short-circuit. (d) Turn-to-turn short-circuit of Phase C.

3.2.2 Thermal faults

The sudden winding faults and/or uncapable of cooling method can result in thermal faults. The thermal faults affect the performance of permanent magnet (PM) directly. PMs for high power density applications are commonly samarium cobalt (SmCo) and neodymium–iron–boron (NdFeB) [81]. Two major types of PM faults are irreversible demagnetisation and PM damage as shown in *Fig. 3.6*.

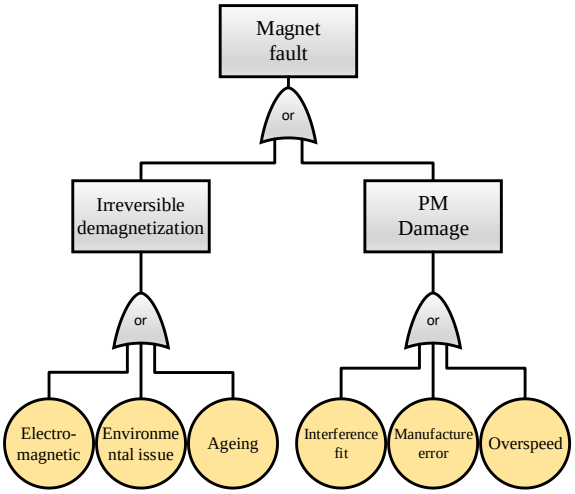


Fig. 3.6 Failure tree analysis of PMSM magnetic faults.

The irreversible demagnetization of the permanent magnet can result in reduced performance and low reliability of the machine and thus reduce the PMSM efficiency. Various aspects can contribute to permanent magnet (PM) irreversible demagnetization such as electromagnetic impacts (abnormal stator current), environmental issues (especially temperature) or aging. Extensive external magnetic field can also contribute to PM irreversible demagnetisation, especially when there are over currents in the machine windings. This has been investigated in [82, 83], where PM demagnetization due to turn-to-turn fault currents has been studied. An iterated process has been proposed to estimate whether the PM is irreversibly demagnetized, based on the comparison of flux density of finite element analysis (FEA) results and the B-H curve. Methods of demagnetization modelling have been reviewed in [84]. Diverse methods could be utilized to model demagnetization, i.e. magnetic equivalent circuit, field, equivalent circuit, Maxwell's Equations and FEA. Compared with other methods, the FEA can provide rather accurate predictions although time-consuming.

The impact of temperature variation to the performance of the spoke-type IPM machines has been studied in [85], where authors showed the sensitivity analysis between temperature variation and performance metrics. High temperature of PM results in deteriorated performance and this conclusion can be adapted to the IPM regardless of a specific type.

The fundamental principles and characteristic of PM demagnetization have been introduced in [86, 87]. There, the intrinsic curve depicts the B-H relation solely due to the magnet and is obtained by subtracting demagnetizing force H from B, while the normal curve represents the combined flux density B value of both the applied field (i.e., the external magnet field) and that contributed by the magnetic material (i.e., the PM). Based on the case shown in *Fig. 3.7*, the B and H plane illustrates the PM intrinsic (blue colour) and normal (orange colour) demagnetization curves under varying temperatures. With the increasing temperature, the intrinsic demagnetization curve significantly shrinks, while the knee point of the normal curve starts to appear - in the second quadrant. When an external magnetic field is applied over the knee point, this causes an irreversible demagnetization. In addition, eddy current loss in the PM contributes to temperature rise, especially for high-frequency applications. Similar to the lamination of back iron, a valid way for the loss reduction of eddy

current is segmentation and insulation of each of the PM along the axial or circumferential direction, which has been practised in [88].

Parameters of modular PMSM has been accounted for the investigation of irreversible demagnetization [89]. The demagnetization withstand capability can be deteriorated in the modular topology if the number of poles is lower than the number of slots. Meanwhile, flux density distribution in the permanent magnet using finite element analysis has been visualized in [82, 90]. These conclusions can be applied to the improvement of PM design robustness to withstand demagnetization, especially overcurrent faults.

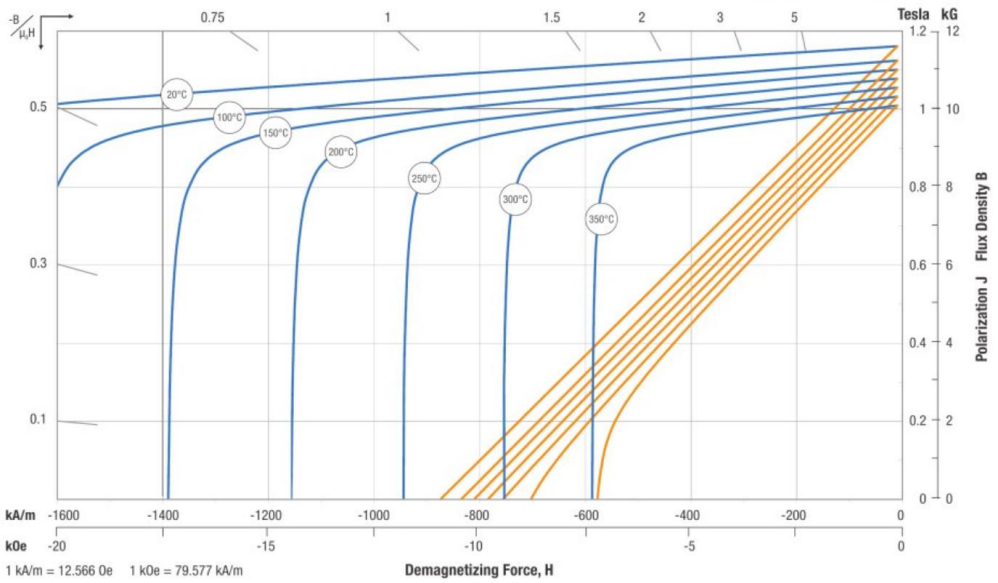


Fig. 3.7 B-H Curve of the Arnold Magnetic Technologies SmCo magnet, blue lines: PM intrinsic demagnetization curve, orange lines: normal demagnetization curves [91].

For the radial flux PMSM, PMs are mounted on the rotor surface or buried in the rotor. For surface mounted PMSM, the rotor sleeve, either alloy, glass fibre or carbon fibre bandage, are used to fasten the magnets to the rotor surface by interference design or preload. The magnitude of interference of alloy sleeve or preload of fibre bandage, considering the centrifugal force in over-speed operation may damage the PM [92, 93]. During manufacturing and assembling process, the PM might have been with minor flaws within the surface mounted PMSM and then been damaged during operation due to increased mechanical stress during high-speed operation. The fixation of magnets for high-speed surface mounted PMSM is a critical design consideration. This can be realized using the FE calculation and the analytical approaches introduced in [94-96]. One example of the damaged PM due to

mechanical stress during high speed is shown in *Fig. 3.8*. A crack can be seen in surface-mounted PM segments because of the improper fixation.



Fig. 3.8 Magnet collapse during the high-speed operation.

3.2.3 Mechanical faults

Compared with the aggressive electromagnetic and thermal issues which lead to PMSM failure, the mechanical issues are often neglected during the preliminary design stage. The potential mechanical issues are often exposed in the manufacturing, assembling and experimental stages. Static, dynamic and mixed eccentricities are the main source of mechanical faults. Four major fault sources for mechanical failure of a PMSM including assembling error, bearing worn, resonance and tightening loose. The assembly error, as shown in *Fig. 3.9*.

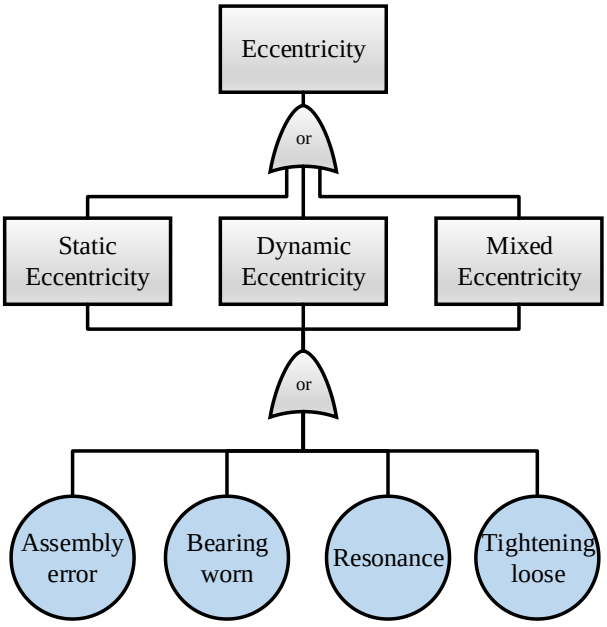


Fig. 3.9 Failure tree analysis of PMSM eccentricity faults.

The assembling error could be from improper design in the dimensional chain, geometric dimensioning or tolerance. Poor lubrication or overload could result in the bearing worn out and lead to eccentricity. Mechanical resonance is often avoided during the design phase but will cause eccentricity which may lead to tightening loose between the endcap and housing. A schematic diagram of mixed eccentricity in radial flux and axial flux PMSM are illustrated in *Fig. 3.10*.

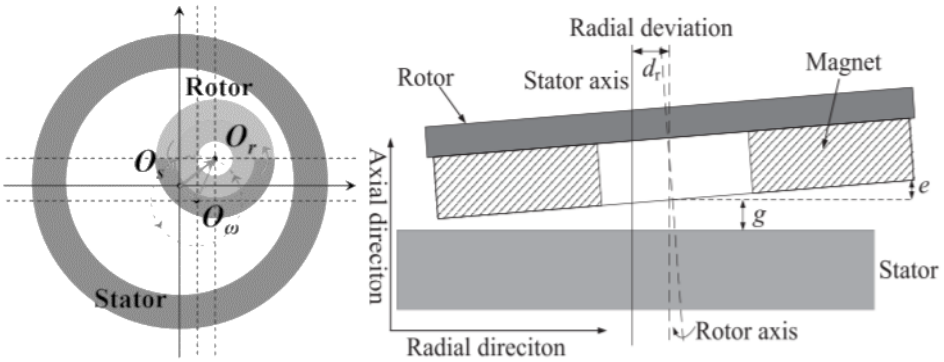


Fig. 3.10 Schematic diagram of mixed eccentricity in radial flux [97] and axial flux [98] PMSM.

The eccentricity will commonly cause vibration of a PMSM. These vibrations can result in worn-out bearings and create noise issues [97, 99-101]. A severe eccentricity may even result in a touch between the rotor and stator. This will completely destroy the machine. One example of a failed machine due to eccentricity is shown *Fig. 3.11*. It can be seen that one part of the rotor is completely worn out due to frictions between the stator and the rotor as there are eccentricity issues.

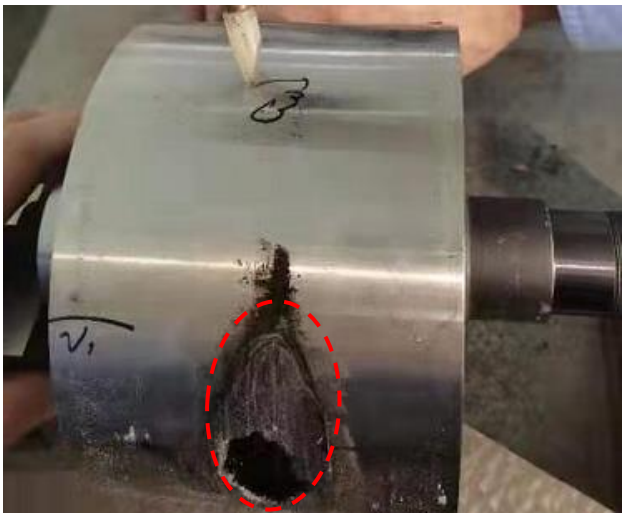


Fig. 3.11 Example of the damaged rotor due to the contact between stator and rotor.

As rotating machinery, mechanical faults in PMSMs are often linked to bearing faults. Severe bearing issues could lead to PMSM dysfunction or even damage the entire machine. Failure in bearings could lead to vibration, noise, crushing even mechanical jamming [102]. Different sources can lead to bearing failure including poor lubrication, improper selection of bearing with wrong axial/radial force calculation during the design process. The application of power electronics in motor drives has seen the increasing of bearing failure caused by common-mode bearing currents [103-105]. Especially the wide bandgap (WBG) devices, such as SiC and GaN, are normally switched at a higher frequency compared with conventional Si IGBTs, this leads to a higher dv/dt, a faster shaft voltage build up and thus a higher amplitude of bearing currents [103]. To avoid such an issue, bearingless PMSM has emerged recently but control of suspension force and rotor position is challenging while suspending and spinning the rotor simultaneously [106].

In this section, different types of machine faults and their major causing sources have been reviewed. For aircraft safety-critical design, these faults need to be carefully handled and considered for fail-safe and fault tolerant design requirements. For example, turn-to-turn SC is a fatal winding fault compared with other electrical faults. A minor eccentricity may have a significant effect on machine performance but may not lead to machine failure. However, a severe eccentricity may cause a single-point failure, which may affect the whole system, although redundant windings have been adopted. To avoid machine fault occurs, which could lead to dismantling an entire machine, non-invasive diagnosis at an early stage of faults occurrence is critically important. These fault diagnosis methods will be introduced in the following section.

3.3 Fault tolerant design of PMSM

For aircraft applications, environmental conditions such as the operating temperature range, vibrations, accelerations, pressures, electromagnetic interference, etc., endanger the performance and safety of PMSM. All of these should be considered in the design and selection of the wire insulation, bearings and fixation. As stated earlier, continuous operation in post-fault mode and fail-safe operation are fundamental requirements of FT applications.

The mechanical faults are mainly due to manufacturing, assembling, vibration, environmental issues, etc. The methods to cope with these faults, by complex mechanical design, are relatively independent of electrical faults. For a general PMSM without redundant windings, fault tolerant design focusing on electrical faults are more attractive, which includes short-circuit current suppress, fault isolation consideration and innovative topologies for fault tolerant capabilities.

3.3.1 SC current

A direct measure to protect the machine is to suppress the SC current below the safety threshold. Generally, machines with higher inductances exhibit an intrinsic advantage to limit the SC current during fault [72]. The relationship between stator slot geometric dimensions and slot leakage inductance, and their suppression effect on SC current, have been studied widely. In [107], it has been found that narrow and deep slots exhibit higher slot leakage reactance which can restrain the SC current. The FEA and experimental tests have been used to investigate the relationship between SC current magnitude and fault location [66, 67]. There, authors have identified that the most fatal SC current occurs at the place where SC coils are close to the slot opening for a stranded coil-winding machine [107]. In [66], the turn-to-turn SC currents could be minimized and inherently limited by the vertically placed strip winding (VSW). Besides, based on VSW, a series of slot/pole combination was compared based on FEM simulation, which low slot/pole-number combinations exhibit lower SC current and lower efficiency [108].

Although a higher reactance is beneficial for SC current retaining, this will compromise the machine power density. The back-EMF of the machine is limited by power converter dc-link voltage, a large reactance of machine would result in low operation speed and reduce the power density of the machine. An analytical SC model of PMSM has been developed and verified to calculate turn-to-turn SC current in [109]. It could be utilized to improve the fault tolerance of PMSM for aircraft application by post-fault mitigation. With the use of three-phase current injection, the SC current of turn-to-turn faults could be suppressed under a permissible level [73]. A three-phase current generates an opposite flux linkage to counteract the electromotive force created by PMs and SC current. Based on this method, the turn-to-turn SC current can be limited under acceptable level in motoring mode; in

generation mode, this method can survive the machine under SC fault.

It is noteworthy that the suppression of the SC hazard is related to thermal management. As a result, cooling solutions, high-temperature electrical insulation materials and demagnetization issues of PM must also be considered.

3.3.2 Fault isolation

Fault tolerant PMSMs are designed with the purpose of isolating fault components. There are three kinds of fault isolation methods: electrical, thermal and magnetic isolations.

3.3.2.1 Electrical isolation

Conventional three-phase winding, either star or delta connections, cannot meet the requirement of fail-safe, as any winding fault could cause the fluctuation of current in the healthy coils. The most direct approach to achieve electrical isolation in a machine is to drive every single phase independently. H bridges have been used to drive each phase in a three-phase machine aiming for electrical isolation between phases in [1, 2]. Continuous outputs are still capable even with a power unit or winding fault. It is feasible to add more phases based on this architecture for higher fault tolerance, as shown in *Fig. 3.12*. Sing-phase H-bridge depends on double power electronics while higher total volt-ampere rating.

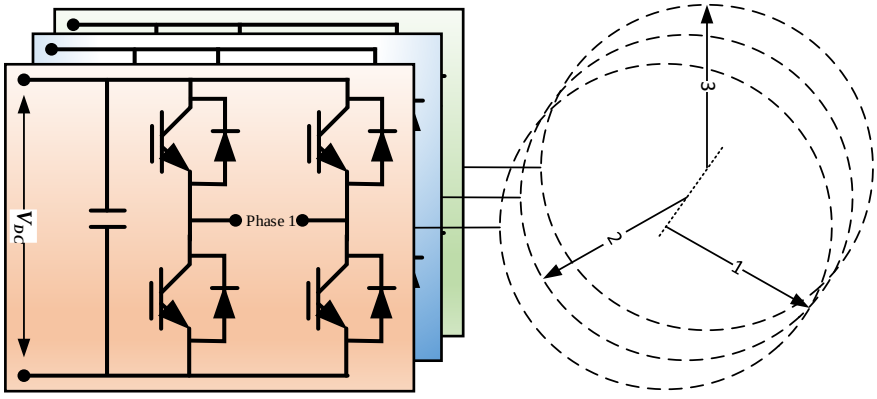


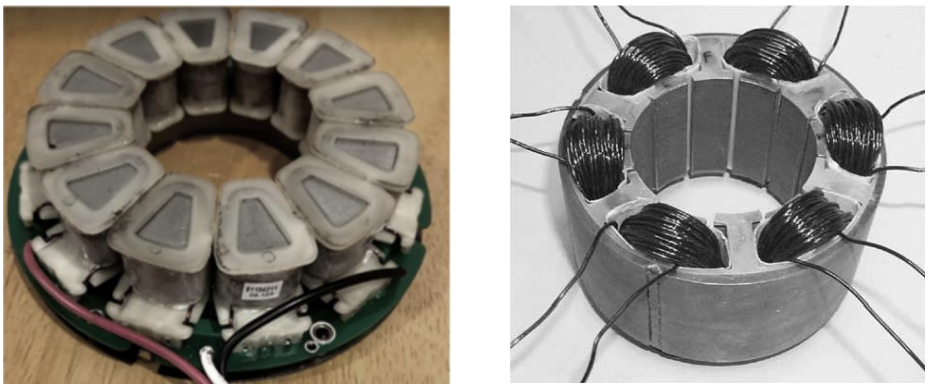
Fig. 3.12 Topology configuration of single phase drive.

3.3.2.2 Magnetic isolation

When SC happens in windings, the resulted faulty current induces extra voltages in remaining healthy windings, Moreover, currents in healthy windings can aggravate the criticality of fault. Magnetic isolation can be achieved by designing negligible

mutual inductance between phases, which benefits from the design of slot/pole combination or winding configuration. Adopting a fractional-slot concentrated-winding (FSCW) [110] (*Fig. 3.13*. a), an axial-flux-path PMSM can improve the competence of magnetic isolation. Based on FSCW, a modular stator with inserted flux gaps into stator teeth has been investigated [111-113]. The flux path could be revised by the stator airgap, then the mutual inductance can be decreased further to achieve better isolation Moreover, the influences of flux gaps on electromagnetic performance were carried out.

Comprehensive comparisons between different winding configurations based on a dual three-phase PMSM can be found in [114]; in a 12/10 combination, the SPM exhibits higher power density and IPM shows better fault tolerance in the case of SC. FSCW has also been applied to axial-flux PMSM for specific applications in [1, 115, 116], as shown in *Fig. 3.13* (b). With the adoption of H-bridges, the modular motor drives exhibit better fault tolerance as a generator.



(a) (b)

Fig. 3.13 Stator with concentrated coils in (a) axial flux PMSM [110] (b) radial flux PMSM [1].

3.3.2.3 Thermal isolation

Fault currents could overheat the faulty coils, which speeds up the aging of insulation and then shorten the life of the motor. Like the magnetic isolation, non-overlapping and non-contact winding arrangements effectively isolate thermal conduction between the faulty and healthy windings. In the meantime, it is important to select the conductor and permanent magnet with high-temperature resistance to cope the requirement of FT operation. A modular stator will be introduced in the following section, which exhibits better thermal isolation.

Above all, PMSM topology with a single layer FSCW layout with single-phase H-bridge converter meets the requirements of FT application. Nevertheless, the main disadvantage of this topology is high rotor losses because of the presence of many lower and higher-order MMF harmonics.

3.3.3 Innovation of topology

3.3.3.1 Multiple phases topology

Multiple independent single-phase machines and multiple three-phase machine have been widely adopted recently. These machines are able to provide a high margin for mission reliability.

For a specific PMSM application, the lower total system losses as a function of the number of phases from 3 to 13, have been studied in [3]; where, the five-phase represents the optimal solution, due to lowest copper loss and highest efficiency. In addition, five-phase PMSMs have attracted more attention in the light of higher performance[4, 5]. Adopting the torque control strategies, a comparison between five-phase and six-phase SPM has been carried out [6]. Similarly, multiple phase topology is also applied to axial flux PMSM. A novel 6-phase axial-flux PMSM with 60 phase-belt toroidal winding configuration has been researched, which exhibits high torque density [7]. In addition, the investigation of how the parity of phases affects PMSM performance has been carried out in [8]; the odd-phase topology performs lower torque ripple while the even-phase counterpart could compensate the unbalanced magnetic pull in case one phase is disabled.

An aerospace application consisting of dual three-phase PMSM with FSCW has been validated [9], which featuring high power-density and fault-tolerance. A design and testing of a dual three-phase PM motor for a safety-critical aircraft actuator has been carried out in [10], which exhibits higher slot filling, better manufacturability based on rectangular section conductor, and lower probability of SC fault.

3.3.3.2 Modular topology

The diagram of modular fault tolerant topology that is derived from multiple three-phase is shown in *Fig. 3.14* (a). A modular stator applied on in-wheel PMSM has been proposed in [11]; one of the highlights of this topology is a concentrated winding configuration with unequal teeth widths and complete thermal and magnetic

isolation. Based on the axial and circumferential segmentation, two candidates have been compared for specific aerospace applications in [12]; the outputs of simulation and experimental tests have validated its fault tolerance. To pursue higher safety margin, an in-wheel machine, consisting of eight sub motors, has been demonstrated in [13]; the experimental results have shown good magnetic isolation between sub motors. Modular axial flux PMSM could be achieved by multiple discs [14] (*Fig. 3.14*. c). For the purpose of avoiding over-designing for reliability as well as taking into account technology readiness level, the dual three-phase topology is a common candidate for the selection of modular FT PMSMs.

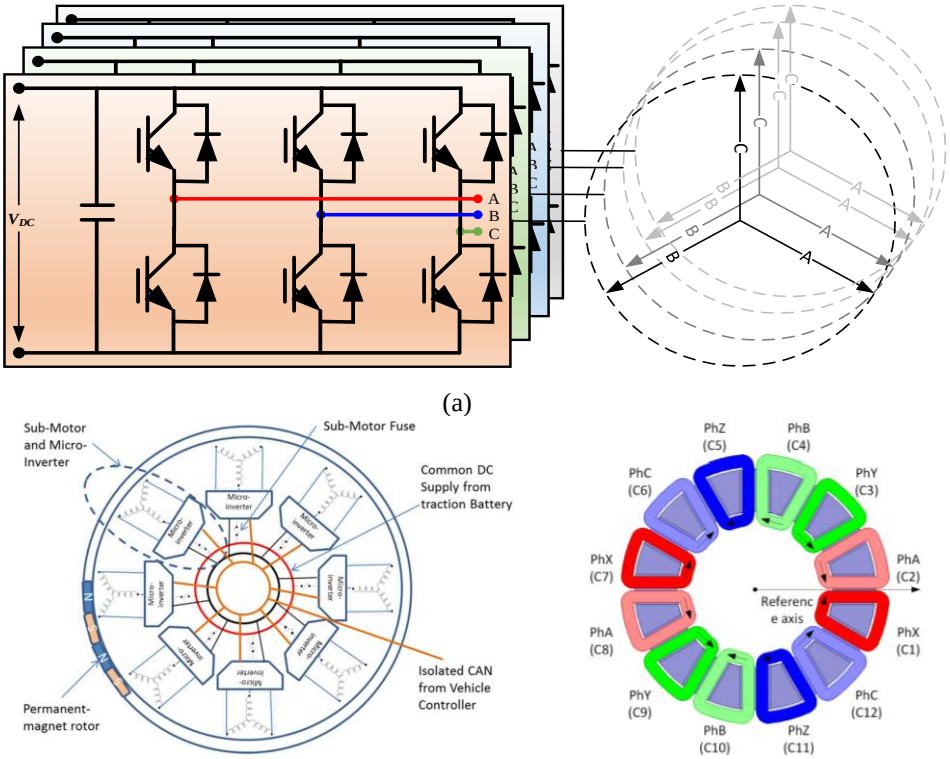


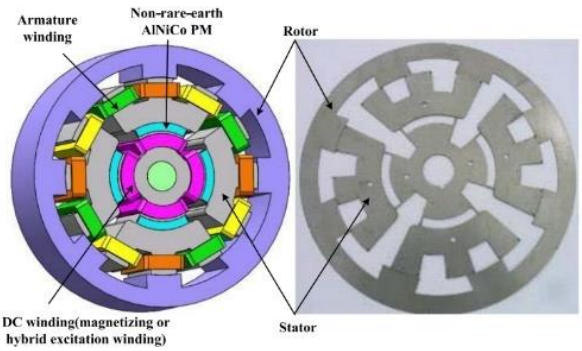
Fig. 3.14 Topology configuration of (a) Schematic of modular multiple three-phase. (b) Example of modular multiple three-phase [13]. (c) 6-phase axial flux PMSM [1].

3.3.3.3 Innovative topologies

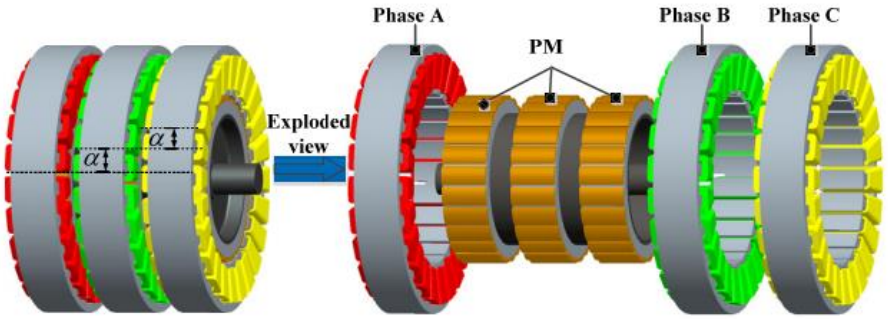
In addition to the conventional PMSM, stator-PM machines have been invented, with PMs arranged in the stator that can easily transfer heat, especially in faulty scenarios. The common feature in these types is the controllable flux which can be amended in the presence of a fault. An out-rotor motor topology with doubly-salient flux controllable has been proposed in [16], as shown in *Fig. 3.15* (a). An innovative feature of this topology is the combination of a double-salient motor and a memory

motor; in the event of a fault, the AlNiCo PMs can be completely demagnetized the motor will operate as a switched reluctance motor. This possesses inherent fault tolerance.

The concept of an integral slot non-overlapping concentrated winding (ISNCW) and its associated machine configuration has been recently proposed in [15], as shown in *Fig. 3.15* (b). This feature exhibits inherent isolation capability between phases and lower SC current. Moreover, the independent structure has merits in maintenance. Similarly, a hybrid excitation synchronous machines (HESM) applied on aircraft starter-generator has gotten much attention recently [17]. Its measured features are used for regulating the field current for the starter-generator mission.



(a)



(b)

Fig. 3.15 Proposed machine topology of (a) doubly-salient flux controllable out-rotor motor [16] and (b) ISNCW [15].

An FT evaluation of mentioned approaches and topologies are listed in Table 3.1, and the tick (√) or cross (×) represents the competence or not. Based on general PMSM topology, all the fault tolerant methods specialize in winding topology to improve the electrical fault isolation, by adding phases or redundant windings. Magnetic and thermal isolation between phases could be improved by non-overlapping windings, such as FSCW. The emerging topology, such as flux

controllable and hybrid excitation PM machine, have inherently competence to suppress SC current because the special PMs which are easy to be demagnetized and controlled in the case of faults. In spite of this, the complex structure, manufacture and assembly issues are evident shortcomings.

Table 3.1 Configuration and evaluation of FT approaches.

Machine topology		Fault isolation			Fail-safe of SC current	Reference
		Magnetic	Electrical	Thermal		
Phase with H-bridge inverter		×	√	×	√	[1, 2]
Multi-phase	***n*** single-phase	√	√	×	×	[3], [4-8]
	n 3-phase	√	√	×	×	[9, 10]
Modular design		√	√	√	√	[1],[11-14]
Separated phase		√	√	√	×	[15]
Flux controllable		×	×	×	√	[16]
Hybrid excitation		×	×	×	√	[17]

3.4 Discussion

Due to the relatively slow progress of battery energy density, the MEAs will be the long-serving workhorses in the aviation industry for decades. Generally, PMSMs can be found in actuators extensively on MEA, integrated with mechanical or hydraulic components. Adopting FT design and jam-tolerant mechanical components, actuators powered by PMSM are qualified for safety-critical applications, such as flight control systems and landing gear systems. Dual-lane redundancy is the main choice to help realize a balance between cost and reliability.

In addition, PM electrical machines operate relatively independent of each other, such as the starter mode or generator mode. The improvement of reliability can be achieved by multiple phases. Multiple three-phase is the mainstream on account of modular power electronics.

Hybrid-electric propulsion has attracted attention because its propulsion system is electrified. This kind of aircraft is concentrating efforts on replacing turbo-engine

with motors, and the reliability of PMSM is in high demand. Similarly, multiple three-phase PMSM is the optimal candidate due to its high reliability and modular architectures. The electric vertical take-off and landing (eVTOL) aircraft has been tested to meet the requirement of urban air mobility. Although the configurations may be diversified, PMSM is the preferred candidate for distributed propulsion. Fault tolerance of PMSM is not an essential competence. Multiple rotor-wings consisted of PMSMs and blades are arranged to provide life, while healthy rotor-wings could compensate for the output in case of a single PMSM shutdown. The reliability design for this kind of application is subject to distributed electric propulsion (DEP) architecture, i.e., redundant windings, motors or distributed propulsion.

In summary, PMSM applications on aircraft are listed in Table 3.2 and the corresponding approaches for improving their reliability are recommended. The recommended approach is determined by the safety level. For safety-critical applications, the reliability is provided by redundancy as opposed to fault tolerant unit, such as flight control system. In aviation electrification, multiple three-phase are the mainstream FT solutions, especially for emerging aircraft.

Table 3.2 PMSM application on aircraft and the approaches for improving reliability.

	Application	Safety-critical	Type of application	Methodology	Approach
MEA	Flight control system	√	Actuators	Redundancy	Dual redundancy and jam-tolerant
	Landing gear	√			
	Nose-wheels and brake				
	Thrust reverser				
	Electric power system	√	Starter/generator	FT design	Multiple three-phase
	Electric taxiing		Motor		
	Fuel pump	√	Motor		
	Hybrid-/all-electric Propulsion	√	Generator		
			Motor		
	eVTOL		Motor	Subject to DEP architecture	

3.5 Conclusion

Aimed at improving the reliability of PMSM applications on aircraft, the approaches consisted of machine design and control should be carried out together. A feasible FT topology, fault detection and diagnosis, and post-fault control are necessary contributors of safety-critical application.

In this chapter, a comprehensive technical review of failure modes, fault tolerant topologies for PMSM in transportation electrification were summarized. The machine faults distributed in electrical, magnetic and mechanical issues were introduced in sequence. To improve the fault tolerance and fail-safe strategy, fault tolerant machine design approaches were also introduced. Multiple three-phase topology is the main candidate for the safety-critical aircraft application, due to its comprehensive improvement in reliability. Based on these methods, approaches of PMSM on aircraft to meet the reliability have been suggested. And, a practice of starter-generator has been illustrated which adopted triple three-machine with on-line fault diagnosis.

Chapter 4 Initial design of the permanent magnet starter-generator

4.1 Introduction

This chapter will present a substantial design process to identify the optimal candidate for a specific starter-generator based on the review of aircraft electrification and PMSM on aircraft.

The iterative machine design process of the main phases and corresponding tasks is shown in *Fig. 4.1*, where the dashed lines indicate the potential loops for iterations. The design process is derived from model-based systems engineering (MBSE), which is a system engineering methodology that focuses on creating and utilizing domain models as the primary means of information.

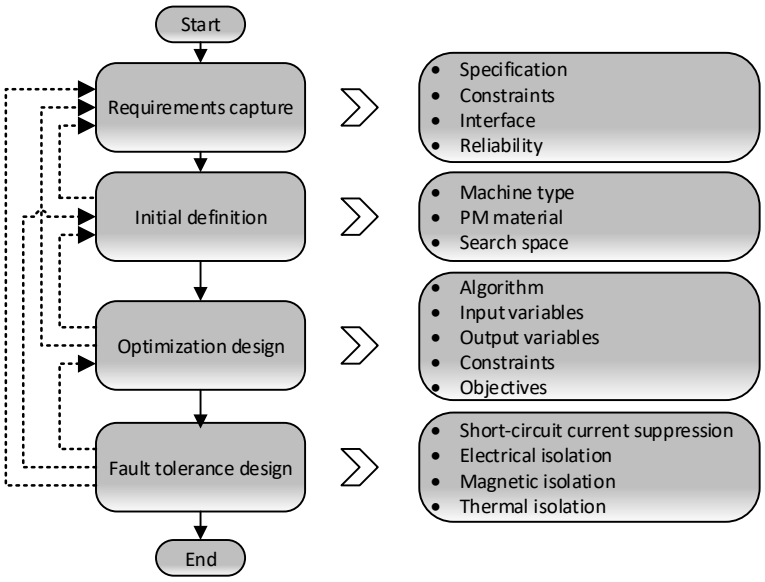


Fig. 4.1 Design process of main phases and tasks.

In the first stage, requirements capture involves collecting as many potential requirements as possible and refining them to form a complete, concise, and consistent set of functional and non-functional requirements. This is a crucial activity in verifying and quantifying all the necessary information that contributes to a complete and coherent machine design.

Initially, the candidate for the specific application of PMSM was designed by adopting the selection of topology and optimization, considering machine type, potential slot/pole combination, and materials. Based on these initial definitions, a multiple-objective and multiple-discipline optimization design process was carried out to achieve a balanced candidate in terms of power density and fault tolerance. An optimization process consisting of objectives and constraints was created to select an optimal candidate using a generic algorithm.

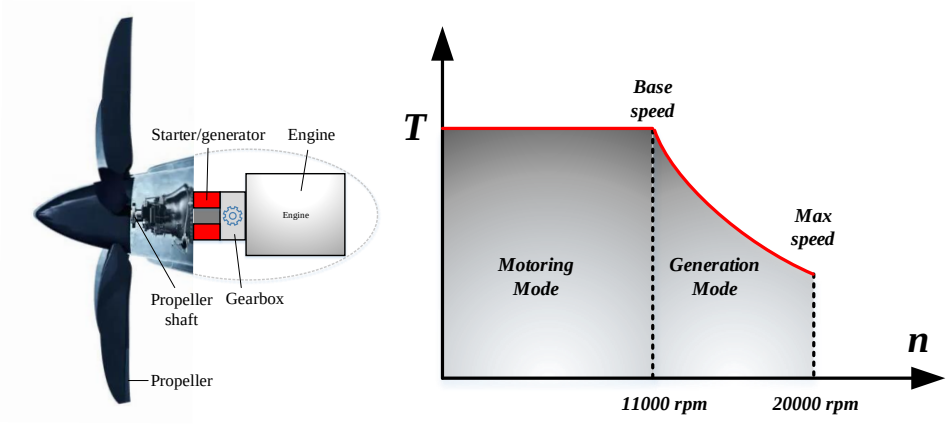
The results of this section will pave the way for improving the performance of PMSM, such as enhancing fault tolerance and final design, which will be presented in the next chapters.

4.2 Requirements capture

4.2.1 Specification

Similar to the starter/generator (SG) on conventional aircraft, integrated SG for MEA of turboprop engines performs similar functions of motoring the engine and generating electricity. The schematic position of the integrated SG is shown in *Fig. 4.2*(a), along with the illustration of torque-speed curve and operation modes.

The candidate starter-generators are designed to provide a continuous speed range for engines, from standstill to ignition speed and maximum speed, with two states divided into the motoring mode and the generation mode, respectively. In the motoring mode, the SG provides output to overcome resistive torque from propellers, gear boxes, and accessories. After successful engine ignition, the SG generates electricity for the entire electrical power system. The torque-speed characteristics of the PMSG are illustrated in *Fig. 4.2* (b).



(a) (b)

Fig. 4.2 Schematic of (a)space limitation and (b) torque-speed characteristics.

Besides meeting the requirements of energy conversion, the specific PMSG must also comply with geometrical and environmental limitations as it is intended to be integrated into the propeller housing. The specifications of the PMSG have been presented in Table 4.1. In addition to the conventional requirements for interface and output, the radial geometrical constraints are limited by the outer diameter of the stator and the inner diameter of the shaft hole. These challenging boundaries are determined by the available space within the engine.

Table 4.1 The Specification of candidate PMSG.

Parameters	Value	Unit
DC-link Voltage	540	V
Base speed	11,000	rpm
Maximum speed	20,000	rpm
Output Power @ 11000 rpm	35	kW
Efficiency at 11000 rpm	95	%
Outer diameter	160	mm
Inner diameter	95	mm
Length	<120	mm

The DC-link voltage of the power converter is set at 540 V. The PMSG is designed to operate at two main speed points: the base speed of 11,000 rpm and the maximum speed of 20,000 rpm. At these speed points, the PMSG should provide an output power of 35 kW. However, the geometrical envelope is limited due to the engine

housing and the hollow shaft space. Specifically, the outer diameter of the PMSG should not exceed 160 mm, the inner diameter of the shaft hole should not exceed 95 mm, and the length of the PMSG should not exceed 120 mm. These limitations pose a challenge in designing a PMSG that meets all the requirements while fitting within the given space constraints.

4.2.2 Reliability

As introduced in the chapter 2.3.7, the electrical power system should provide power to all loads continuously during healthy operation. The reliability of the current electric power system is ensured at the system level rather than at the level of a single starter/generator unit to avoid single-point failures. The current multi-stage starter-generators are incompetent of fault isolation.

Fault tolerance is another critical design objective for this specific application. As a safety-critical application, the machine should be able to maintain operation after specific electrical faults, such as open circuits and short circuits in windings. Based on a review of fault tolerant topologies, the modular topology, which consists of multiple three-phase units, has a better balance between reliability and cost. It has become a mainstream solution for improving the fault tolerance of PMSM applications.

4.2.3 Interface

Interface design includes all the connections between this machine and other facilities, such as electrical, mechanical, and cooling systems. As an embedded application in the aeroengine, oil is available for cooling. As a prototype in testing, both water and oil cooling sources are available, allowing for the adoption of high power loading and achieving a higher power density.

Two distinct options for cooling are slot cooling and jacket cooling. Slot cooling is an advanced method where fluid is passed axially down the machine through a slot. The key benefit of this type of cooling is the close proximity of the fluid to the conductors, resulting in a short thermal path and effective heat removal directly from the source. This enables a continuous high current density of more than 20 A/mm^2 [117] to be maintained. However, the area required for the cooling duct competes

with the area for the conductors, so there is typically a compromise between copper loss and cooling effectiveness. Meanwhile, jacket cooling is also an option due to its relatively simple structure compared to slot cooling.

4.3 Initial definition

4.3.1 Machine type

Limited by the narrow space and hollow rotating shaft, the candidate design should take full advantage of the radial direction to arrange electrical components, such as the stator, stator sleeve, airgap, and rotor assembly (either surface mounted or interior PM).

In the selection of rotor type, a surface mounted permanent magnet is much more feasible due to the limitation of narrow radial space. Besides, Halbach PM array is adopted to pursue a thin rotor assembly and hollow shaft design. Oppositely, the interior PM rotor assembly is not feasible for this specific application due to its thicker space requirement than the surface mounted one.

4.3.2 Slot/pole selection

In addition to meeting the requirements of the winding theory, the number of slots, $\boldsymbol{Q}$, is intended to be set as a multiple of six to achieve better performance in unbalanced axial force. So, the number of slots was set from 12. The upper limit of the outer diameter of the motor is fixed, which determines the maximum number of slots, and is less than 48 due to manufacturing difficulties and teeth strength limitations.

Generally, the higher of pole number, $\boldsymbol{p}$, leads to higher switching losses in the power electronics during higher frequency operation. Then, the number of poles is limited to 12. The potential slot/pole combinations of the machine have been calculated theoretically [118] and listed in Table 4.2.

Based on the specific slot/pole combination, the arrangements of windings were divided into four types, listed in Table 4,3, which including FSCW, integer slot, fractional slot, and concentrated winding.

All the 18 slot/pole combinations were investigated.

Table 4.2 The winding factor of varied slot/pole combination.

Q/p	6	8	10	12
12	-	0.866	*0.933*	-
18	*1*	*0.617*	0.735	*0.866*
24	-	*1*	*0.588*	-
30	-	0.909	*1*	-
36	*0.966*	*0.945*	*0.942*	*1*
42	-	*0.953*	*0.953*	-
48	-	*0.966*	*0.954*	-

Table 4.3 Classifications of slot/pole combinations.

Principle	FSCW	Integer-slot	Concentrated winding	Fractional slot
Candidates	18/12, 12/10	18/6, 36/6, 24/8, 30/10, 36/12,48/8	12/8, 18/8, 18/10, 24/10	30/8, 36/8, 36/10, 42/8, 42/10, 48/10

Furthermore, as this starter-generator will be integrated into an aeroengine, space must be reserved for the engine shaft, which has an outer diameter of Ø95 mm. To improve the airgap flux density while considering the limitation of a thin rotor back-iron, a Halbach array PM arrangement will be selected.

4.3.3 Material

The goal of material selection is to choose appropriate materials for all active parts of energy conversion that offer low loss and higher power density.

For the stator and rotor back iron, they consist of thin steel laminations. Considering good permeability and low core losses, the selected material for stator and rotor lamination is N10 0.1 strip, which thickness is 0.1 mm and can accommodate the 1100 Hz fundamental frequency and the high core saturation flux density required to achieve high power density.

For the permanent magnet, it should provide high magnetic power product and be able to avoid demagnetization at high temperatures. Samarium cobalt (SmCo) is better than neodymium-iron-boron permanent magnets (NdFeB) in thermal performance. The samarium cobalt (SmCo) of Recoma 33E (supplier: Arnold

Magnetic Technologies, Sheffield, UK) was selected as the permanent magnet for this machine. This material has a maximum operating temperature of 350 ℃, making it much safer for future applications, such as integration into the aeroengine. Besides, it has higher remanence, 1.16 T, than other products. Moreover, PM segmentation in the machine's axial direction was adopted to decrease eddy current losses. Similar to the lamination of back iron, segmentation and insulation of each PM along the axial or circumferential direction is a valid way to reduce eddy current loss, as practiced in [88]. The thin slices of PM can be coated with a thin insulation coating to minimize eddy current loss. In this case, the thickness of PM slice is 3 mm, considering the performance and manufacturing readiness level.

For the fixation of PMs on the rotor, a robust sleeve is necessary for the rotor assembly. Feasible materials could be alloy, glass, or carbon fibre. Carbon fibre is an ideal material due to its specific strength and minimal eddy current loss, but it can be costly. The diameter of coil for phase winding is determined by optimization process, which will be carried out in the following chapter.

4.4 Machine design process

Multiple-objective optimization and multiple-criterion decision maker were adopted to select optimal parameters based on specific slot/pole combination. The design of electrical machines is a multi-objective, multidisciplinary design as opposed to a sole electromagnetic issue. The electromagnetic, mechanical, and thermal performance of an electrical machine depend heavily on its dimensions or electrical inputs. This philosophy of optimization is an effective process to get a balanced design.

The following design process of machine optimization starts from the selection of slot (***Q***) / pole (***p***) combination with corresponding winding arrangement, distributed winding (DW) or concentrated winding (CW). The computational efficiency and accuracy results of the iterative process depend on the elements which could be divided into following tasks.

4.4.1 Multiple-objective and multiple-discipline optimization design

The typical optimization model consists of variables, objectives, constraints,

variables space and algorithms. At the start of the process, it is essential to select the appropriate input and output variables. It is important that the input variables selected are sensitive enough to have direct effects on the output performance, such as geometric dimension and electrical load. Electrical load is primarily determined by winding turns and current density. To avoid interference, input geometric variables should be assigned in reasonable scopes.

Similarly, the output variables serve as criteria or constraints during iterations. Prior to the start of the workflow, these output variables should be assigned specific values. As constraints of this case, output power (P_{out} > 35 kW), torque ripple, efficiency (η> 95%), winding temperature ($T_{winding}$ <200 ℃) and line-line voltage (U_{ll}< 513 V) were chosen. The LPTN-based software, motor-CAD, provides the thermal analysis, such as the temperature rise and peak temperature of all parts.

The pursuit of high power-density in aircraft applications is a critical objective, defined as the ratio of the rated output power (P_{out}) to weight (W). Besides, the small short-circuit current (I_{sc}) is another objective for this application to cope the severe winding fault. The three objectives provide direction to the optimization process. Above all, the process of optimization design is illustrated in *Fig. 4.3*.

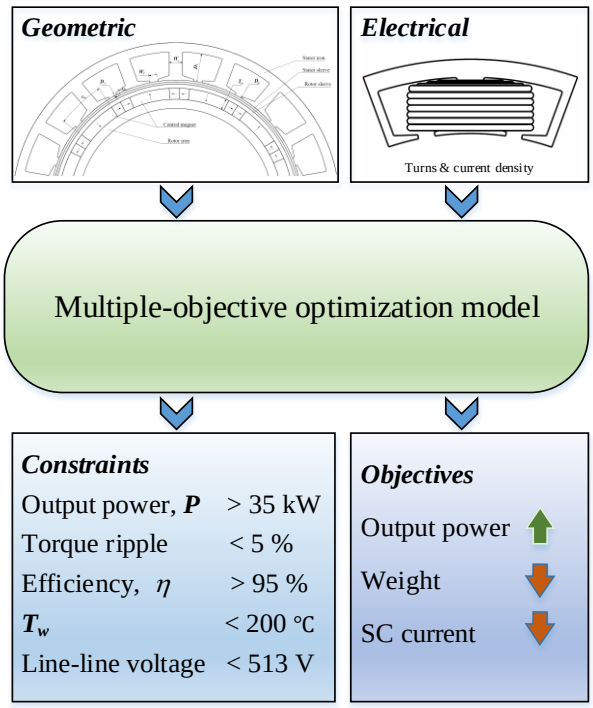


Fig. 4.3 Block process of optimization.

Afterwards, the multiple criterion decision maker (MCDM) method could be adopted to rank the comprehensive performance of different slot/pole combinations. Adopted this method for every candidate is a fair way to rank their performance at rated operation point.

4.4.2 Objectives and constraints

In order to efficiently obtain reliable results in the search space, it is the top priority step to correctly define the objectives and constraints. As previously mentioned, high power density is a key target. In other words, under the premise of ensuring the rated power output, the machine weight of active parts which include lamination of stator, rotor, PMs, windings and shaft, $\boldsymbol{W}$, should be optimized as light as possible. Likewise, higher efficiency, $\boldsymbol{\eta}$, means less energy loss.

Subsequently, the competence of fault tolerant is another core objective for this PMSG. To cope the most fatal fault in the electrical machine [80], the suppression of the stable peak value of SC,I_{sc}, is the most direct way in this case. This purpose could be accomplished by high reactance design [107]. Not only the electrical parameter but also the geometric dimensions play an important role for suppressing the faulty current. In the 2D model, the narrow and deep slot type has higher slot leakage reactance which restrained the SC current.

4.4.3 Search space

The surface mounted, Halbach array of permanent magnet topology has been chosen in foregoing section, as the fundamental topology [119]. Meanwhile, 2mm carbon fibre bonding is designed to bond the Halbach array PMs on rotor for every combination. Filament-wound composite sleeves of permanent magnet motor rotors offer a superior design alternative for higher performance applications in high speed. Besides, carbon fibre encapsulation is a perfect fit for systems that must operate reliably in extreme conditions while reducing system weight.

To balance the manufacturing difficulties and advantages of Halbach array, every pole could be divided into three parts with different magnetization direction (showed in *Fig. 4.4*). For every single pole, the magnetization direction of central magnet aligns with the radial direction, and other two parts are vertical to the central magnet

with adverse direction. For the optimization design, the arc of the central magnet could be a variable.

Besides some fixed parameters, a set of variables have been selected which closely affect the performance of the motor, such as diameter of stator bore D_b, width of tooth W_t, depth of slot D_s, opening of slot W_s, depth of tooth tip D_t, angle of tooth tip α_t thickness of magnet T_m and angle of central magnet α_m, showed in *Fig. 4.4*. It is worth mentioning that the scope of same variable in different slot/pole combination are varied. The range of variable should be distributed reasonably to avoid geometry conflict.

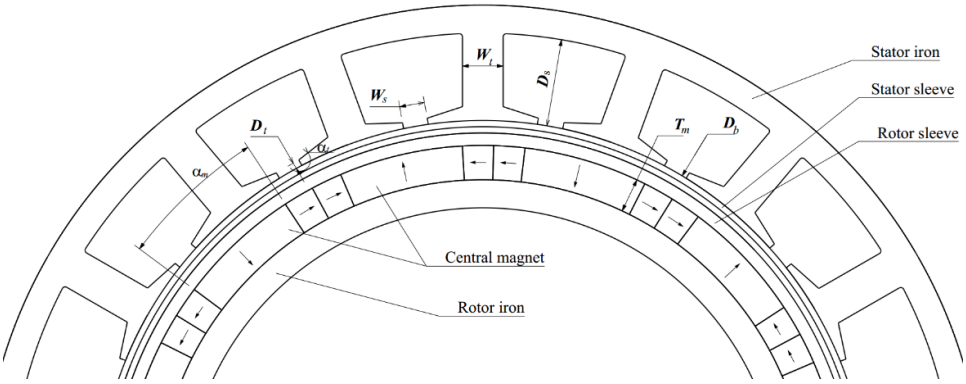


Fig. 4.4 Schematic of the motor assembly.

Besides, the current density and winding turns were selected as input variables in the optimization models. All the 18 combinations have been given same range of current density, from 20 to 25 A/mm^2, available by slot cooling method. And, the turns of single phase winding varies from 30 to 50 turns.

4.4.4 Exploration of the solution space

The amount of optimization designs is determined by design of experiments (DoE) and optimization algorithm. Based on the commercial software, modeFRONTIER, an optimization model was created, as shown in *Fig. 4.5*.

The nondominated sorting genetic algorithm (NSGA-II) was adopted for the optimization work. The number of designs is determined by number of generations and size of initial group, which should be compromised between reliable results and runtime. The amount of initial designs and generations are 110 and 50, respectively. for every slot/pole optimization. Due to the reasonable definitions of variables range, for every slot/pole combination, the scope of 5050 designs is feasible from search

space to optimize proper candidate design. The computation time for every design is about 60 seconds, and the total time-consumption is acceptable.

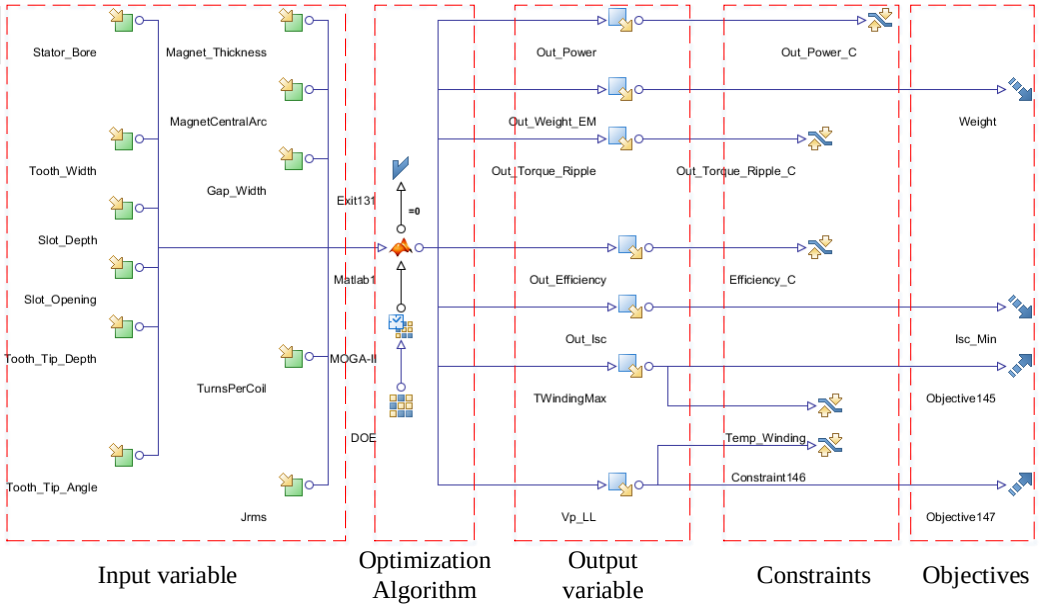


Fig. 4.5 The optimization model of PMSM.

4.4.5 Evaluation and rank

After the optimization analysis based on the joint simulation, optimization software modeFRONTIER and electromagnetic software Motor-CAD, all the feasible designs could be filtered out. Based on the results, it was determined that there are no feasible designs available in the combinations of 12/8, 18/6, 36/6, 18/10 and 30/8.

To determine the optimal candidate for each slot/pole combination and establish the final overall rank, a linear Multiple-Criteria Decision Making (MCDM) approach was adopted. A comprehensive explanation of this methodology will be provided in a later section, namely section 4.4.5.2.

4.4.5.1 Results

The curves of weight, short circuit current and efficiency of all the combinations are depicted in *Fig. 4.6*, *Fig. 4.7* and *Fig. 4.8*, respectively. There was no general trend among them. The final candidate will be a trade-off among these three objectives. It is difficult to choose the best design from different criteria.

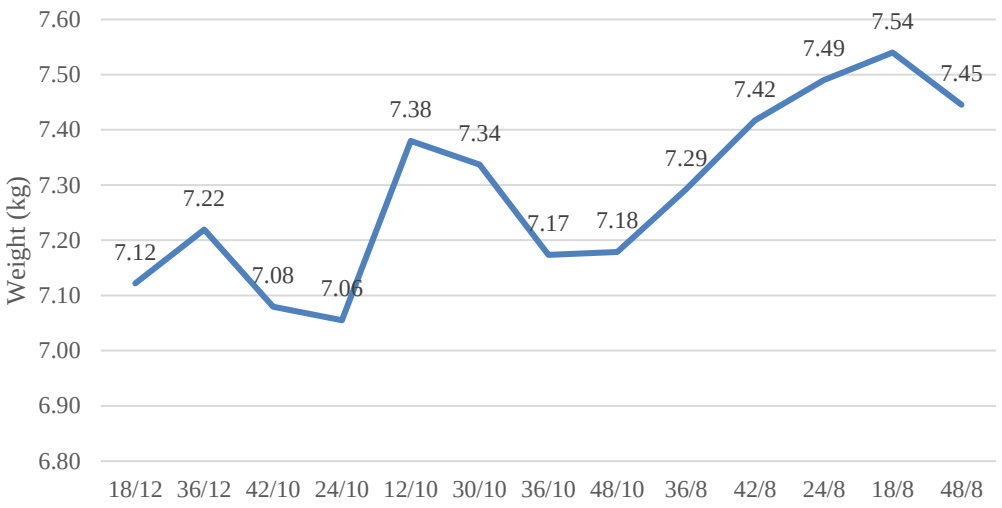


Fig. 4.6 Weight (kg) of the optimal combinations.

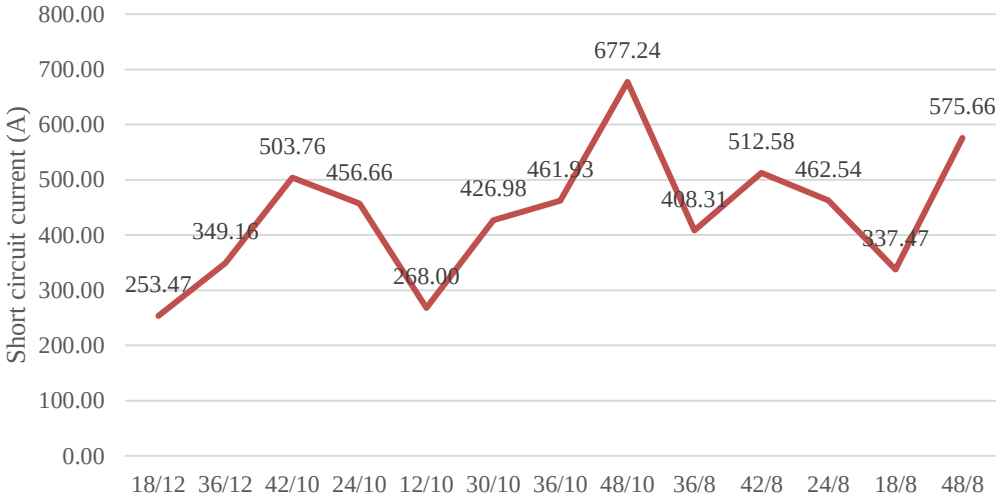


Fig. 4.7 Short circuit current (A) of the optimal combinations.

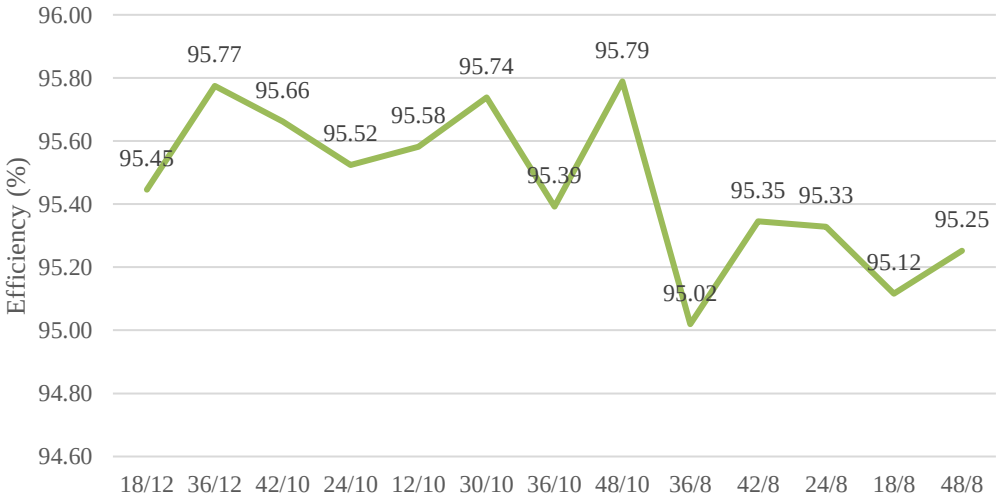


Fig. 4.8 Efficiency of the optimal combinations.

4.4.5.2 Rank

In *Fig. 4.9*, bubble charts are used to visualize weight-SC current plane values, with the colour of the bubbles representing the efficiency. In two-objective optimization, a Pareto front is a general method for obtaining the optimal design, based on same constraints, such as maximum temperature rise in windings. There is an obvious trend line in this figure.

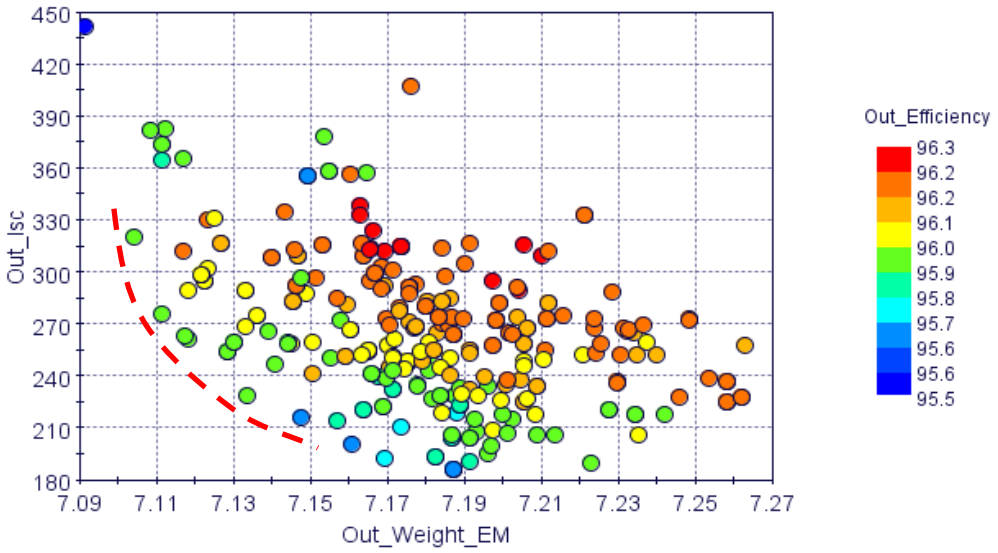


Fig. 4.9 Visualization results of feasible design in 18 slot/12 pole combination.

4.4.5.2.1 Linear Multiple-Criteria Decision Making (MCDM)

Linear Multiple-Criteria Decision Making (MCDM) is a decision-making approach that involves multiple criteria or objectives and seeks to find an optimal solution that satisfies these criteria. It provides a structured framework for decision-making when there are multiple conflicting criteria. By assigning appropriate weights and applying mathematical operations, these methods help in finding the best compromise solution or trade-offs among different objectives.

The weighted sum method (WSM) is a straightforward approach where each criterion is multiplied by its weight and then summed up to obtain a single measure of performance for each alternative. The candidate with the highest value is considered the most desirable.

In the context of linear MCDM, "weight" refers to the relative importance assigned to each criterion. The weights reflect the decision-maker's preferences and are used

to quantify the importance of each criterion in the overall decision-making process.

The weights are typically represented as numerical values, often ranging from 0 to 1, where a weight of 0 indicates that the criterion is not important at all, and a weight of 1 represents the highest level of importance. The sum of all weights is usually normalized to ensure that they form a valid weighting scheme. The overall score of an alternative is calculated as:

$$Score = \sum (w_{ij} \times C_i) \qquad (4-1)$$

where w_{ij} is the weight assigned to criterion i, and C_i is the score of alternative A on criterion *i*, rather than the real values.

4.4.5.2.2 Calculation process

For objectives to be maximized (efficiency, η) and objectives to be minimized (short-circuit current I_{SC} and weight W), their normalized values are different. For objectives to be maximized, its normalized value = (Actual value - Minimum value) / (Maximum value - Minimum value), while for objectives to be minimized, its normalized value = (Maximum value - Actual value) / (Maximum value - Minimum value).

The weighting factors for three objectives, η, I_{SC} and W, are the same, 1/3. The minimum and maximum values of three objectives in all candidates are, 95.02% to 95.79% of η, 253.47 A to 677.24 A of I_{SC}, and 7.06 kg to 7.54 kg of W, respectively. The detailed process is outlined blow.

1) Normalize the objective values

Normalized η = (95.45 - 95.02) / (95.79 - 95.02) = 0.5603

Normalized I_{SC} = (677.24 - 253.47) / (677.24 - 253.47) = 1

Normalized W = (7.54 - 7.12) / (7.54 - 7.06) = 0.8571

2) Apply weights

Weighted η = Normalized η * η Weight = 0.5603 * (1/3) = 0.1868

Weighted I_{SC} = Normalized I_{SC} * I_{SC} Weight = 1 * (1/3) = 0.3333

Weighted W = Normalized W * W Weight = 0.8571 * (1/3) = 0.2857

3) Calculate the ranking value

Ranking Value = Weighted η + Weighted I_{SC} + Weighted W

= 0.1868 + 0.3333 + 0.2857 = 0.8058

Therefore, the ranking value for candidate 18/12 is approximately 0.81. The values of the calculation process are outlined in the Table 4.4.

Table 4.4 Linear MCDM values of 18/12 candidate.

Objective	Actual value	Maximum value	Minimum value	Normalized value	Weighted Value
η (%)	95.02	95.79	95.02	0.5603	0.1868
I_{SC} (A)	253.47	677.24	253.47	1	0.3333
W (kg)	7.12	7.54	7.06	0.8571	0.2857
Weighted sum					0.8058

The same process was performed for other candidates as well. In Table 4.5, it illustrates the comprehensive rank of potential slot/pole combinations based on η, I_{sc} and W. In the results, the specific PMSG has the top three candidates in sequence: 18/12, 36/12, and 42/10.

Table 4.5 The comprehensive rank of feasible combination.

$Rank^1$	Case	η(%)	I_{SC}(A)	W(kg)	Ranking value
1	18/12	95.45	253.47	7.12	0.81
2	36/12	95.77	349.16	7.22	0.81
3	42/10	95.66	503.76	7.08	0.73
4	24/10	95.52	456.66	7.06	0.72
5	12/10	95.58	268.00	7.38	0.68
6	30/10	95.74	426.98	7.34	0.65
7	36/10	95.39	461.93	7.17	0.59
8	48/10	95.79	677.24	7.18	0.58
9	36/8	95.02	408.31	7.29	0.39
10	42/8	95.35	512.58	7.42	0.36
11	24/8	95.33	462.54	7.49	0.34
12	18/8	95.12	337.47	7.54	0.31
13	48/8	95.25	575.66	7.45	0.24

Meanwhile, to review the detailed performance, the 18 slot/12 pole combination

could provide 35.0 kW output power at base speed, with the weight of electromagnetic components, 7.12 kg. The power density can reach 4.92 kW/kg with housing water jacket. Additionally, it can be improved to 7.0 kW/kg, with slot cooling or the combination of housing water jacket and potting. The cooling methods will be covered in Chapter 6.

4.5 Conclusion

In this chapter, a permanent magnet starter/generator has been designed following the core challenges, high power density and competence to suppress of SC current.

A comprehensive design process for multiple objective optimization was carried out. Based on the abundant potential candidates, multiple criterion decision maker was adopted to select final optimal one. Furtherly, this method was utilized to select final design from varied slot/pole combinations.

The conventional 18 slot/12 pole surface mounted PM electrical machine shows the better comprehensive electromagnetic performance than other topologies, under the restriction of specification and space envelop. But, this conventional topology is not capable of fault isolation. More work will be carried out to investigate post-fault performance and iterate topologies for pursuing higher fault tolerance in following chapters.

Chapter 5 Fault tolerance improvement of PMSM candidate

Regarding the need for reliability in this safety-critical application, it is crucial that the electrical machine is robust and able to operate continuously even in the presence of specific faults. In other words, fault tolerance (FT) is a key design objective for this specific application.

In addition to directly inhibiting the short-circuit (SC) current for the sake of an FT design, fault isolation is another design philosophy that seeks to isolate the faulty part from the entire machine. This involves three fundamental and interrelated aspects: electrical, magnetic, and thermal isolation. For fault tolerant design in electrical machines, the majority of efforts focus on the winding design.

5.1 Winding design

As discussed in Chapter 3, the most direct and efficient approach to achieving electrical isolation is to use an H-bridge for each individual phase to ensure independent power supply. However, due to the high cost and power rating requirements of power electronics, multiple three-phase topologies have become a popular compromise, offering benefits in cost, redundancy, and post-fault performance. Multiple three-phase topologies provide a higher level of margin for mission reliability but may reduce the basic reliability of the system due to the increased number of electronic components. The mainstream multiple three-phase topologies include dual, triple, and quadruple three-phase topologies.

5.2 Topology Feasibility of multiple three-phase

In this section, the feasibility of different winding arrangements, including double

layer (DL) and single layer (SL), for 13 slot/pole combinations with multiple three-phase were investigated. The dual, triple, quadruple, and sextuple three-phase topologies were analysed in sequence based on qualitative analysis using winding theory [118]. The feasibility of the topology of multiple three-phase was determined based on the slot/pole combination and the winding layers. The results of this analysis are summarized in Table 5.1, where a tick ('√') indicates feasibility and a cross ('×') indicates infeasibility for forming multiple three-phase.

Compared with DL windings, the SL windings feature of higher self-inductance, low mutual inductance, lower short circuit current and coupling. The tick ('√') and cross ('×') represent the feasibility whether this topology can form multiple three-phase, separately. Then, the conclusions of Chapter 3 will be iterated, concerning the comparison of topologies and corresponding competence of FT.

Table 5.1 The feasibility of multiple three-phase topology.

Case	18/12	36/12	42/10	24/10	12/10	30/10	36/10	48/10	36/8	42/8	24/8	18/8	48/8
DL	√	√	√	√	√	√	√	√	√	√	√	√	√
SL	×	√	×	×	√	×	√	×	×	×	√	×	×

The schematic arrangement of winding topology for these 13 slot/pole combinations are illustrated in the following content.

5.2.1 Dual three-phase layout

Dual three-phase winding topologies are the widespread option of FT design, due to its balance between redundancy and cost. All the feasible winding arrangements of dual three-phase were listed in detail. The target of the work is to investigate the optimal topology for fault tolerant design. Several conclusions could be conducted from these topologies.

5.2.1.1 Double layer dual three-phase

All the combination with double layer winding could be transformed to dual three-phase by dividing the winding symmetrically or duplicating. The configurations are varied due to slot/pole combination.

The target of topology layouts in this section is to pursue independent arrangements,

while one set of three-phase winding were arranged in the slots without overlapping to another set. The detailed layouts of feasible dual three phase in these slot/pole combinations has been investigated, and one set of three-phase is illustrated in *Fig. 5.1*. The one set of three-phase in 18/12 combination has three options, as shown in *Fig. 5.1* (a). Its first two options can arrange one set of three-phase winding in a semi stator, while the third option was arranged on alternate teeth.

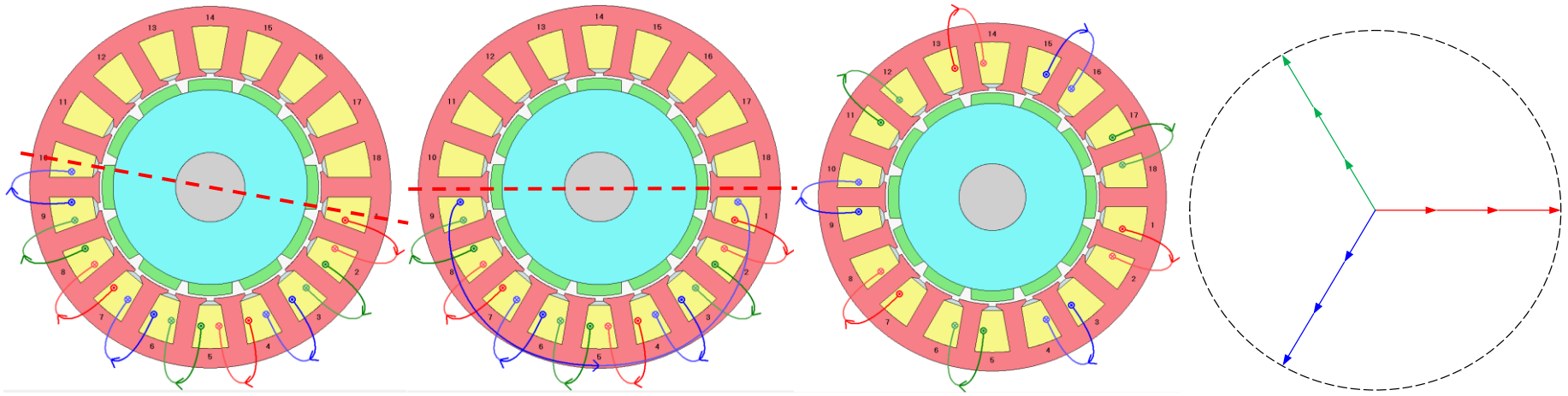
The 36 slot/12 pole exhibits most options for dual three-phase arrangement, as shown in *Fig. 5.1* (b); the windings in other options are all overlapping which cannot meet the requirements of thermal isolation. Similar demerits are existed in other all combinations but 12/10 combination.

Besides the conventional arrangement, some slot/pole combinations could arrange three-phase winding in semi stator in order to avoid overlapping or adjacent between two sets of three-phases, such as 36/12, 24/8 and 48/8, as shown in *Fig. 5.1* (b), (l) and (m), respectively. Nevertheless, this layout may result in unbalanced impedance during one three-phase.

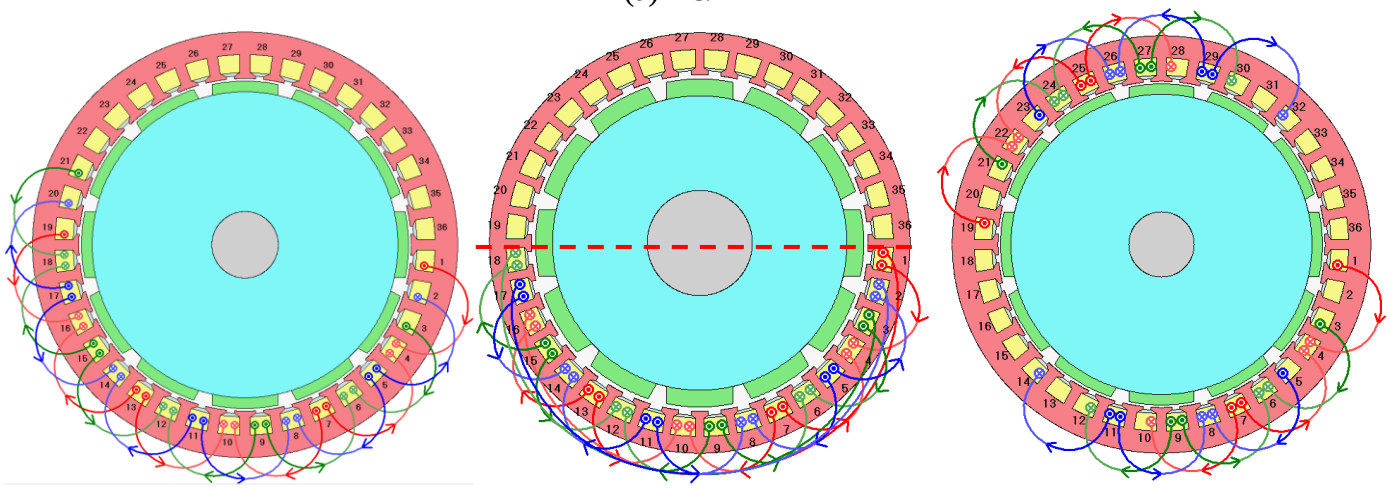
5.2.1.2 Single layer dual three-phase

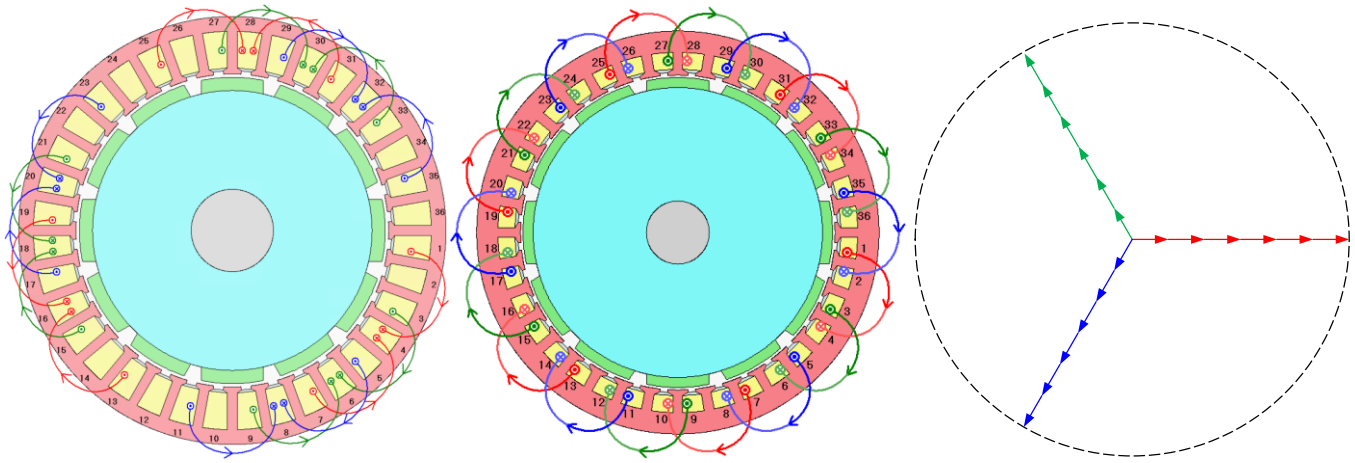
The options of SL winding layout are less than double layer, which only exist in 36/12, 12/10, 36/10, and 24/8 combination. The feasibility of SL winding layout for dual three-phase is determined by the number of slots, which must be a multiple of 12. The feasible winding topologies are illustrated blow, in *Fig. 5.2*. The slot/pole combination of 12/10 is an optimal candidate, which has been prototyped by peers [114], due to merits of higher fault tolerance in fault isolation and post-fault performance.

Based on the definition of isolations introduced in Chapter 3, the fault-tolerance of all the slot/pole combinations were evaluated qualitatively. Above all, the comprehensive evaluation of fault tolerance of these 13 combinations which met the specification, have been investigated in the three aspects, electrical (E) / magnetic (M) / thermal (T) isolation in Table 5.2. The criterion of three kinds of isolation has been given in Chapter 3.4.1.2. The definitions of tick (‘√’) and cross (‘×’) represent whether this topology is feasible or not; moreover, the plus (‘+’) and minus (‘-’) means the performance of FT design.

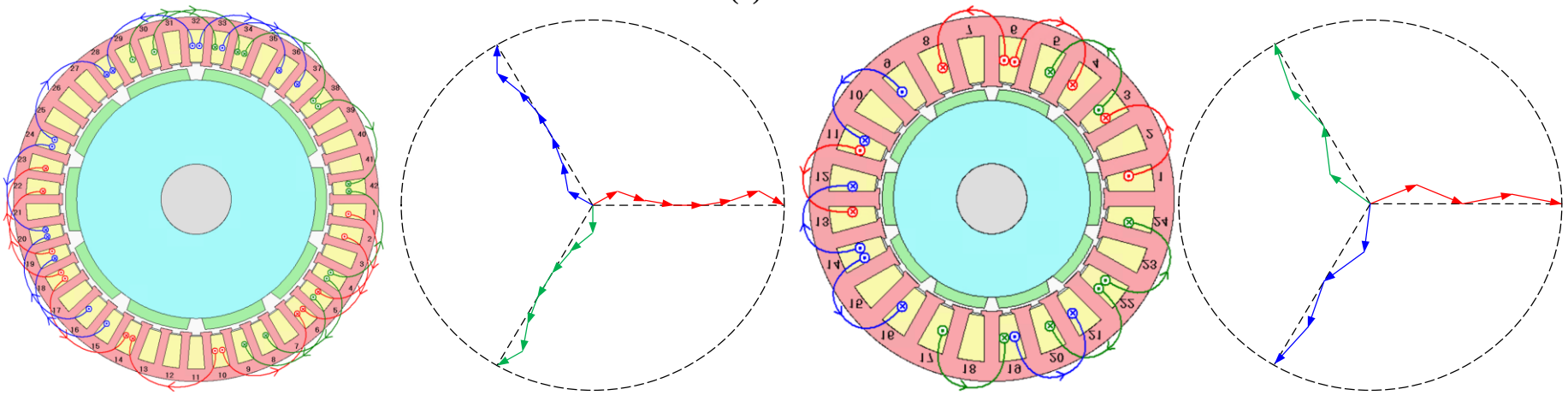


(a) 18/12

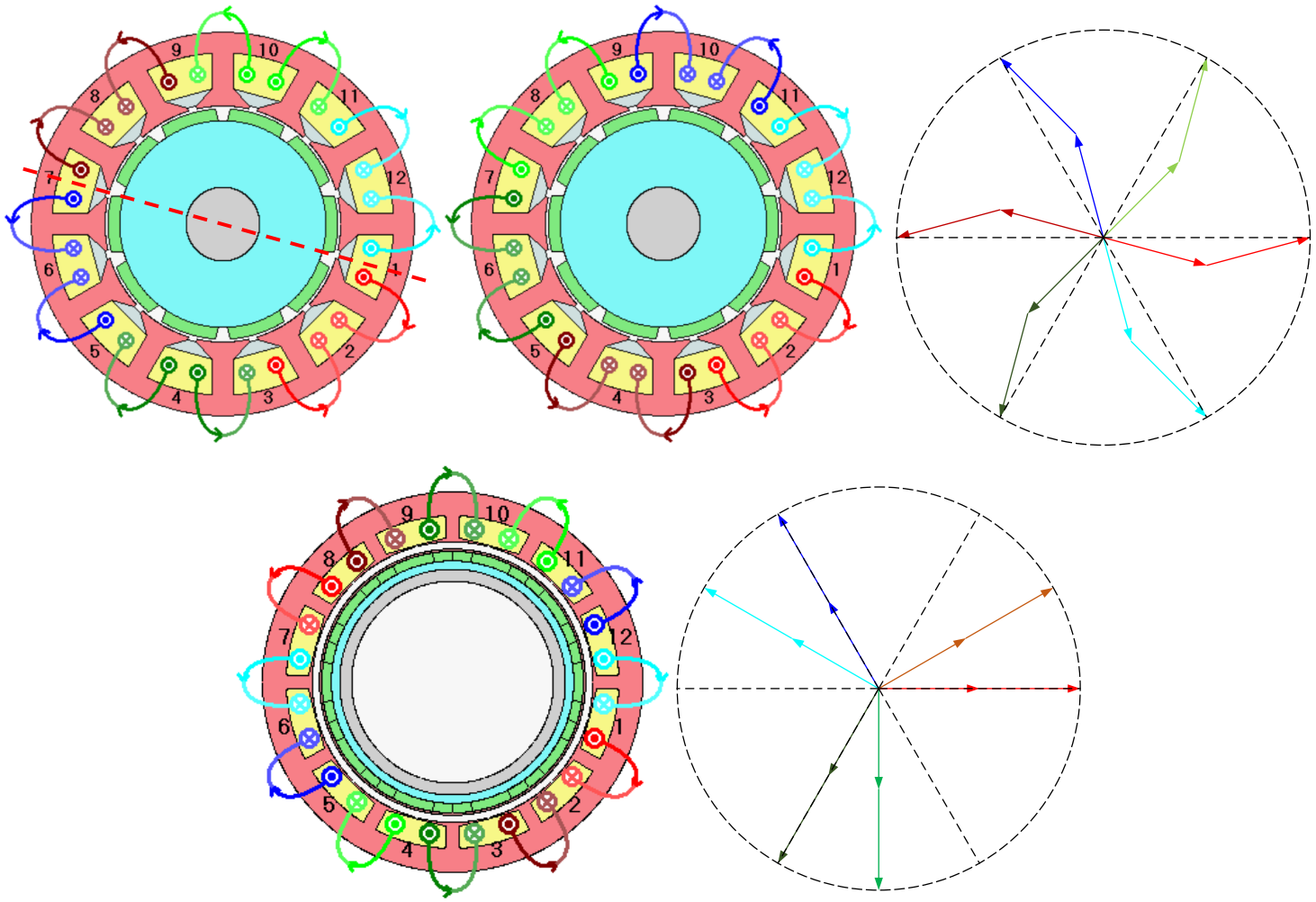




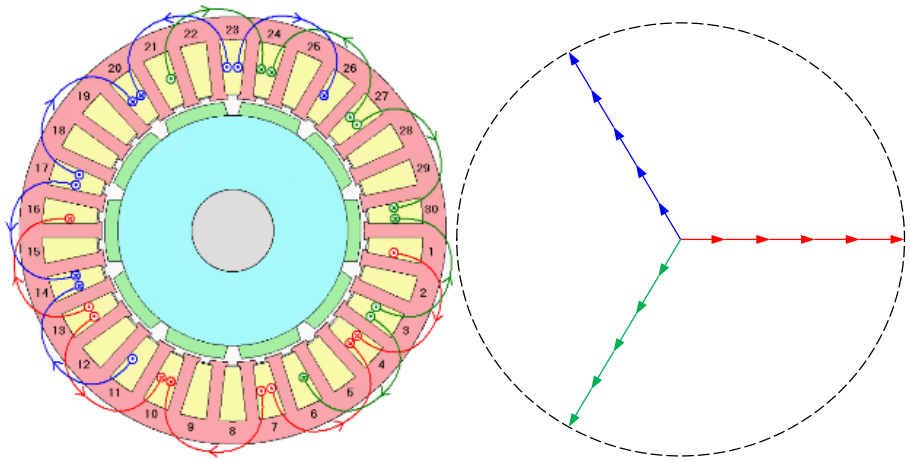
(b) 36/12



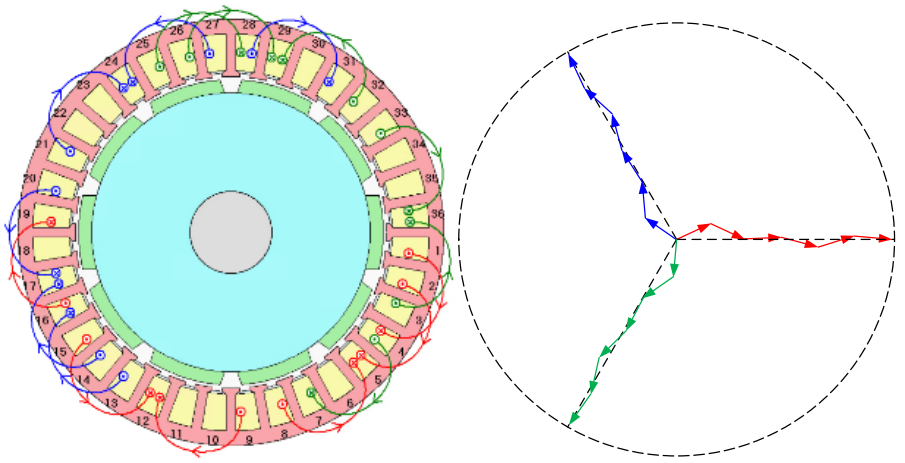
(c) 42/10 (d) 24/10



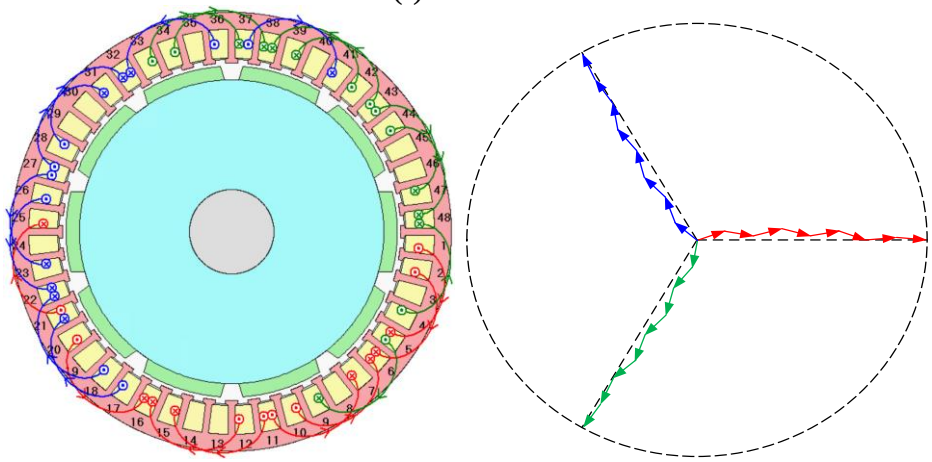
(e) 12/10



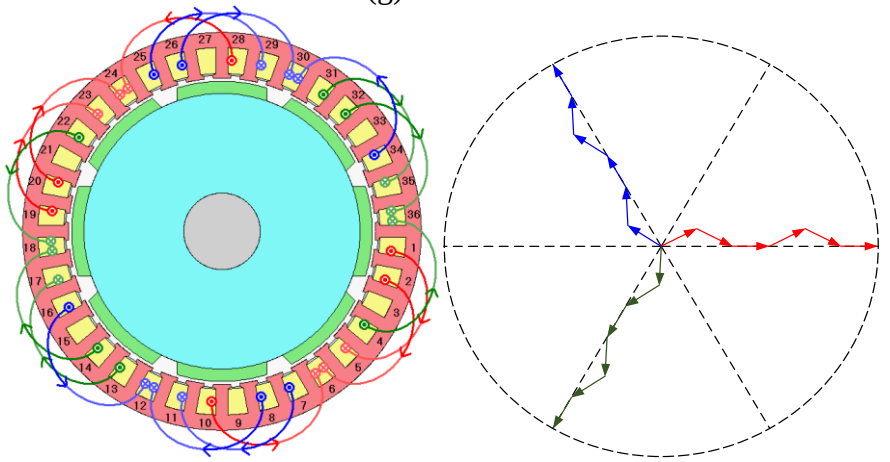
(f) 30/10



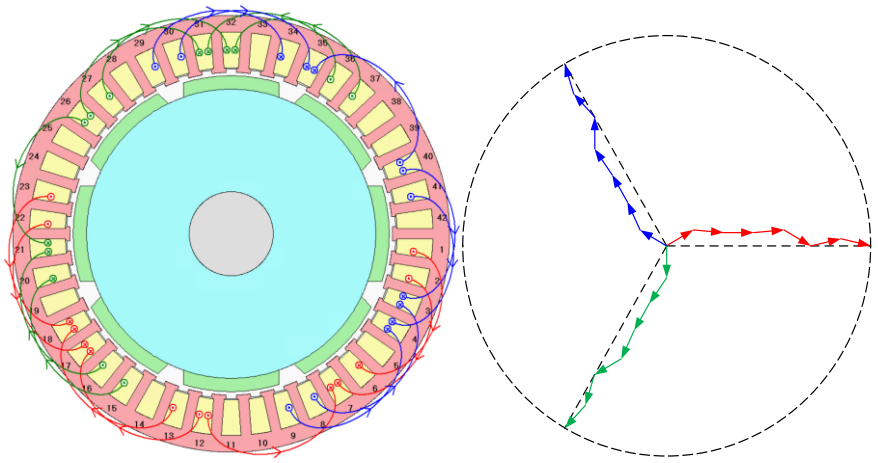
(g) 36/10



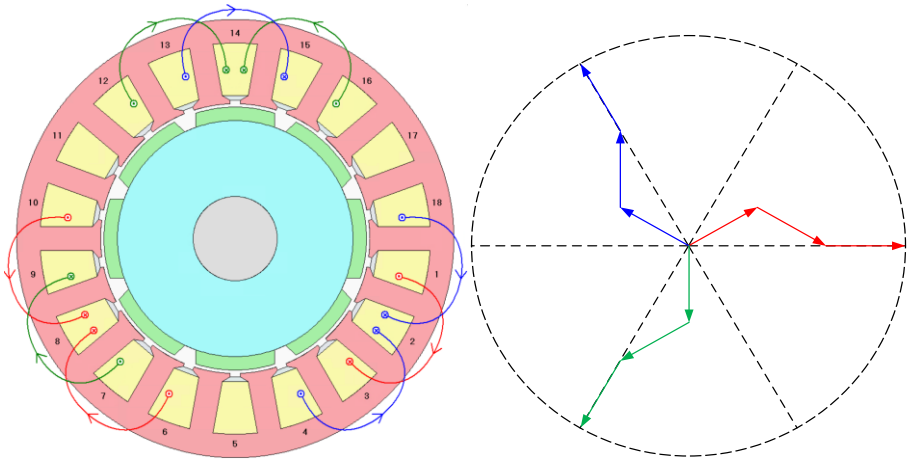
(h) 48/10



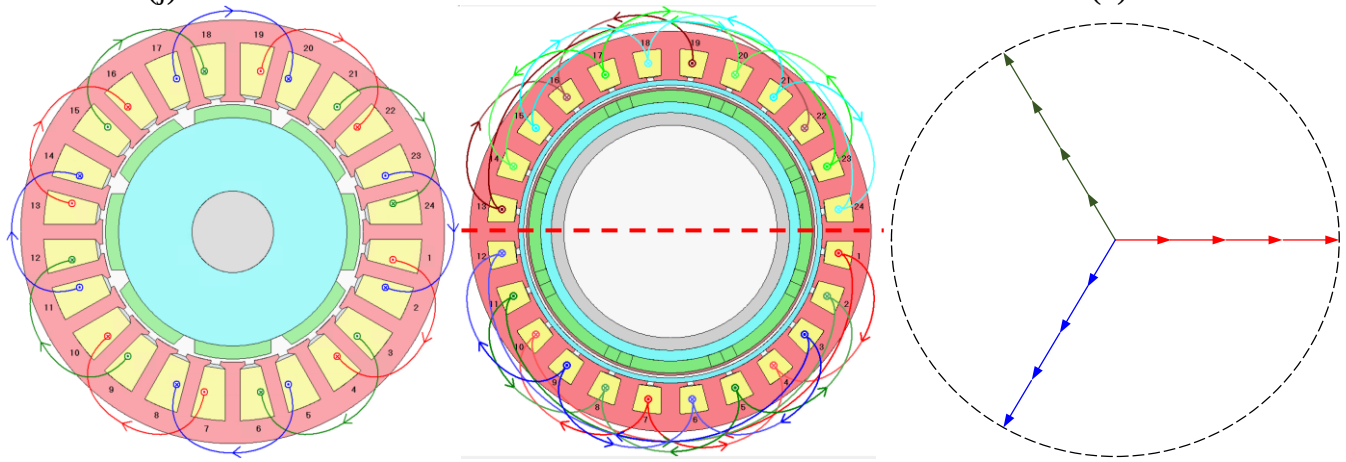
(i) 36/8



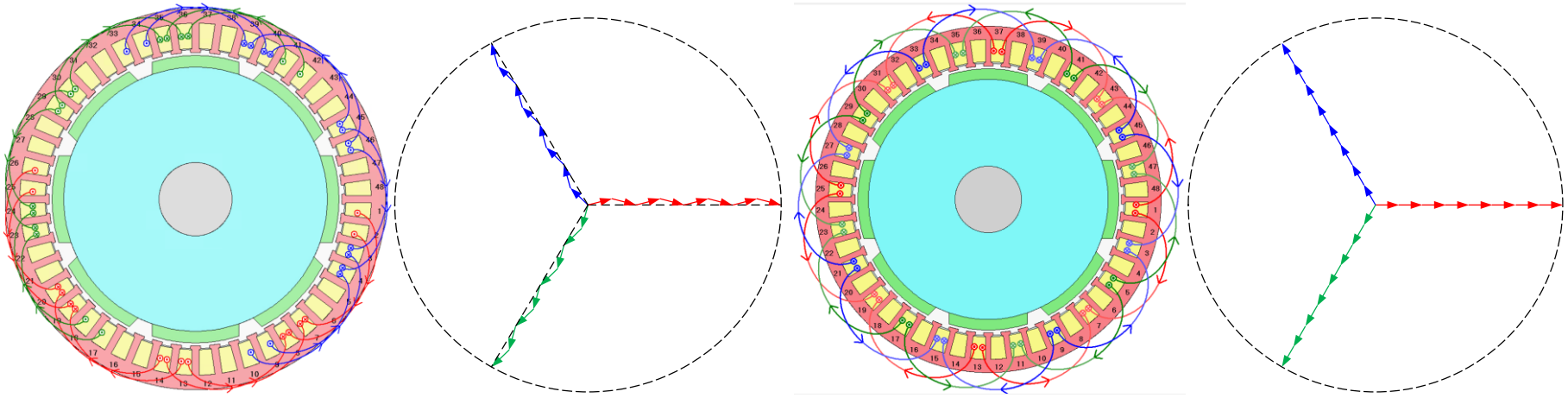
(j) 42/8



(k) 18/8

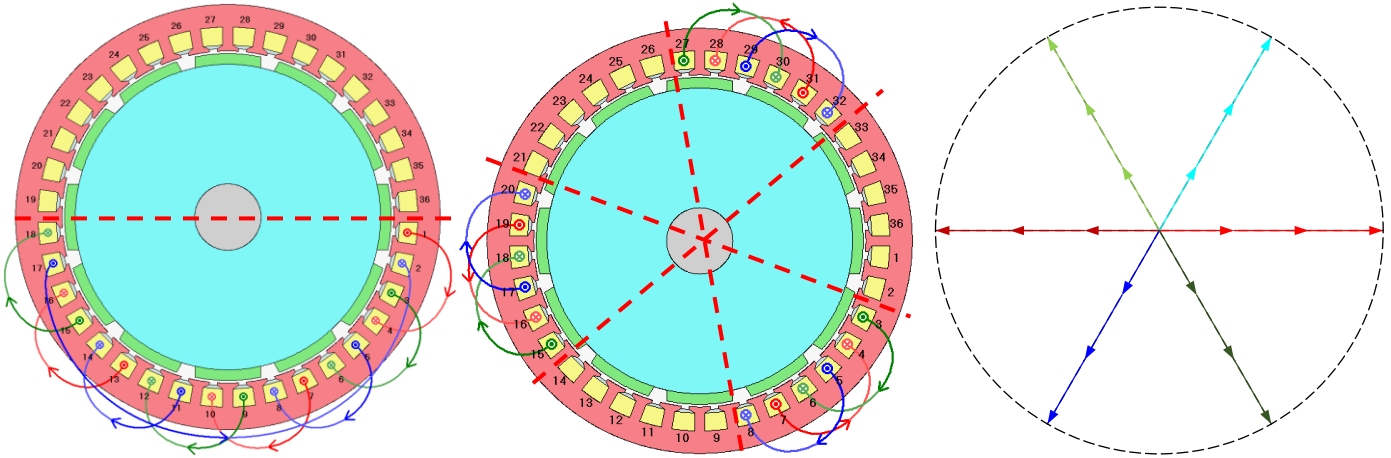


(l) 24/8

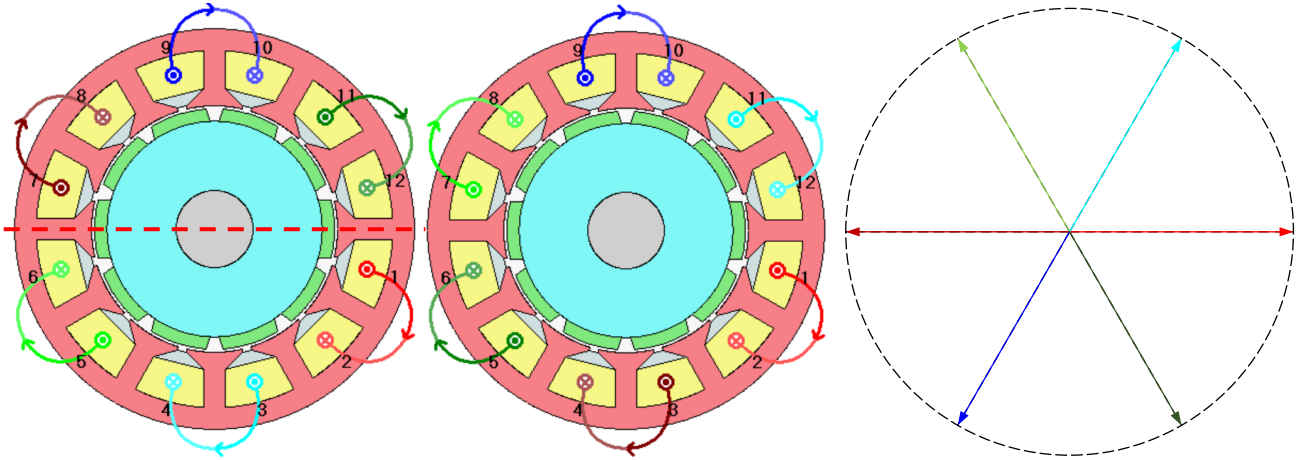


(m) 48/8

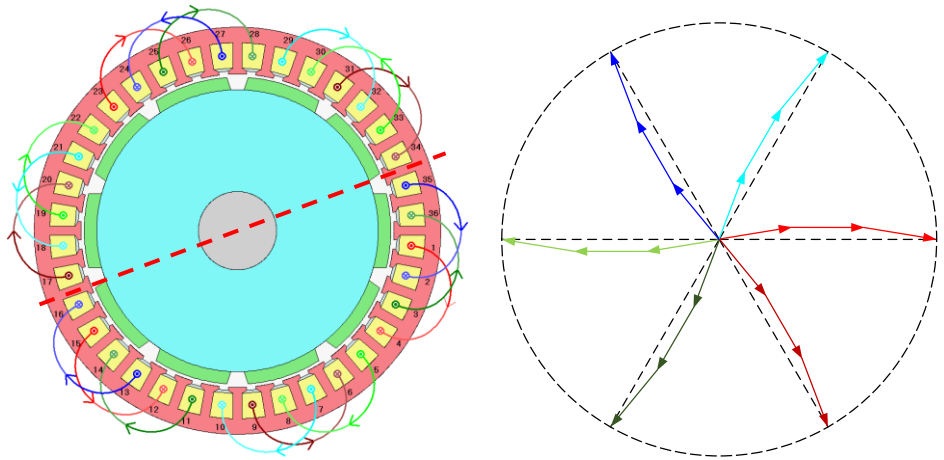
Fig. 5.1 Double layer three-phase based on selected slot/pole combinations.



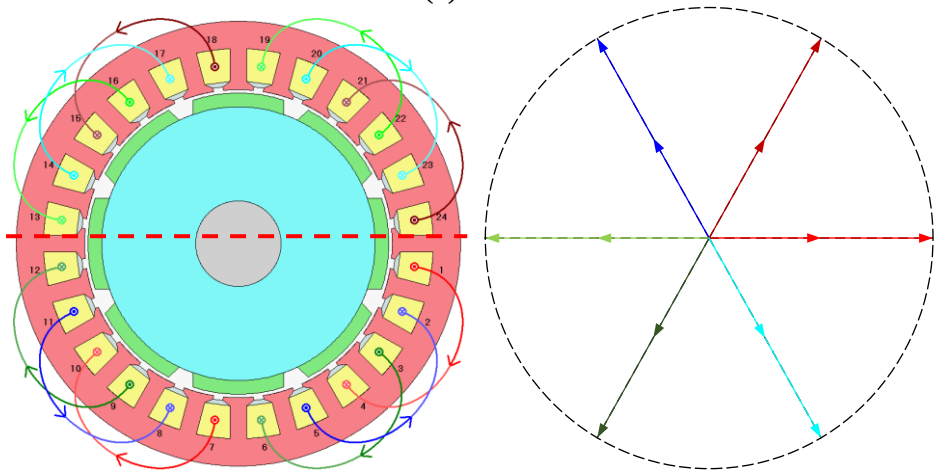
(a) 36/12



(b) 12/10



(c) 36/10



(d) 24/8

Fig. 5.2 Single layer three-phase based on selected slot/pole combinations.

Table 5.2 The FT evaluation of dual three-phase winding.

Cases	DL and FT				SL and FT			
	DL	E	M	T	SL	E	M	T
18/12	√	+	+	-	×	-	-	-
36/12	√	+	-	-	√	+	+	+
42/10	√	+	-	-	×	-	-	-
24/10	√	+	-	-	×	-	-	-
12/10	√	+	+	-	√	+	+	+
30/10	√	+	-	-	×	-	-	-
36/10	√	+	-	-	×	-	-	-
48/10	√	+	-	-	×	-	-	-
36/8	√	+	-	-	×	-	-	-
42/8	√	+	-	-	×	-	-	-
24/8	√	+	-	-	√	+	+	+
18/8	√	+	-	-	×	-	-	-
48/8	√	+	-	-	×	-	-	-

The combinations of 18/12 and 12/10 have the FSCW layout, which means their windings are independent as opposed to overlapping. Based on the illustration of DL concentrated windings, the single three-phase could be arranged in one side of the stator lamination if the pole pairs are even, such as four or six pole pairs. Besides, to pursue further fault-tolerance, the winding could be set in the semi stator if the amount of slots is a multiple of 12. In the combination of 36/12 and 24/8, they are feasible to avoid the overlapping and contact between different three-phases.

5.2.1.3 Quantitative evaluation

To further pursuit higher competence of fault-tolerance, quantitative analysis was carried out. To illustrate the mutual inductance which between the two set of three-phase windings (ABC and $A'B'C'$), there is a quantitative ratio which determined by maximum mutual inductance (L_m) over minimum self-inductance (L_s) in dual three-phase inductance matrix, as shown in the matrix (1). The value represents the effect between phases. The smaller value means the lower effect between different three-phases, which is beneficial for the safety in the case or electrical faults. Compared

with faulty phases or windings, the rest windings are insusceptible due to lower mutual inductance.

$$\mathrm{L} = \begin{bmatrix} L_S & L_m \\ & L_S \end{bmatrix} = \begin{bmatrix} L_A & & & L_{AA'} & L_{AB'} & L_{AC'} \\ & L_B & & L_{BA'} & L_{BB'} & L_{BC'} \\ & & L_C & L_{CA'} & L_{CB'} & L_{CC'} \\ & & & L_{A'} & & \\ & & & & L_{B'} & \\ & & & & & L_{C'} \end{bmatrix} \tag{5.1}$$

For example, the inductance matrix of optimal 18/12 slot/pole candidate of is listed below. The maximum mutual inductance is 33.15 μH, between Phase C and Phase A', while the self-inductance is 203.49 μH. The ratio could be calculated, 16.3 %. The ratio of all the candidates were measured and compared in the following content.

$$Inductance = \begin{bmatrix} 203.53 & 73.75 & 53.65 & 13.05 & 13.09 & 33.14 \\ & 203.54 & 73.72 & 13.09 & 13.05 & 13.09 \\ & & 203.52 & 33.15 & 13.09 & 13.05 \\ & & & 203.53 & 73.75 & 53.65 \\ & & & & 203.53 & 73.71 \\ & & & & & 203.49 \end{bmatrix} \tag{5.2}$$

$$L_{m_\max}/L_s = 16.3\% \tag{5.3}$$

5.2.2 Triple three-phase layout

For higher reliability, triple three-phase topologies move forward to improve the fault-tolerance of specific application, such as generator or motors for aircraft. The feasible slot/pole combinations among them are listed in Table 5.3. The detailed winding arrangements are shown in *Fig. 5.3*.

Table 5.3 Feasible slot/pole combination for triple three phase.

Case	Triple three-phase	
	DL	SL
18/12	×	√
36/12	×	√
36/10	×	√
36/8	√	×
18/8	√	×

Based on the illustrations, 18/12 slot/pole combination with SL winding layout exhibits ideal winding arrangement to meet the requirements of fault-tolerance. In this topology, all the phases/windings are independent and non-overlapping; the unique arrangement is beneficial for the thermal and magnetic isolation.

In the 36/12 combination with SL winding layout, it is feasible to set windings of every three-phase in a 120° sector, by changing the position of Phases A, A' (winding4), and A'' (winding7). The demerit of this transformation may result in unequal impedance of every phase and consequent unbalance between phases. In the 36/10, 36/8 and 18/8 combination, they are feasible to be arranged as triple three-phase. However, the windings are distributed winding which overlapped and unfeasible to achieve magnetic and thermal isolation.

Above all, the single layer 18/12 triple three-phase topology is the optimal candidate for this application.

5.2.3 Multiple three-phase (Phases>9)

Based on the illustrations of dual and triple three-phase, multiple three-phase could be achieved further in specific slot/pole combinations. All the feasible multiple three-phase topologies are shown in Table 5.4. Quadruple and sextuple phase topologies are feasible in specific combinations.

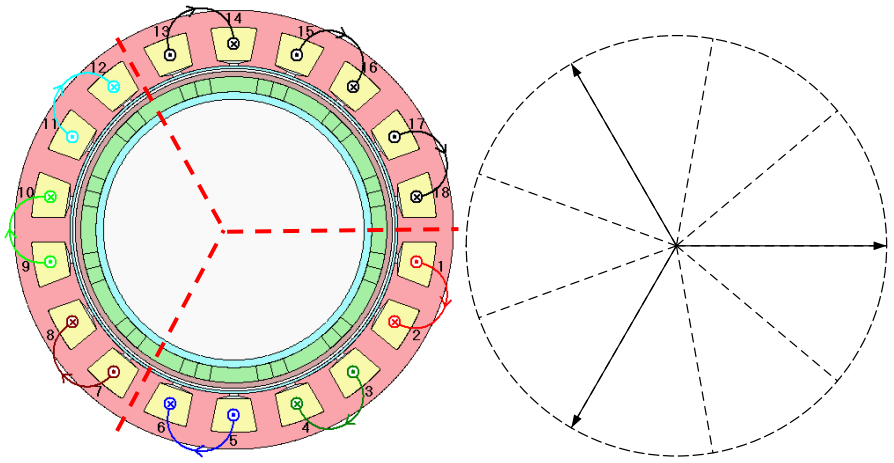
Table 5.4 Feasible slot/pole combination for quadruple and sextuple three-phase.

Case	Quadruple three-phase		Sextuple three-phase	
	DL	SL	DL	SL
18/12	×	×	√	×
36/12	√	×	√	√
12/10	√	×	×	×
36/10	×	×	×	√
36/8	√	×	×	√
24/8	×	√	×	×
18/8	×	×	√	×
48/8	√	√	×	×

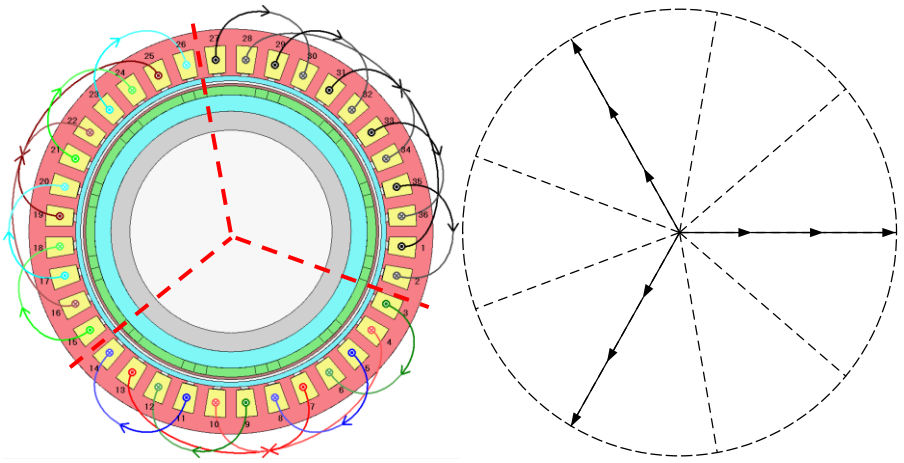
As shown in *Fig. 5.4*, 18/12 slot/pole combination could be arranged as sextuple three-phase, with DL FSCW winding layout. For 24/8 slot/pole combination, it could be designed as quadruple three-phase with SL distributed windings. Besides, 36/10 and 36/12 shot/pole combination can form a sextuple three-phase, with single layer distributed winding. All these layouts can be divided into three-phase units. These independent units can be driven by independent converters to achieve electrical isolation. The obvious benefits of quadruple and sextuple three-phase are capable to maintain more output than dual or triple three-phase topology in case of faulty scenarios.

More three-phase topologies can improve the reliability further, and the decrease the power rating of converter modules. Quadruple three-phase topology are selected for high power electrical machine applied on aircraft as propulsion unit.

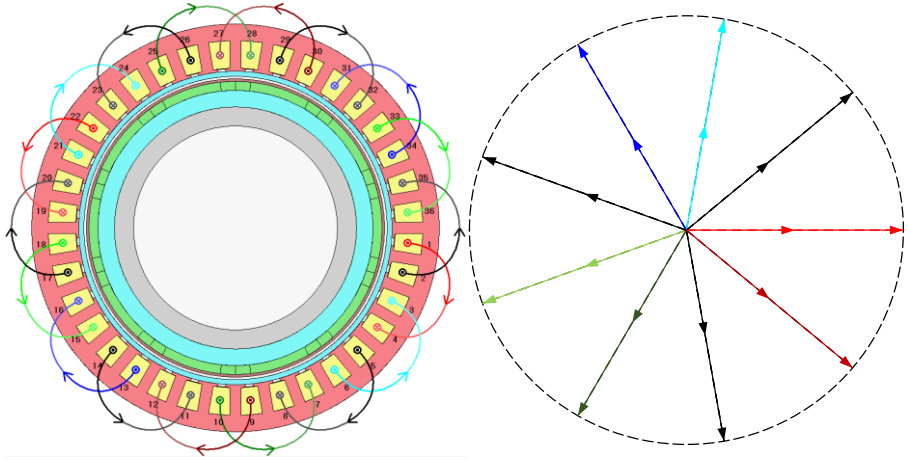
But, this approaches can increase the cost significantly. Besides, more power electronics reduce the fundamental reliability. In the thesis, quadruple and sextuple three-phase 36/12 are not suggested for this specification.



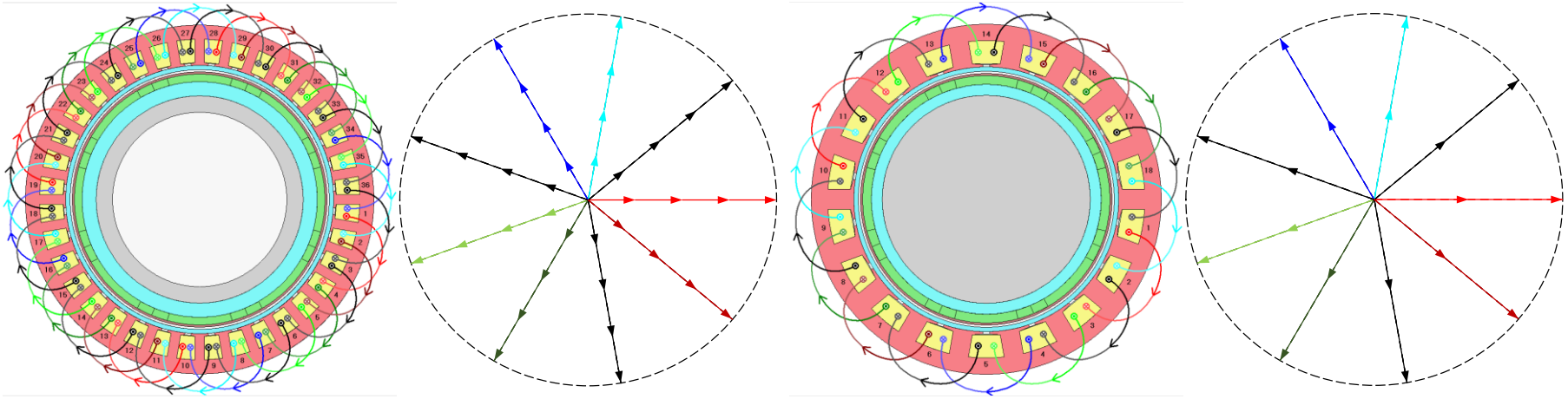
(a) 18/12



(b) 36/12



(c) 36/10



(d) 36/8 (e) 18/8

Fig. 5.3 Feasible topology of triple three-phase.

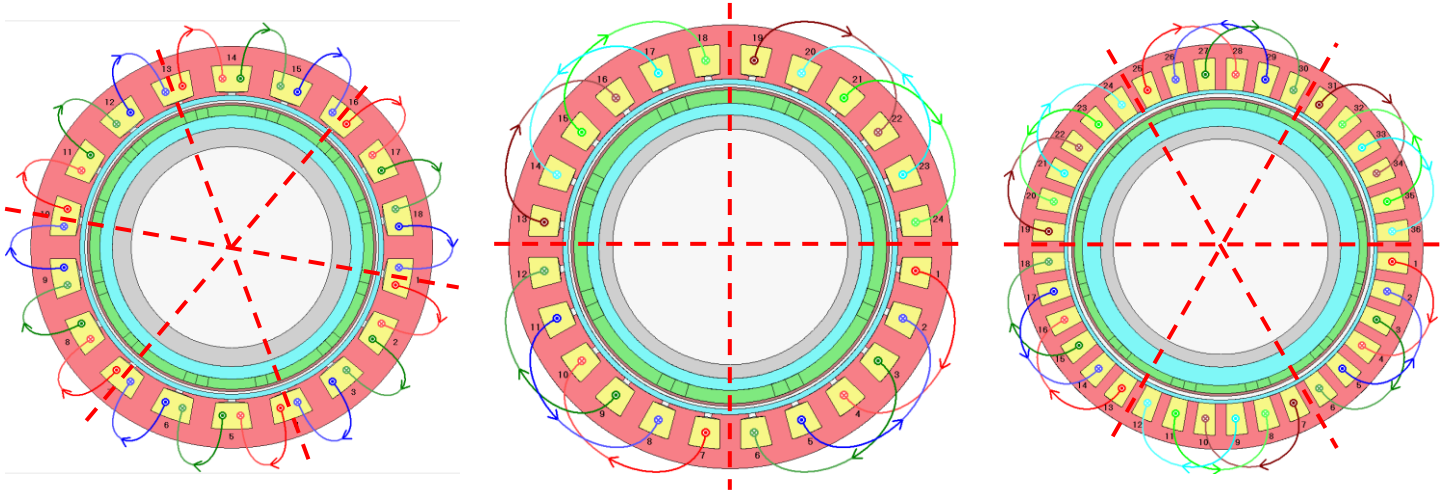


Fig. 5.4 (a) Sextuple three-phase 18/12. (b) Quadruple three-phase 24/8. (c) Sextuple three-phase 36/12.

5.2.4 Conclusion of suggested selection

From the perspective of fault-tolerance, the dual and triple three-phase configurations emerge as potential candidates for addressing most specifications, striking a balance between reliability and cost.

5.3 Validation of topology

In this section, the potential candidates were analysed by FEA method, including the dual and triple three-phase. Besides the healthy operation, behaviour under fault scenarios were investigated as well.

5.3.1 Dual three-phase

As shown in *Fig. 5.5*, 18/12, 36/12, 12/10 and 24/8, these four combinations were selected as the potential candidates for further verification. Every single topology was named by slot/pole and layers of winding, SL or DL. It is worthy to recap the difference between 18/12 DL-1 and DL-2. Both of them can arrange the two sets of three-phase in semi stators, along with the red dash line. Compared with DL-1, single set of three-phase in DL-2 can be arranged in a semi stator, without contacting in slot between two sets.

All the models were created in an electromagnetic simulation software, ANSYS Maxwell. In general, a modular model based on slot/pole combination could be extracted to analysis rather than a whole model. The unit may vary based on different slot/pole combinations. The fundamental slot/pole unit which designed by periodic boundary condition, can exhibit all the behaviour of the topology with low cost of calculation.

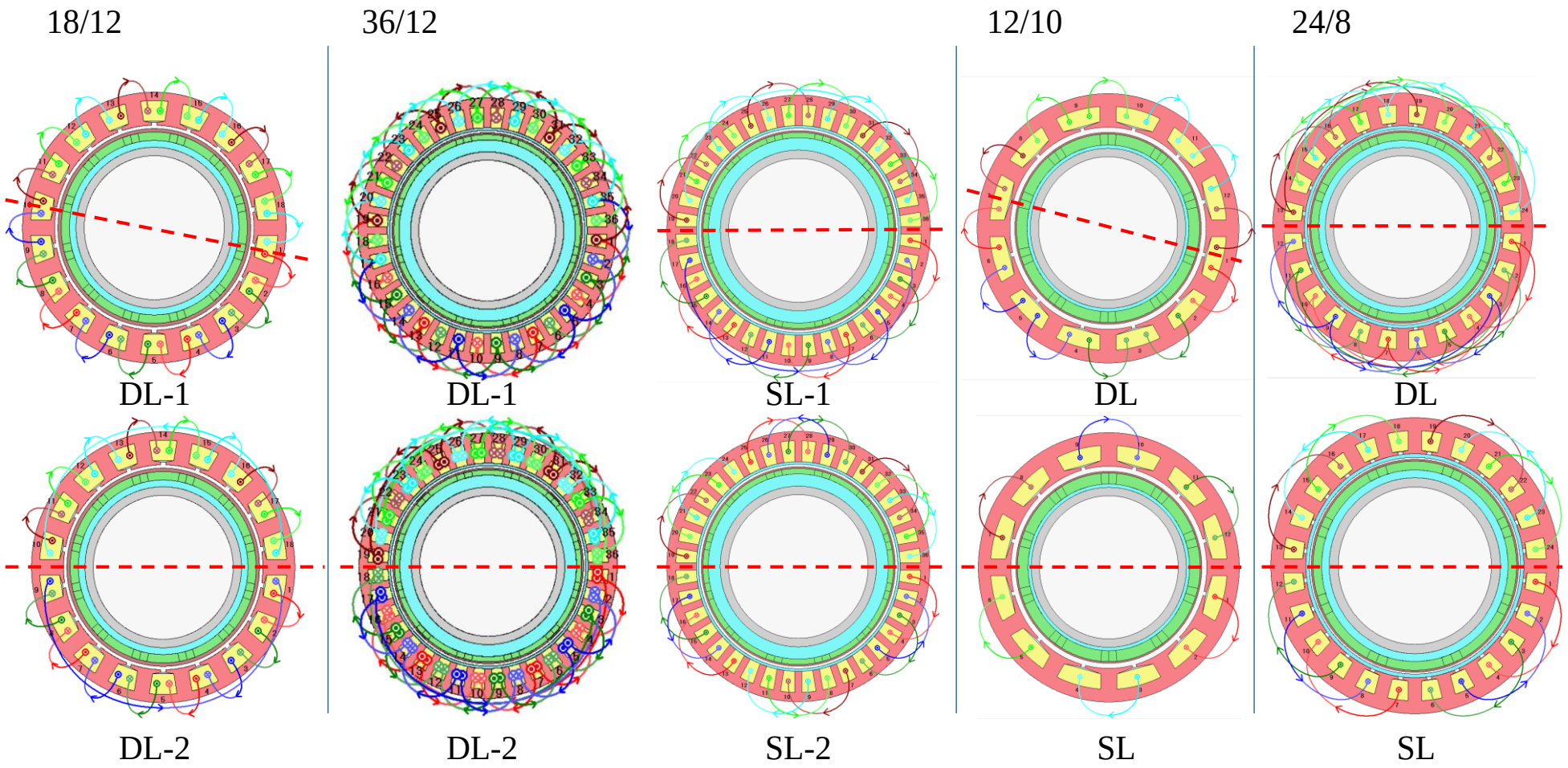
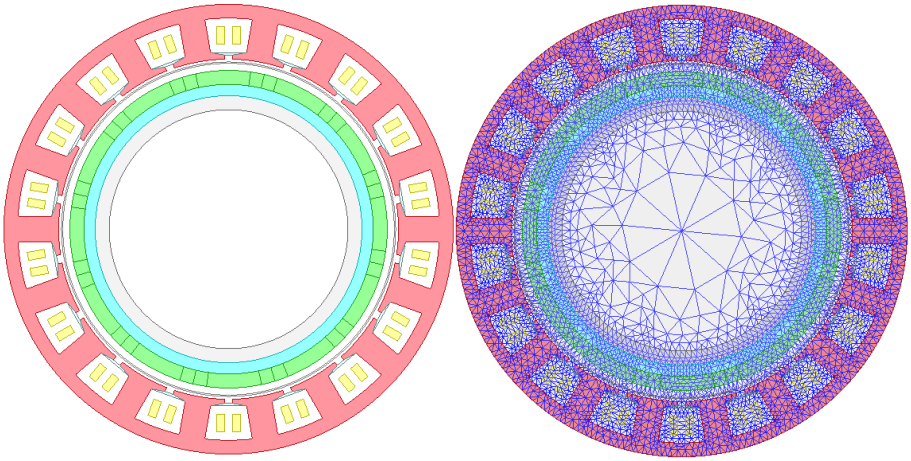


Fig. 5.5 Potential candidates for dual three-phase

5.3.1.1 Case study of dual three phase 18/12

The 18/12 DL-1 was selected as the example to illustrate the whole analysis process. A whole model was created as shown in *Fig. 5.6*, with the FEM model and meshing plots. The reason to create a whole model is to compare the change of the topology with proposed topology in the following content.



(a) (b)

Fig. 5.6 Dual three-phase, 18slot/12pole in ANSYS Maxwell: (a) topology Model; (b) meshing plots.

5.3.1.1.1 No-load operation

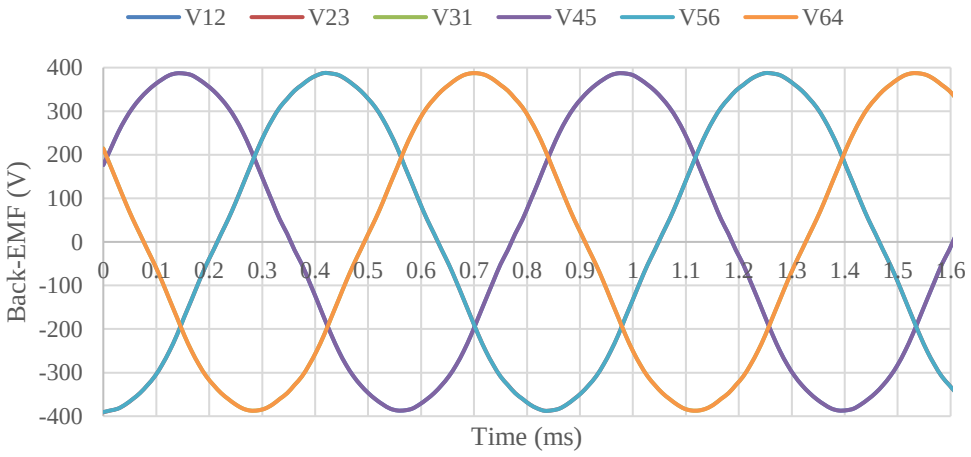
The investigation of no-load operation is the first step to validate the fundamental performance. The flux plots of no-load can be visualized directly for checking the design of PM array. The back-EMF can be measured under the no-load operation and the components of harmonics can be analysed directly.

Due to the fault tolerant winding layout, the phasor diagrams of two sets of three-phase are same and overlapped. Then, one three-phase windings were selected to analysis, such as Phase ABC or Phase $A'B'C'$. The waveforms of back EMF of Phase ABC and its fast Fourier transform (FFT) results are shown in *Fig. 5.7* (a) and (b). The amplitude of fundamental component is 356.0 V. Based on the FFT results, the waveform of back EMF shows fine sinusoidal because of low harmonic component.

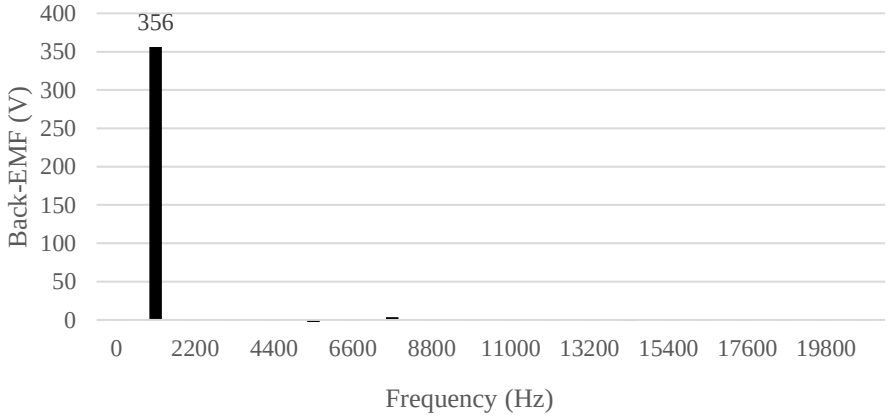
5.3.1.1.2 On-load operation

Based on the curves of torque-speed, the efficiency map is a comprehensive illustration of the performance, which can be drawn by the MotorCAD. The contour of efficiency on speed-torque plane provides the results from standstill to maximum speed with clear and visualization of values.

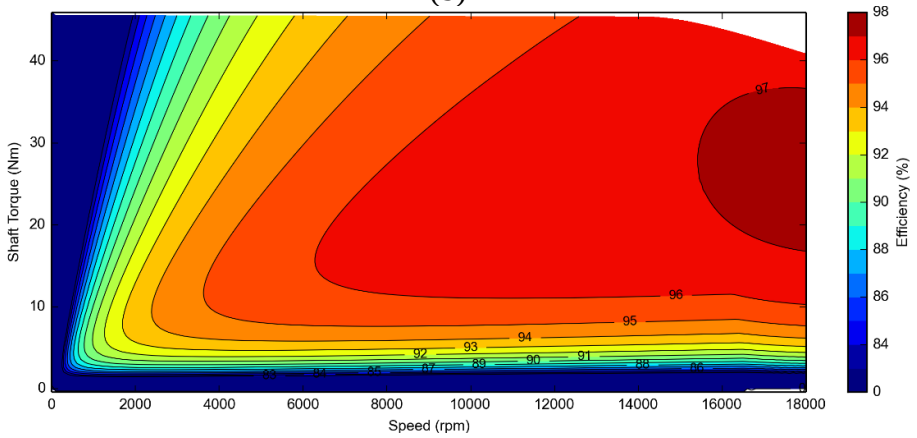
The efficiency map of 18/12 DL-1 is shown in *Fig. 5.7* (c). The key operation point, base speed and max speed, can maintain high efficiency (>95%) output. And, the machine has power margin prepared in consideration of possible downgraded operation, due to faults.



(a)



(b)



(c)

Fig. 5.7 The waveform of (a) no-load line-line back EMF, (b) analysis of harmonics and (c) efficiency map.

5.3.1.1.3 Post-fault performance

For the sake of reliability in safety-critical application, these topologies have been designed to maintain operation continuously in fault scenarios, open circuit and short circuit. In order to validate the fault tolerant performance, the post-fault behaviour has been investigated. Some typical faults such as open circuit and short circuit fault are seeded in a virtual way by means of different external electrical circuits in Ansys.

1) Open circuit (OC) operation

This fault means no current in the open circuit, therefore no energy conversion in the OC windings. This type of fault could be modelled by replacing the winding resistance value with a mega-ohm one, as shown in *Fig. 3.5* (b), which will result in almost no current flow. The post-fault performance under OC is easy to predict. The output torque will decrease correspondingly due to the absence of those phases.

A three-phase open-circuit is modelled for this case. Compared with normal operation, the output of three-phase OC has been examined and compared. Because of the absence of one set of three-phase, output torque has been reduced half. Torque ripple shows increment slightly. Unbalanced radial force spikes dramatically by reason of the winding arrangement, two sets of windings mounted in half stator, respectively. This kind of effect can intensify the noise and vibration, as well as the unbalanced load on bearing pairs. These effects cannot be mitigated from electrical machine itself. The post-fault performance can be improved from advanced machine control.

2) Short circuit (SC) operation

The types and hazard level of short-circuit may be varied due to the uncertainty of faulty location and SC turns.

Firstly, the symmetrical SC fault, which also called phase-to-phase SC, was selected to analysis the post-fault performance. Similarly, the equivalent circuits could be achieved by modifying the external electrical circuits. It can be achieved by connecting the three-phase directly, as shown in *Fig. 3.5* (c). The SC current will cause a drag torque to decrease the output. Both of the SC current and drag torque are determined by rotating speed and other parameters of machine, and their value can be estimated by theoretical approach.

$$i_{sc} = \frac{j\omega N\hat{f}}{R + j\omega L} \tag{5.4}$$

$$T_{drag} = p\left(\frac{j\omega N\hat{f}}{R + j\omega L}\right)^2 R/\omega \tag{5.5}$$

$$T_{drag} = p\left(\frac{N\hat{f}}{L}\right)^2 R/\omega \tag{5.6}$$

Where *p*, pole pairs

f, magnet flux

N, number of turns

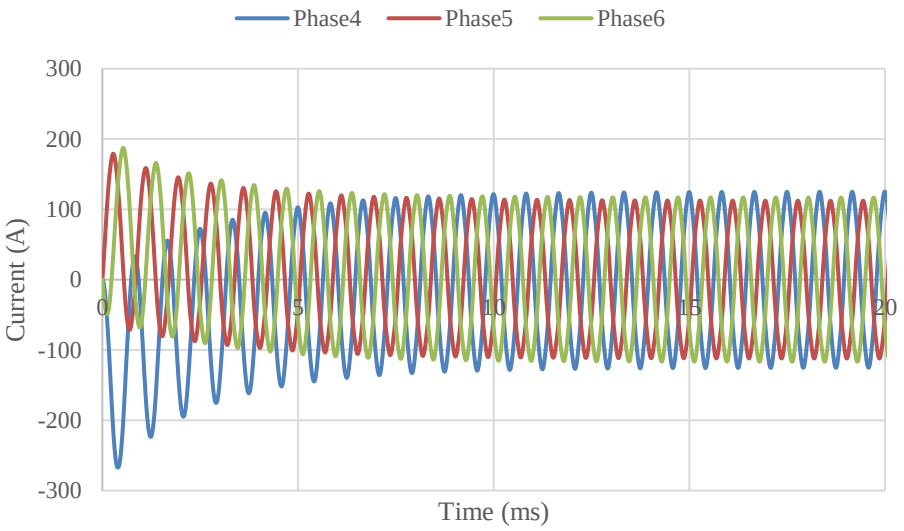
ω, electrical angular speed,

L, winding inductance (shorted winding section)

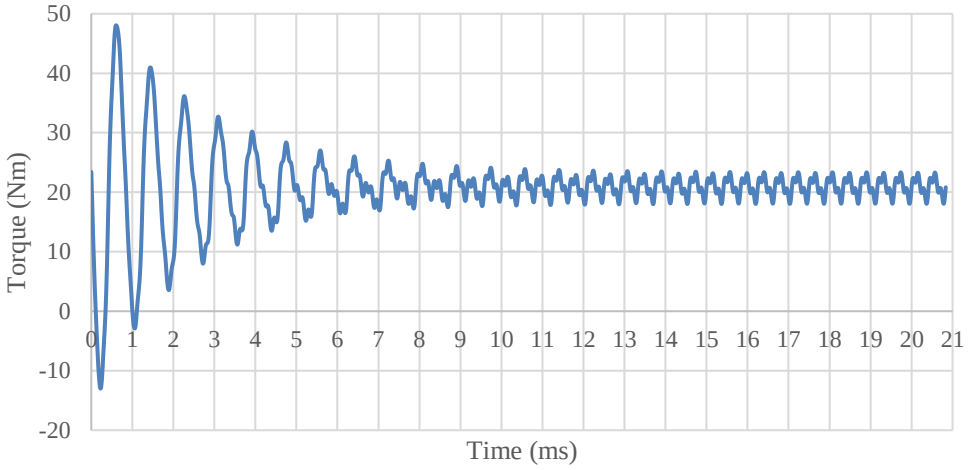
R, winding resistance (shorted winding section)

Then, for the fatal electrical fault, turn-to-turn short-circuit, an independent circuit was created to represent the faulty windings by assigning a relevant value of inductance and resistance determined by the faulty turns, as shown in *Fig. 3.5* (d). It has been reviewed that single turn winding and located near the slot-opening is the fatal combination of short-circuit fault.

By FEM approach, the transient process of SC faults can be simulated. The current waveform in the phase-to-phase SC is exhibited in *Fig. 5.8* (a). The sudden phase-to-phase SC introduced a fluctuation of phase current. The transient peak value of phase current is 191.0 A. After a short duration, the waveform of SC current resumes to sinusoidal types, and the stable peak current is 122.5 A which is considered as the reference for wires, power electronics and thermal management. Steady state current is limited by the phase inductance and is within the thermal limit of the motor. The transient drag torque causes conspicuous torque ripple, which is flatten in stable status, in *Fig. 5.8* (b). Besides, the SC operation causes a conspicuous shock for machine which torque ripple and unbalanced axial force rise rapidly with the half torque loss than normal.



(a)



(b)

Fig. 5.8 The SC behaviour: (a) SC current in the fault phases (b) output torque.

The performance comparison of healthy and faulty scenarios is listed in Table 5.5. Output torque, torque ripple and radial force were included. In these topologies, whatever the fault types, the output torque decease compared with healthy status. SC fault can introduce significant rise in torque ripple and radial force. The radial force under post-fault operation must be considered when selecting bearing pairs.

Table 5.5 The FT Evaluation of Dual three-phase winding.

Status	Torque (Nm)	Torque ripple (%)	Unbalanced radial force (N)
Normal	46.0	4.3	0.9
Open circuit	22.9	5.9	240.0
Short circuit	20.7	25.6	583.7

5.3.1.2 Comparison of candidates

Similar to the dual three-phase 18/12 DL-1 topology, the rest of feasible topologies were carried out by the same process, including the no-load, on-load and faulty simulations.

5.3.1.2.1 Inductance

The inductance comparison of selected ten candidates was carried out, as shown in *Fig. 5.9*. In general, the dual three-phase 12/10 exhibit high inductance design in both SL and SL winding layout. The high inductance design is beneficial to suppress the SC current efficiently. In addition, the ratio of self-inductance and mutual-inductance in 12/10 SL shows the lowest value, 4.1%. It means the better magnetic isolation than other candidates. The ratio is also low in 36/12 DL-1, and its inductance is the lowest than other candidates.

Although every set of three-phase windings could be arranged in one semi-stator, the mutual inductance is high in 18/12 DL-2 and 36/12 SL-1, with the ratio 25.7 % and 27.4 %, respectively. It can be proved that these topologies are unreasonable, due to high mutual inductance, and an unbalanced impedance. In the comparison of inductance, 18/12 topology did not exhibit better performance than others. In contrast, 12/10 topology has better performance in high inductance design.

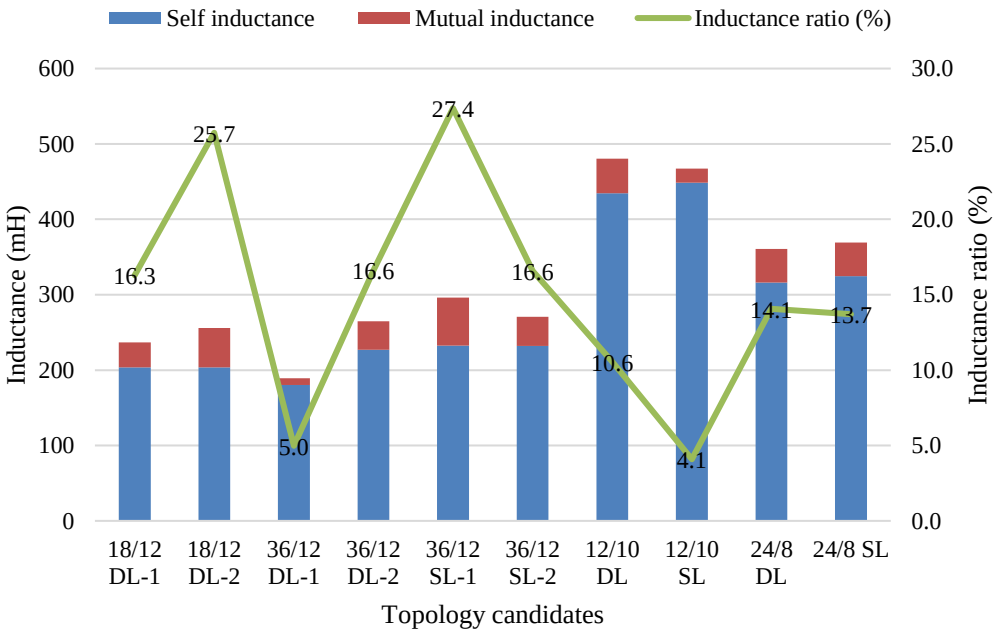


Fig. 5.9 Illustration and comparison of inductance of candidates.

5.3.1.2.2 Comparison of on-load and post-fault

All the ten candidates were carried out to investigate the on-load and post-fault performance. All the topologies meet the specification of this specific application. The output may vary based on the different slot/pole combinations. The output torque is a straightforward result of the performance under different scenarios. The faults of three-phase OC and SC were embedded to investigate the impact of faults. As shown in *Fig. 5.10*, the blue bars represent the healthy operation while the red and the green bars stand for the values of post-fault, OC and SC fault, respectively.

As mentioned earlier, the output torque of OC is easy to estimate based on the amount of absent phases. In this case, the output torque of all the topologies halves almost due to the missing of one set of three-phase and another set of three-phase operating continuously.

The SC faults could cause a transient shock of machine in the torque and current. The values depict the stable value rather than peak value. After a short duration, SC current in faulty phases resumes to sinusoidal waveforms, and the stable current were close to the rated value.

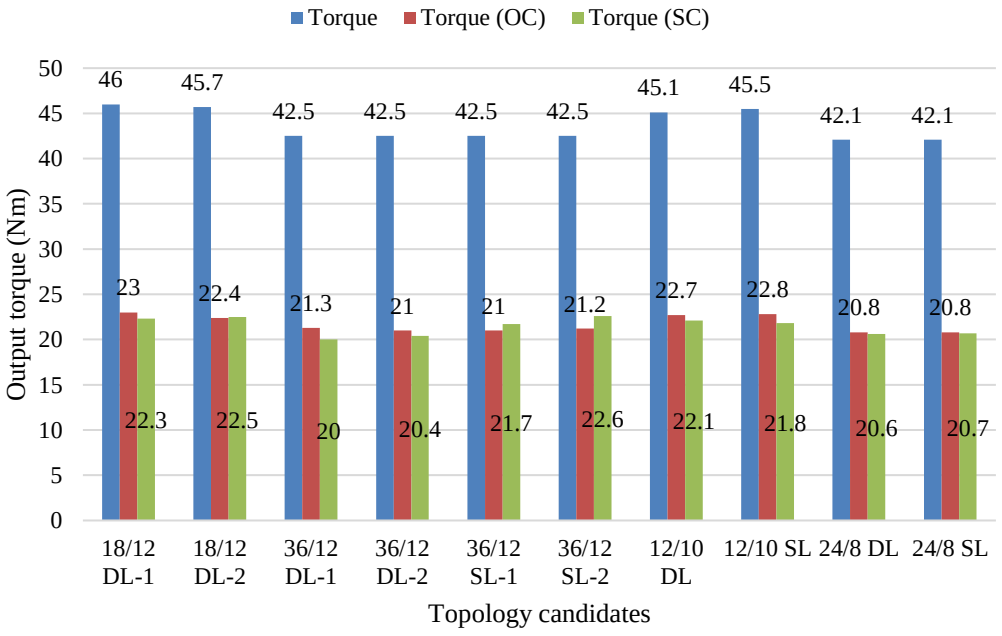


Fig. 5.10 Comparison of output torque of candidates under difference operation.

The change of torque ripple can provide a comparison under faults, as shown in *Fig. 5.11*. Due to the absent of phases, electrical machine operate under open circuit will

increase torque ripple. In the case of SC fault, all the torque ripples increase dramatically. The increased magnitude of torque ripple is based on the winding arrangement. The 18/12 DL-2 and 36/12 SL-2 topologies exhibit high torque ripple, around 25%. 36/12 DL-2 reveals the lowest torque ripple in the case of short circuit, around 6.9%.

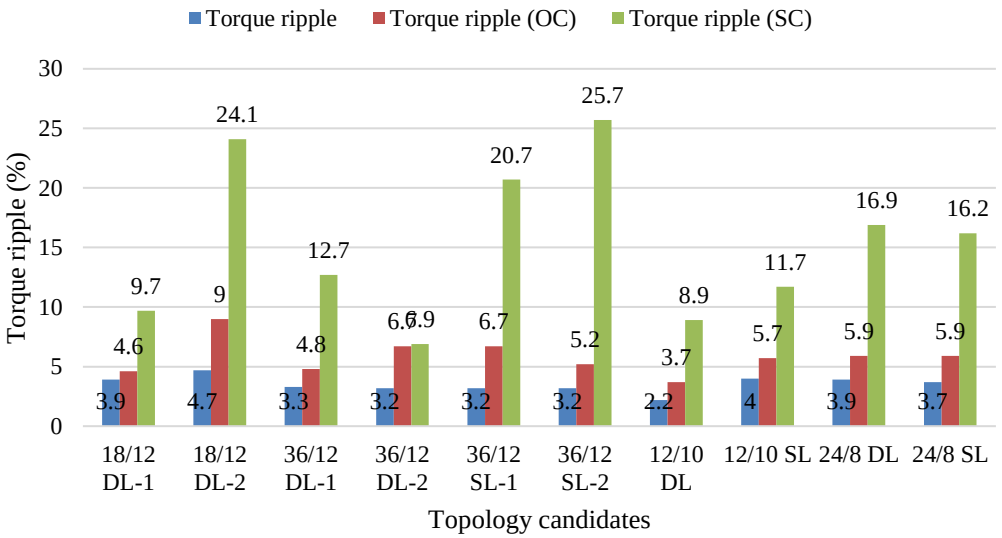


Fig. 5.11 Comparison of torque ripple of candidates under difference operation.

For a well-designed and healthy electrical machine, its axial force on the rotor should be negligible due to balanced winding arrangement. The occurrence of winding faults may result in an axial force which may cause further damage in eccentricity or bearing pairs.

The peak values of periodic axial force of all candidates were calculated and shown in *Fig. 5.12*, including the modes of healthy, OC and SC fault. Under the healthy operation, all the designs exhibit negligible axial force (blue bar); these bars were too low to visualize from the figure. However, they increase significantly under the faulty scenarios.

In the 36/12 SL-2, its peak value (red bar in *Fig. 5.12*) of periodic unbalanced axial force, under the OC fault, was still small enough to neglect. This value in 12/10 DL and SL were much higher than other topologies, 498.4 N and 490.2 N respectively. Results of other topologies were relatively close, around 200 N.

In general, the response (green bars *Fig. 5.12*) of axial force in SC is much more significant than OC fault. These indexes were fluctuant in different slot/pole combinations and layouts. Although the 12/10 SL, which has FSCW layout, is the best option for the requirements of fault isolation, its axial force under SC fault shows the highest value than others. The peak value of the periodic axial force is more than 2000 N. Due to the balanced winding arrangement, the axial force of 36/12 SL-2 is almost impervious to the OC fault.

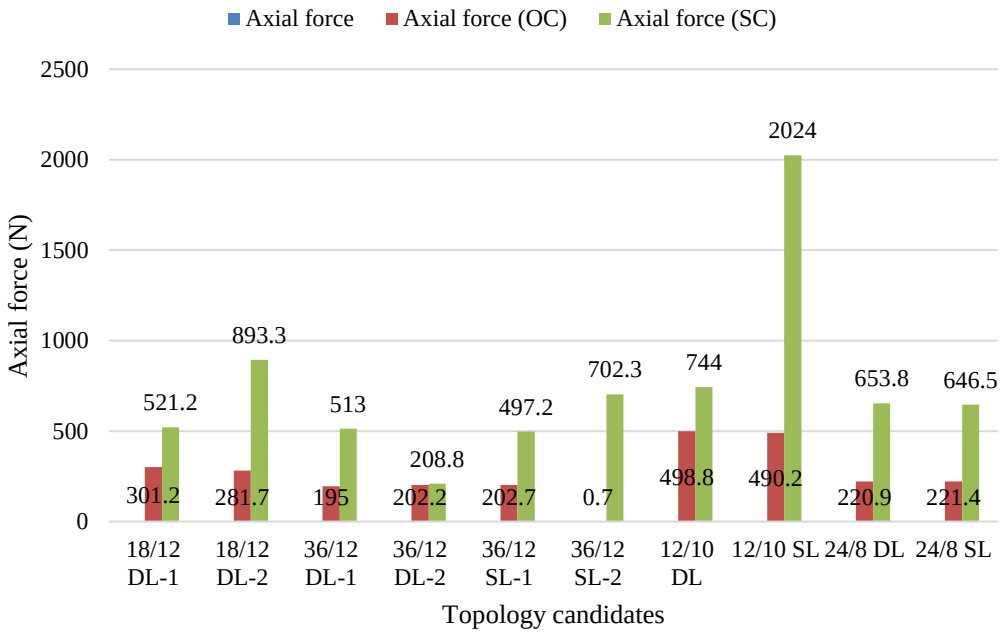


Fig. 5.12 Comparison of axial force of candidates under difference operation.

In the *Fig. 5.13*, it provides a straightforward comparison of current under different operation modes. The rated currents for every candidate are varied from 78.2 A to 97.8 A. In general, the line current maintains same in the case of OC fault, because there is no current flow in the open-circuit windings.

However, the fluctuations of the SC current differed from one another. As introduced in the aforementioned content, SC current exhibits a transient process from peak value to a stable one. All the values of short circuit current exhibited in the figure are the peak value. The 12/10 SL exhibits the highest peak value 208 A in the SC windings than other candidates. These peak values provide an estimation for selecting the insulation class of windings.

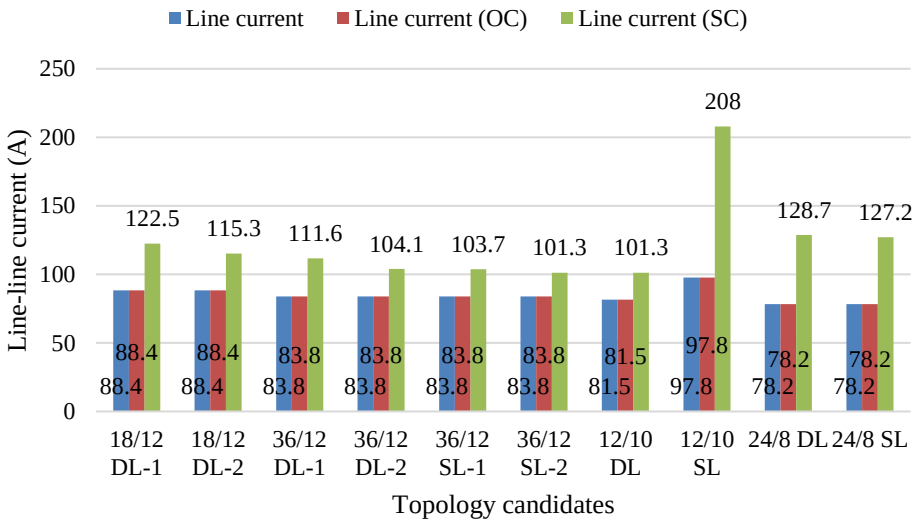


Fig. 5.13 Comparison of line-line current of candidates under difference operation.

Based on these comparisons, there is no candidate exhibit overwhelming merits than others. Although the 12/10 SL has the lowest mutual inductance ratios, its axial force and short circuit current were the worst. In spite of 36/12 DL-1 reveals a combination capacity in this comparison, its distributed wing are hidden trouble in the case of thermal isolation. Due to the FSCW layout, 18/12 SL-1and 12-10 DL are balanced options.

5.3.2 Triple three-phase

Single layer 18/12 slot/pole combination is feasible to achieve a triple three-phase topology. The initial winding arrangement and diagram of phasor are shown in *Fig. 5.14*. Due to FSCW layout, all the nine windings are independent and non-overlapping. The nine coils were divided into nine phases, or three modules of three-phase layout, M1, M2 and M3. The three modules consist of coils 1-2-3, 4-5-6 and 7-8-9, respectively. Every module can operate as sub-motor equally, to achieve an electrical isolation. This layout is visualized to illustrate the competence of fault isolation.

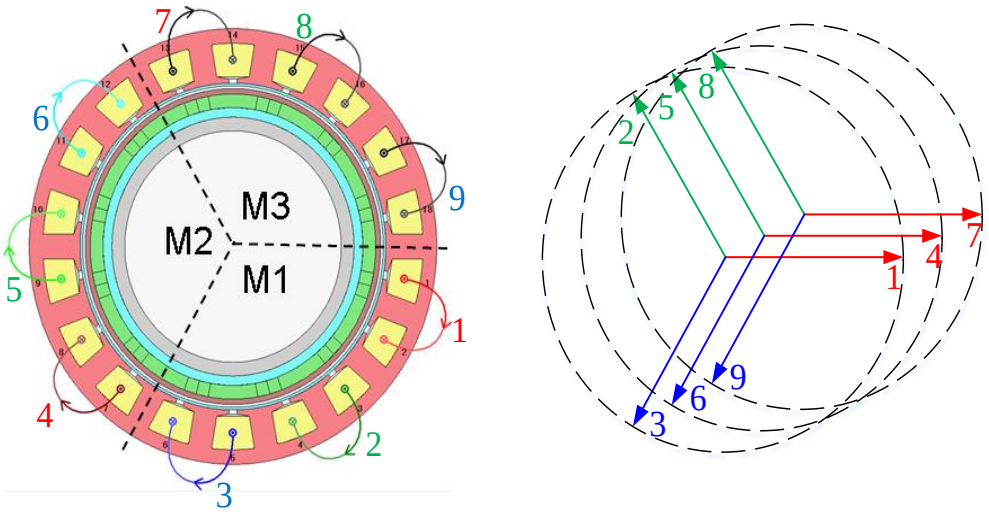


Fig. 5.14 Topology of triple three-phase (a) Winding arrangement. (b) Diagram of phasor.

5.3.2.1 Healthy operation

The same FEA process was carried out for the validation of triple three-phase topology. A whole model was created and its flux path under on-load operation is shown in *Fig. 5.15*. The back-EMF of windings under no-load and the output torque were shown in *Fig. 5.16*. The average output torque is 44.2 Nm with a torque ripple of 4.6 %.

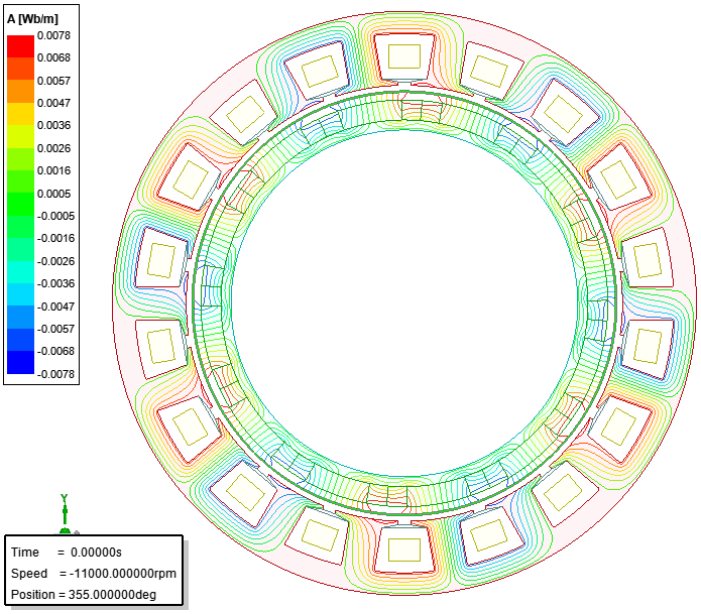
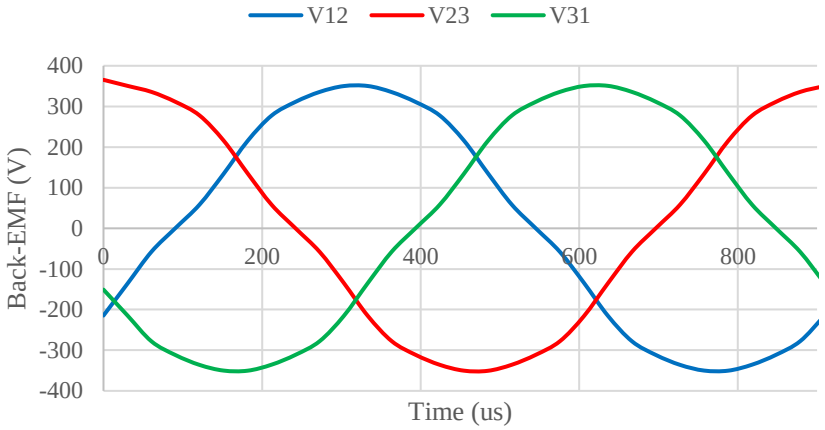
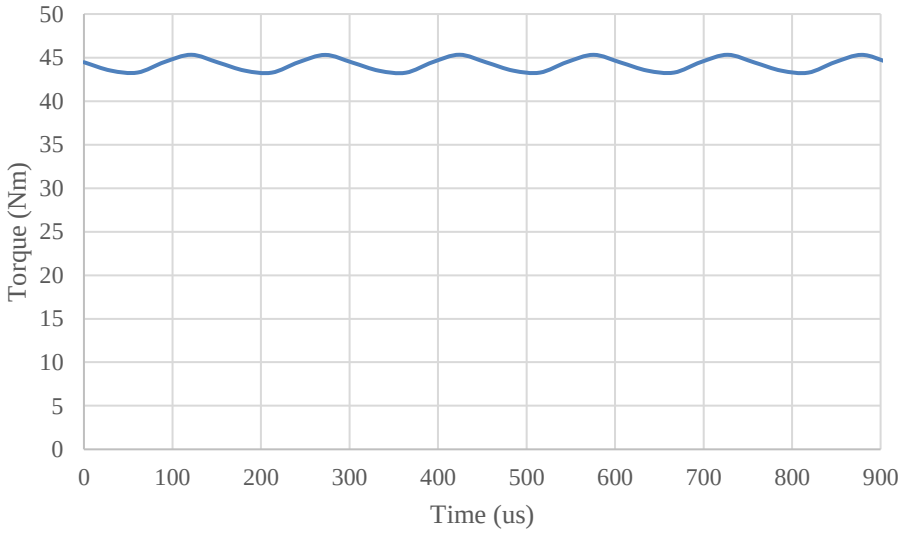


Fig. 5.15 Model of triple three-phase 18/12.



(a) Back-EMF



(b) Output torque

Fig. 5.16 Diagram of back-EMF and output torque.

5.3.2.2 Faulty scenarios

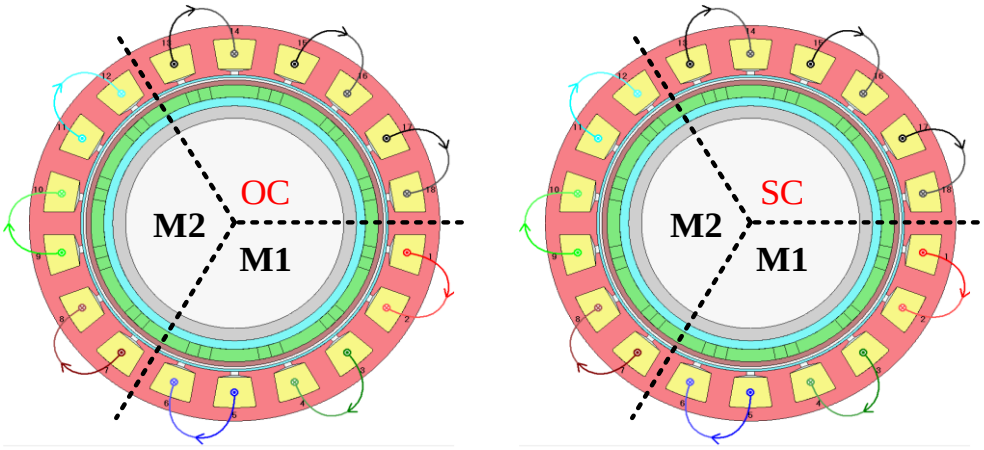
In conventional three-phase topology, OC and SC fault could occur in any coil to form single point of failure. Compared with conventional three-phase or dual three-phase topologies, there are more combinations of faults existed in triple three-phase topology.

Several potential winding faults may include but not limit to the type shown in the Table 5.6. The fault 1 represents one module with OC fault, and other two modules are healthy (1/3 OC, 2/3 healthy). Similarly, fault 4 represents one module with SC fault, and other two modules are healthy (1/3 SC, 2/3 healthy). Descriptions of other faults are similar and given. The turn-to-turn SC is relatively complex due to combination of faulty turns and position.

Table 5.6 Faults combination of triple three-phase topology.

Feasible fault	Category	Description of fault	
1	Open circuit (OC)	1/3 OC, 2/3 Healthy	
2		2/3 OC, 1/3 Healthy	
3		3/3 OC	
4	Short circuit (SC)	1/3 SC, 2/3 Healthy	
5		2/3 SC, 1/3 Healthy	
6		3/3 SC	
7	Turn-to-turn SC	Variable	Turns
8			Location

To investigate the fault M3 module was selected to embed these winding faults, such as feasible fault 1 and 4, which were illustrated in the *Fig. 5.17*.



(a) OC in M3 (b) SC in M3

Fig. 5.17 Schematic diagram of potential location of winding faults. (a) OC in M3. (b) SC in M3.

The performance validation of post-fault utilizes the similar process which carried out in the dual three-phase topology. In the case of OC faults, the output torque goes down in proportion of absent phases. The torque ripple increases based on the arrangement of winding. The curves of output torque were depicted in *Fig. 5.18*, including the modes under the healthy, one module OC (1/3 OC), two modules OC (2/3 OC) and all the modules OC (3/3 OC) faults, from top to bottom. The average output torque and torque ripple are listed in Table 5.7. The results validate previous estimation that output torque decrease with the absent phases. However, torque ripple

did not increase obviously, due to balanced winding arrangement.

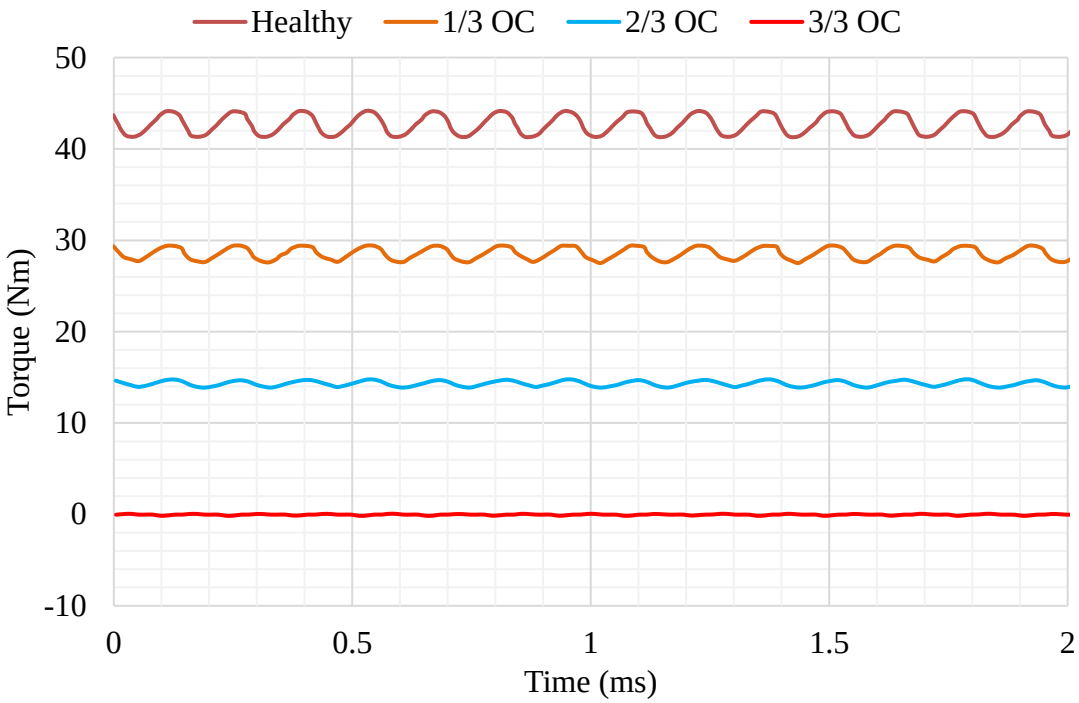
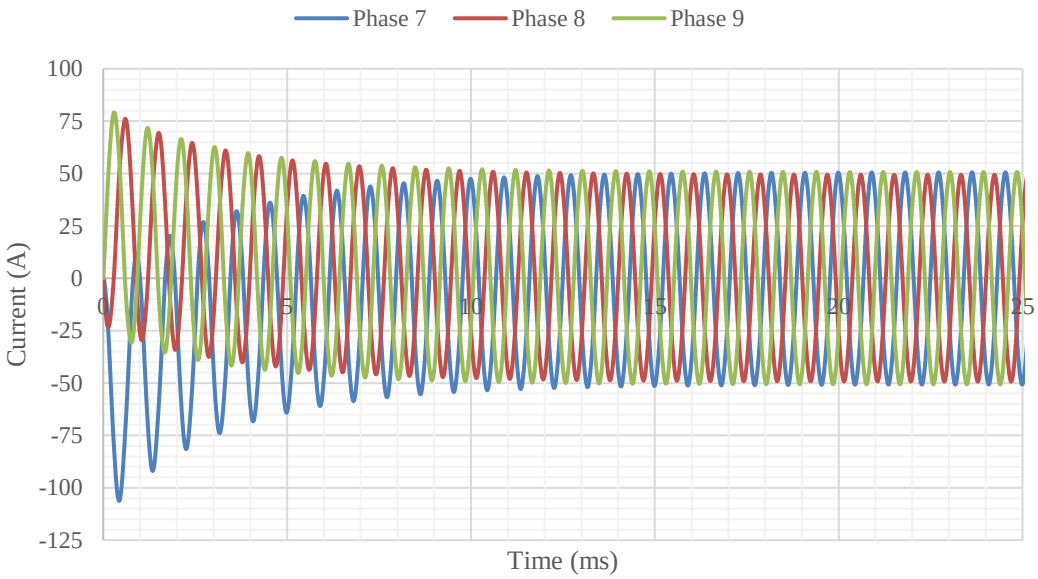


Fig. 5.18 Comparison of torque under open circuit scenarios.

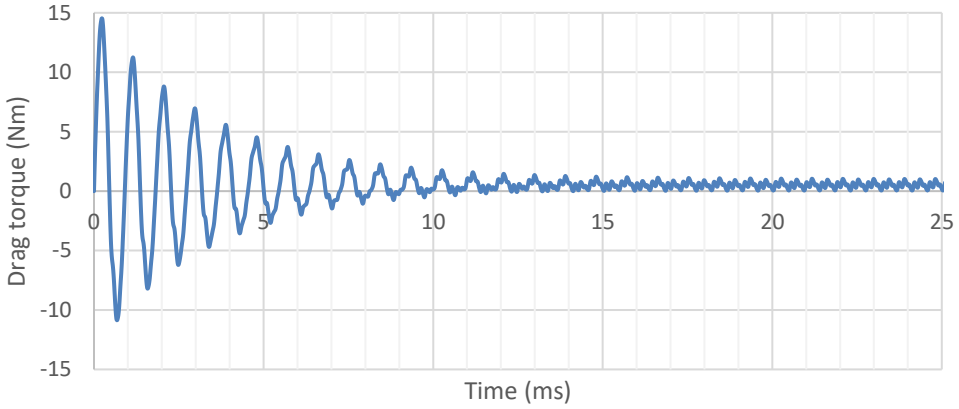
Table 5.7 The comparison of output under varied scenarios.

Feasible fault	Description of fault	Average torque (Nm)	Torque ripple (%)
1	M1, M2 & M3 no-load	0	0
2	M1 Healthy; M2 & M3 OC	14.3	6.3
3	M1 & M2 healthy; M3 OC	28.6	6.6
4	All the modules healthy	42.7	6.7

In the case of short circuit, short circuit current and brake torque were analysed and shown in *Fig. 5.19.* After short duration, the short circuit current in the wingdings of M3 will become sinusoidal wave and the DC component of the winding will dismiss. In addition, the brake torque will decrease to zero.



(a) Short current in M3



(b) Brake torque generated by the M3 in the case SC.

Fig. 5.19 Current in the M3 and brake torque.

5.4 Improvement of fault tolerance

Based on the analysis of dual and triple three-phase topology, the post-fault behaviour has been validated comprehensively. Dual three-phase 18/12, 12/10 and triple three-phase 18/12 were investigated. The competence of these topologies benefits of FSCW layout. More innovations have been taken to improve the fault tolerance.

5.4.1 Splits in stator teeth

For the further improvement of fault tolerance, design of split-in-teeth was proposed to change the geometrical topology of stator. This innovation was expected to modify

the flux path and decrease the mutual effect between different three-phases. Then, several ducts were designed in the stator lamination, and the two sets of three-phase windings were arranged in the semi-stator.

Sensitivity analysis of the split-in-teeth for dual three-phase 18/12 and 12/10 were carried out. The location of split-in-teeth were set near outside, centre and inside of the teeth, as shown in the *Fig. 5.20*. Parametric analysis of the duct size was investigated. The size of the gap was varied from 0 to 10 mm in height (half stator thickness), 1 to 4 mm in width (half stator tooth width), respectively, as shown in the *Fig. 5.21* and Table 5.8. For every location of duct, there were 20 combinations consisted of width and height, to compare output performance.

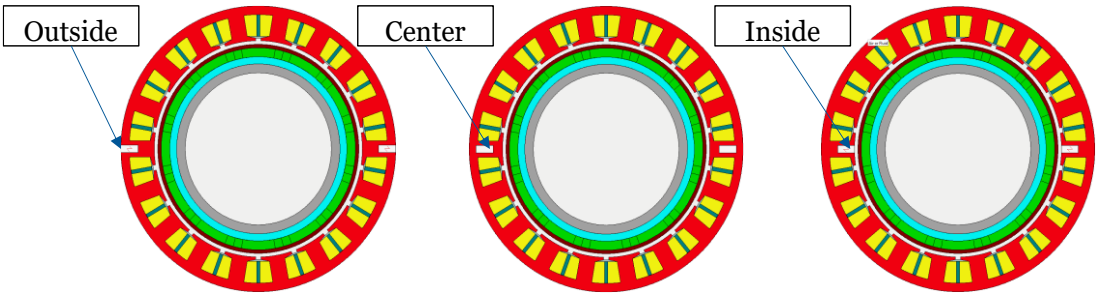


Fig. 5.20 Position of the ducts.

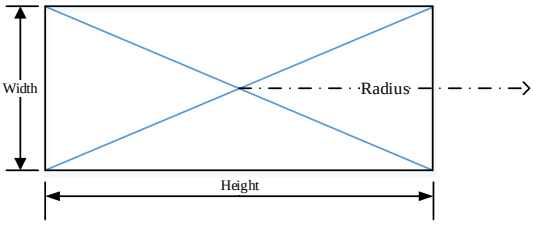


Fig. 5.21 Size of the duct.

Table 5.8 The range of variables in duct.

Variables	Range (mm)
Width	1~half tooth width
Depth	1~ (D-d)/4
Position	Inside, outside and centre

The input power $P_{_in}$, output power $P_{_out}$, inductance ratio and torque ripple were selected as indexes to illustrate the impact of ducts on the performance. A 3D map which depicted by the parametric results, can be used to illustrate the effect of topology change, as shown in *Fig. 5.22*. The map exhibits the results between $P_{_out}$ and varied ducts in the centre of teeth. Compared with the conventional topology,

the biggest centre duct, 4mm width with 10 mm length, causes the biggest output power drop, about 2.6%.

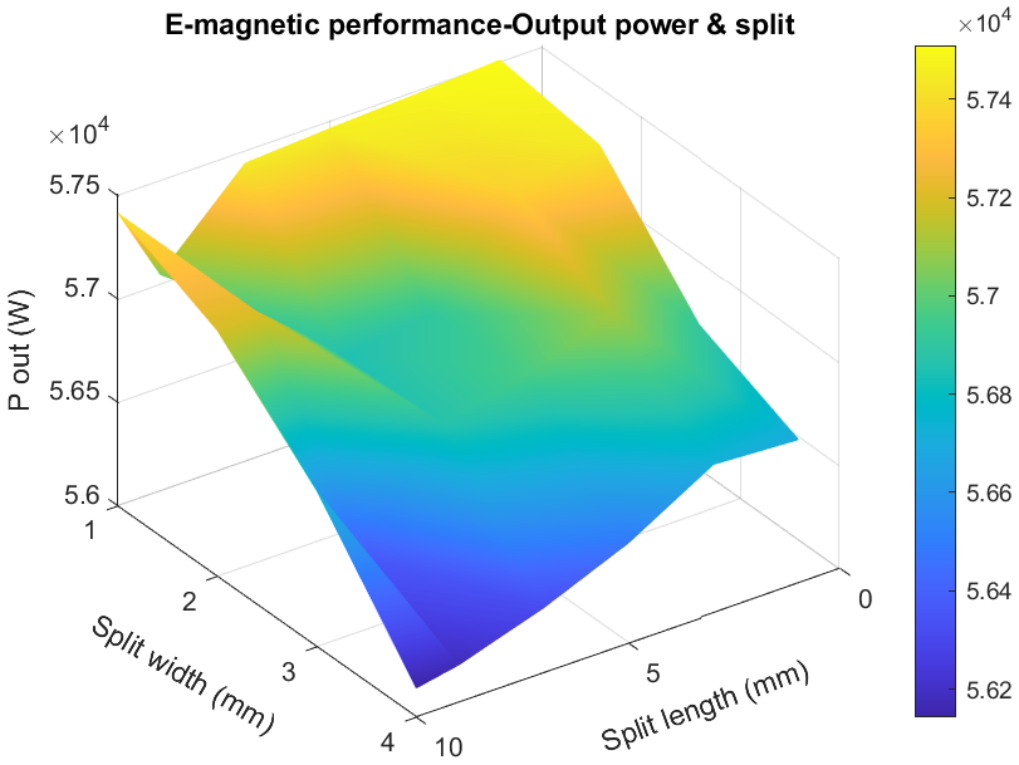
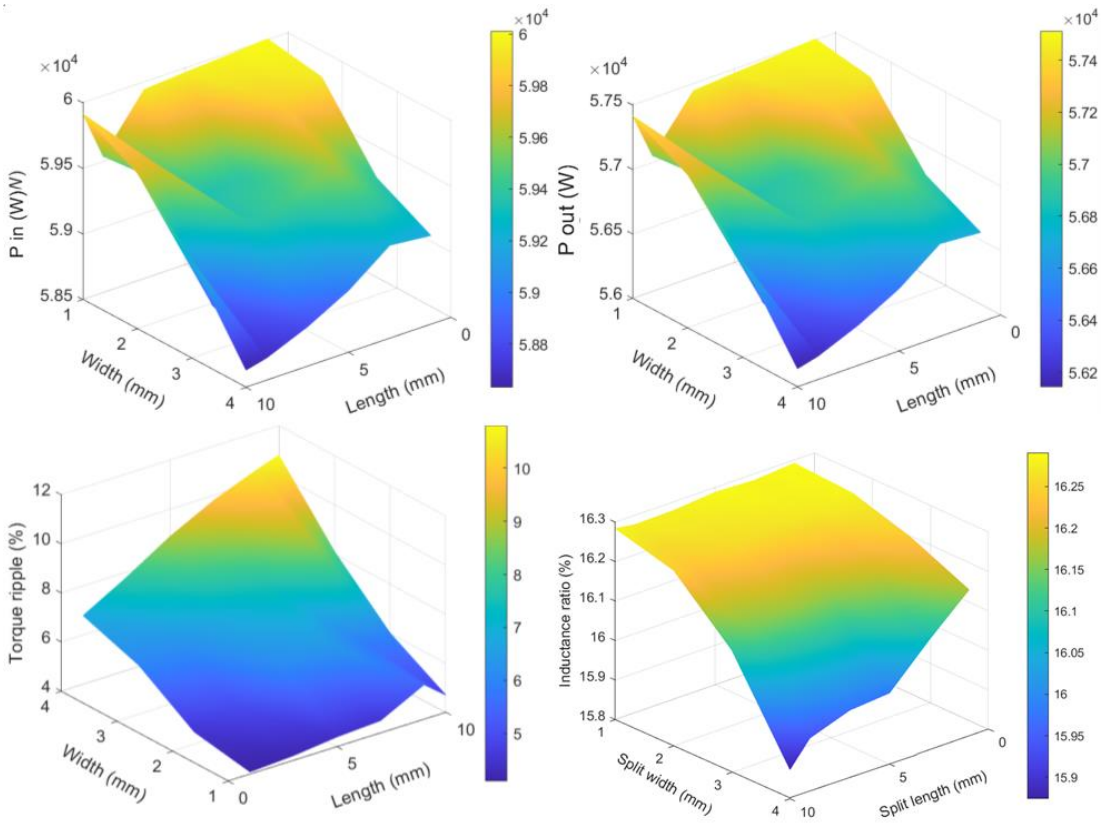


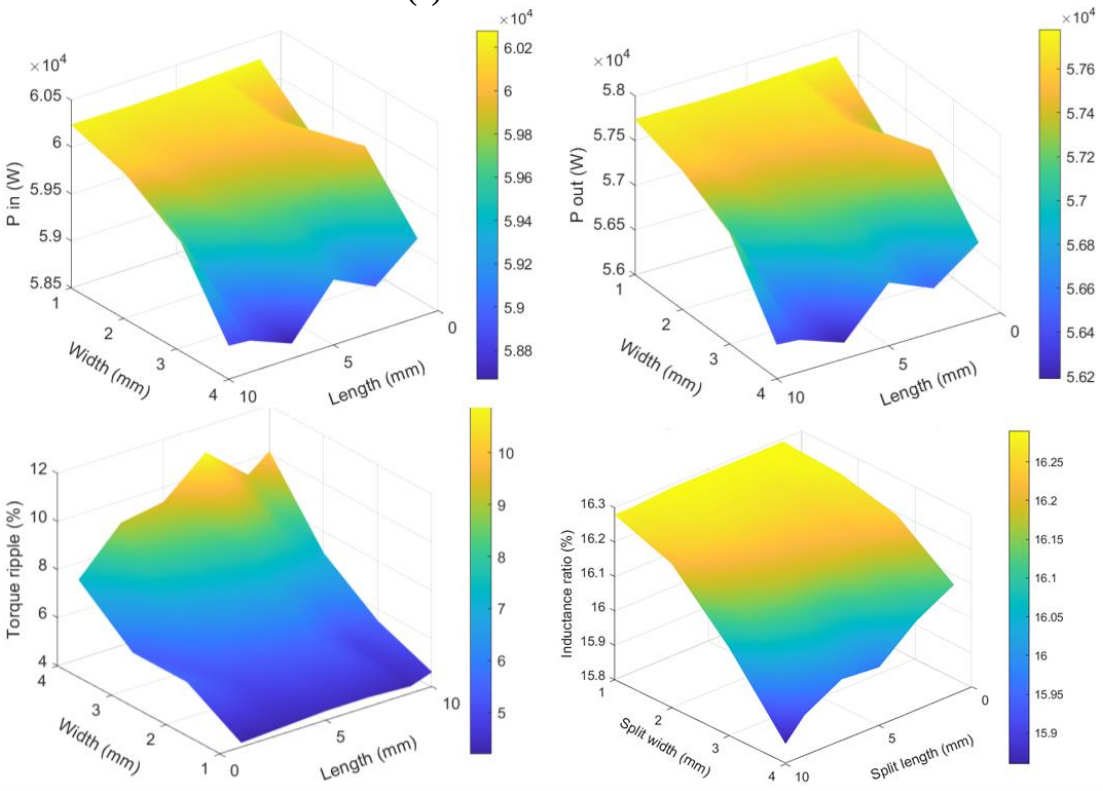
Fig. 5.22 Sensitivity analysis of split size and output power.

All the results of are shown in the *Fig. 5.23*. The tendency of $P_{_in}$ and $P_{_out}$ are similar. Due to reduction of input power, the output decreased accordingly. These diagrams exhibit that the bigger size of split-in-teeth, the more power loss. The ducts in the stator can result in flux saturation in the stator teeth and then limit the capacity of energy conversion.

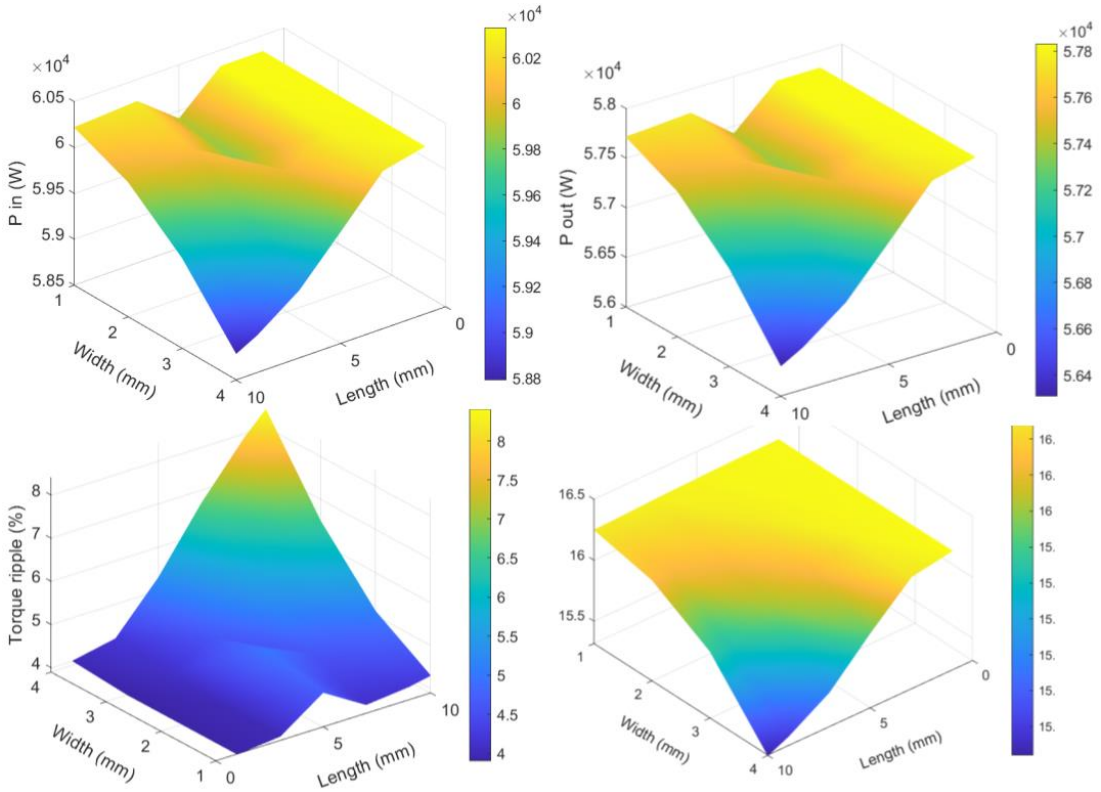
With the increase of duct area, the inductance ratio decreased due to the lower mutual inductance. The trend of torque ripple was depicted in the maps, which increased significantly. Similar trend was found in the dual three-phase 12/10 DL, as shown in *Fig. 5.24*.



(a) Centre duct in 18/12

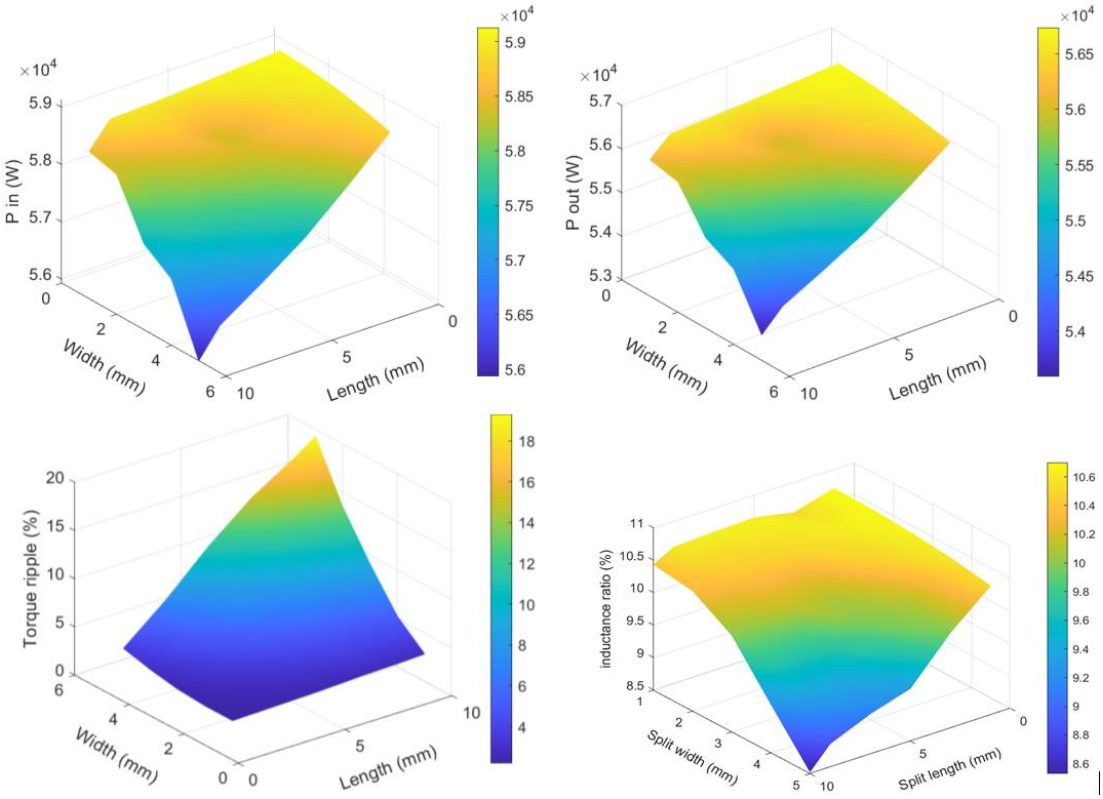


(b) Inside ducts

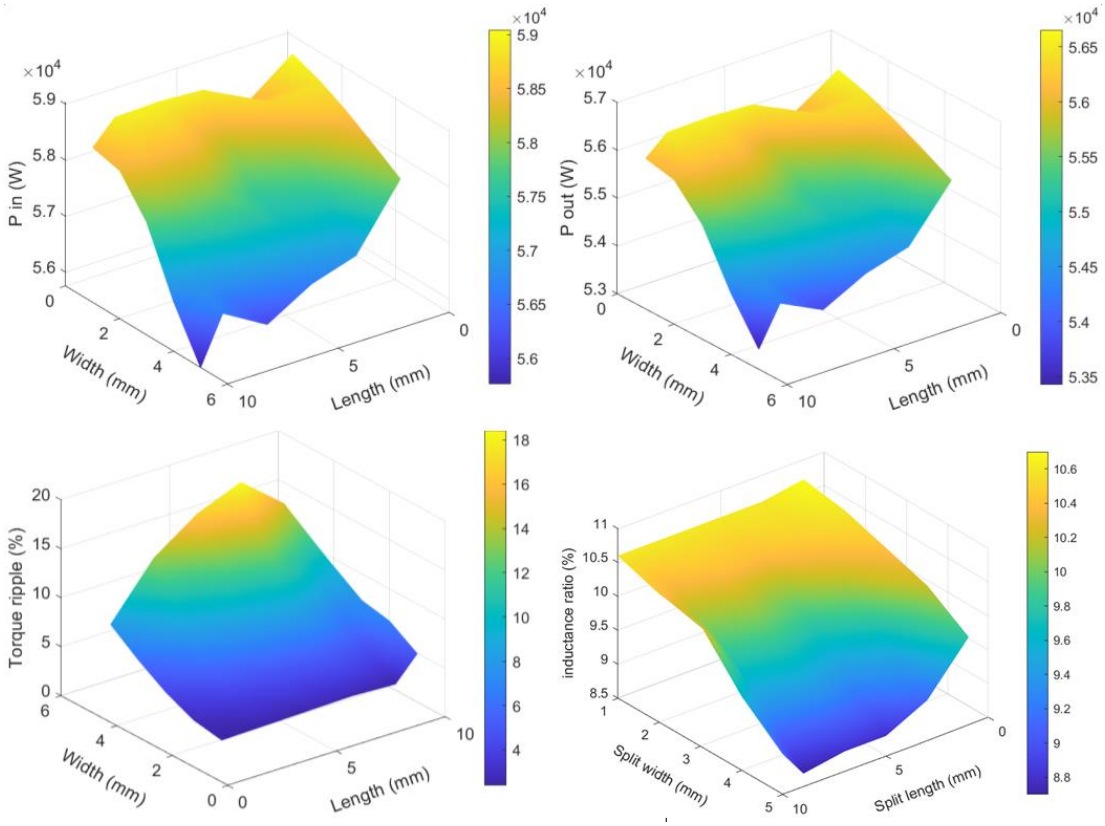


(c) Outside ducts

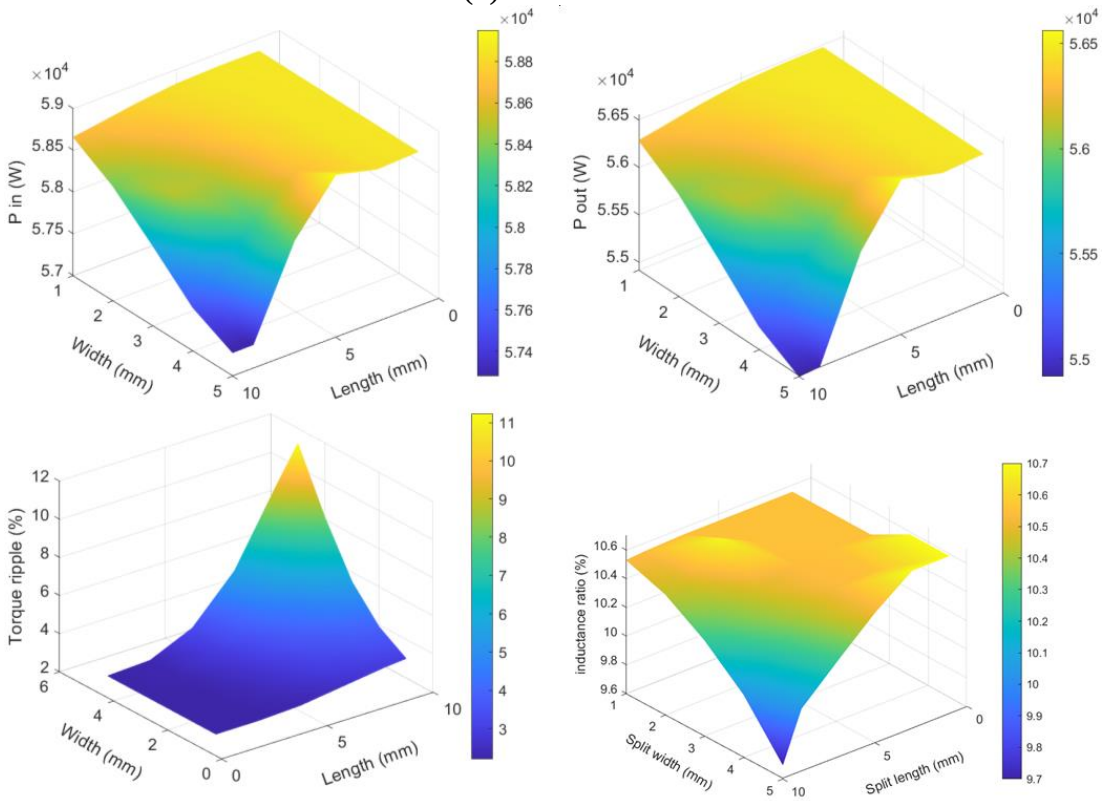
Fig. 5.23 Dual three-phase 18/12 DL-1with (a) centre duct (b) inside ducts (c) outside ducts in stator.



(a) Centre ducts



(b) Inside ducts



(c) Out ducts

Fig. 5.24 Dual three-phase 12/10 DL with (a) centre duct (b) inside ducts (c) outside ducts in stator.

Both the partial splits in the 18/12 and 12/10 combinations show a similar conclusion: the larger the slit size, the lower the inductance ratio. Given this observation, it is worthwhile to explore the effects of full slits on the pursuit of higher fault tolerance.

Moreover, the full slits can improve independence and enhance isolation between two sets of three-phase, particularly in terms of thermal isolation due to increased thermal resistance resulting from the airgap between two sets. From a manufacturing perspective, the cost of the stator can be reduced by using smaller segments rather than a whole stator.

The through gaps were inserted to investigate the performance. The whole stator was partitioned by two splits. The 18/12 combination was selected for illustration. The comparison of position and size of split-in-teeth were carried out, as shown in *Fig. 5.25*. Any duct in the stator can decrease the power and inductance ratio. The inside duct, which close to the airgap, exhibits relatively low effect on the performance. The effects caused by centre duct and through duct are almost the same on power loss. All kinds of ducts introduce more cogging torque and higher torque ripple shown in *Fig. 5.26*. Ducts in the centre of teeth exhibit the highest torque ripple.

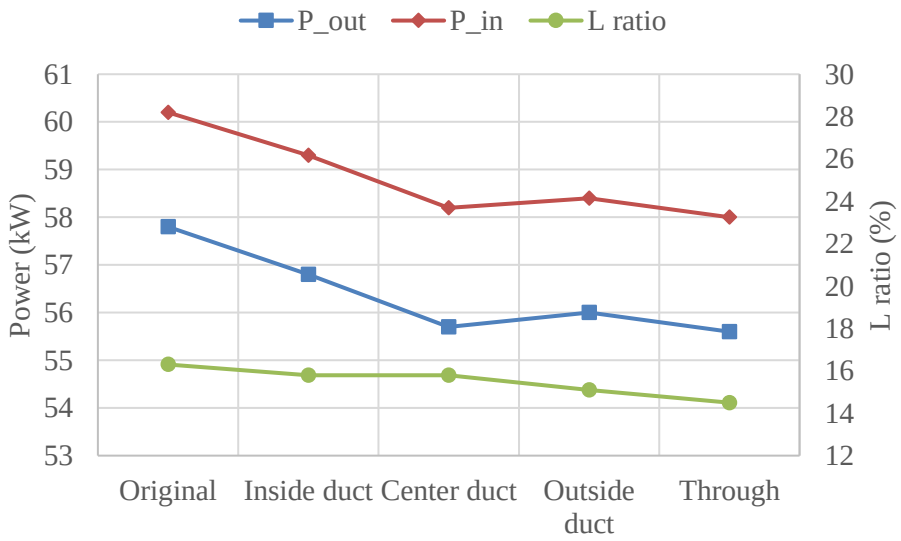


Fig. 5.25 Comparison of power and inductance ratio with the different ducts in 18/12.

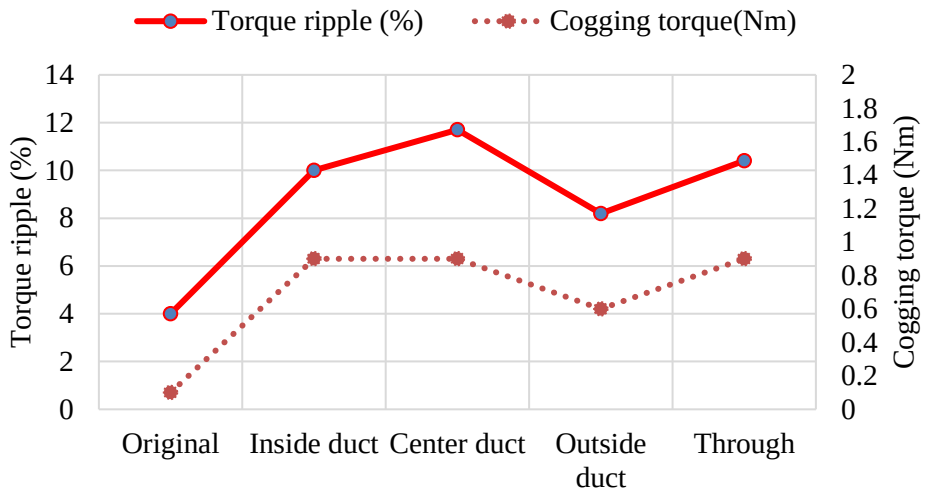


Fig. 5.26 Comparison of power and inductance ratio with the different ducts in 18/12.

The efficiency of machine is insensitive about the duct. In addition, flux plots are hardly changed with different type splits due to the FSCW in 18/12 or 12/10. The design of split-in-teeth can increase the magnetic isolation by decreasing mutual inductance.

However, the windings were still adjacent in one slot. These windings in the two sets of three-phase cannot be isolated thoroughly by the split, shown in *Fig. 5.27*. This kind of design is not feasible for double layer topologies. Besides, detent force exists in the machine due to asymmetry of back-EMF affected by the split. For a single layer FSCW, the stator could be split by the gap on the unwounded teeth.

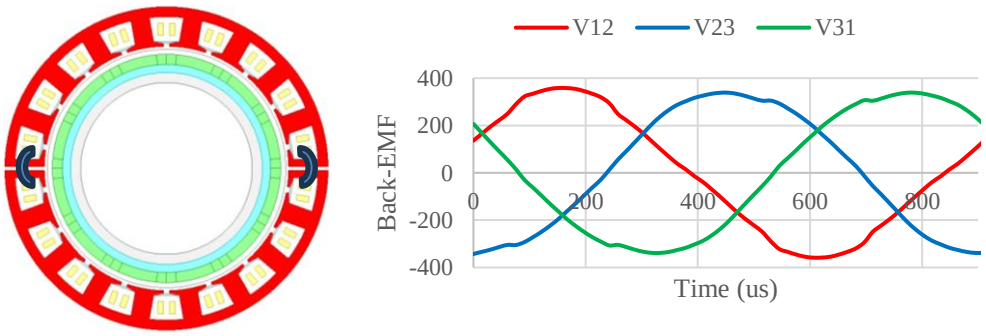


Fig. 5.27 Schematic of windings and splits, and asymmetrical back-emf in 18/12.

5.4.2 Modular design

Above all, the final slot/pole combination for modular design is SL 18/12 with triple three-phase. The whole stator could be partitioned by through ducts to get independent segments.

Table 5.9 Evaluation of fault tolerance of 18/12 slot/pole combination.

Cases	winding	Fault-tolerance			
		E	M	T	P
Single three-phase	SL	-	-	-	-
Dual three-phase	DL	+	-	-	-
Triple three-phase	SL	+	+	+	-
Triple three-phase with splits	SL	+	+	+	+

5.4.2.1 Independent set of three-phase

Single layer 18/12 has been approved that it is feasible for triple three-phase. Three ducts could be applied to split the stator assembly into three sets while every set of three-phase was arranged in an independent segment. There are three segments which means the topology is physical isolation between every segment. Compared with conventional topology, this topology exhibits thorough fault tolerance. The evaluation and comparison of fault tolerance for 18/12 slot/pole combination are listed in Table 5.9. This evaluation is mainly dependent on the isolation of electrical, magnetic, thermal and physical (abbrev. in E, M, T and P in the Table 5.9).

To compare the effects of slits on triple three-phase machine, parametric analysis was carried out and the output torque is shown in *Fig. 5.28*. The results show that the output curves are not sensitive to the length of the slits, even with the trough slits. However, the topology with the through slit (20 mm) exhibits an increase of torque ripple, more than 10%.

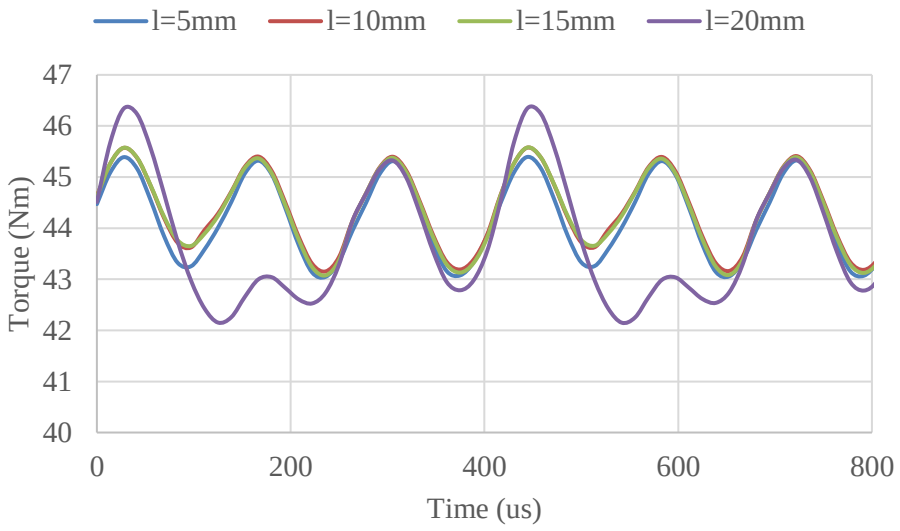


Fig. 5.28 Output torque of triple three-phase machine with varied splits.

To compare the impacts of slits on performance, a comprehensive comparison was carryout out. The topology of 18/12 combination was selected, with conventional three-phase, dual three-phase, triple three-phase and innovations (slits), respectively. The impacts of output average torque and inductance ratio to the existence of slits in these topologies are shown in *Fig. 5.29*. The results of output average torque are relative stable. The inductance ratio exhibits a sharp decrease with the proposed design, from 45.6% to 17.0%, 2.2%, with dual three-phase and triple three-phase, respectively. Besides, the values of inductance ratio prove that it is sensitive to the winding arrangement rather than the length of the splits on the stator.

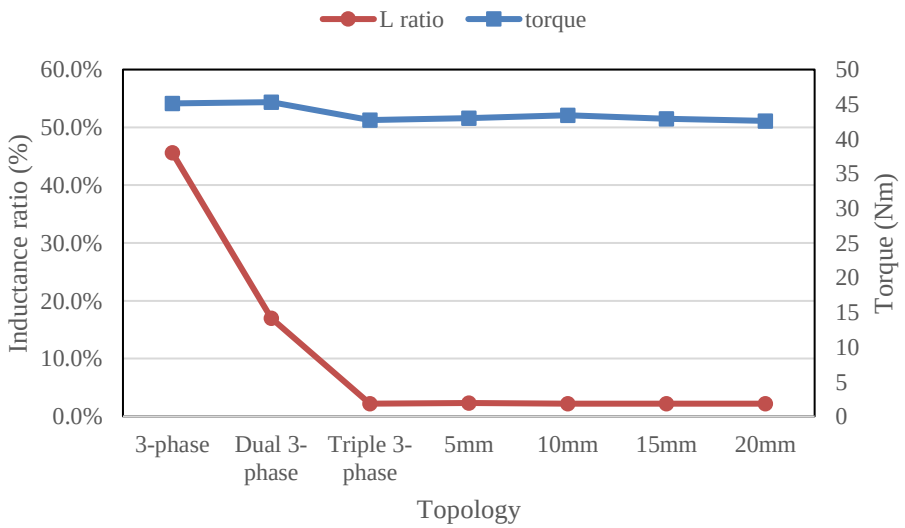


Fig. 5.29 Effects of slits on output torque and inductance ratio.

Torque triple is sensitive to the size of split-in-stator. The result of parametric analysis between split-in-stator and torque ripple is shown in *Fig. 5.30*. Compared with width, length of split has big compact on torque ripple. A dramatic increase of the torque ripple occurs in the topology with three through split, 20 mm length, 13.6%.

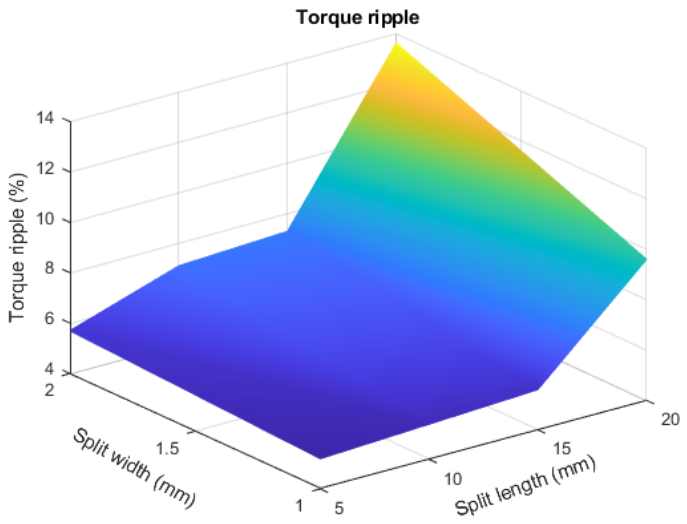


Fig. 5.30 Torque ripple of triple three-phase with varied split.

With the transformation from three-phase to dual or triple three-phase, the serial coils become in parallel type, which benefit for reducing amplitude of phase current to the power converter. The current of the phase triple three-phase topology reduces to the 1/3 of three-phase counterpart in the converter side.

For the comparison of post-fault performance, the symmetrical short circuit was investigated. The equivalent out circuit was created in the FEM software Ansys, as shown in *Fig. 5.31*. Triple three-phase with varied splits on stator were simulated shown in *Fig. 5.32*. The fluctuations are similar as introduced in the aforementioned content, which magnitudes of current decrease from a transient peak value to a stable value. Table 5.10 provides the details of healthy and faulty current under varied topologies. All the stable peak values restore to their rated values. In general, the healthy current and fault current are lower compared with conventional three-phase machine, which are also safe for power electronics.

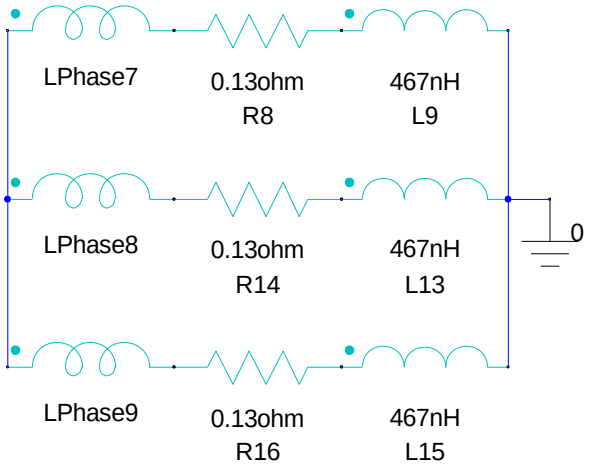


Fig. 5.31 Out circuit of phase-to-phase SC in one module.

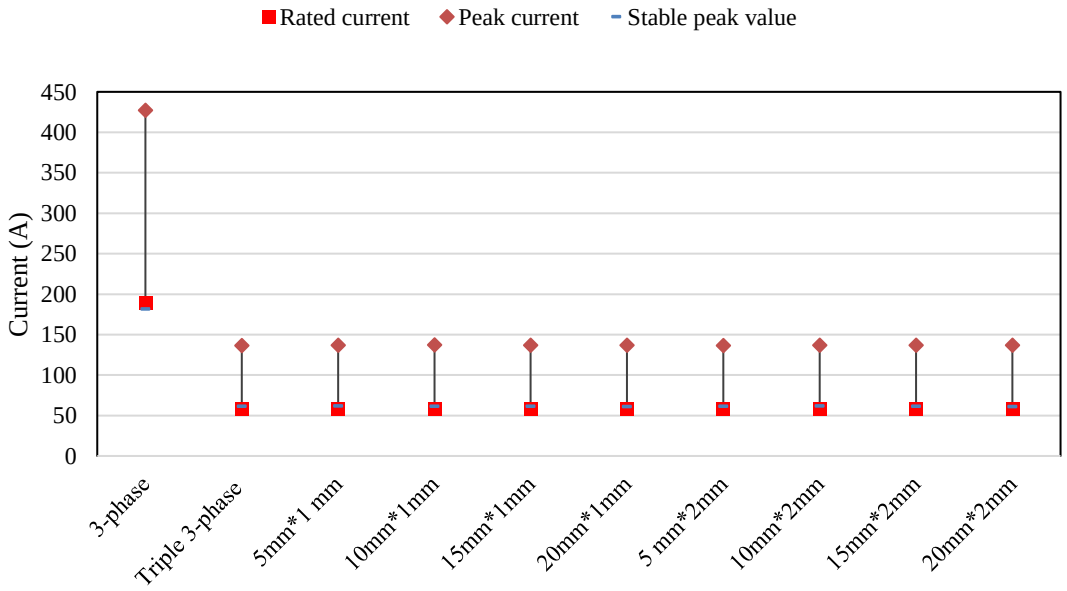
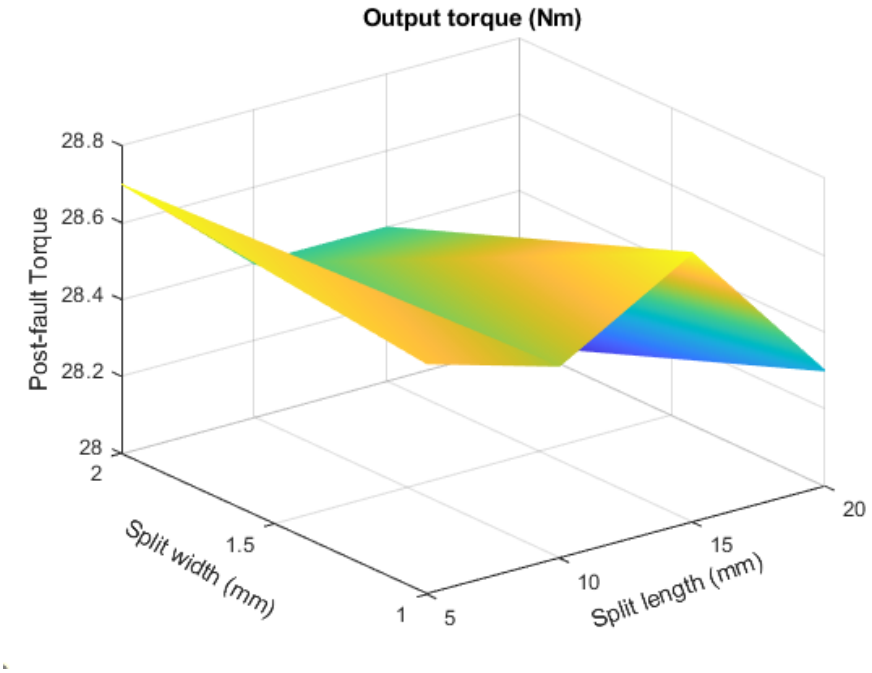


Fig. 5.32 Fluctuations of faulty current in the SC phases.

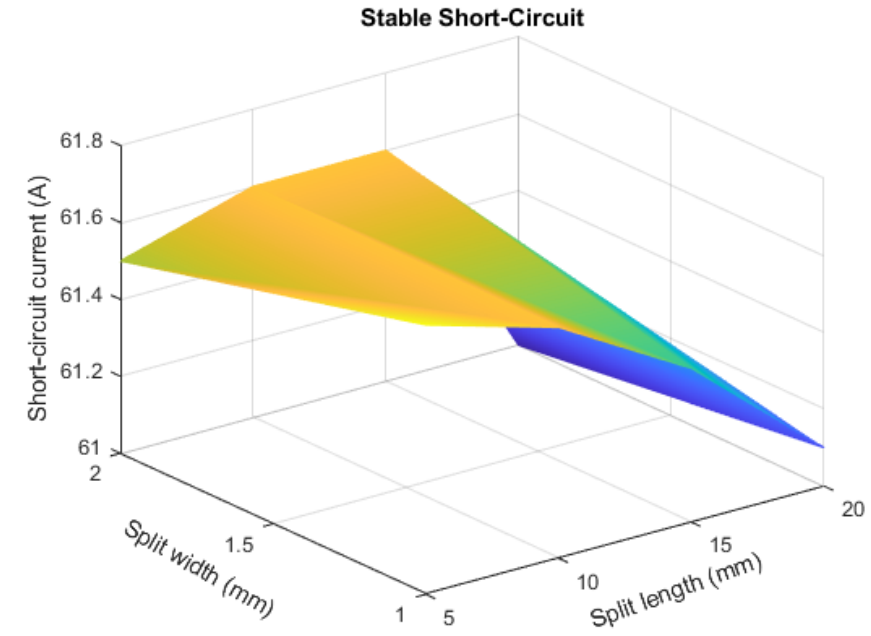
Table 5.10 Comparisons of currents in varied topologies.

Topology		Current (A)		
		Rated	Transient peak	Stable peak
Three-phase		189.2	427.2	181.8
Triple three-phase			136.6	61.4
Triple three-phase with splits	5 mm × 1 mm	57.8	137	61.7
	10 mm× 1 mm		137.2	61.4
	15 mm × 1 mm		137.1	61.4
	20 mm × 1 mm		136.8	60.8
	5 mm × 2 mm		136.7	61.4
	10 mm × 2 mm		137	61.6
	15 mm × 2 mm		136.9	61.4
	20 mm × 2 mm		136.8	61.1

The 3D maps provide more intuitive tendency of output and variables. In the *Fig. 5.33*, although topologies with bigger splits decrease the output, the results of SC current were reduced at the same time.



(a)



(b)

Fig. 5.33 Varied sizes of splits with (a) torque and (b) current of post-fault.

The triple three-phase machine exhibits better competence of FT than three-phase. Further improvements have been verified by splits in stator whilst higher torque

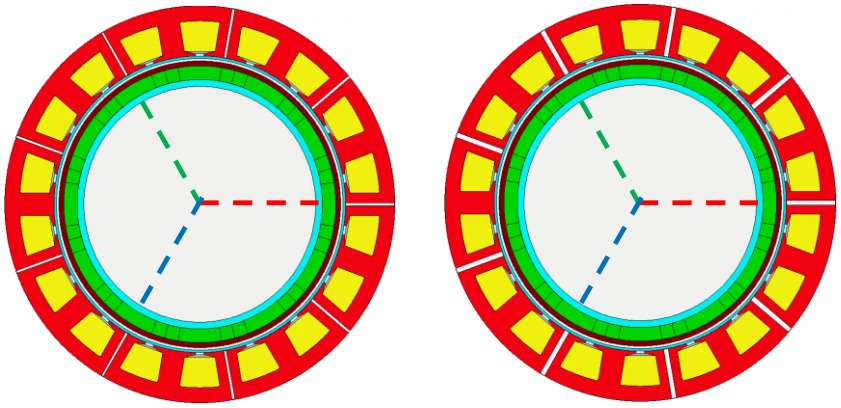
Table 5.11 Average and torque ripple in varied splits and size.

Comparison	Number of slits	Average torque (Nm)	Torque ripple
20mm*1mm	3	43.7	9.6 %
	9	43.2	3.7%
20mm*2mm	3	43.4	13.6%
	9	41.6	4.3%

ripple has been introduced by through slits.

5.4.2.2 Independent segment of single phase

To pursue lower torque ripple, more full splits were designed in the stator, as shown in *Fig. 5.34*. It has been proved that the torque ripple in triple three-phase 18/12 with 9 slits is lower than 3-slits counterpart. Two kinds of width, 1 mm and 2 mm were calculated, and their results are shown in Table 5.11. The topology with 2-mm width slits decreases the torque ripple from 13.6% to 4.3%, although the average torque was reduced simultaneously.



(a) (b)

Fig. 5.34 Triple three-phase with 9 slits in stator. (a) 1-mm slits. (b) 2-mm slits.

In general, nine-slit topologies exhibit lower torque ripple than three-slit topologies. The wider slits can introduce higher torque ripple. Based on the presence of splits, the designed modular machine has nine independent stator segments consisted of coil and stator lamination. This topology could provide thorough FT. Besides, this topology has potential advantages in interchangeability and serviceability. The faulty segment could be extracted and replaced with a new one easily.

5.5 Comprehensive evaluation

Bases on the aforementioned content, the optimal topology of this thesis is a triple three-phase 18/12 PMSM machine, with the innovation of modular stator.

5.5.1 Iterated optimization process.

Due to some modifications on conventional topology, an iterated optimization process (*Fig. 5.35*) based on specific topology was carried out again, like the process shown in Section 4.4. For example, the width of splits was introduced as a new variable compared with previous model. In addition, the winding temperature was extracted to evaluate the thermal management. The details of settings are listed in Table 5.12. After the iterated process with algorithm, all the feasible designs are filtered and drawn by constraints, as shown in *Fig. 5.36*.

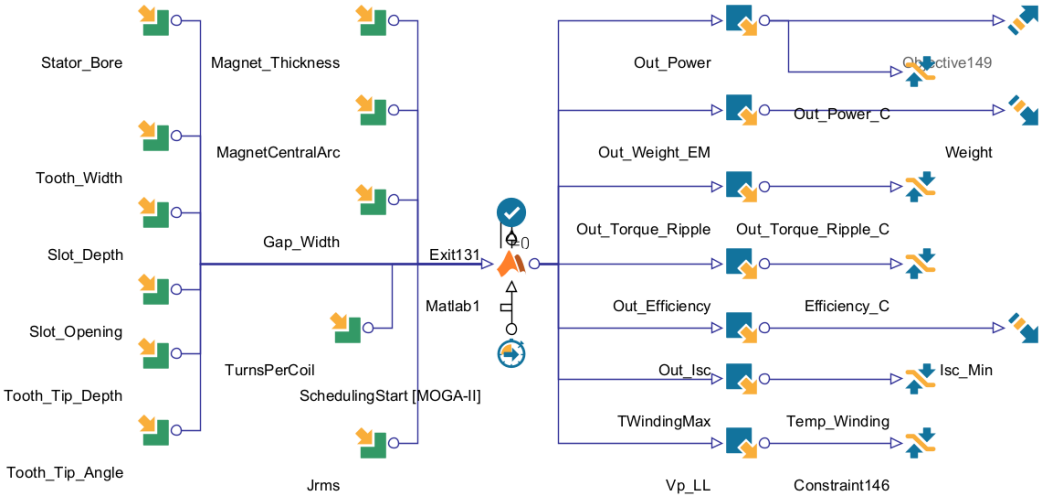


Fig. 5.35 The iterated model for optimization based on proposed model.

Table 5.12 Differences of iterated model and previous model.

Item	Iterated model	Settings		
		Scope	Constraints	Objectives
Input variables	Width of split	0 ~ 3 mm	/	/
	Turns of coil	36 ~ 40	/	/
	Current density	18 ~ 26 A/mm^2	/	/
Output variables	Maximum winding temperature	/	<160 Celsius degrees	Maximize
	Voltage of line-to-line	/	< 513 VDC	Maximize

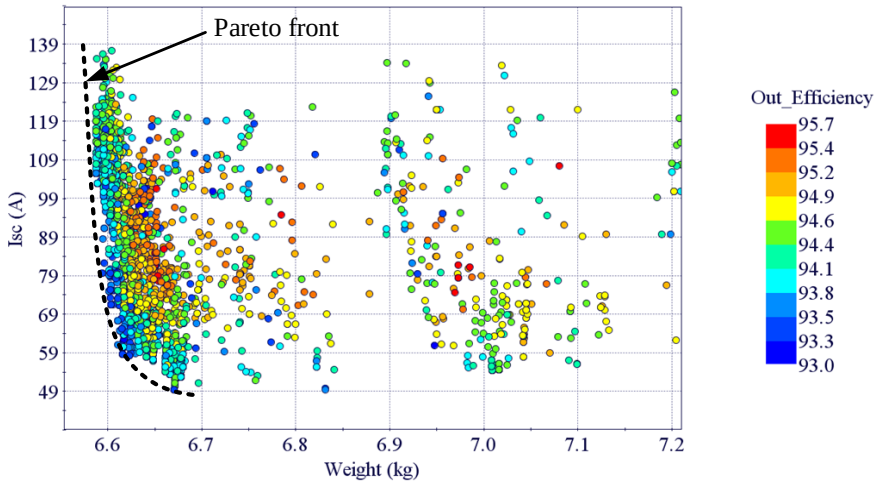


Fig. 5.36 Bubble chart of weight (kg), short-circuit current (A) and efficiency (%).

Bases on the multiple-criterion-decision-maker method, designs can be rank under varied weighting factor for selection optimal candidate. As a result of the rank, Table 5.13 shows the parameters of the optimal design and the output results. And, the schematic topology of optimal candidate is shown in *Fig. 5.37*. The following sections provide detailed information about electromagnetic and thermal management.

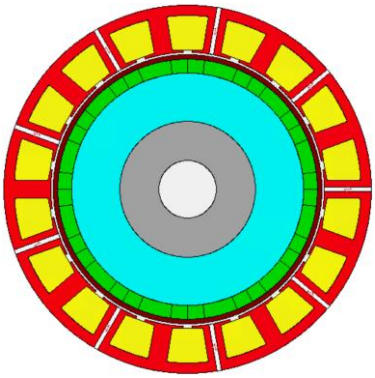


Fig. 5.37 Schematic topology of optimal candidate.

Table 5.13 Parameters of optimal design and output performance.

	Variables	Value	Unit
Input	Stator bore	119	mm
	Tooth width	8	mm
	Slot depth	16	mm
	Slot opening	4	mm
	Tooth tip depth	1	mm
	Tooth tip angle	0	degree
	Magnet thickness	6	mm
	Central magnet angle	90	degree
Output	Average torque at 11000 rpm	26.7	Nm
	Efficiency	95.3	%
	Output power	33.6	kW

5.5.2 Validation of FT topology

To illustrate the FT topology of the triple three-phase 18/12 PMSM, a schematic diagram was utilized to show the phasor of winding. There are nine segments consisted of nine windings as shown in Fig. 5.38. The total nine windings were divided into three sectors, I, II and III, respectively. The number of pole pairs is six then the electrical angle is 6 times of mechanical angle. The angles between windings are listed in Table 5.14. The phasor diagrams of three sectors are overlapped but independent. This structure illustrates the independence of every module. In case of electrical fault in one module, while other two sectors main operation. This structure meets the requirements of isolation.

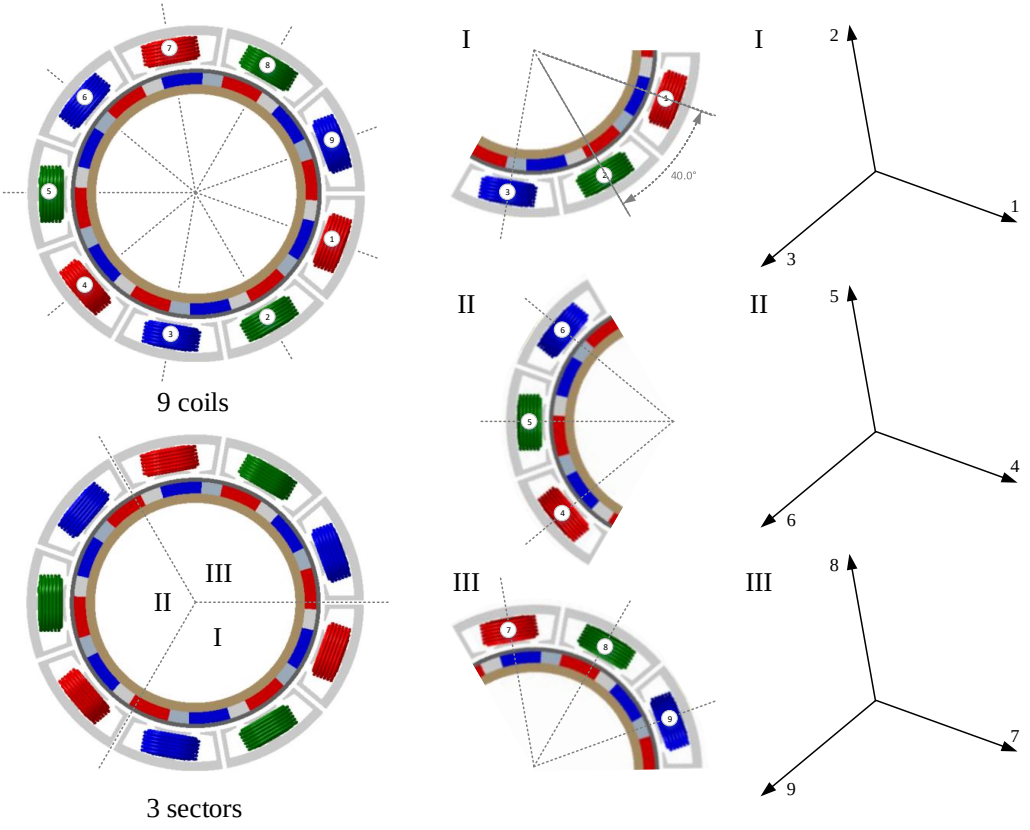


Fig. 5.38 Schematic diagram of phasor.

Table 5.14 Angle of windings.

Coils	1	2	3	4	5	6	7	8	9
Mechanical angle	0	40	80	120	160	200	240	280	320
Electrical angle	0	240	480	720	960	1200	1440	1680	1920
Simplified angle	0	240	120	0	240	120	0	240	120
Sector		1			II			III	

5.5.3 FEA simulation

A detailed finite element analysis (FEA) for the proposed triple three-phase machine was given to illustrate the comprehensive performance. To compare the performance between healthy and faulty operations, the whole machine model is created. The FEA results of no-load and on-load operation will be illustrated respectively.

5.5.3.1 Inductance matrix

Inductance values could be obtained from FEM results based on the optimal candidate. *Fig. 5.39* illustrates a three-dimensional stem plot of self-inductance and mutual inductance among nine phases. In comparison with self-inductance in the diagonal position, mutual inductance is relatively small. Designing a fault tolerant machine with high self-inductance and low mutual-inductance has obvious benefits. Self-inductance could suppress the SC current, while low mutual inductance can decrease the interaction between different modules. According to the triple three-phase inductance matrix, there is a quantitative evaluation by comparing the ratio between maximum mutual inductance (M) and minimum self-inductance (L). In this case, the value is 3.4%.

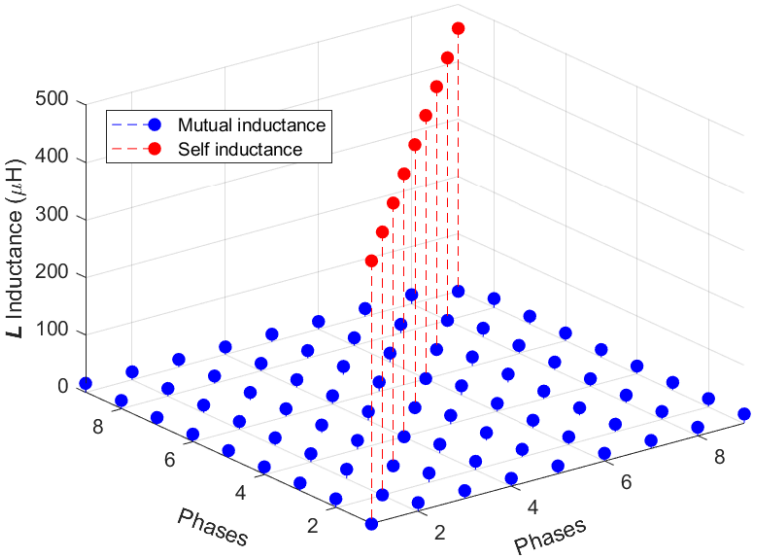


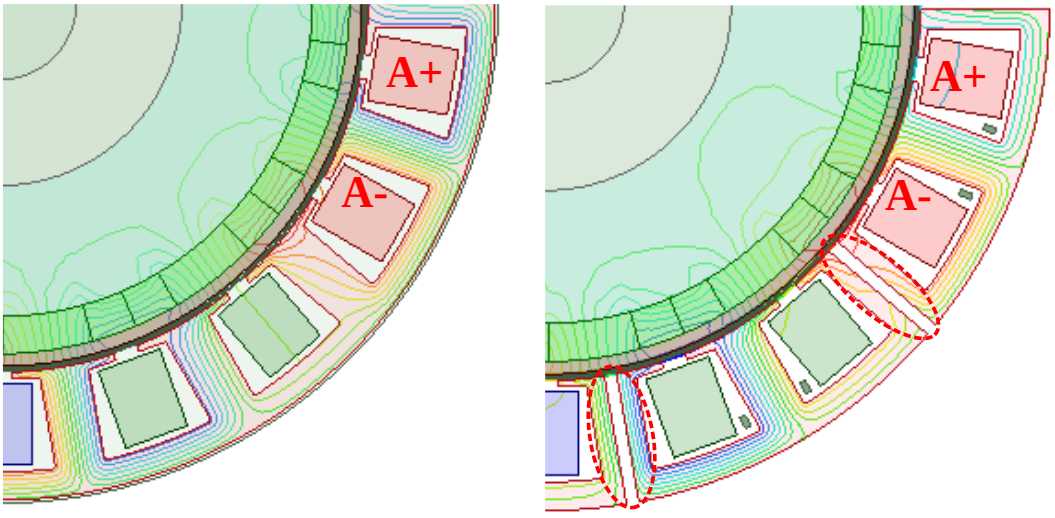
Fig. 5.39 Matrix diagram of self-inductance and mutual inductance.

5.5.3.2 No load

5.5.3.2.1 Flux linkage

The speed of machine was set at 11000 rpm for the following investigation. A comparison of the flux linkage distribution of a modular triple three-phase machine with a conventional topology is presented in *Fig. 5.40*. Due to the modular design

and segment gaps, the flux path has been changed significantly between the adjacent phases. The segment gaps make it more difficult for some of flux to get into adjacent phases, because the reluctance of gap is significant high than stator. The existence of segment gaps influence the flux distribution, which benefits the magnetic isolation of phases. Meanwhile, the thermal dissipation path is changed as well.



(a) (b)

Fig. 5.40 Flux plot distributions under open-circuit in (a) conventional topology (b) modular segments.

The fluctuation of flux density in the airgap based on varied rotor position and time is shown in *Fig. 5.41*. Similarly, the comparison of flux density of airgap is shown in *Fig. 5.42*, while the position of poles and stator tooth aligned in the direction which represented the maximum linkage of Phase A. Take the stator gap which close to Phase A- as an example, the airgap flux density is different near this place, as shown in *Fig. 5.42*. The curves represent the end time of one period. Both of the curves are almost overlapped. The existence of stator gaps exhibits little effect on the flux density.

The demerits of this sort of design have been validated that the presence of segment gaps could make the cogging torque magnitude higher because of more flux leakage through the tooth tips [113]. Moreover, the unequal slot-opening width and segment gaps can cause affect the cogging torque in peak value and periodicity.

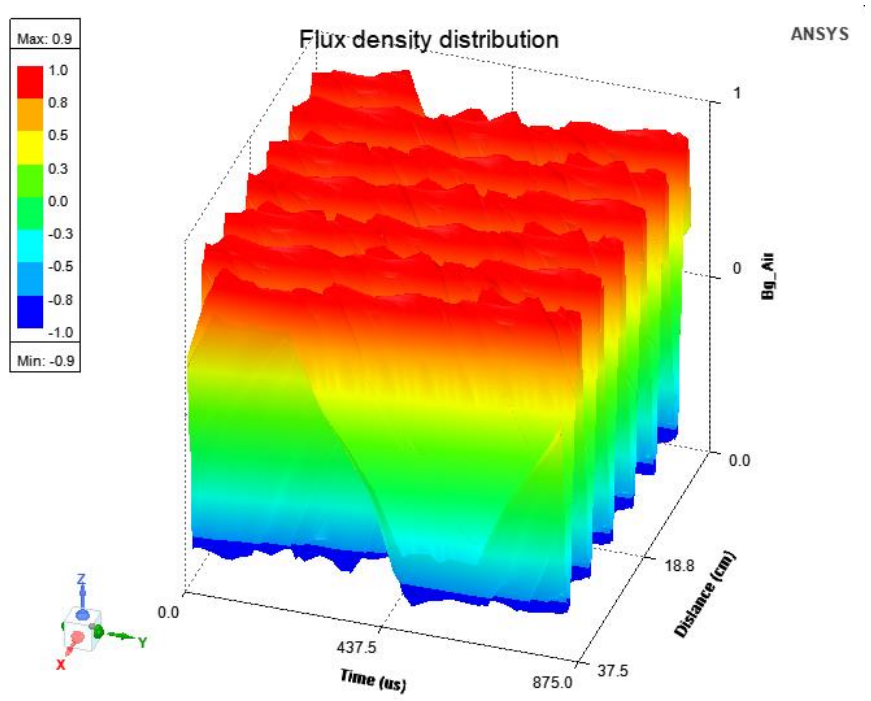


Fig. 5.41 The fluctuation of flux density in the airgap based on varied rotor position and time.

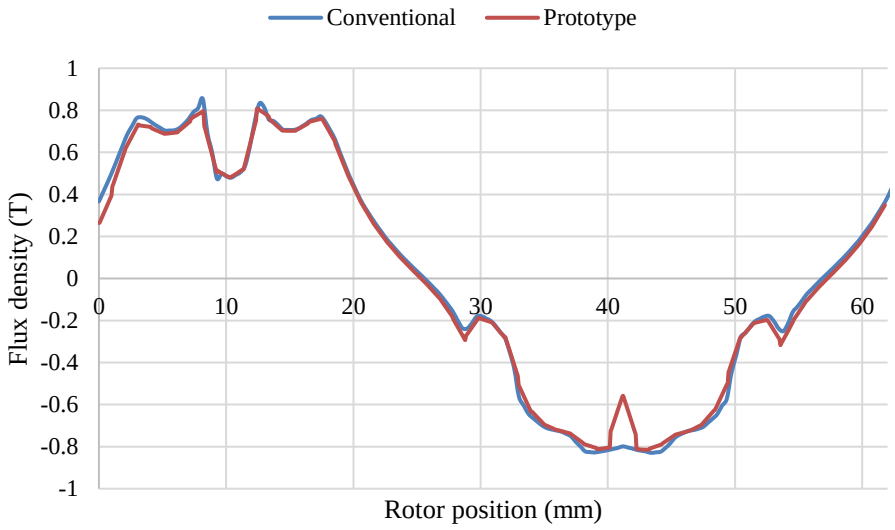


Fig. 5.42 Air gap flux density versus rotor position.

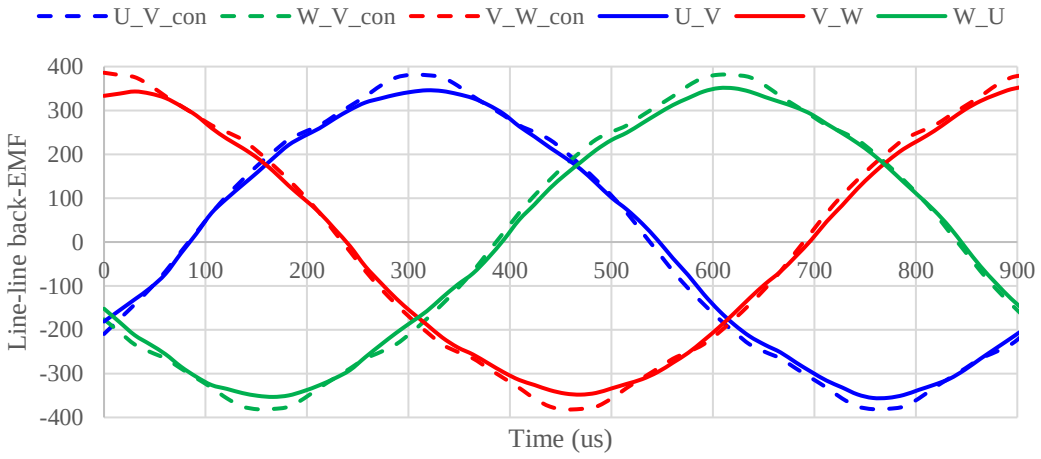
5.5.3.2.2 Back-EMF

Due to topology design, the spatial results of three modules are totally same and overlapped, including but not limited to linkage, back-EMF or current. Consequently, the results will focus on one three-phase module, such as first module.

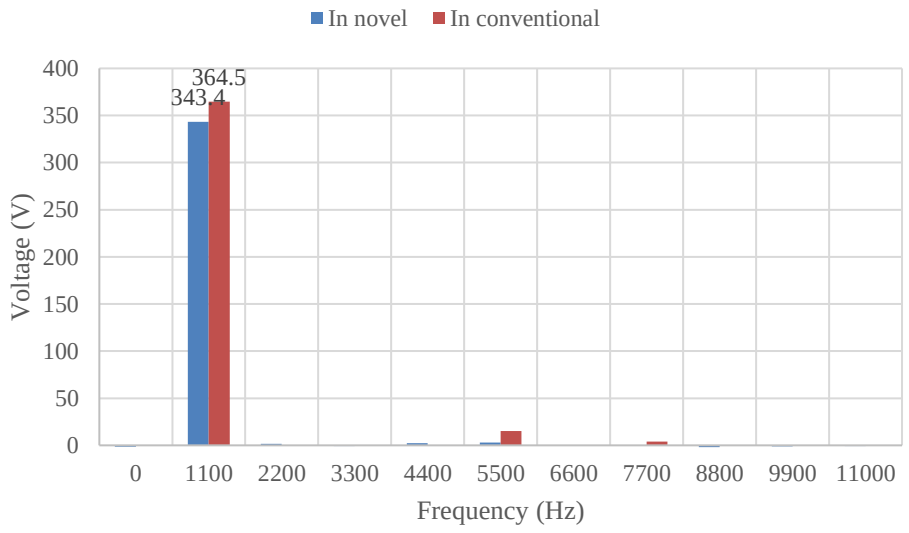
The back-EMF of PMSM is determined by the airgap flux density and winding factor. In the conventional topology, winding factor, comprising of winding

distribution factor and coil pitch factor, could be calculated by general theoretical equations. The winding factor for conventional 18 slot/12 pole combination is 0.866. For this case, triple three-phase with segment gaps in stator, the winding factor has been changed, mainly in coil pitch factor.

The comparison of line-line voltage and FFT spectra in conventional and proposed modular topology are as shown in *Fig. 5.43*, at 11000 rpm. The fundamental magnitudes of line-line back-EMF in conventional and proposed modular topology are 364.5 V and 343.4 V, respectively. These comparisons demonstrate the effect of the stator gap on performance, which results in a 5.8 % reduction in line-line back-EMF.



(a)



(b)

Fig. 5.43 FEA results of three-phase. (a) single modular back-EMF voltage @ 11000 rpm. (b) Spectra.

5.5.3.3 On load

At the rated-speed operation, 11000 rpm, the output performance has been checked. The fluctuation of output torque is shown in *Fig. 5.44*, while the average output torque, T_{avg}, is 26.7 Nm. When the machine operated under the healthy operation, the effect of radial force could be negligible. As a fault tolerant application, the triple three-phase machine could maintain operation in the presence of faults, such as the faulty segments will be isolated due to the safety strategy. It is worth to investigate the comparison of radial force under healthy and faulty operations. The rotor radial force under the healthy operation is about 10.4 N, as shown in *Fig. 5.45*. Although there is no industry standard to evaluate the quality of axial force, its results under varied operation scenarios can provide a basis for the selection of bearing pairs, especially concerning the post-fault operation.

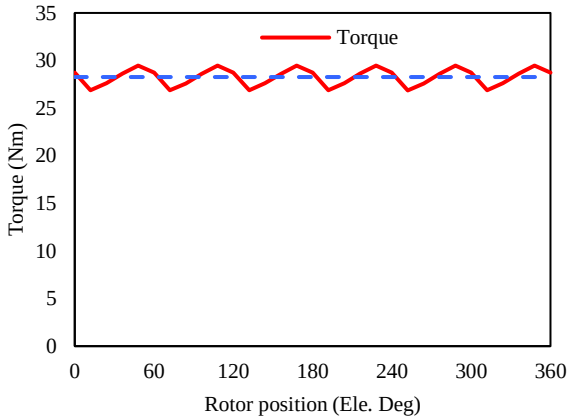


Fig. 5.44 Output torque verse rotor position.

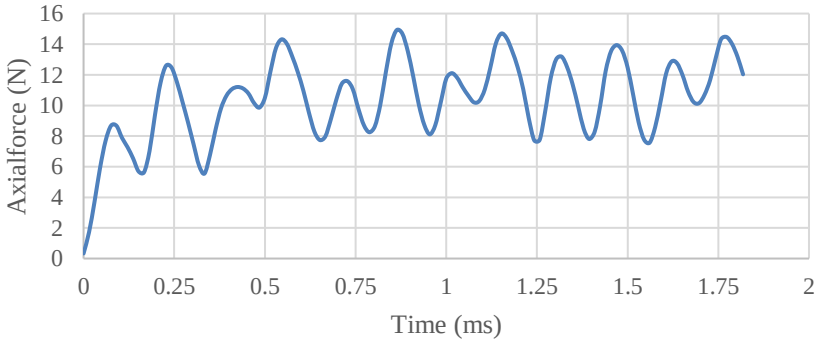


Fig. 5.45 The radial force on rotor under the on-load operation.

5.5.4 Faulty scenarios

A detailed FEA model was carried out to investigate the performance of machine under faulty scenarios. To compare the performance between healthy and faulty

operations, the whole machine model is created. The FEA results, including the open-circuit, on-load operation and short-circuit operation, will be illustrated, respectively.

As the requirement of fault tolerance for this machine, it should maintain operation continuously in the presence of electrical faults, in other words, short circuit or open circuit faults in the windings. Generally, the potential fault mode could be one single-point fault or combinations. Although this topology has three three-phases/modules, 9 phases, the potential failure modes are limited due to the fault tolerant design. The single layer fractional slot concentrated windings could avoid the faults between modules, or phases.

Therefore, the potential winding faults of this machine could be partial open circuit or short circuit in single module or single phase. The investigation of post-fault performance could pave the way for the corresponding safety strategy. To simplify the investigation, faults were introduced in one set of three-phase, specifically in Module 3 (M3), while the other modules remained healthy. The potential failure modes and fault's location are listed in Table 5.15. Meanwhile, the equivalent circuit diagrams of M3 under varied operations have been illustrated in *Fig. 3.5*. All of the faulty operations have been simulated respectively.

Table 5.15 Potential failure modes and fault's location.

Failure mode	Module status		
	M1	M2	M3
Partial open-circuit	Healthy	Healthy	Faulty
Partial short-circuit	Healthy	Healthy	Faulty
	Healthy	Healthy	Turn-to-turn faulty

5.5.4.1 Three-phase (M3) OC fault

The open-circuit faults have been assumed occurred in the M3, replacing the real resistance by a giant one. There is no current flow in the circuit, nor energy conversion. The machine will lose similar ratio output power, according to the absence of phases. Therefore, the degradation of performance is also predictable.

Compared with normal operation, the case of three-phase open-circuit has been examined and compared in Table 5.16. Because of the absence of one three-phase, output torque has been reduced one third. Torque ripple increases slightly, but

maximum radial force spikes dramatically due to the winding arrangement. In short, the machine could be faulty-safe and maintain operation with about two thirds power, with higher torque ripple.

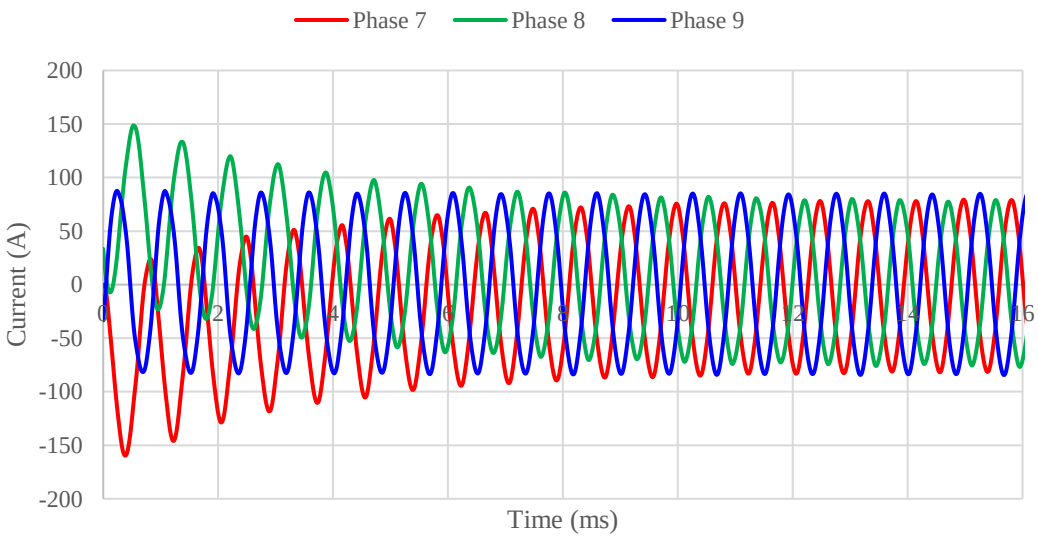
Table 5.16 Output comparison under varied scenarios.

Mode	Torque (Nm)	Torque ripple (%)	Max. radial force (N)
Healthy	28.3	9.2	13.2
M3 OC	19.0	11.6	171.4

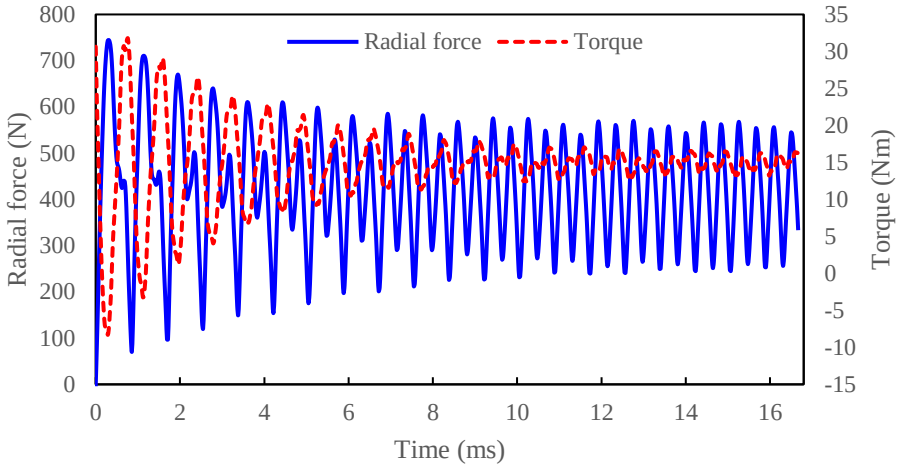
5.5.4.2 Three-phase (M3) SC fault

The three-phase SC fault could be illustrated by the equivalent circuit as shown in *Fig. 3.5* (b). This sort of fault is possible to occur by the faults in the power electronics. The behaviour and impact of SC fault are more sophisticated than OC fault because the SC current is existent continuously in the windings.

The fluctuations of output are shown in *Fig. 5.46*. The SC current comprising of AC and DC components will restore relatively sinusoidal status after a short duration while the DC attenuation as shown in *Fig. 5.46*(a). The difference between peak values were caused by different mutual inductances between the three phases. Due to isolated winding layout, the phases which close to another set of three-phase, have higher mutual inductance than phases which far away to another set of three-phase. The drag torque generated by SC current in the phases of M3 will play a role of brake, reluctant effect to the output torque. Meanwhile, the SC operation causes a shock for machine resulting higher torque ripple and rotor radial force.



(a)



(b)

Fig. 5.46 Output of the machine under three-phase short-current. (a) Phase current plots. (b) Fluctuation of radial force and torque.

The fluctuations of metrics in the post-fault operations, between OC and SC, are totally different. In the OC fault, the radial force increases dramatically and maintains, while its torque ripple exhibits a small increase, from 9.2% to 11.6%. Oppositely, the value under the SC fault will adjust from peak value to relative lower value. By selecting proper bearing pairs, the faulty machine could operate continuously.

5.5.4.3 Turn-to-turn SC fault

As aforementioned, the most severe fault for electrical machine is the turn-to-turn short-circuit, which caused by the failure of insulation in coil. In this model, a turn-to-turn fault is supposed in Phase 9 (M3). The SC turns and remaining healthy parts of phase 9 are magnetically coupled but electrically isolated, as the equivalent circuit. The coil of phase 9 could be split into two independent parts SC part and remaining part. In the SC part, SC current flow exists in the independent circuit.

The turns of SC winding and its location in the slot are the key variables to affect the SC current [73]. And, the most severe condition is the single-turn SC fault occurs closer to the slot opening, as shown in Fig. 14. The target of this model is to investigate the potential maximum SC current in the coil. To estimate the worst case, the model of single turn short circuit which close to the slot-opening is proposed as illustrated in *Fig. 5.47*.

The output torque under this specific fault is shown in *Fig. 5.48*. The output torque 26.5 Nm is slightly lower than healthy output 28.3 Nm. The torque ripple increases dramatically, from 9.2% to 32.8%, which could be a criterion for fault diagnosis to

evaluate if turn-to-turn short-circuits is occurring. The main challenge under this fault is the SC current, which is high enough to affect adjacent healthy winding for the thermal concern. The potential safety strategy to cope this sort of fault is to downgrade output by low speed and load.

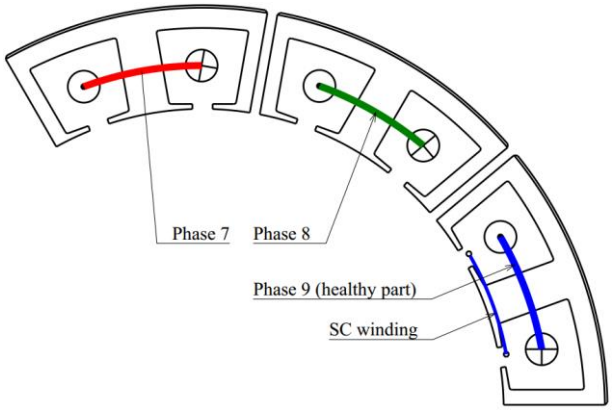


Fig. 5.47 Schematic diagram of SC winding and healthy winding of Phase 9 in the module 3 (M3).

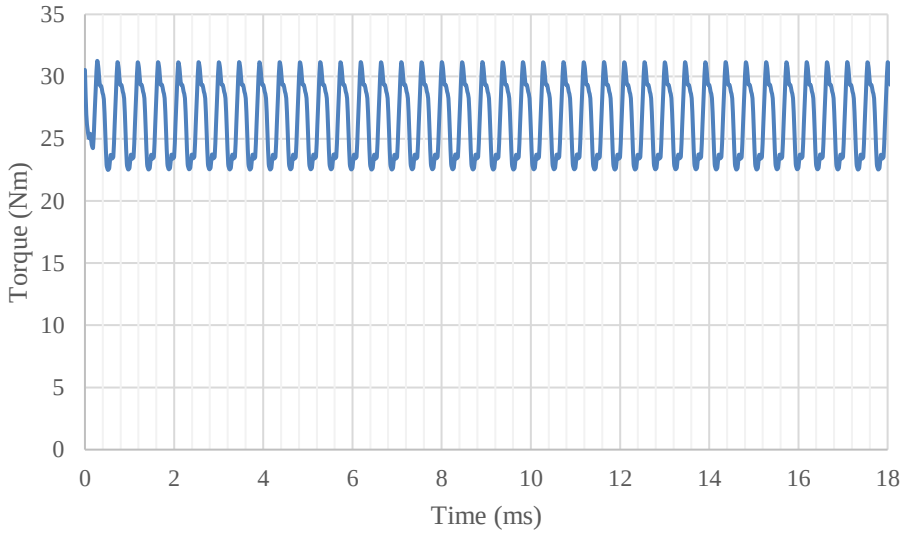


Fig. 5.48 The output torque under the turn-to-turn SC fault in Phase 9.

5.5.4.4 Demagnetization

As stated before, the irreversible demagnetization of the permanent magnet is a potential issue which result in efficiency decline, reduced performance and low reliability of the machine. This fault can be caused by faulty current or thermal issues.

In the case of winding fault, faulty current may increase dramatically. The phase-to-phase SC fault was added in Module 3, and the phase current value appears at 0.375 ms. The flux density contour was extracted and shown in *Fig. 5.49*. The maximum

flux density is 1.58 T and the demagnetization coefficient is zero. This analysis proves current-dependent demagnetization will not occur in the case of short-circuit scenario.

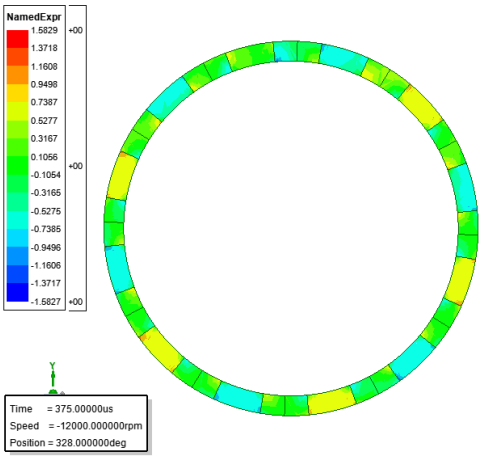


Fig. 5.49 Flux density distribution on permanent magnets and the demagnetization coefficient.

5.6 Conclusion

To ensure safe operation in fault scenarios, fault partition designs have been implemented to provide electrical, magnetic, and thermal isolation. The feasibility of multiple three-phase topologies was evaluated based on their electromagnetic performance, and feasible fault tolerant (FT) designs were investigated in detail. Considering the balance between reliability and cost, dual and triple three-phase topologies were considered the most suitable candidates, while quadruple and sextuple three-phase topologies were deemed too complex.

After a thorough analysis, a triple three-phase 18 slot/12 pole, single layer concentrated winding was selected as the initial candidate for the application, based on its compromise between redundancy and complexity. To further improve fault tolerance, a design was proposed that involves splitting the stator into independent segments. The performance of healthy and faulty scenarios was validated through FEA approach, and this investigation will be presented in detail in the upcoming chapters.

Chapter 6 Thermal management and machine losses

As a high-power machine, thermal management plays a critical role in achieving high performance. Reliable and feasible cooling methods are key pillar in maintaining continuous machine operation.

6.1 Thermal management

Thermal energy, losses, is an inevitable outcome of energy conversion in the operating electrical machine. The losses increase the temperature of all the components in the machine. The volume loss densities in electrical machine is varied from 0.15 to 5 MW/m^3, with the corresponding current densities, varied from 2.5 to 15 A/mm^2 [120]. The current prototype of high power density electrical machines has achieved much higher current density, such as 27.2 A/mm^2 in [121] and 27.5 A/mm^2 in [64], which means effective cooling methods for operation are decisive.

The goal of thermal management is to prevent the temperature from rising above safe levels by implementing effective heat dissipation methods. If the temperature increases beyond safe levels, it can cause insulation failure, leading to potential electrical faults as discussed in previous sections. Higher operating temperatures also pose a risk to the mechanical and electrical safety of the winding insulation, which can lead to further machine failures. Additionally, extreme temperature or time cycling can cause unwanted movement between conductors and iron, resulting in insulation separation from the conductors and eventual damage. Therefore, it is crucial to implement reliable and efficient cooling methods to maintain the temperature within safe limits and ensure the long-term performance and reliability

of the electrical machine.

6.2 Limitation and selection of materials

The life of an insulation system is strongly dependent on temperature, and even the best insulation will fail quickly if operated significantly far from its rated value. The life of winding insulation is doubled for every 10℃ reduction in average operating temperature.

The selection of thermal management for this machine was based on the maximum allowed temperatures for critical motor components or parts, which vary significantly. To adapt to the high temperature risk of the operating environment and avoid demagnetization, samarium cobalt (SmCo) Recoma 33E (supplier: Arnold Magnetic Technologies) was chosen as the permanent magnet material. Recoma 33E has a maximum operating temperature of 350℃, which is much higher than that of neodymium–iron–boron (NdFeB) permanent magnets. However, for the winding insulation, the safety temperature limitation was set at under 200℃ due to concerns about the insulation materials. In other words, the selected cooling solution should maintain these components safely during continuous operation.

6.3 Loss modelling

To determine the temperature distribution in an electrical machine, it is prerequisite to estimate the losses and thermal characteristics of the magnetic, conductive and insulating portions of the machines.

General thermal energy in electrical machines derives from the power losses in electrical components and magnetic circuit. In the perspective of material, the losses in electrical components and magnetic circuits are also defined as copper loss and ferrite loss. For the different applications, the main contribution of losses may be varied.

6.3.1 Copper loss

Copper loss of PMSM means the location of loss, which generated in the conductors, copper windings. Due to Joule effect, the power of losses in the winding is converted to heat. Additionally, for high frequency PMSM, AC loss is an inescapable

contribution whilst it is neglected in general PMSM. In other words, copper loss consists of DC copper loss and AC copper loss.

6.3.1.1 DC loss

DC losses are proportional to the winding resistance R and square of electrical current I^2, which equals to I^2R. For the machine, the DC copper loss of stator is calculated from:

$$W_{cu} = N_{ph} I_s^2 R_{ph} \tag{6.1}$$

Where N_{ph} is the number of phases, I_s is the rms phase current and R_{ph} is the per phase resistance. If only DC losses are considered, R_{ph} is calculated as:

$$R_{ph} = R_{dc}^{Tcal} = \left(\frac{1 + \alpha(T_{calc} - 20)}{1 + \alpha\left(T_{ref} - 20\right)}\right) R_{dc}^{Tref} \tag{6.2}$$

Where R_{dc}^{Tcal} is the DC resistance per phase at the reference temperature, α is the temperature coefficient of resistivity at 20 degrees C, T_{calc} is the average winding temperature used in the calculation and T_{ref} is the average winding temperature that R_{dc}^{Tref} is calculated or measured at. For this specific machine which fundamental electrical frequency is 1100 Hz, the AC effects are considered, because the skin effect and proximity effect at high frequencies would greatly increase the AC copper loss of high speed permanent magnet machines [122]. Then, the R_{ph} is calculated as:

$$R_{ph} = R_{dc}^{Tcal} + R_{ac}^{Tcal} \tag{6.3}$$

Where R_{ac}^{Tcal} is given by

$$R_{ac}^{Tcal} = R_{dc}^{Tref} \left[\frac{\left(\frac{R_{ac}}{R_{dc}} - 1\right) \cdot \left(\frac{n_{calc}}{n_{ref}}\right)^{\zeta}}{\left(\frac{1 + \alpha(T_{calc} - 20)}{1 + \alpha\left(T_{ref} - 20\right)}\right)^{\beta}} \right] \tag{6.4}$$

where R_{ac}/R_{dc} is the ratio of AC + DC resistance to DC resistance at rotational speed n_{ref} and temperature T_{ref}. ζ is the frequency scaling parameter which controls how the AC loss component scales with frequency and $\boldsymbol{\beta}$ is the temperature exponent parameter which controls how the AC loss component scales with temperature. All AC winding losses are treated electrically.

6.3.1.2 AC loss

For the round conductors, the AC loss is calculated using the following equation:

$$P_{AC} = \frac{\pi l_a d_c^4 \sigma (\omega B)^2}{64} \cdot \frac{1}{\left(1 + \alpha (T - T_0)\right)} \tag{6.5}$$

Where: l_a and d_c are the active length and diameter of the conductors in meters, respectively; ω is the electrical frequency, and B is the magnitude of the flux density in the slot region; T and T_0 are the winding temperature and reference temperature; σ is the electrical conductivity of the conductor material and the α is temperature coefficient of resistivity of the conductor material.

When the skin depth of the conduction is less than their height, the calculated loss value is reduced as the induced eddy will find it harder to flow. It is assumed that below the skin depth, no current can flow. So, the losses are decreased by the ratio of the effective conductor area divided by the total conductor area:

$$\frac{A_e}{A} = \frac{\delta}{2r} \tag{6.6}$$

δ is the skin depth; r is the conductor radius.

The effects of winding strands and bundle arrangement in the slot on the ac copper loss have been investigated in [123], which optimal strands arrangement could halve the AC copper loss. Besides, it is feasible to decrease the AC copper loss of the winding by increasing the parallel branches of the winding. However, the increased strands mean the higher possibility of circulating current which leads to additional current losses. So, it is a trade-off study about the design of parallel branches or diameter of every strands.

FEM is also an effective tool to calculate the AC loss in the windings. A parametrical investigation was carried out to compare and select the optimal selection between AC loss and number of winding strands. The results in shown in *Fig. 6.1*. The strands were variable from 5 to 10, while the 7 strands exhibited the lowest AC loss. This value was adopted in the winding process.

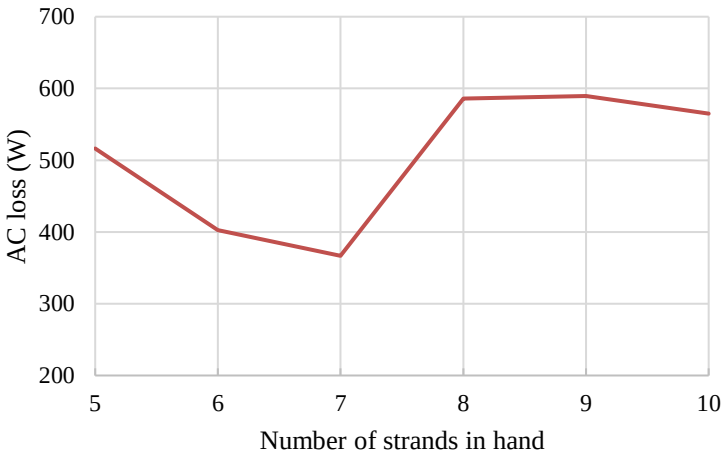


Fig. 6.1 AC copper loss with varied stands of winding.

6.3.2 Magnetic circuit loss

Losses in magnetic circuits are a consequence of alternating magnetic induction in ferromagnetic materials, and it is divided in hysteresis losses and eddy currents losses. Steinmetz's equations serve as the foundation for core loss calculation in this thesis. These empirical equations are utilized to estimate the total core losses per unit volume in magnetic materials when exposed to external sinusoidally varying magnetic flux. Steinmetz's equations will be introduced below.

6.3.2.1 Hysteresis loss

Variation of magnetic field in a ferromagnetic material implies setting in motion magnetic dipoles and changing their orientation. The origin of hysteresis losses is friction between adjacent magnetic dipoles during periodic rotation. Specific hysteresis losses P_H are proportional to operating frequency f and to surface encircled by the hysteresis curve in the B-H plane. By introducing coefficient σ_H which is equal to the ratio of the specific mass of ferromagnetic material, hysteresis losses per unit mass are

$$P_H = \sigma_H \cdot f \cdot B_m^n \tag{6.7}$$

$$n = \alpha + \beta \cdot B \tag{6.8}$$

Where B_m is the magnetic induction, and the exponents of α and β are determined by BH curve of selected material, N10 0.1 strip. The α and β are 1.59 and 0, respectively. Then, the equation 6.7 is given.

$$P_H = \sigma_H \cdot f \cdot B_m^{1.59} \tag{6.9}$$

6.3.2.2 Eddy-current loss

Several conductive contours can be induced within each piece of ferromagnetic. Therefore, the change in magnetic induction causes spatially distributed currents which contribute to losses in magnetic circuits, called eddy current losses.

Total losses in magnetic circuit due to eddy currents are proportional to the squared angular frequency and squared magnetic induction. Specific losses due to eddy currents are

$$P_V = \sigma_V \cdot f^2 \cdot B_m^2 \tag{6.10}$$

Where σ_V is coefficient of proportionality, dependent on the specific conductivity and specific mass of the material.

$$\sigma_V = \pi^2 \cdot \sigma \cdot \frac{d^2}{6} \tag{6.11}$$

Where σ denotes the conductivity and d represents the thickness of one lamination sheet. These factors influenced the decision to select a thin iron sheet with a thickness of 0.1 mm and 3 mm PM slices.

To calculate the losses using theoretical equations, a series of data points distributed throughout the entire model need to be computed. Alternatively, MotorCAD and Maxwell were employed to calculate the loss components, which provided the corresponding results.

6.3.2.3 FEA simulation

The selection of stator lamination materials, N10 0.1 strip, is able to accommodate the 1200 Hz fundamental frequency and the high core saturation flux density needed to achieve high power density. The rotor magnets array is segmented and laminated in the axial dimension. Moreover, the 3-mm thickness magnet slices could be coated with a thin insulation coating to minimize eddy current loss.

After a short duration, the core losses comprising of eddy current and hysteresis loss are stable as shown in *Fig. 6.2*. Besides, the conduction losses in the stator windings are typically the main source of loss in PMSMs, which are the sum of two components: the DC loss and the AC loss. The DC loss could be predicted easily by

theoretical equations, whereas the AC loss is a more complex combination by different effects, skin effect and proximity effect. Based on the different method, the loss distributions of the machine are shown in Table 6.1.

Meanwhile, the efficiency map from standstill to maximum speed is exhibited which made clear the visualization of values of torque-speed with the efficiency values, in *Fig. 6.3*.

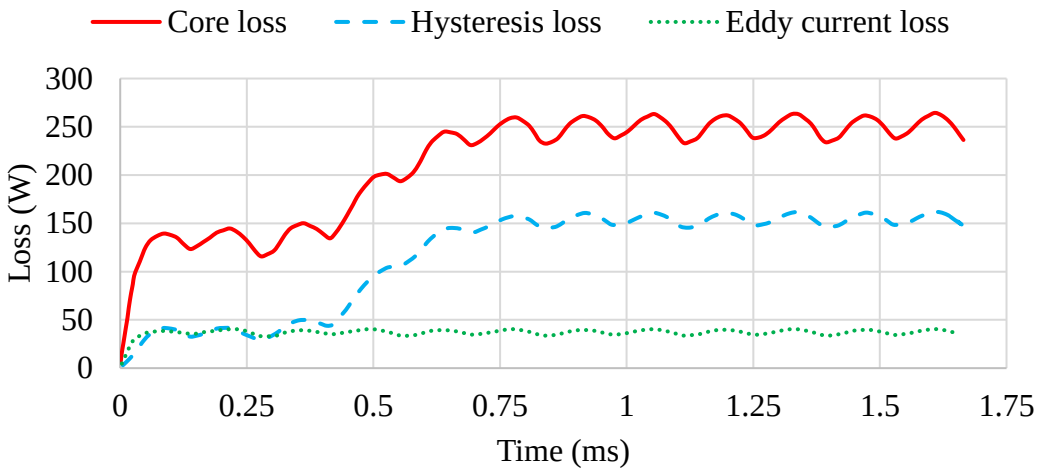


Fig. 6.2 Core loss and its components: eddy current loss and hysteresis loss.

Table 6.1 Loss distribution.

Loss	Core loss	Magnet loss	DC loss	AC loss	Total loss
Value (W)	265.0	23	839	324.2	1447

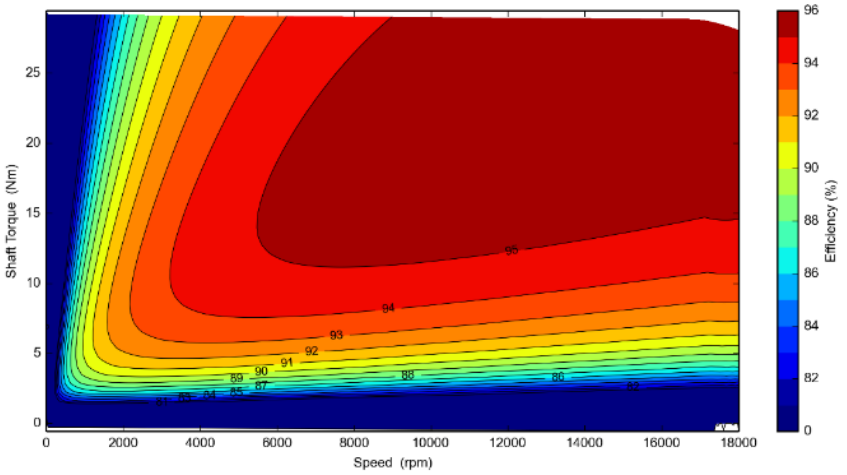


Fig. 6.3 Efficiency map of the whole speed range

6.4 Cooling methods

The target of feasible cooling methods should resolve the heat transfer consisted of conduction and convection. The conduction cooling is defined as the transfer of heat from winding to cooler part (housing water jacket) by direct contact. The convection cooling involves the transfer of heat from winding by coolant or air flow. A range of convection cooling options have been commonly utilized, such as the cooling in the windings and laminations.

Besides, advanced cooling methods based on potting materials attract attentions, which can form a bridge to connect end-winding and housing. Moreover, phase change cooling shows extra benefits because it could store useful heat energy or convert it to electrical energy.

In this thesis, three kinds of cooling methods (slot cooling, housing jacket cooling, and enhanced cooling) were carried out to investigate the thermal management, and the corresponding machine design have been done. In the case, the setting of the oil and its property are listed below in Table 6.2.

Table 6.2 Property of the coolant: oil and water.

Coolant properties	Oil	Water	Unit
Thermal conductivity	0.12	0.62	$W/m\cdot$℃
Density	770	992	kg/m^3
Specific heat	2.1	4178	$J/kg/$℃
Kinematic Viscosity	1.02e-5	6.59e-4	m^2/s

6.4.1 Slot cooling

It has been proved that the main heat source is from the winding consisted of DC loss and AC loss in this machine. Then, the slot cooling is the most direct method to transfer the heat of machine. By this method, all the windings and stator laminations will be immersed in the coolant. Gap in the slots, or extra ducts in the stator will provide channels for coolant to dissipate the heat directly, from front end to the rear end-winding. The non-magnetic and non-conductive oil is an ideal coolant for slot cooling than water, although lower capability of conduction.

To avoid high churning loss caused by coolant and rotating rotor assembly, semi-flooded cooling is a compromise cooling method. An oil sleeve is needed to separate

the stator zone and rotor assembly, for maintaining the coolant flowing in the stator zone, as shown in *Fig. 6.4*. The direction of the arrows illustrates the direction of the flow.

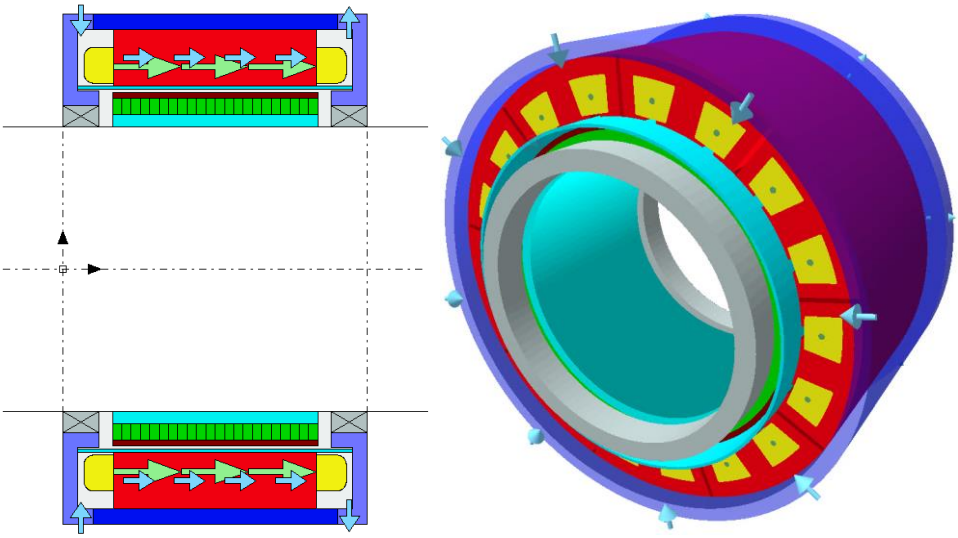


Fig. 6.4 Section of flow direction with slot cooling.

This oil sleeve is made of non-metallic material, such as carbon fibre, glass fibre or PEEK, due to the high specific strength than alloy. The key point of this structure is the sealing design of coolant. However, the existence of the oil sleeve results in a thicker air gap with lower flux density in it. In this case, the thickness of the stator sleeve is 1 mm. Besides, the demerits of this solution are the cost and complexity of assembly.

The exploded view of a high speed machine with an oil sleeve is shown in *Fig. 6.5*.

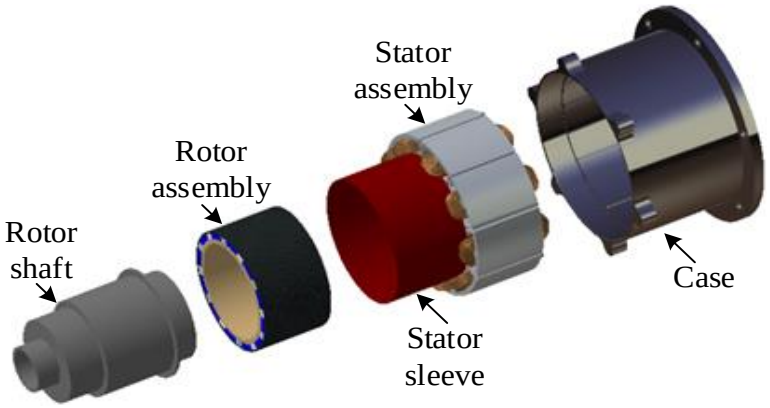


Fig. 6.5 Exploded view of a high speed machine with an oil sleeve.

6.4.2 Housing jacket cooling

As aforementioned, one of the advantages of the modular design is the interchangeability and serviceability. Every independent segment could be extracted and replaced with a new one easily. So, the liquid jacket cooling could keep inner space simple, dry and the segments away from coolant. The cross section of housing jacket cooling is shown in *Fig. 6.6*. Water was selected as the coolant due to the high convection heat, which could transfer heat quickly.

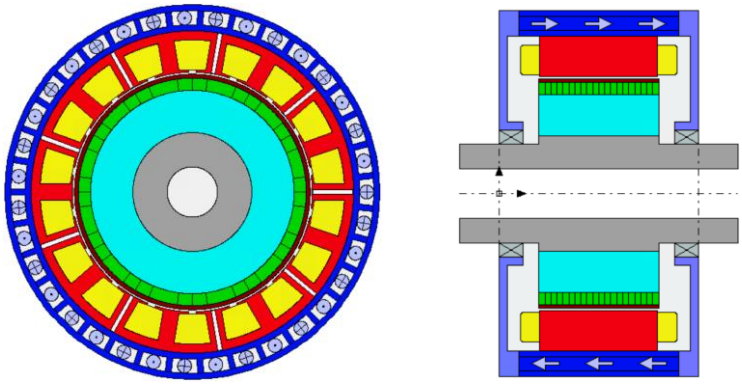


Fig. 6.6 Section of flow direction with water jacket cooling.

The exploded view of electrical machine components with housing water jacket is shown in *Fig. 6.7*. For the housing jacket design, channel dimensions, cross-section shape and the flow rate are related to the performance of the coolant jacket. It has been proved that the axial cooling path exhibits a higher heat transfer coefficient, while the tangential path has the merits with lower pressure drop.

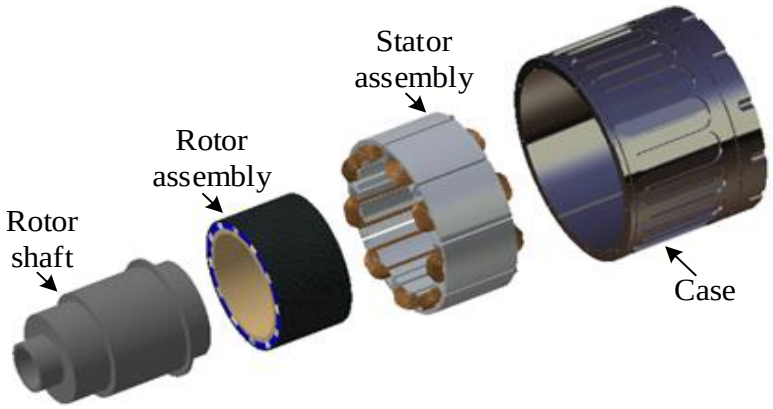


Fig. 6.7 Exploded view of a high speed machine with housing water jacket.

The cooling paths and shape of cooling ducts are varied. The heat transfer capacity does not determine by the topology, but the total cooling surface. In this machine, housing water jacket with axial cooling path is the optimal choice for the readiness level to manufacture. Computational Fluid Dynamics (CFD) method is adopted to

analysis the thermal behaviour.

To ensure the interference fit between stator and housing for good contact, a steel sleeve was design to mount the modular stator segments, and this will be covered in Chapter 8.2. Above all, as a common external cooling method, housing water jacket is selected for this machine, due to the better cooling performance and manufacturing readiness level.

6.4.3 Enhanced cooling

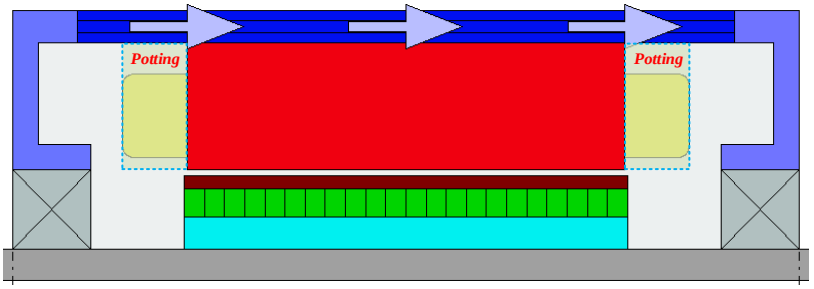
By slot cooling method, coolant can transfer the heat of windings, including the end-winding, to the outside of machine directly. For housing jacket cooling, end-winding may become the hottest position because it is far away to the housing.

When forced air cooling is not enough and direct liquid cooling is not preferred, high thermal conductivity encapsulation materials can be used in indirectly liquid-cooled motors to meet design and operation requirements. Potting the stator windings provides a direct thermal connection to the motor housing, which has been shown to reduce winding temperatures by up to 50°C at a given power output, and increase power output by 15-25% at a given temperature, compared to an unpotted motor [124].

End-space potting can be a bridge to connect end-winding and housing, as shown in *Fig. 6.8*.



(a)



(b)

Fig. 6.8 The (a) main process and (b) schematic of potting in the end-winding.

6.5 Analysis and results

6.5.1. Methods

General approaches for thermal analysis of electrical machines have been and presented [125]. The theoretical and numerical methods have strengths and weaknesses in accuracy, calculation speed/computation time and available resources. Computational Fluid Dynamics (CFD), which is a numerical approach based on the finite volume method, has been extensively utilized and validated [126-128]. Lumped parameter thermal network (LPTN) is a recent trend to analyse thermal management. Similar to the electrical circuit, the thermal network consists of thermal source, resistance and path of thermal dissipation. Based on an improved 3D LPTN method, aimed to multisector triple three-phase electrical machine, has been proposed in [129].

To improve the thermal conduction by decreasing the equivalent thermal resistance between the hot spot and the cooling channel, a small extension of back-iron has been proposed [130]. As the machine hot-spot, cooling on its end-windings by pipes, is a direct way to improve thermal management [131]. Comparative study of electrical machine cooling system has been reviewed [132]. To avoid overheating in the high power density electrical machine, the cooling methods could be a cooling jacket, stator cooling, rotor cooling or their combinations.

In this paper, the LPTN and CFD approaches were adopted to analyse the thermal performance of the triple three-phase machine. *Fig. 6.9* exhibits the schematic of the LPTN method, including all the details of the thermal management. By this method, temperature rise of every component can be calculated. Meanwhile, the CFD models were created to investigate different details, as shown in *Fig. 6.10*.

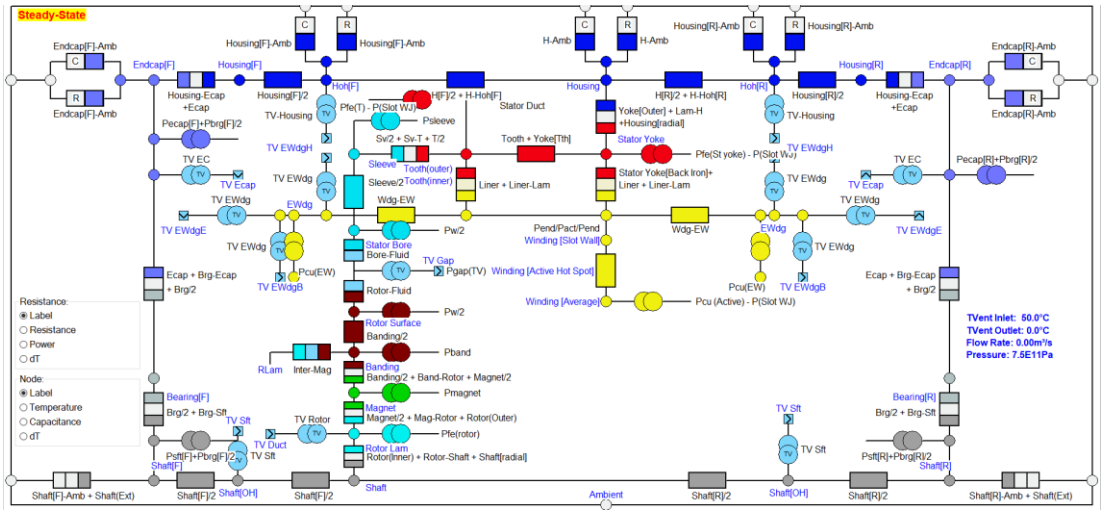


Fig. 6.9 Overview of Lumped parameter thermal network applied on this machine.

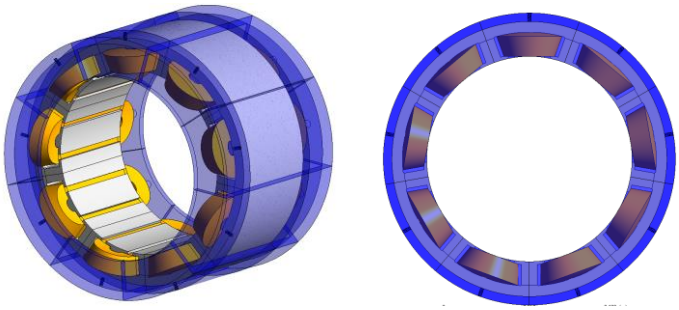


Fig. 6.10 Model created for CFD analysis.

6.5.2. Results

As the main component of machine loss, the potential hot spots locate in the mid-winding and end-winding. Due to presence of segments gaps, the heat transfer in this position has been changed, from conduction to convection. In this section, the thermal managements based on varied combination of cooling method and structure are carried out. Both CFD and LPTN were utilized to analyse the thermal management.

It is worth noting that the optimal candidate can pursue higher output and high power density with advanced cooling solution. To exhibit the differences between these cooling solutions, the output was 50kW rather than 35 kW in these comparison and improvement.

6.5.2.1 Slot cooling

Based on the slot cooling, coolant can contact the heat source directly. A stator sleeve was adopted to separate the cooling zone. The position and size of inlet can determine

the effect of method. Due to the modular design, one segment was created to analyse, as shown in *Fig. 6.11*. The velocity streamline can be simulated for optimizing the cooling path to reduce pressure drop and pursue better effect of slot cooling.

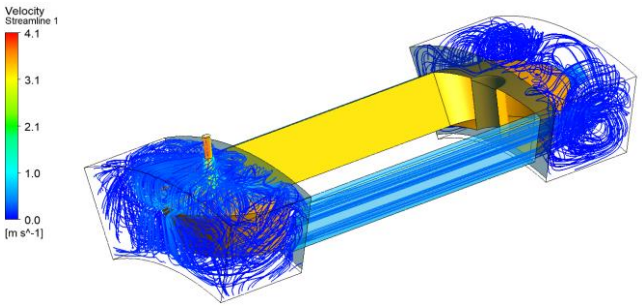


Fig. 6.11 Illustration of velocity streamline of coolant in one segment.

It is worthy to investigate the influence of segment gap to the thermal behaviour. 3D conjugate heat transfer CFD analyses were performed to observe the full temperature distribution and to identify the location of the hot spots within the machine. Given the negligible power loss expected in the rotor, stationary components only were considered in the analyses. A comparative study was made, this included both the non-segmented design, used as reference case, and the segmented machine. Gaps in-between the segments were assumed to be air in one case and aluminium in another case. *Fig. 6.12* shows the configurations considered and the corresponding temperature distributions in the middle section, where the highest temperature was recorded.

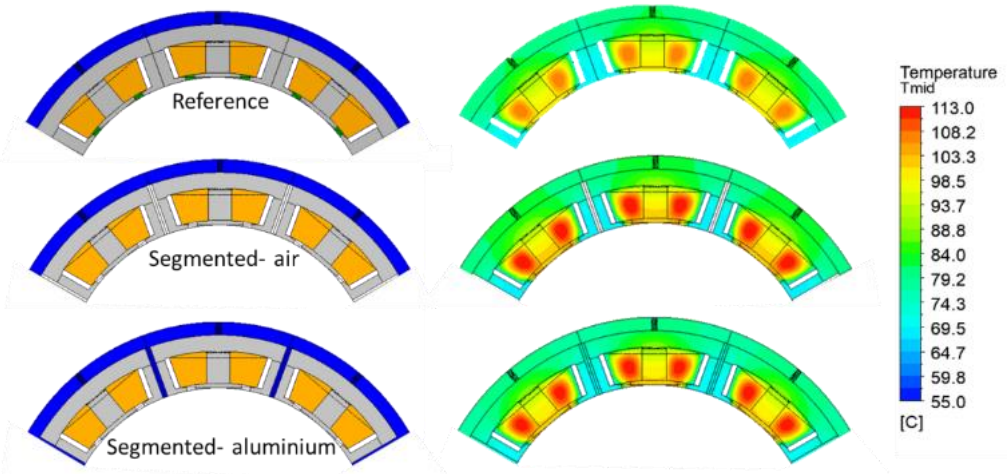


Fig. 6.12 The result of temperature rises with varied segment gap size and filling.

The existence of segments gaps has no significant effect on the heat transfer directly. The slight temperature rise observed can be addressed to the increased power loss,

however this appear to be negligible. Additionally, it can be seen that the use of a high conductive material, in-between the segments, does not lead to a significant benefit in terms of temperature reduction.

In general, slot cooling can provide an effective cooling effect. Besides, the leakproof design are the prerequisite of the cooling.

6.5.2.2 Housing jacket cooling

In general, the effect of housing jacket cooling is not comparable to the slot cooling. Based on the same output, in other words, the same losses can generate a higher temperature rise based on housing jacket than slot cooling. As shown in *Fig. 6.13*, maximum temperature in end-winding and mid-winding are all overheat than 200℃.

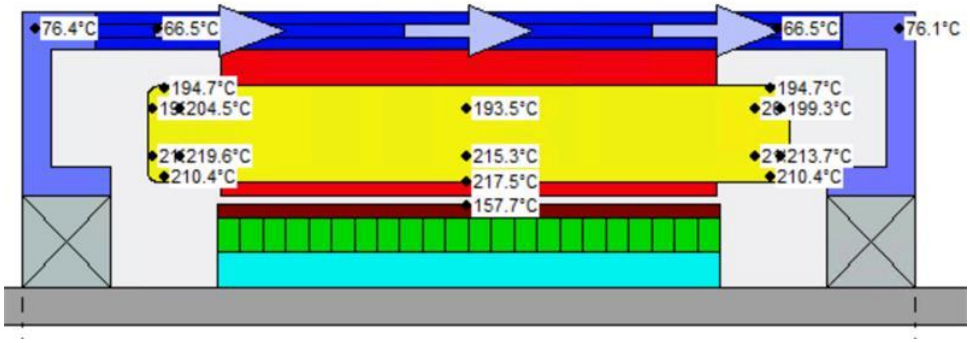
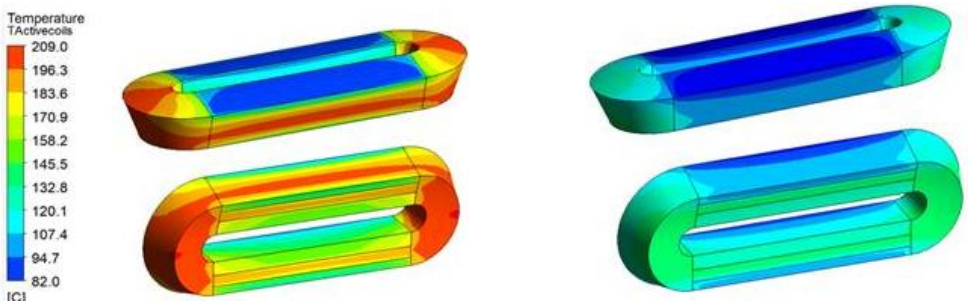
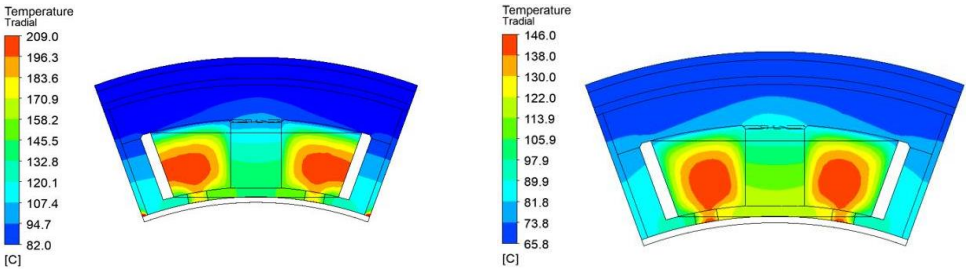


Fig. 6.13 Temperature distribution of components based on housing water jacket.

End-winding potting was adopted to pursue a cooler machine. As shown in *Fig. 6.14*, results by CFD model can illustrate the change of heat distribution. In the 3D model, temperature in the end-winding became much cooler than housing jacket only, due to the presence of potting in the end-winding. More than 60℃ reduction can be found in end-winding and mid-winding. Based on this improvement, maximum temperature of all the components can operate meet the requirement of insulation. The illustration of the potting improvement for this topology is shown in *Fig. 6.15*.



(a) Housing water jacket only ***VS*** housing water jacket + potting



(b)

Fig. 6.14 Comparison of temperature rise in stator (a) Temperature distribution in 3D model. (b) Axial section of segment.

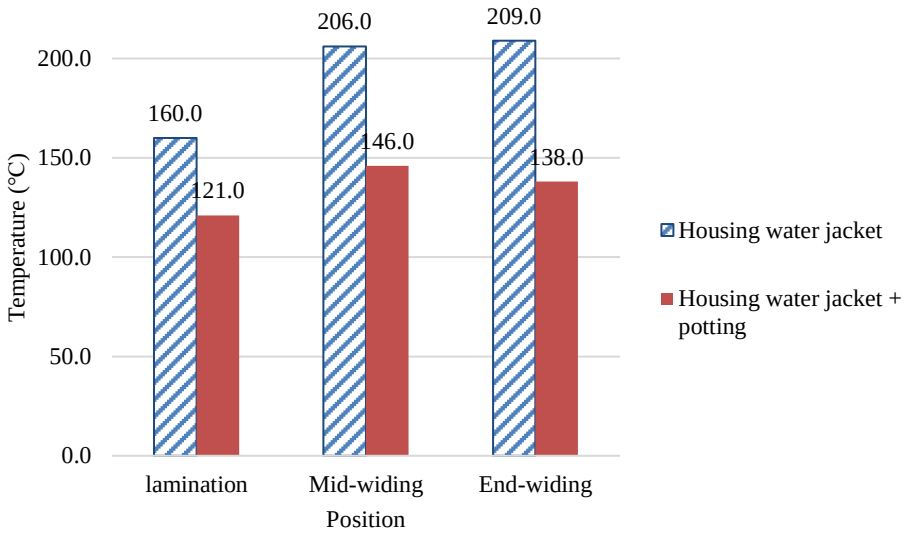


Fig. 6.15 Illustration of the potting improvement.

6.5.2.3 Conclusion

Based on the results, slot cooling proves to be an effective method for heat dissipation from the windings. This cooling technique involves immersing both the windings and stator laminations in a coolant. The presence of gaps in the slots or additional ducts in the stator provides direct channels for the coolant to dissipate heat. The advantage of this cooling approach has been confirmed through validation using the CFD method.

However, it is important to note that implementing slot cooling in practice can be relatively complex due to challenges related to sealing and precision. Ensuring proper sealing and achieving the required precision are key considerations when implementing this cooling solution in real-world applications.

Considering the primary objective of validating fault tolerance, the housing water jacket cooling system has been selected for the first prototype machine in this thesis due to its maturity and reliability. Additionally, this solution offers the advantage of interchangeability, allowing for easy extraction and replacement of individual segments. By utilizing the housing water jacket, the inner space can be kept simple, dry, and separate from the coolant. Furthermore, enhanced cooling is planned for implementation in future prototype.

6.5.3. Effect of thermal isolation

In general, every segment generates nearly equal loss in the healthy operation and similar temperature rise, while abnormal heat in faulty segment may damage other segments. To investigate the interaction between segments, a series of extra losses were added into a specific segment, to simulate the effect of SC segment on healthy segment.

The combination of housing water jacket and end-winding potting were selected for this case. The maximum temperature of SC segment and the minimum temperature of other segments were calculated and illustrated in *Fig. 6.16*. It can be found that the maximum temperature of faulty segment rises with the increase of extra losses, from 94.3℃ to 127.0℃. The minimum temperature from other segments is stable. The results can illustrate the relative thermal isolation between segments in case of SC fault.

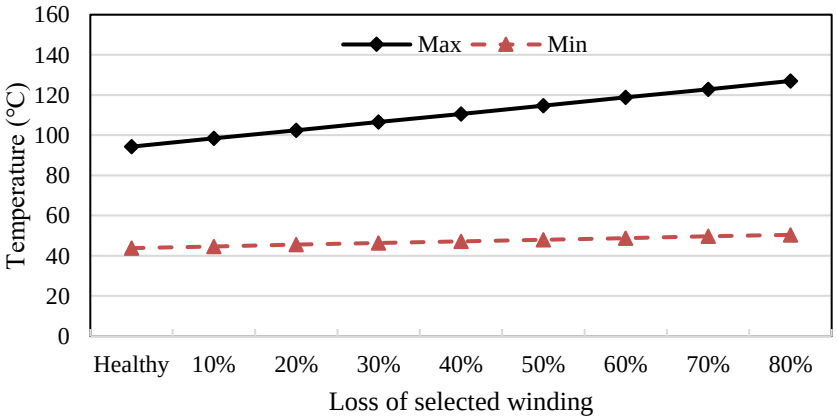


Fig. 6.16 Validation of thermal isolation.

6.6 Discussion

In this chapter, the fundamental background of thermal management was introduced, including the requirements of thermal management, limitation or selection of material, components of machine loss and cooling methods.

Based on varied cooling methods, results of thermal management can be calculated by LPTN or CFD. Slot cooling shows better cooling effect than housing water jacket. But, the latter methods could be improved comparable level, combined with end-winding potting.

For the modular triple three-phase machine, the presence of segment gaps in the stator did not affect the temperature rise. To simulate short-circuit in specific windings, extra loss was added. The results illustrate low effect between segments. This kind of effect can be regarded as thermal isolation. In the post-fault operation, it is feasible to operate continuously while one segment suffering damage of high heat.

Chapter 7 Prototype design and performance analysis

7.1 Introduction

Based on the results of electromagnetic, fault tolerant and thermal analysis, the machine was further designed for prototyping purpose. In this Chapter, more work was carried out to complete the detailed machine design. To achieve a comprehensive fault tolerant electrical machine, fault monitoring is a pillar to complete the design process. To support this high-speed machine, corresponding mechanical analysis is comparably critical, including fixation of PM and rotor dynamic.

7.2 Fault monitoring design

As is stated above, signal-based technique like MCSA allows fast diagnosis of all kinds of faults. Meanwhile, extra sensors were recommended for fault tolerant machine design, which could provide online testing during the operation rather than off-line investigation. Based on that, search coils and extra thermal sensors can provide direct results on operation monitoring.

7.2.1 Search coils

7.2.2.1 Configuration

As aforementioned, search coils are easy to be arranged in the stator slots, like general windings for monitoring potential faults. As shown in the *Fig. 7.1*, search coils were arranged for fault diagnosis in this case. There are 12 search coils designed to prognosis. 9 search coils were arranged in the wounded teeth like concentrated phase winding, and other three search coils were set in the segment gaps. Each search coil is independent with terminals coming out, and the turns for each coil is 5. The turns of search coil can reference the turns of phase winding and its back-EMF. The number of coil turns of every phase is 40 and its peak induced voltage is 320 V (at

11000 rpm). Then, the peak voltage of search coil could be estimated.

$$U_{search} = 320 \times 5/40 \ V = 40 \ V \tag{7.1}$$

To facilitate its preparation, the diameter of the coils can be minimized. The induced current flowing in the search coil is assumed to be a normal sensor current, which can be acquired by an oscilloscope during operation.

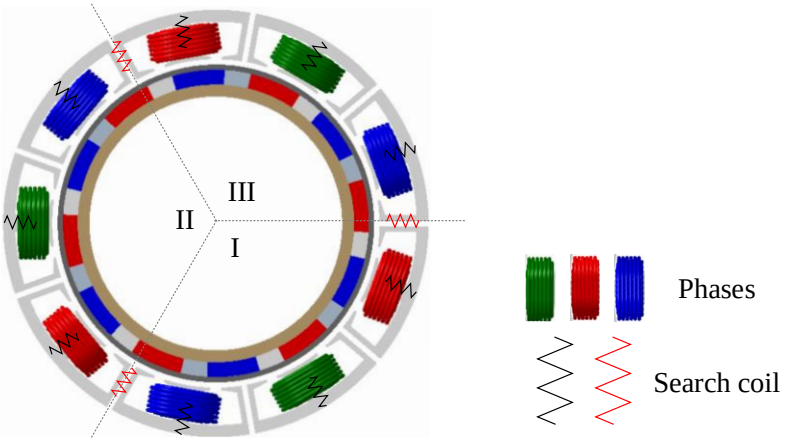


Fig. 7.1 The arrangement of search coil for the prototype machine.

7.2.2.2 Results

For healthy electrical machine, the rotating PM assembly will induce a sinusoidal voltage in every search coil during rotating operation. Similar to the back-emf of the phase winding, the waveform of search coils in each module (M1, M2 or M3) resembles that of a three-phase winding. Besides, the curves of U/V/W of in every module are almost corresponding and overlapped with other modules. One case result of operation speed at 11000 rpm is shown in *Fig. 7.2*.

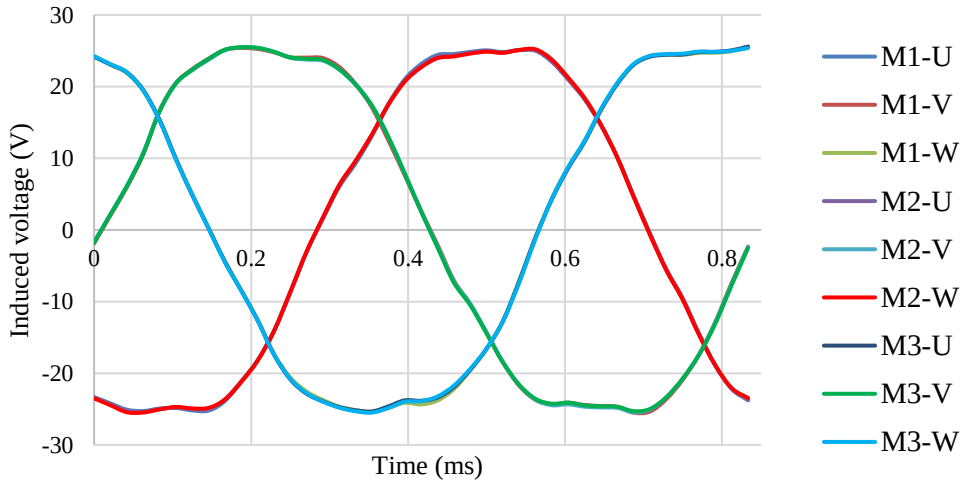
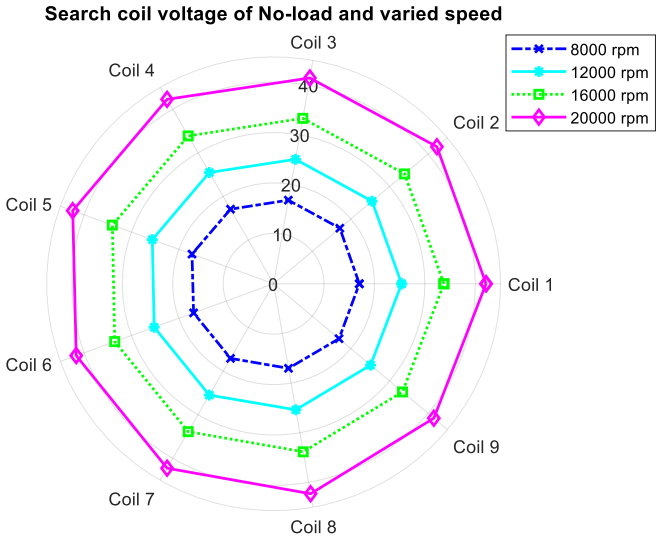
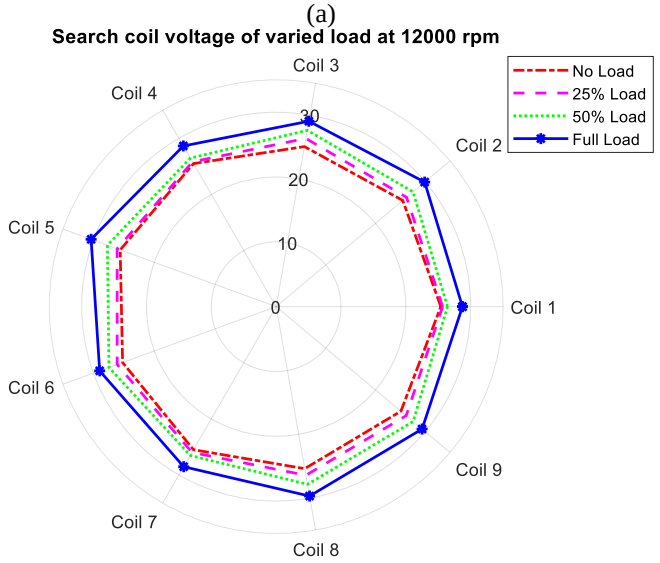


Fig. 7.2 Induced voltage in search coils with electrical machine speed at 11000 rpm.

In this electrical machine, there are nine search coils embedded in the modular machine. Radar maps can be used to illustrate the magnitude of voltage of each search coil, as shown in *Fig. 7.3*. The induced voltage in search coils is proportion to the rotating speed, as shown in *Fig. 7.3* (a). Due to the armature reaction, the flux generated by the phase windings can increase the peak value of induced voltage in search coil, with the increasing of load, as shown in *Fig. 7.3* (b). These results can be a benchmark to evaluate potential faults in winding, demagnetization or eccentricity faults.



(a)



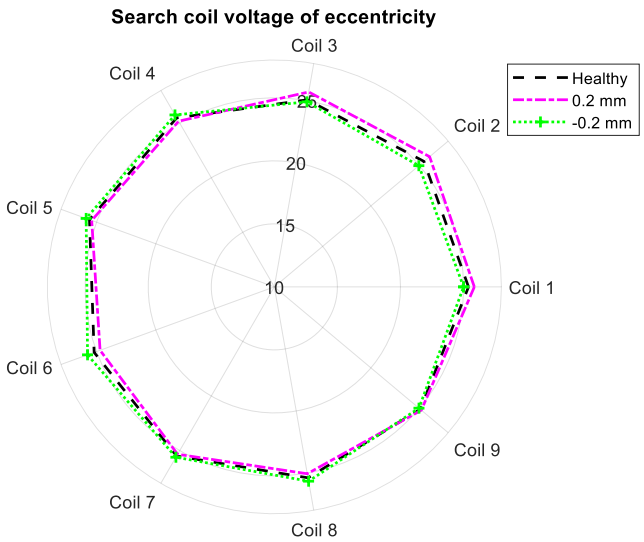
(b)

Fig. 7.3 Voltage of search coils (a) No-load at varied rotor speed (b) Varied load at 11000 rpm.

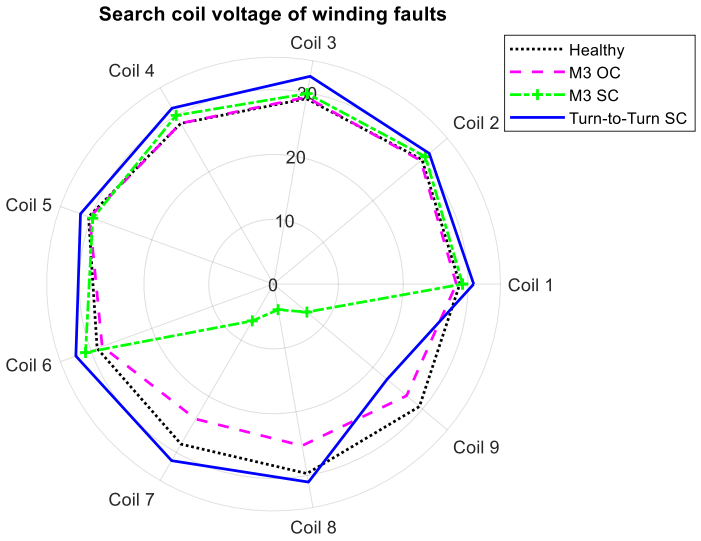
The induced voltage of search coils is independent to the parameters of machine. Then, the voltage distribution of search coils under varied scenarios was conducted.

Faults of static eccentricity were injected in this topology. A 0.2 mm static eccentricity was added in the positive and negative specific axis (along search coil 5), respectively, as shown in *Fig. 7.4* (a). The eccentricity can change the distance between PMs and search coils, and the magnitude of induced voltage can be changed based on the value of eccentricity. When the X-axis displacement was 0.2 mm, the voltage magnitude of coils 1, 2 and 3 increased, while the values of 4, 5, 6 and 7 decreased. Compared with the healthy operation, the distribution of induced voltage in the nine search coils exhibited a specific directional shift. This kind of change can be utilized to locate the direction and value of eccentricity.

Similarly, effects of varied winding faults were investigated. Module 3 (M3) was selected as the set to inject winding faults. The results of OC and SC were shown in *Fig. 7.4* (b). The values of search coils 7, 8 and 9 exhibit different degree drop but the trends were totally different. In the case of OC, the values exhibit a slight drop due to the absence of winding excitation. Nevertheless, in the case of SC, the counteract of flux by PM and SC windings induces lower voltage. Values in search coils 7, 8 and 9 are close to zero. In the fatal winding faults, turn-to-turn SC, a single-turn SC was added in the Phase C of Module 3. Accordingly, a drop of search coil 9 can be utilized to recognize the fault.



(a)

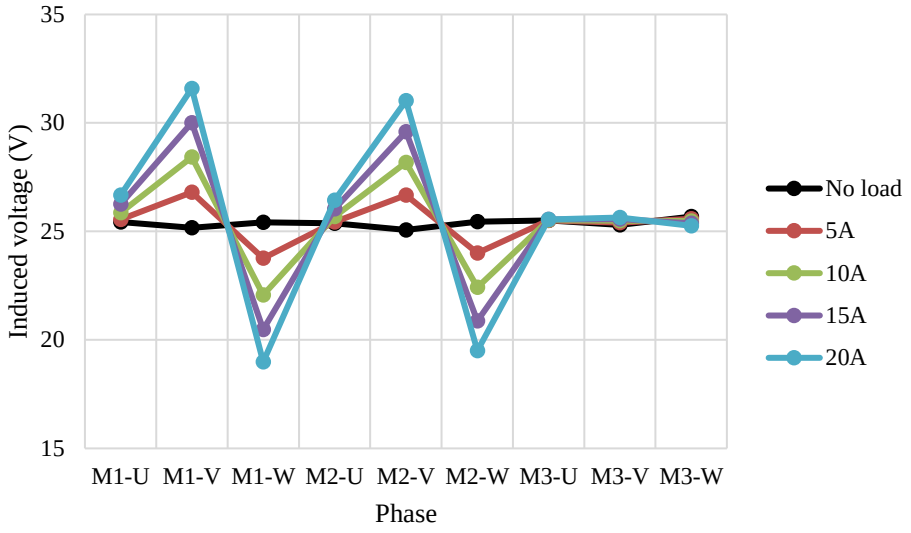


(b)

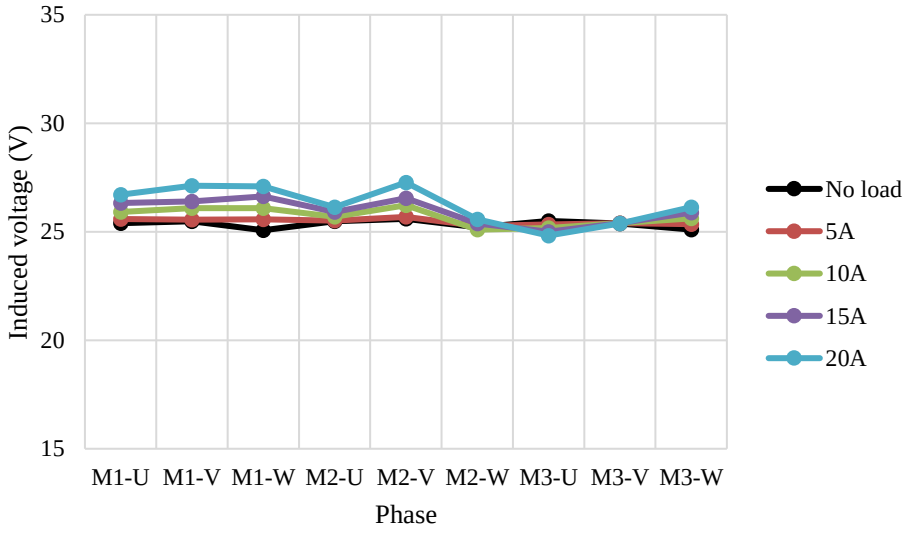
Fig. 7.4 The induced voltage in the varied faults (a) Eccentricity. (b) Winding faults in Module 3: open-circuit, phase-to-phase SC and turn-to-turn SC.

It is worth mentioning that the induced voltage in faulty scenarios is affected by the direction of rotating. With the armature reaction, the induced voltages in search coils are determined by multiple parameters. Besides the rotating speed and phase current, the rotating direction affect the induced voltage as well.

A series of OC faults were compared under 11000 rpm, while the phase current of healthy parts was varied from zero to 20 A. The clockwise or anticlockwise rotation exhibit different effect on the search coils, as shown in *Fig. 7.5*. The plots depict the peak value of induced voltage, in every phase with OC in M3 (M3-U, M3-V and M3-W). Thanks to magnetic isolation, the value in M3 remains relatively stable regardless of varying current in other phase windings. However, due to the effects of armature reaction and initial position of PMs, clockwise rotation generates varying magnitudes and high fluctuations in search coils located in healthy windings. In contrast, induced voltage by anticlockwise rotation is relatively stable.



(a)



(b)

Fig. 7.5 Peak value of induced voltage in search coil (a) clockwise (b) anticlockwise.

Above all, the results of search coils can provide an online method for fault diagnosis. Their results can be used to analyse and quantize the faults. Based on the results under faulty scenarios, the induced voltage is sensitive to the phase current, then this method is recommended for no-load diagnosis.

7.2.2 Thermal sensors

During the electrical machine operation, the hotspots of temperature always appear in the end winding and middle of active winding. Therefore, resistance temperature

detectors (RTDs) were embedded in the end-winding and middle active winding of every segment, as shown in *Fig. 7.6*. RTDs are arranged to monitor the real-time temperature of windings during operations. Compared with healthy scenarios, any unusual temperature rise can be recognised as a sign of winding fault, especially turn-to-turn SC. To investigate the temperature difference in the end winding on both sides, RTDs were embedded in the end winding and arranged alternately.

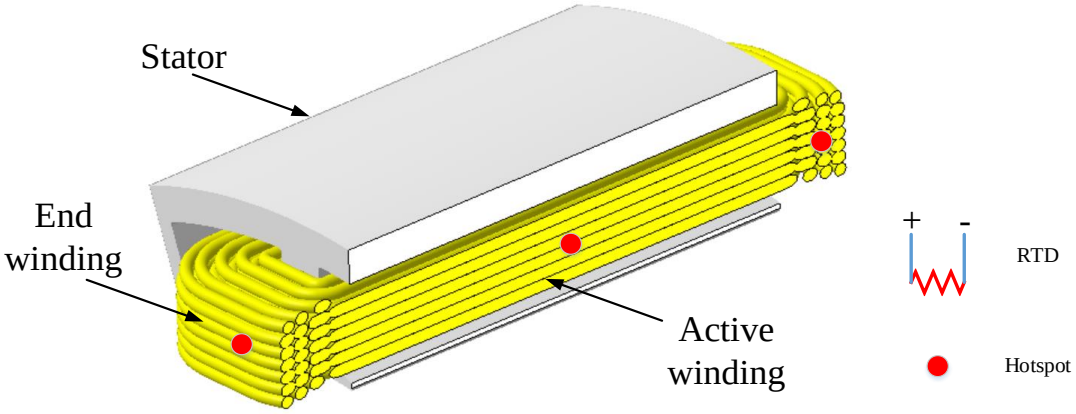


Fig. 7.6 Schematic of hotspot in the windings.

7.3 Mechanical analysis

For the design of a high speed electrical machine, it involves a multi-physics design process rather than just an electromagnetic problem, even mechanical issues show more challenges than electromagnetic side. Besides the eccentricity, mechanical issues mainly locate in the rotor, such as PM retention, rotor strength, rotor dynamic and selection of bearing pairs.

7.3.1. Rotor stress

The surface mounted PM machine has been selected for this machine. The main purpose of rotor sleeve is to maintain the PM contacted with rotor to transfer torque, despite high speed and centrifugal force.

Compared to an alloy sleeve, a carbon fibre sleeve was selected as the candidate due to its light weight and non-magnetic properties, which avoiding eddy current loss. Carbon fibre is a common orthotropic material, meaning it exhibits different mechanical properties in different directions, as shown in *Fig. 7.7*. The elastic module E and mechanical stress $\boldsymbol{\sigma}$ is excellent in direction 3.

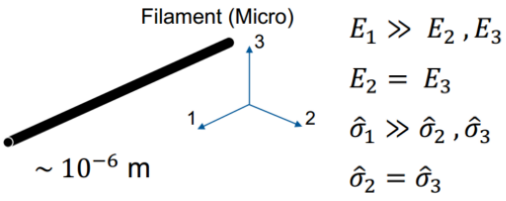


Fig. 7.7 Schematic of orthotropic of carbon fibre.

The pre-compress carbon fibre sleeve is manufactured by filament. With the fixation of carbon fibre, the rotor assembly is incorporated by sleeve, PM and rotor iron from outside to inside, as shown in *Fig. 7.8*.

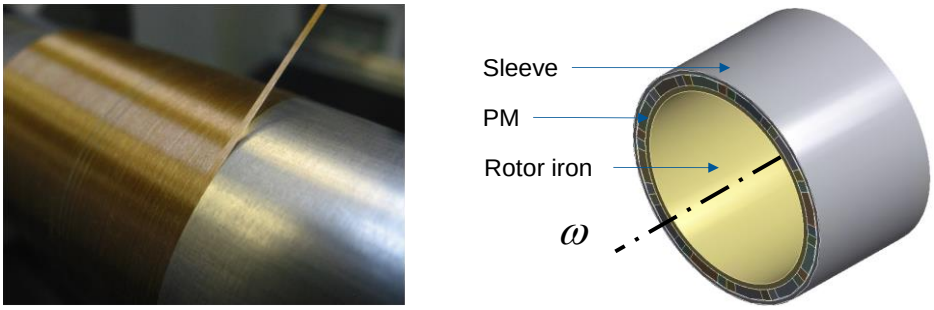


Fig. 7.8 Rotor assembly of surface mounted PMSM.

7.3.1.1 Theoretical method

From the view of electromagnetic, thick carbon fibre can increase the thick of air gap which will decrease flux density in the air gap. The main trade-off in this section is to determine the proper thickness of the carbon fibre to meet the demand of mechanical stress. The equation between stress and strain of carbon sleeve has been defined blow.

$$\begin{bmatrix}\sigma_r \\ \sigma_\theta\end{bmatrix} = \begin{bmatrix}Q_{11} & Q_{12} \\ Q_{12} & Q_{22}\end{bmatrix}\begin{bmatrix}\varepsilon_r \\ \varepsilon_\theta\end{bmatrix} \tag{7.2}$$

$$\begin{cases} Q_{11} = \dfrac{s_{22}}{s_{11}s_{22} - s_{12}^2}, s_{11} = \dfrac{1}{E_r} \\ Q_{22} = \dfrac{s_{21}}{s_{11}s_{22} - s_{12}^2}, s_{22} = \dfrac{1}{E_\theta} \\ Q_{11} = \dfrac{-s_{12}}{s_{11}s_{22} - s_{12}^2}, s_{12} = \dfrac{-v_{\theta r}}{E_r} = \dfrac{-v_{r\theta}}{E_\theta} \end{cases} \tag{7.3}$$

Where r, θ are the radial and circumferential directions, E the Young's modulus, v the Poission ratio, ε the strain and σ the stress.

The 3D problem could be simplified as 2D model analysis. To maintain the carbon fire safe, mechanical stress of every point in sleeve should meet a balance.

Considering the rotation, the differential equation of 2D model can be concluded here. Based on the preload force, every point in carbon fire has a deformation in radial and circumferential directions during the rotating operation.

$$\frac{d\sigma_r}{dr}+\frac{\sigma_r-\sigma_\theta}{r}+\rho\omega^2 r=0 \tag{7.4}$$

Where ρ is density of carbon fibre and ω the rotation speed. Replacing the strain in radial and circumferential, the axial deformation u_r, stress of axial σ_r and circumferential σ_θ can be solved.

$$u_r=Ar^k+Br^{-k}-\frac{(1-v_{\theta r}v_{r\theta})}{9E_r-E_\theta}\rho\omega^2 r^3 \tag{7.5}$$

Where ***A*** and ***B*** are the coefficients of the boundary conditions, which can be calculated by using existing definitions. E_r and E_θ are the Young's modulus of radial and circumferential directions.

$$K=\sqrt{E_\theta/E_r} \tag{7.6}$$

Then, radial and circumferential stress of any point of carbon sleeve can be calculated.

$$\sigma_{r1}=\frac{E_rK^2r^{k-1}(A-Br^{-2k})+E_rv_{\theta r}r^{k-1}(A+Br^{-2k})}{1-v_{\theta r}v_{r\theta}}-\frac{(3+v_{\theta r})}{9-K^2}\rho\omega^2r^2 \tag{7.7}$$

$$\sigma_{\theta1}=\frac{E_\theta r^{k-1}(A+r^{-2k})+E_\theta v_{r\theta}r^{k-1}(A+Br^{-2k})}{1-v_{\theta r}v_{r\theta}}-\frac{(3+v_{r\theta})}{9-K^2}\rho\omega^2r^2 \tag{7.8}$$

$$\begin{cases}\sigma_r(r=r_1,\omega)=0\\ \sigma_r(r=r_2,\omega)=0\end{cases} \tag{7.9}$$

$$\begin{cases}A=\dfrac{3+v_{\theta r}}{9-K^2}\dfrac{\left(r_1^{3+k}-r_2^{3+k}\right)\left(r_1^{2k}-r_2^{2k}\right)}{r_1^{k-3}}\dfrac{1-v_{\theta r}^2}{E_r(k+v_{\theta r})r_1^{k-1}}\rho\omega^2r_1^2\\ B=\dfrac{3+v_{\theta r}}{9-K^2}\dfrac{1-v_{\theta r}^2}{E_r(-k+v_{\theta r})r_1^{k-1}}\dfrac{r_1^{3+k}r_2^{2k}-r_2^{3+k}r_1^{2k}}{r_1^{-k-3}\left(r_2^{2k}-r_1^{2k}\right)}\rho\omega^2r_1^2\end{cases} \tag{7.10}$$

Above all, the specific point of sleeve could by analysed by theoretical methods above. The maximum mechanical stress appears in the contact face of carbon sleeve and permanent magnet because of the friction force between them.

7.3.1.2 FEA method for mechanical analysis

To get and view the overall deformation and mechanical stress directly, finite element analysis (FEA) was utilized for this case. Because of the symmetrical topology, one pole model was selected. Based on the ANSYS Workbench, a 2D static structural analysis was carried out, as shown in *Fig. 7.9*. By assigning boundary conditions, a rotor unit was created to investigate the mechanical performance. Unlike the materials of rotor iron and permanent magnet, properties of carbon fibre has more parameters and listed in Table 7.1. As a common orthotropic material, its Young's Modulus in X direction is very high, and it was wound along the circumferential direction of the rotor.

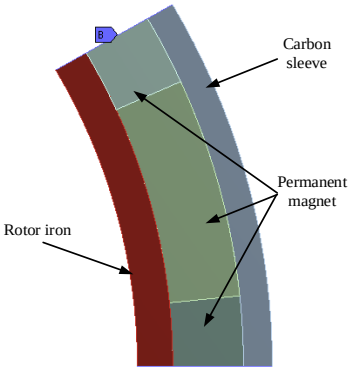


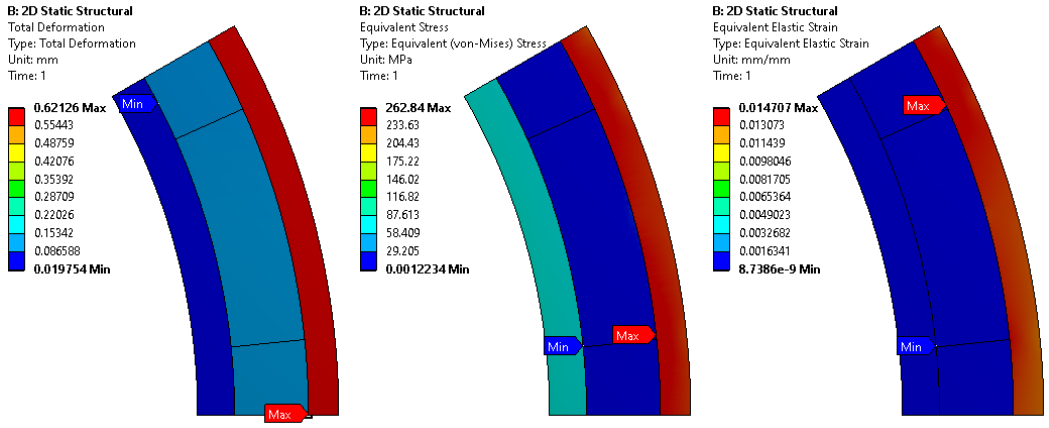
Fig. 7.9 Model created for mechanical analysis.

Table 7.1 Properties of selected carbon fibre.

Property	Value	Unit
Density	1800	Kg/m^3
Young's Modulus X direction	2.3E+11	Pa
Young's Modulus Y direction	2.3E+10	Pa
Young's Modulus Z direction	2.3E+10	Pa
Poisson's Ratio XY	0.2	-
Poisson's Ratio YZ	0.4	-
Poisson's Ratio XZ	0.2	-
Shear Modulus XY	9000	MPa
Shear Modulus YZ	8214.3	MPa
Shear Modulus XZ	9000	MPa

The deformation, equivalent stress and elastic strain distribution can be generated, as

shown in *Fig. 7.10* The contour maps exhibit the overall results. The maximum values of these outputs are 0.62 mm, 262.84 MPa and 0.014, respectively. All the results are far below the allowable values.



(a) (b) (c)

Fig. 7.10 FEA results at 20000 rpm. (a) Deformation. (b) Equivalent stress. (c) Equivalent elastic strain.

The contour map exhibited the overall results, for my concern, the maximum stress of sleeve is 241 MPa, far below the permissible stress, 1000 MPa.

7.3.2. Modal analysis

Resonance is a phenomenon that can appear in mechanical parts or assemblies, and it can be described as sensitivity to a certain vibration frequency. Resonance occurs when a natural frequency is at or close to a forcing frequency, such as rotor speed. Although resonance should be rare, certain machinery types are very prone to resonant whirl.

To ensure the machine operate safely, modal analysis is a critical check for the whole speed range. The vibration frequency or the corresponding critical speed should be far away from the operating speed point. The main target of this analysis is to check the frequency and critical speed by a study of the dynamic properties in the frequency domain.

Similarly, FEM method was adopted to carry out modal analysis. As shown in *Fig. 7.11*, a 3D model was created. The rotating assembly is consisted of rotor shaft, rotor iron, PM and bearing pair. The machine rotor is a simple supported structure. Then, in the rotor design, the length of bearing pair is an important variable. Besides, to

achieve a high stiffness of shaft, this distance between bearings should be as short as possible. Meanwhile, hollow shaft can increase the stiffness of rotor shaft.

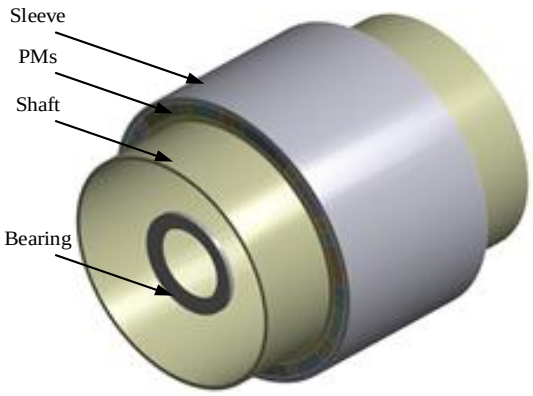


Fig. 7.11 Model created for mechanical analysis.

The modal analysis was carried out. The first four modes were extracted and listed in *Fig. 7.12*. The frequency and critical speed are listed in Table 7.2. The first and second nature frequencies could be neglected, because critical speed are close to zero. The third frequency is 681 Hz, which corresponding critical speed is about 40860 rpm. The requirement of maximum speed for this machine is 20000 rpm, which is much less than the critical speed. Therefore, resonance could be avoided.

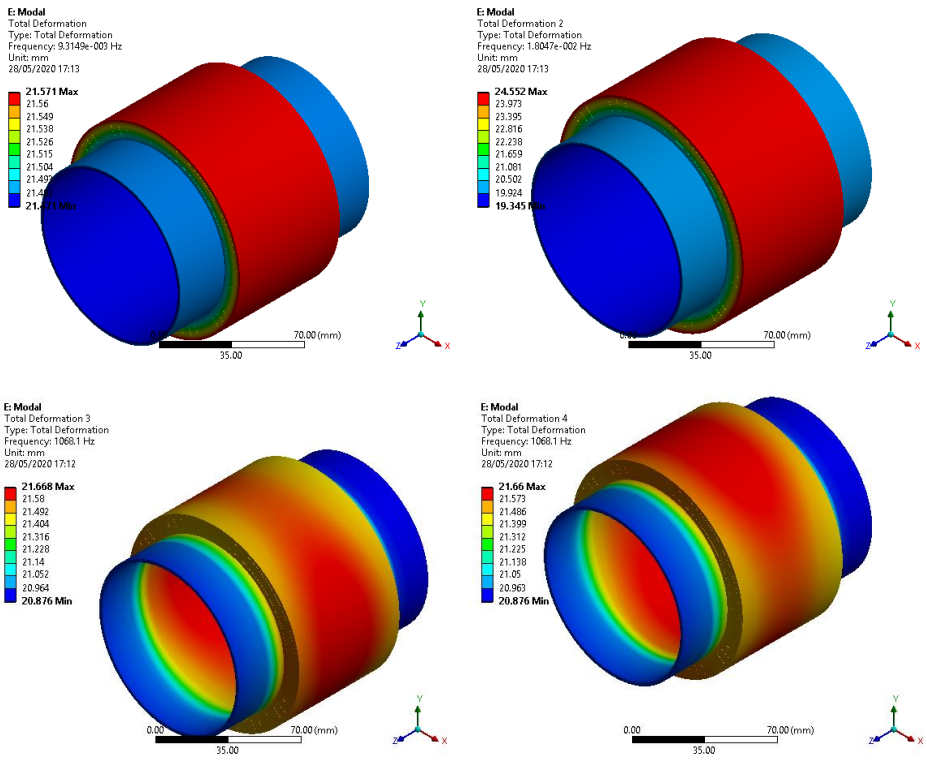


Fig. 7.12 Results of modal analysis.

Table 7.2 Frequency and critical speed.

Mode	Frequency (Hz)	Critical Speed (rpm)
1	0	0.6
2	2.1e-002	1.3
3	681.0	40860
4	681.0	40860

Campbell diagram has been extensively utilized to illustrate the operation frequency and critical speed. As shown in *Fig. 7.13*, the horizontal axial is the operation frequency related to the rotating speed, from zero to the maximum. For this case, the maximum frequency of machine is 2000 Hz. The black slope line represents the machine, starting from static to maximum. These horizontal lines in the top are the natural frequencies. There is no cross between machine operation line and natural frequency until the maximum speed.

In all, this machine can operate safely, from the perspective of modal analysis.

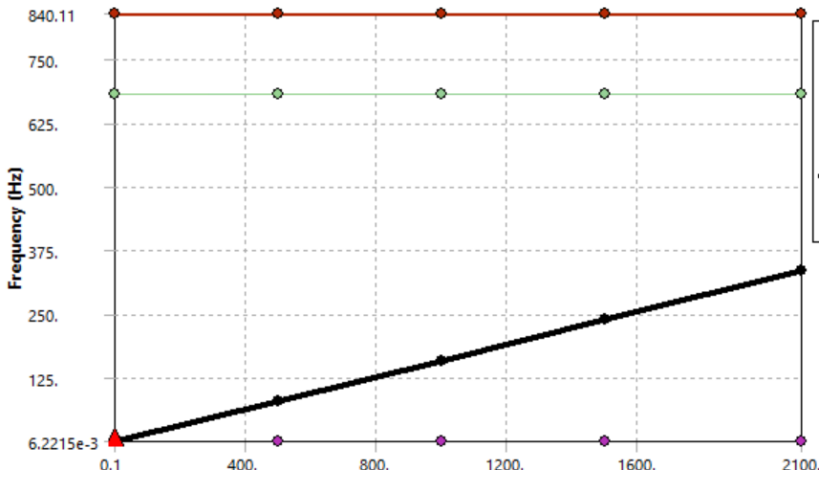


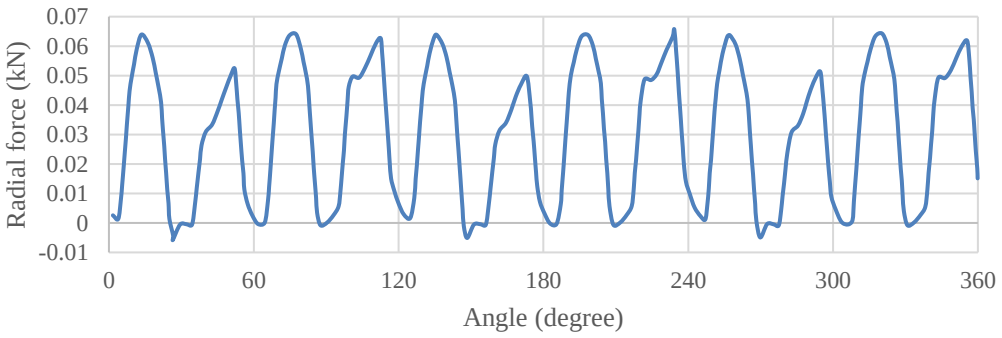
Fig. 7.13 Campbell diagram of first four critical speeds.

7.4 Electromagnetic force

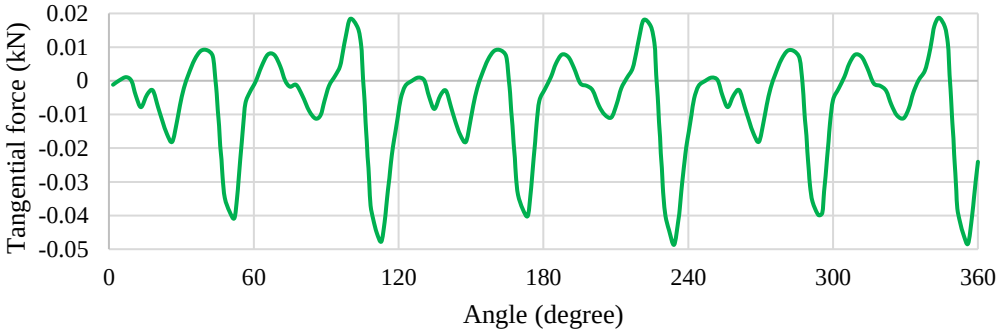
As introduced, noise and vibration have been regarded as an important design target. This issue can be intensified by a combination of excitations (electromagnetic forces) and the structural dynamics of the motor (analysed in last section). The electromagnetic force is essential to investigate which can be divided into stator and rotor. The results of investigate can support the selection of bearings, especially the faulty scenarios.

7.4.1 On-load electromagnetic force

As shown in *Fig. 7.14*, the axial force, comprising both axial and tangential components, varies due to changes in the rotor position. The peak value is about 67 N in the radial direction. The magnitude value can be referenced for bearing selection, as continuous load. In general, this force can be ignored due to symmetrical design in the healthy operation.



(a)



(b)

Fig. 7.14 Electromagnetic force on rotor at initial position. (a) Radial force on rotor. (b) Tangential force on rotor.

7.4.2 Rotor force under faulty modes

As shown in *Fig. 7.15*, the radial force under faulty scenarios, open-circuit and short-circuit, increase dramatically. To assume a fault occurred in the machine, module 3 was set as OC or phase-to-phase SC fault. Due to the winding arrangement, the peak value of radial force increase from benchmark 67 N to 167.6 N and 746.5 N, respectively.

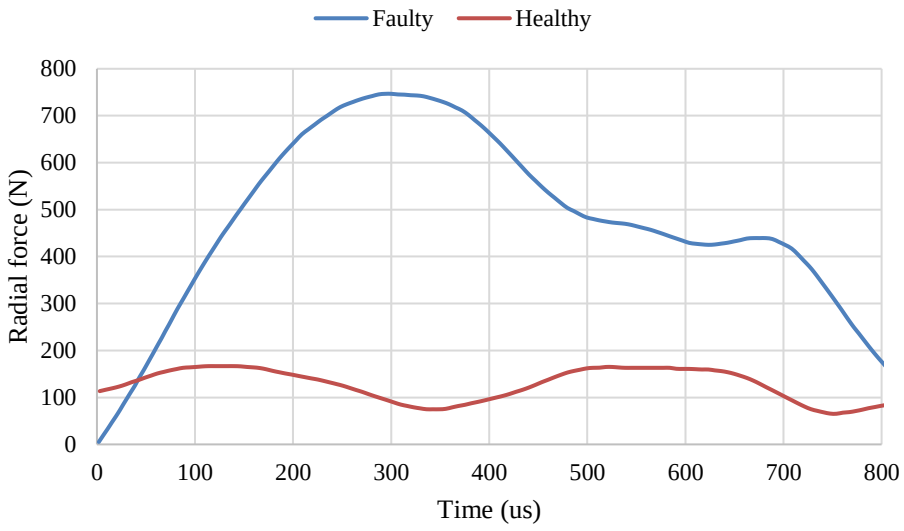


Fig. 7.15 Radial force under faulty operation.

The selection of bearing is determined by the type of load on the rotating shaft. As analysed above, the dominant load on the rotor shaft is radial force. The connection between rotor shaft and prime mover is achieved by flexible shaft coupling. Then, the axial force along the shaft can be neglected. The single row angular contact ball bearing meets the requirement of bearing. This kind of bearings are designed to accommodate radial and axial loads acting simultaneously and at high-speed operation. Based on this results and dimension, SKF 7010 bearings were selected for this machine.

7.5 Mechanical design

Based on the electromagnetic topology and selected cooling method, the corresponding mechanical design was carried out, focusing on the housing and interface design.

7.5.1 Assembly of segment

In this case, there are nine independent segments. To achieve a precise location and stable installation, design of fins on housing are adopted for accurate positioning. In the initial design, all the segments were inserted in the housing directly for interference fit. But this process may damage the housing due to difference of material property. The lamination is made of steel, but the motor housing is made of aluminium. These material properties are quite different on hardness and stiffness. An extra steel sleeve was design to assemble all the nine segments in advance, as

shown in *Fig. 7.16*. The thickness of this steel sleeve is 3 mm, concerning the mechanical strength.

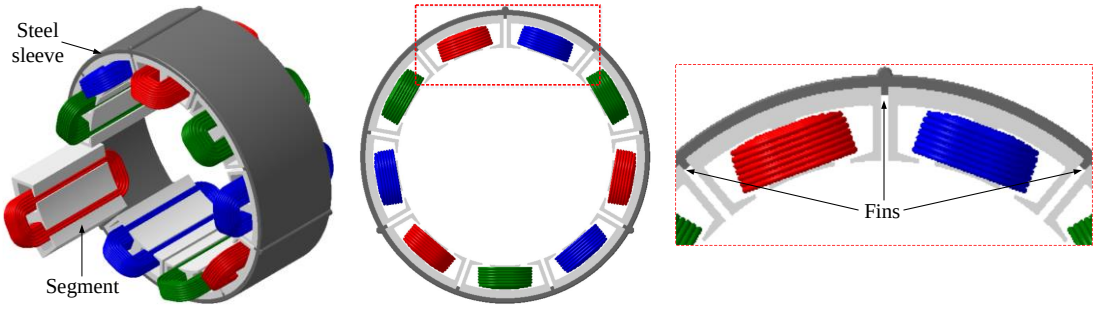


Fig. 7.16 Steel sleeve for assembling the segments.

7.5.2 Cooling structure

For the first prototype, housing jacket cooling was selected for the prototype machine (35 kW) due to the manufacturing readiness level, to validate the novelty in FT improvement. For the future prototype, the improvement of winding potting will be utilized to pursue higher performance (50 kW).

As shown in *Fig. 7.17*, the cooling path can be formed by two-layer structure, inner housing and outer housing. To improve the thermal management, fins were designed on the surface of outer housing. The inlet and outlet of coolant locate in the outer housing.

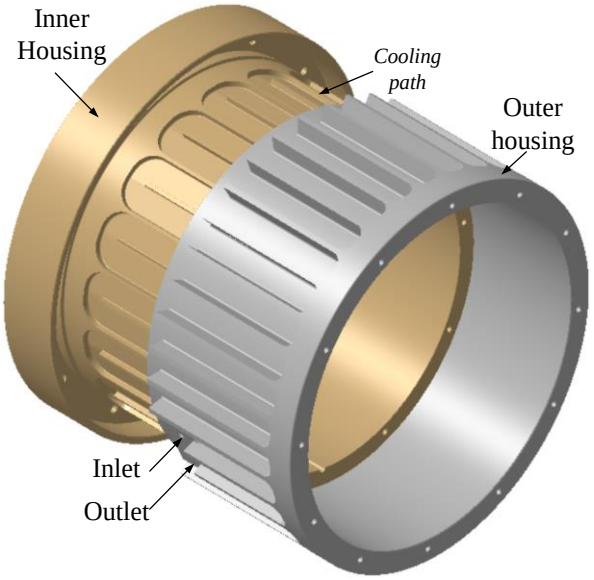


Fig. 7.17 Structure of housing for water jacket.

7.6 Interface design

The interface design of electrical machine consists of mechanical, electrical and cooling interface.

7.6.1 Mechanical interface

The schematic connection of testbed, flange and prototype machine is shown in *Fig. 7.18*. The mechanical interface includes the connection with test rig and coupling, then its dimensions are determined by the rig flange and shaft couplings. The electrical machine is aligned in the test rig with blots and nuts. The holes in the housing of electrical machine meet the dimension of flange. Besides, the shaft is connected with prime mover with couplings. Bellows coupling is a flexible coupling which have an excellent torsional rigidity in order to accurately transmit the velocity, angular position, and the torque. It was selected for this test rig. The setup of test rig is illustrated in Chapter 8.

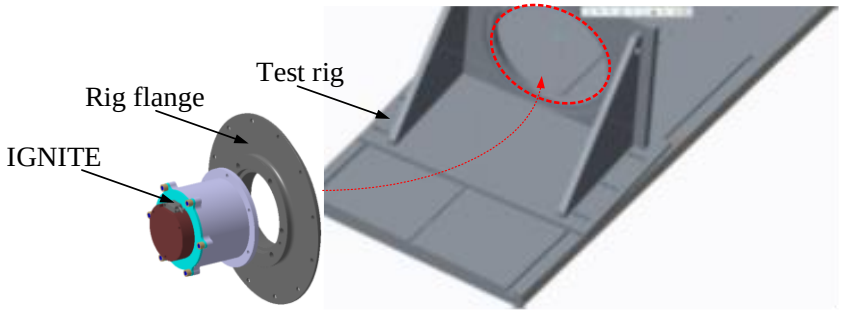


Fig. 7.18 Schematic of testbed and flange.

7.6.2 Electrical interface

There are 9 windings (3 modules), 12 search coils, 18 RTDs and 1 resolver embedded in this machine. For the concern of fault tolerance, three independent receptacles for three modules are necessary to provide electrical isolation. To make the connections flexible, all the leads of phase winding are connected to the receptacle rather than neutral points inside of the machine. Then, there are six contacts in every receptacle. With regard to the size of the contact in the receptacle, it is determined by the operating current.

The selection of connector is based on the quantity of pins and ampere ratings. To prepare the potential faulty test, this contact could be type 8, which max current rating per contact is 45 A. To avoid electromagnetic interference (EMI) between phase winding and sensors, connectors for sensors are independent. The contact of

for sensors can be type 22, which max current rating per contact is 3 A. The definitions of electrical interface of phase windings and sensors are listed in Table 7.3 and Table 7.4.

Table 7.3 Definition of electrical interface of windings.

No.	Position	Definition	Description	Contact
1	M1	A+	Independent receptacle for Modular 1 (M1)	8
2		A-		
3		B+		
4		B-		
5		C+		
6		C-		
1	M2	A+	Independent receptacle for Modular 2 (M2)	8
2		A-		
3		B+		
4		B-		
5		C+		
6		C-		
1	M3	A+	Independent receptacle for Modular 3 (M3)	8
2		A-		
3		B+		
4		B-		
5		C+		
6		C-		

Table 7.4 Definition of electrical interface of embedded sensors.

No.	Position	Definition/position	Description	Contact
1	Resolver	R1	Ref+	22
2		R2	Ref-	
3		S1	Sin+	
4		S2	Sin-	

5		S3	Cos+	
6		S4	Cos-	
1	Search coil	M1-U+	For phase U in M1	22
2		M1-U-		
3		M1-V+	For phase V in M1	
4		M1-V-		
5		M1-W+	For phase W in M1	
6		M1-W-		
7		M2-U+	For phase U in M2	
8		M2-U-		
9		M2-V+	For phase V in M2	
10		M2-V-		
11		M2-W+	For phase W in M2	
12		M2-W-		
13		M3-U+	For phase U in M3	
14		M3-U-		
15		M3-V+	For phase V in M3	
16		M3-V-		
17		M3-W+	For phase W in M3	
18		M3-W-		
19		SC1+	Three search coil were arrange between three modules	
20		SC1-		
21		SC2+		
22		SC2-		
23		SC3+		
24		SC3-		
1	RTD	RTD-U1+	Embedded in the middle of winding in the slot per phase	22
2		RTD-U1-		
3		RTD-V1+		
4		RTD-V1-		

5	RTD-W1+		
6	RTD-W1-		
1	RTD-U2+		
2	RTD-U2-		
3	RTD-V2+		
4	RTD-V2-		
5	RTD-W2+		
6	RTD-W2-		
7	RTD-U3+		
8	RTD-U3-		
9	RTD-V3+		
10	RTD-V3-		
11	RTD-W3+		
12	RTD-W3-		
13	RTD-U1-e+		
14	RTD-U1-e-		
15	RTD-V1-e+		
16	RTD-V1-e-		
17	RTD-W1-e+		
18	RTD-W1-e-		
19	RTD-U2-e+		
20	RTD-U2-e-	Embedded in the end winding per phase	22
21	RTD-V2-e+		
22	RTD-V2-e-		
23	RTD-W2-e+		
24	RTD-W2-e-		
25	RTD-U3-e+		
26	RTD-U3-e-		
27	RTD-V3-e+		
28	RTD-V3-e-		

29	RTD-W3-e+
30	RTD-W3-e-

The arrangement of pins for sensors are flexible, while the size of pin can be as small as possible. The section of selected receptacle for phase and sensors are shown in *Fig. 7.19*.

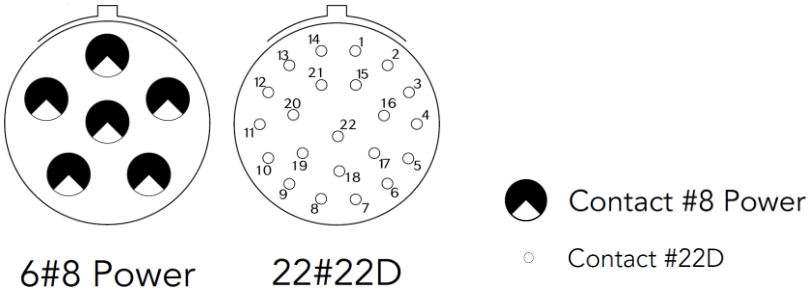


Fig. 7.19 Candidates of feasible layout of receptacles for phase and sensor connector.

7.6.3 Cooling interface

For cooling interface, 6 mm push-in connectors are mounted on the outer housing for inlet and outlet, as shown in *Fig. 7.20*. The size is close to the cooling path of water jacket. The similar section area can avoid pressure drop of coolant. It is flexible to push-in and pull-out during the test, while its pressure ranges of up to 14 bar.



Fig. 7.20 Interface of inlet and outlet for machine cooling.

7.7 Conclusion

Based on the candidate of topology, final design of this electrical machine was carried out in this chapter. To achieve a thorough high-reliability electrical machine, fault monitoring design was completed, based on extras sensors, such as search coils and RTDs. All the sensors can provide real-time results to evaluate the potential symptom of faults.

Mechanical analysis of this machine is focusing on rotor stress and modal analysis, due to the high speed operation. The proper thickness of carbon fibre sleeve was

checked. Loads on the rotor shaft have been investigate for the bearing selection. Based on these results, detailed considerations for mechanical design and assembly were carried out. To ensure the design of electrical isolation, independent electrical interfaces are highlighted.

Based on these details, machine can be manufactured for prototyping.

Chapter 8 Prototyping and experimental validation

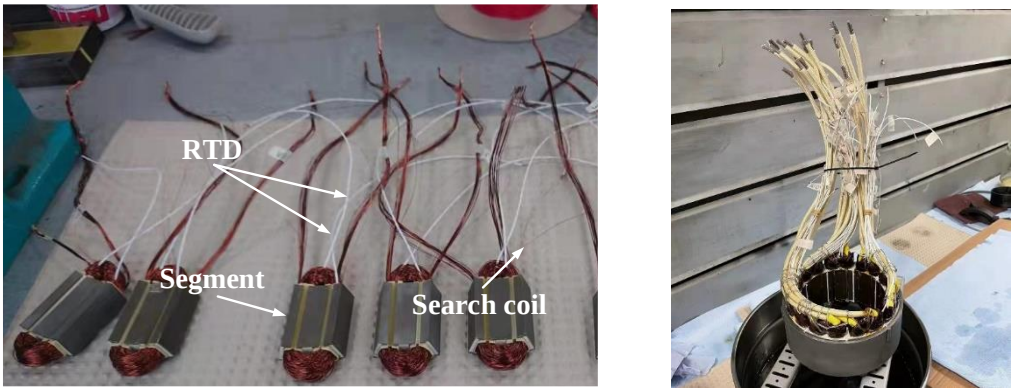
8.1 Introduction

All the practical work was introduced in this chapter. Based on the modular design, all the segments were manufactured and assembled independently. After the assembling, fundamental static parameters were measured. A comprehensive test was carried out. Based on the healthy operation, the combinations of faulty scenarios were checked.

8.2 Manufacturing and Assembly

8.2.1 Stator assembly

Firstly, the winding wires meet the standard of IEC 60317, class 200, which coating is based on polyamide-imide resin. Class 200 is a thermal class that requires a minimum temperature index of 200 and a heat shock temperature of at least 220 °C. Due to modular design, every stator segment was manufactured independently. Besides the phase windings, extra sensors were embedded in every segment, such as search coils and RTDs. After that, all the nine segments were mounted in the steel sleeve as an integrated stator assembly, as shown in *Fig. 8.1*.



(a) (b)

Fig. 8.1 Schematic of search coils and resistance temperature detectors (RTDs) in (a) segments and (b) Stator assembly.

Based on the illustration in Chapter 7.2.2 and 7.3.2, a detailed layout of temperature sensors is shown in *Fig. 8.2*. Housing water jacket has been designed for thermal management of this prototype machine. An asymmetrical temperature distribution can be predicted in the machine during the operation in some extent. Phases in module 1 are general cooler than other phases, because they are much closer to inlet than other phases. During the test, the results of this potential issues will be recorded.

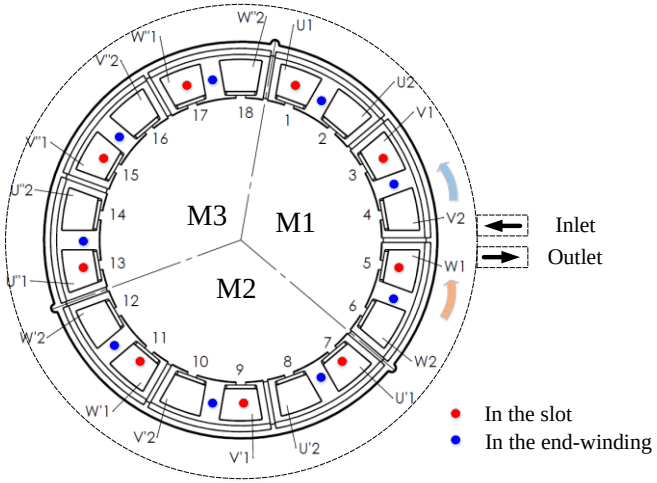


Fig. 8.2 Distribution of temperature sensors in the prototype machine.

8.2.2 Rotor assembly

As shown in *Fig. 8.3*, a stepped shaft was designed and manufactured, considering the interface of coupling, bearing pairs and resolver. Rotor consists of carbon fibre sleeve, permanent magnet array and back iron.

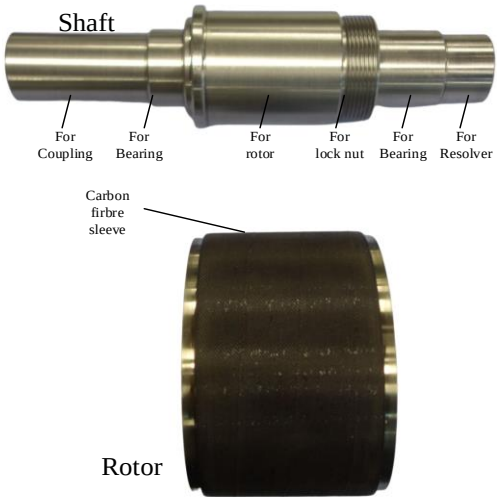


Fig. 8.3 Rotor shaft and rotor assembly

After assembly of rotor, check of static and dynamic balancing is essential work to avoid noise and vibration during the rotating. This check can be completed on specific equipment.

8.2.3 Housing

Housing design for this prototype machine includes the design of cooling path and interfaces of mechanical and electrical socket. For the thermal design, cooling path was milled on the surface of inner housing, and fins on the out surface of outer housing. The assembly of stator and housing is shown in *Fig. 8.4*.

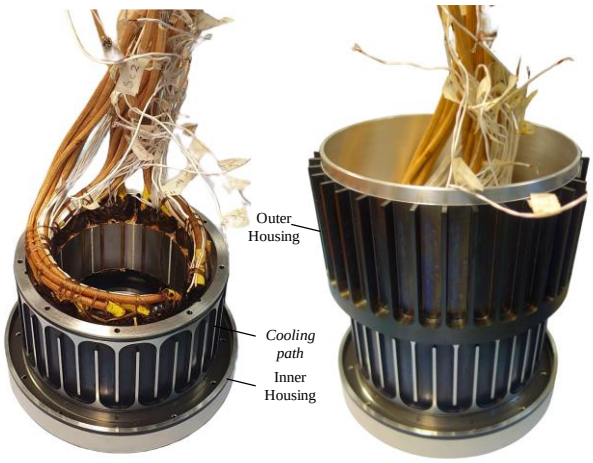


Fig. 8.4 Assembly of stator and housing.

8.2.4 Overall structure and assembly

As shown in *Fig. 8.5*, the prototype machine was assembled completely. There are three independent connectors for windings of triple three-phase. To avoid potential

electromagnetic interference, other pins of sensors were arranged in small connectors.

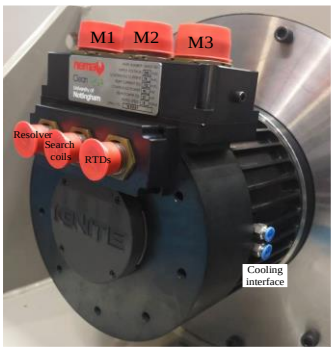


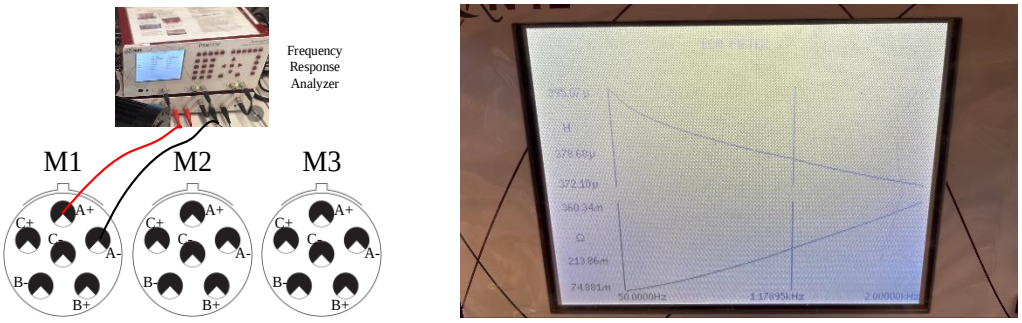
Fig. 8.5 Prototype machine.

8.3 Static measurement

Static measurement is the fundamental test for the following procedures. The resistance and inductance can be used for checking the prototype and modelling the topology for machine control, and the industry standard was referred [133]. In these tests, resistance and inductance of per phase in three modules (M1, M2 and M3) were tested.

8.3.1 Resistance and inductance of per phase

Phase resistance can be measured by the Frequency Response analyser. Using the feature of LCR Meter mode, resistance and resistance per phase can be measured by connecting the two terminals of the open winding to the equipment, as shown in *Fig. 8.6*. The max. speed of the machine is 20 krpm, and its corresponding max electrical frequency is 2 kHz. Besides the measurement of DC resistance, the measurements of AC resistance for every phase were carried out, from 50 Hz to 2000 Hz.



(a) (b)

Fig. 8.6 The (a) schematic diagram of resistance measurement and (b) example of measurement.

The resistance is fluctuant with temperature. So, all the tests were carried out in the same ambient temperature, 20°C. As introduced in the Chapter 6, AC copper loss in the winding is linked to operation frequency. With the increase of frequency, AC loss will increase, as well as the AC resistance. In one phase, the measured value of DC loss and AC loss under varied frequency are shown in *Fig. 8.7*. These tests can be completed by the LCR meter. The frequency was given from 50 Hz to 20 KHz. In the high frequency operation, the AC copper losses are dominant rather than DC loss. Hence, it proves that the reduction of AC loss is important especially for high frequency application.

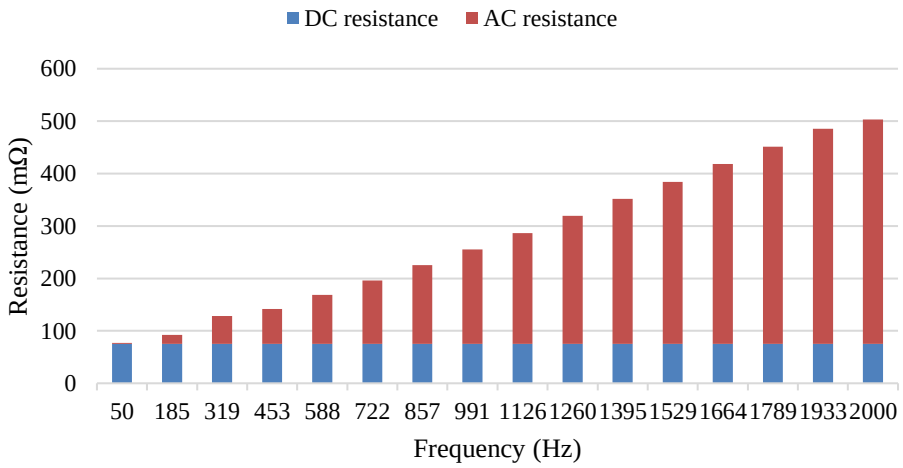


Fig. 8.7 Comparison of measured phase resistance DC and AC (varied frequency).

The *Fig. 8.8* exhibits the comparison of measured value of DC and AC resistance in every phase of all the modules (M1, M2 and M3). The phase resistances with DC power supply exhibit similarity across the three modules. However, the AC resistances display some variation, which is a predictable phenomenon. The AC resistance is primarily influenced by the skin effect and proximity effect. In high-frequency electrical machines, various factors related to the winding, such as the arrangement of strands-in-hand, bundle shapes, and their placement within the slot, can impact the AC resistance [134, 135]. Litz wire is employed as a substitute for round wire to mitigate the skin effect and proximity effect, thereby reducing AC resistance and AC loss [117].

These fluctuations can lead to unbalanced copper losses during operation, resulting in different temperature rises in the windings.

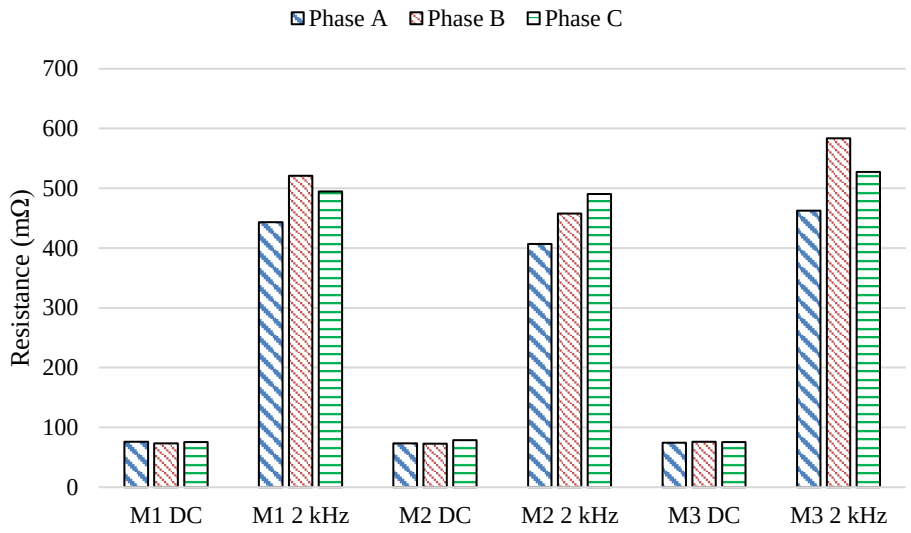


Fig. 8.8 Comparison of phase resistance at DC and AC power supply (at 2k Hz).

Fig. 8.9 illustrates the value comparison of phase inductance at 1.2 kHz and 2 kHz. Compared with resistance, the values of inductance are much stable to the frequency of AC supply. Because multiple modules of three-phase stator windings are distributed sequentially around the circle, the three-phase inductances within one unit are no more symmetrical. The asymmetric inductances may bring errors to the detection of the initial position of the rotor. This impact could be eliminated by the pulse voltage injection into stator windings [136].

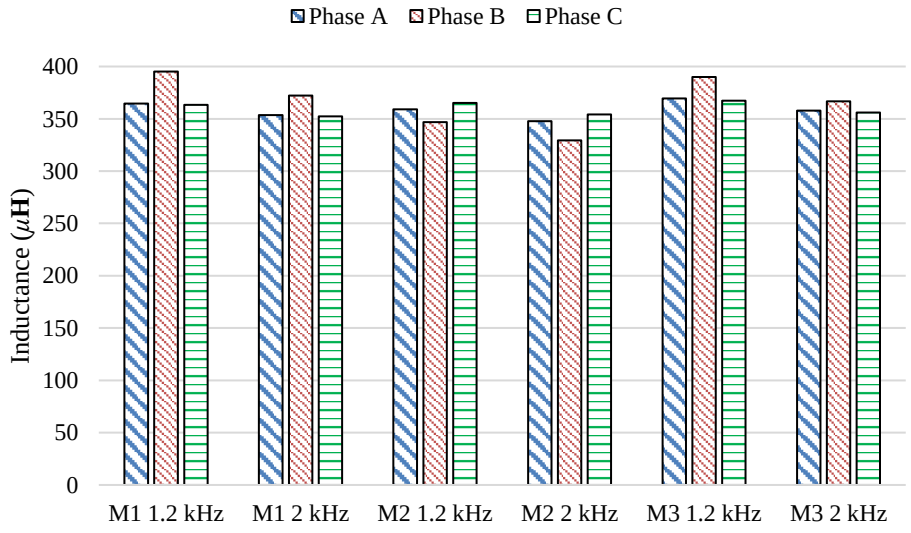


Fig. 8.9 Comparison of phase inductance at 1.2 kHz and 2 kHz power supply.

8.3.2 D-axis and Q-axis Measurement

The direct-quadrature-zero (dqz) transformation, as known as Park's transformation, has been extensively utilized for three-phase circuit of machine. Adopted this

method, the abc frame of three-phase can become a rotate dq reference frame. The process of transformation is shown blow, where θ is the rotor position.

$$i_{dq0} = \frac{2}{3}\begin{bmatrix} cos\theta & \cos(\theta - 120^{\circ}) & \cos(\theta + 120^{\circ}) \\ -\sin\theta & -\sin(\theta - 120^{\circ}) & -\sin(\theta + 120^{\circ}) \\ 1/2 & 1/2 & 1/2 \end{bmatrix}\begin{bmatrix} i_a \\ i_b \\ i_c \end{bmatrix} \quad (8.1)$$

The dqz transformation is often utilized to simplify the analysis of three-phase synchronous machines or to simplify calculations for the control of three-phase inverters. In analysis of three-phase synchronous machines, the transformation transfers three-phase stator and rotor quantities into a single rotating reference frame to eliminate the effect of time-varying inductances and transform the system into a linear time-invariant system. Besides current, flux linkage and voltage are also feasible by this transformation.

Due to different rotor topology of SPMSM and IPMSM, flux path, the L_d and L_q in SPMSM and IPMSM are different. In the former topology, L_d and L_q are almost equal, as known as non-salient motor; in the latter topology, L_d is less than L_q, then it is called salient motor. Hence, accurate values of L_d and L_q, are important for the machine control. There are two methods adopted for the measurement. First method is based on specific rotor position and second method is based on the whole cycle position.

8.3.2.1 Alignment-Based method

In the rotor side, the d-axis inductance is the inductance measured when flux passes through the magnetic poles. The q-axis inductance is the inductance measure when flux passes between the magnetic poles. To measure the inductance of d-/q-axis, the balanced three-phase current condition must be maintained and the method has been presented in [137].

This measurement can be completed by DC power supply with specific d-/q-axis alignment, without a converter. The rotor positions of d-/q-axis alignments are shown in *Fig. 8.10*, while angle between rotor and phase A is 0° and 90°, respectively. When the poles are aligned with of phase A winding with angle of 0° and 90°, L_d and L_q can be derived from the measured equivalent inductance, as shown in *Fig. 8.11* (a) and (b). For the measurement of d-axis inductance, the alignment into d-axis

is done by phase A connected to the positive potential (+) and phase B and C are grounded (-); while, in the measurement of q-axis inductance, the phase B terminal is set to the positive potential (+) of the voltage source, phase C is grounded (-), and Phase A terminal is floating.

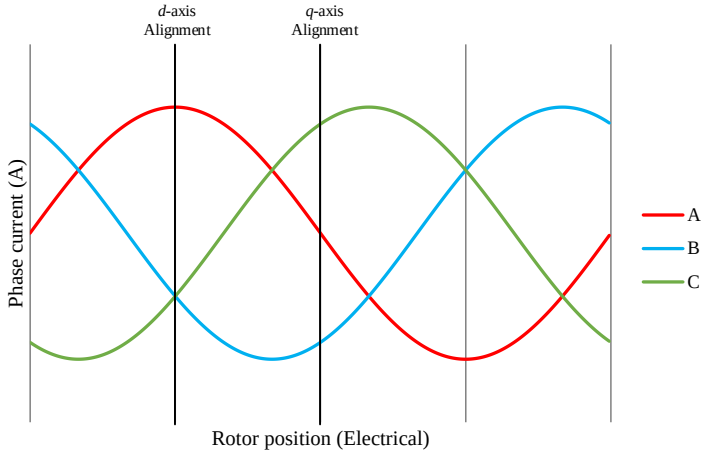


Fig. 8.10 The schematic position of d-/q-axis alignment.

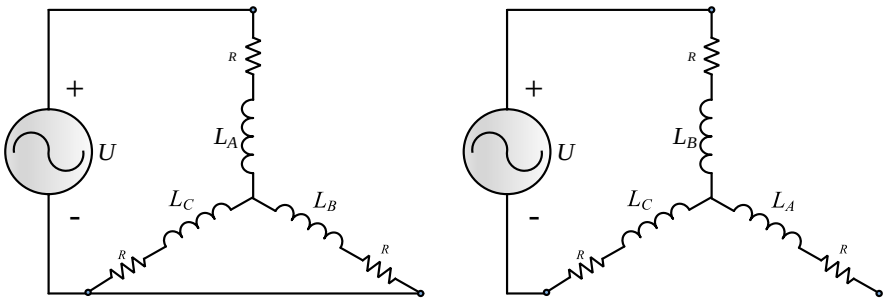


Fig. 8.11 The connection for measuring inductance (a) d-axis alignment (b) q-axis alignment.

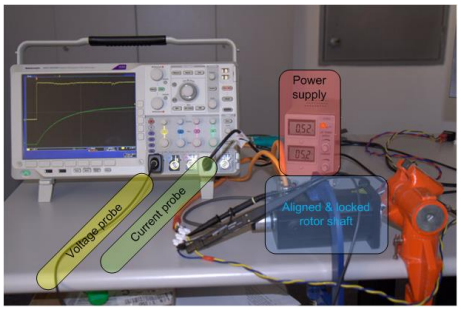
After the alignment of d-/q-axis with phase A, the rotor is locked by table vice to avoid the rotating during the measurement. Then, the equivalent circuits, switching circuits, can be used to calculated inductance by examining current as a function of time. By providing a step signal (power supply, ***U***), the rising edge current I_r and trailing edge current I_f can be listed below.

$$I_r = I_0\left(1 - e^{-t/\tau}\right) \tag{8.2}$$

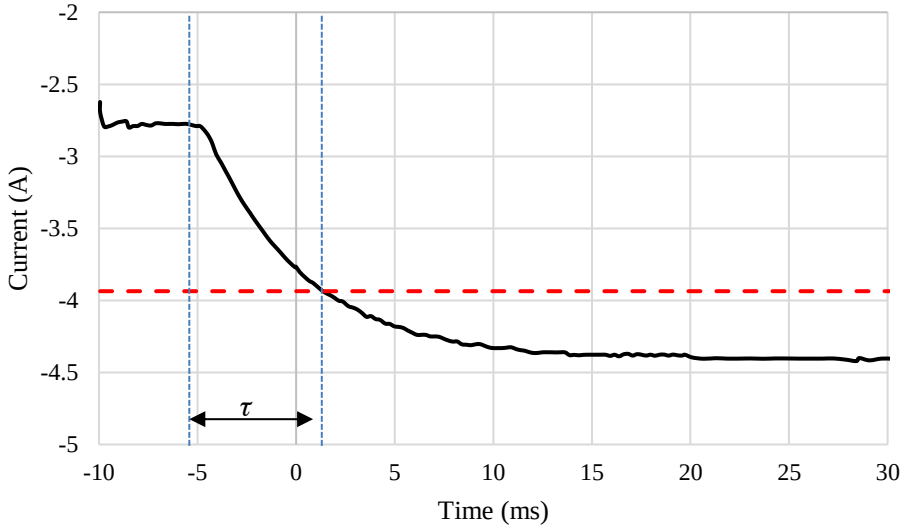
$$I_f = I_0 e^{-t/\tau} \tag{8.3}$$

The current $I_0 = U/R$. Time constant, τ, is defined by $\tau = L/R$ where L is the inductance and R is the resistance, 76 mΩ. Both of the equations above can be used

to calculate inductance. During the test, the time τ relates to the 0.632 I_0 in rising edge or 0.368 I_0 in falling edge. The setup is shown in the *Fig. 8.12*, and the example of falling current in switching circuit is also shown. The measured results are presented in the Table 8.1.



(a)



(b)

Fig. 8.12 (a) RC circuit test (b)Waveform of current of the RC circuit test.

Table 8.1 Results of L_d and L_q.

Module	Inductance	Time constant (ms)	Inductance value (μH)
M1	L_d	4.90	372.4
	L_q	5.35	406.6
M2	L_d	4.75	361.0
	L_q	5.20	395.2
M3	L_d	4.20	319.2
	L_q	5.0	380.0

8.3.2.2 Position-based method

As a comparison, an alternative method was utilized to measure the L_d and L_q. This method collects the values of inductance and resistance of two kinds of connection. For every three-phase winding, there are six connections to collect the values of inductance at every position. In the first connection (AB), phase A connects to the positive potential (+) and phase B is grounded (-), while Phase C is not connected. In the seconded connection (AB-C), phase A and Phase B are connected to the positive potential (+) and phase C is grounded (-); then the connections go next and so on. The schematic of connection is shown in *Fig. 8.13*.

With the feedback of resolver mounted on the shaft, the rotor position was rotated every 5°, then the value of inductance and resistance by LCR meter were recorded. To compare the value of machine at rated speed and maximum speed, the values at 1100 Hz and 2000 Hz were measured. Example of connection AB is shown in *Fig. 8.14*. The measured value is fluctuated due to varied rotor position. The distribution of results closes to sinusoidal curve which amount of peak value for every test is a multiple of pole pairs.

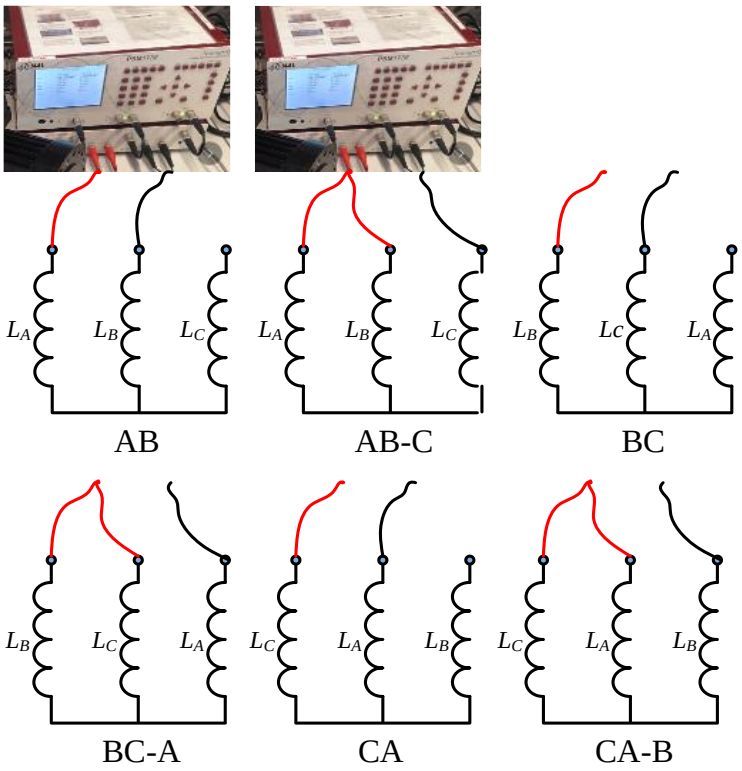


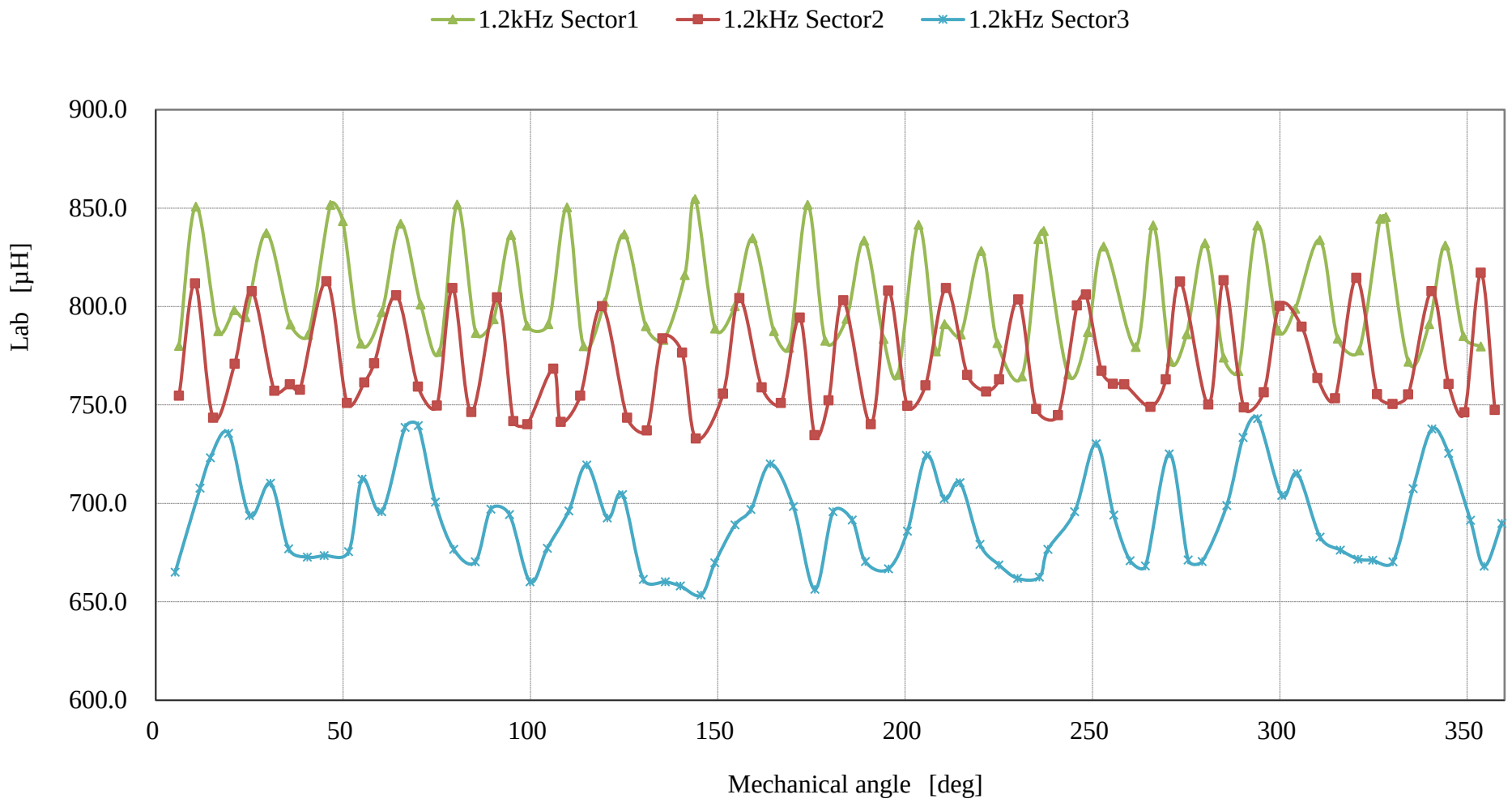
Fig. 8.13 The connections for measuring inductances.

The box-whisker map was adopted to illustrate the fluctuations of measured

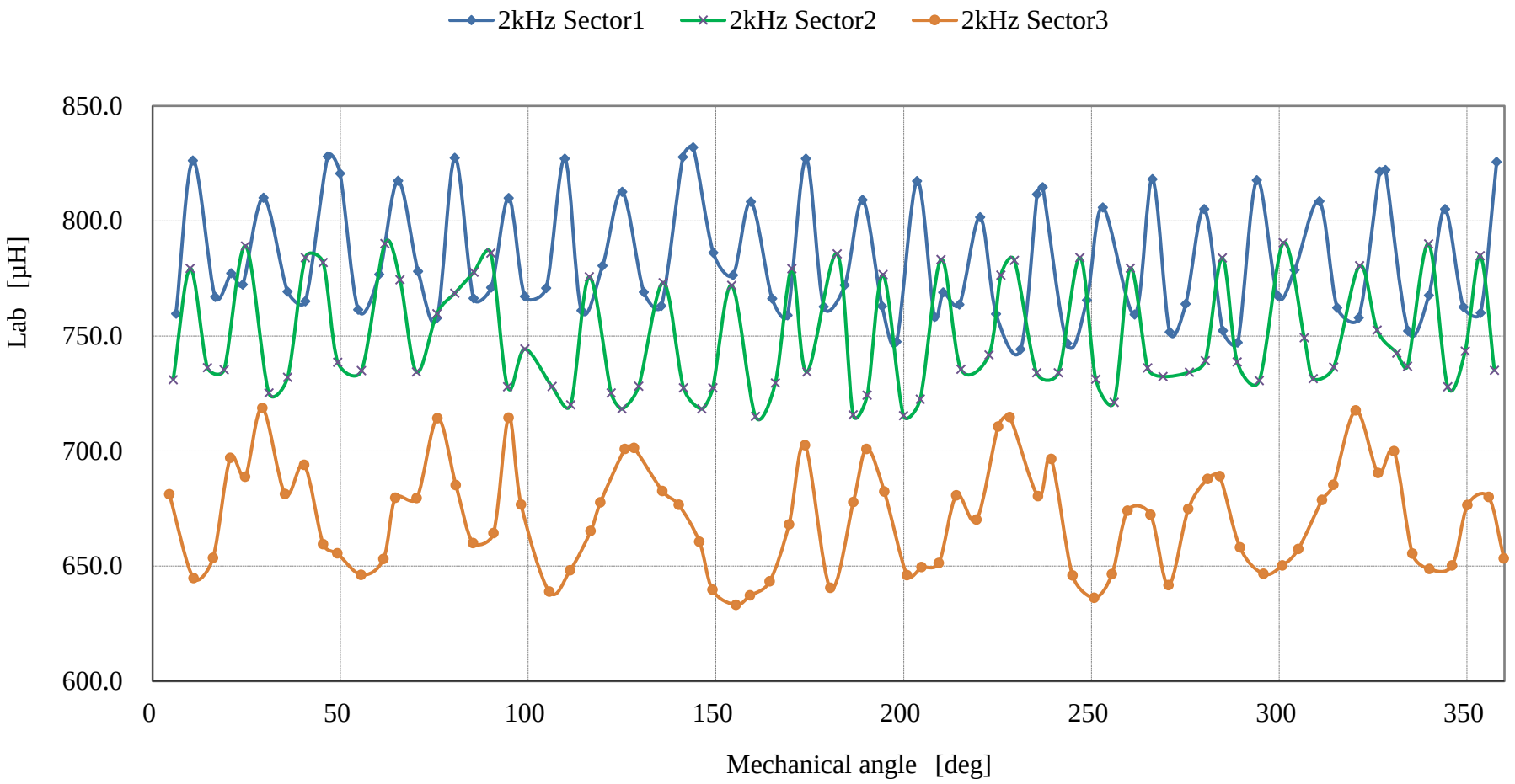
resistance and inductance with different connection in three modules, as shown in *Fig. 8.15* This type of plot follows a standardized approach for displaying dataset information using the five-number summary, including the minimum, maximum, sample median, and the first and third quartiles. The results also show that the measured values of parameters are not identical in three modules, similar to what is depicted in Figure 8.8 and Table 8.1.

Achieving identical electrical parameters for the phases requires meticulous attention to the manufacturing process. Factors such as ensuring the same number of winding turns, the length of leading wires, and even the layout of wire strands (which impacts AC resistance) all play a crucial role in achieving this goal.

Based on theoretical equations from Electric Machinery [138], the L_d and L_q can be calculated as blow, shown in Table 8.2 and Table 8.3, at 1100 Hz and 2000 Hz, respectively. These two different methods were adopted to measure and calculate L_d and L_q. The motor inductances under different frequency (rotation speeds) can serve as control parameters for accurate control of the motor, and accordingly control performance and energy efficiency of the motor are improved.

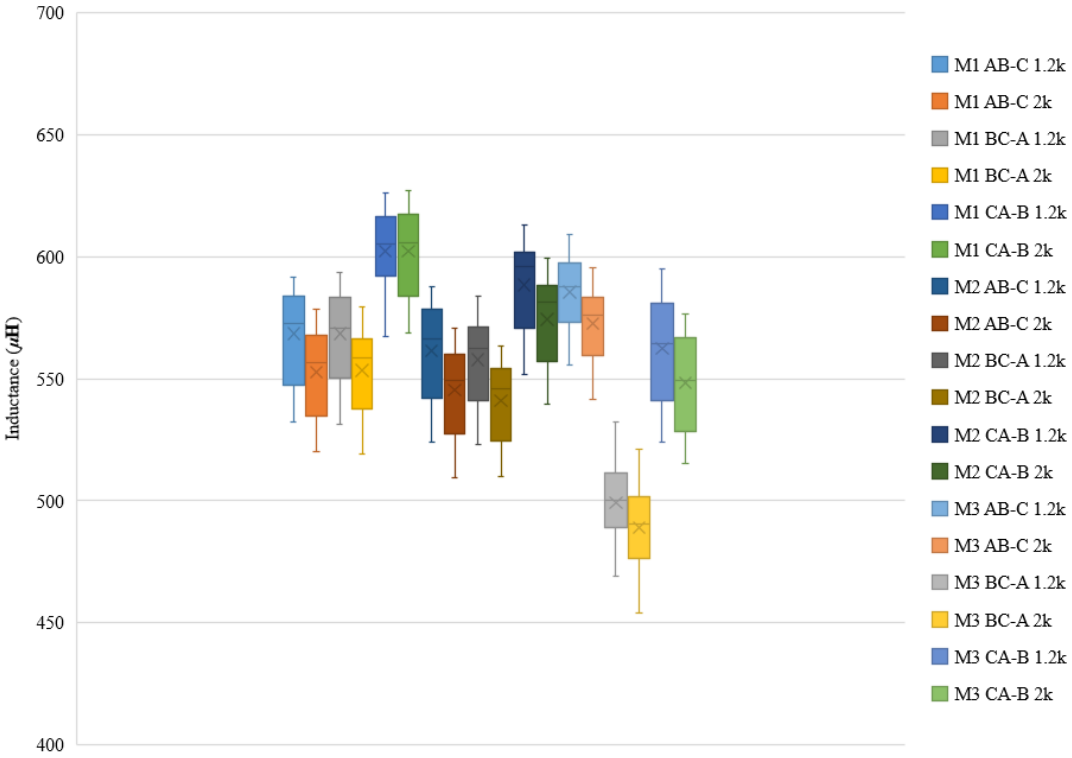

1.2kHz Sector1
1.2kHz Sector2
1.2kHz Sector3
900.0
850.0
800.0
750.0
700.0
650.0
600.0
Lab [µH]
0
50
100
150
200
250
300
350
Mechanical angle [deg]

(a)

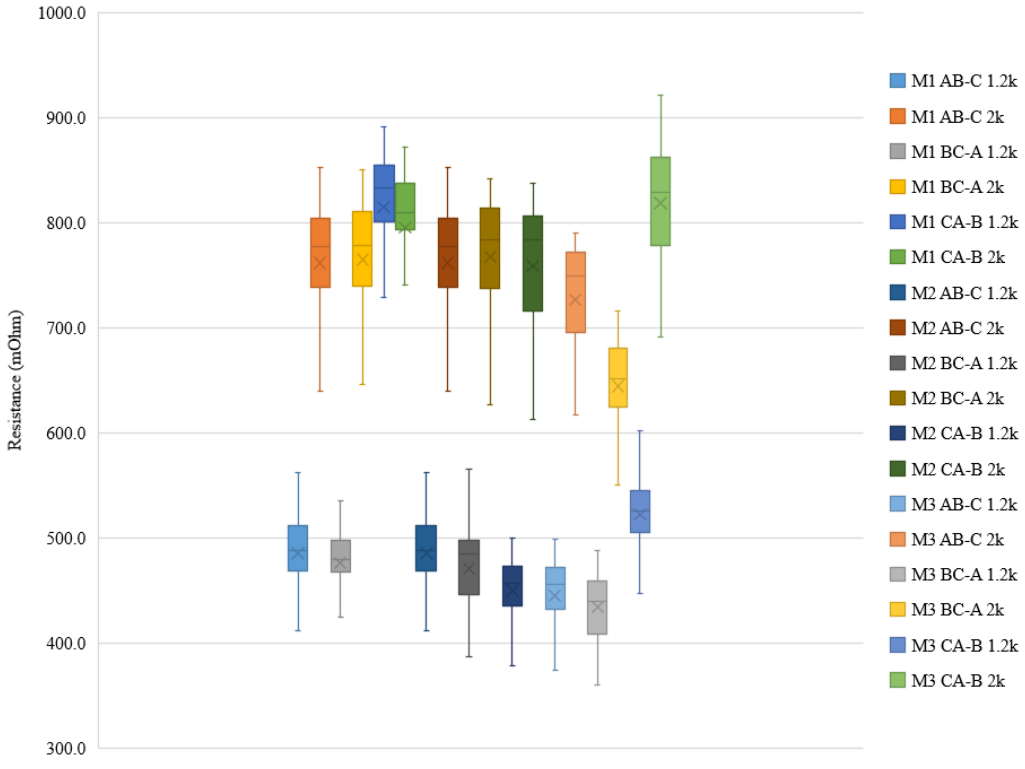


(b)

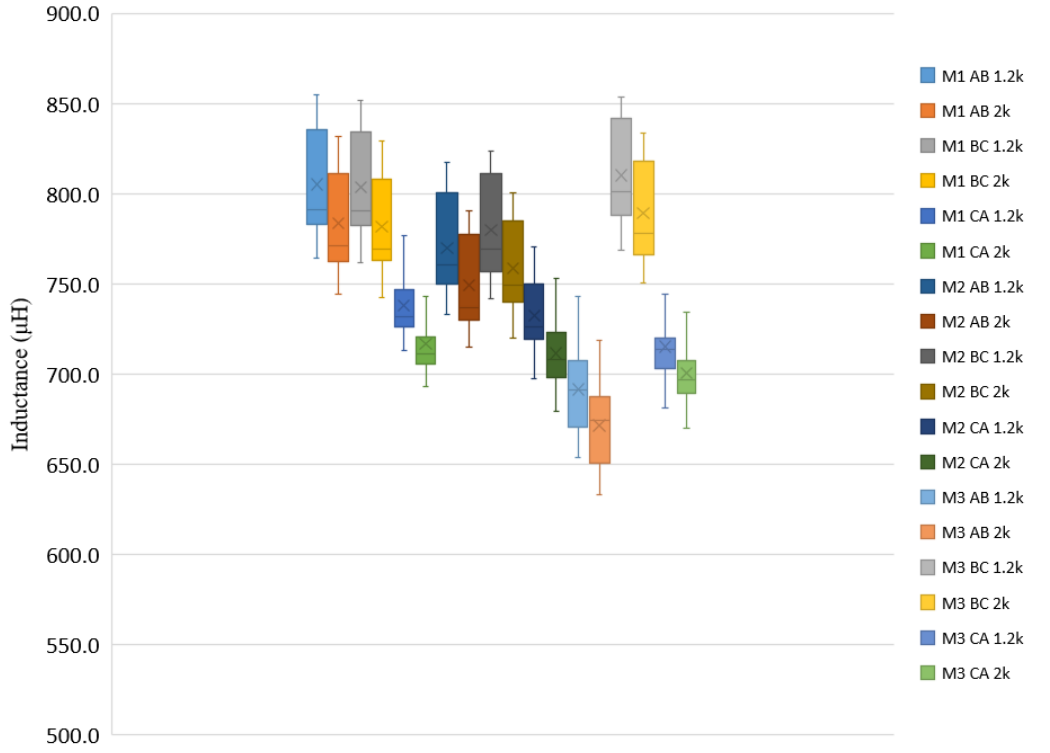
Fig. 8.14 Example of measured inductance of connection of AB with rotor position (a) at 1200 Hz. (b) at 2000 Hz.


700
650
600
550
500
450
400
Inductance (μH)
M1 AB-C 1.2k
M1 AB-C 2k
M1 BC-A 1.2k
M1 BC-A 2k
M1 CA-B 1.2k
M1 CA-B 2k
M2 AB-C 1.2k
M2 AB-C 2k
M2 BC-A 1.2k
M2 BC-A 2k
M2 CA-B 1.2k
M2 CA-B 2k
M3 AB-C 1.2k
M3 AB-C 2k
M3 BC-A 1.2k
M3 BC-A 2k
M3 CA-B 1.2k
M3 CA-B 2k

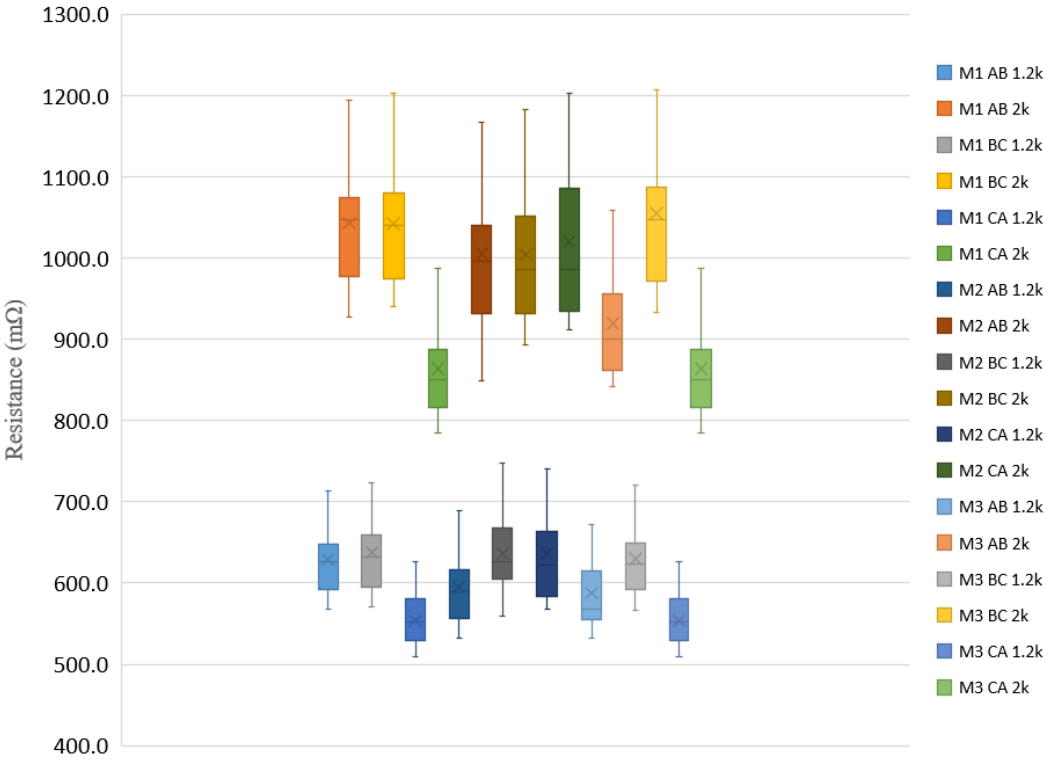
(a)


1000.0
900.0
800.0
700.0
600.0
500.0
400.0
300.0
Resistance (mOhm)
M1 AB-C 1.2k
M1 AB-C 2k
M1 BC-A 1.2k
M1 BC-A 2k
M1 CA-B 1.2k
M1 CA-B 2k
M2 AB-C 1.2k
M2 AB-C 2k
M2 BC-A 1.2k
M2 BC-A 2k
M2 CA-B 1.2k
M2 CA-B 2k
M3 AB-C 1.2k
M3 AB-C 2k
M3 BC-A 1.2k
M3 BC-A 2k
M3 CA-B 1.2k
M3 CA-B 2k

(b)



(c)



(d)

Fig. 8.15 Fluctuation of measured resistance and inductance with different connection in three modules (M1, M2 and M3).

Table 8.2 Calculated L_d and L_q at 1100 Hz.

Module	Inductance	Calculated inductance at 1100 Hz ($\boldsymbol{\mu}$**H**)			
		AB and AB-C	BC & BC-A	CA and CA-B	Average value
M1	L_d	399.62	399.46	362.29	387.12
	L_q	405.58	403.99	375.77	395.11
M2	L_d	380.79	385.68	364.06	376.84
	L_q	389.18	394.31	368.34	383.94
M3	L_d	338.33	396.37	351.40	362.03
	L_q	353.06	413.67	363.75	376.83

Table 8.3 Calculated L_d and L_q at 2000 Hz.

Module	Inductance	Calculated inductance at 2000 Hz ($\boldsymbol{\mu}$**H**)			
		AB and AB-C	BC & BC-A	CA and CA-B	Average value
M1	L_d	387.46	388.86	350.52	375.61
	L_q	396.33	392.89	366.30	385.17
M2	L_d	371.87	376.13	350.77	366.26
	L_q	377.17	382.44	360.80	373.47
M3	L_d	327.04	386.93	341.22	351.73
	L_q	344.13	402.35	359.20	368.56

8.4 Dynamic test

8.4.1 Setup of test-rig

To support the electrical machine test, relevant systems are necessary, such as the test-rig, electrical or cooling device. Several cables were assembled to connect electrical machine, converters and DC power supply, for energy conversion. A power converter is an electrical device for converting electrical energy. It can convert AC into DC and vice versa; change the voltage or frequency of the current or do some combination of these. In this prototype, the modular sectors are connected with three converters. Moreover, corresponding data loggers were prepared for collection signals of thermal, vibration and torque, to host PC. The schematic of the whole setup is shown in *Fig. 8.16*.

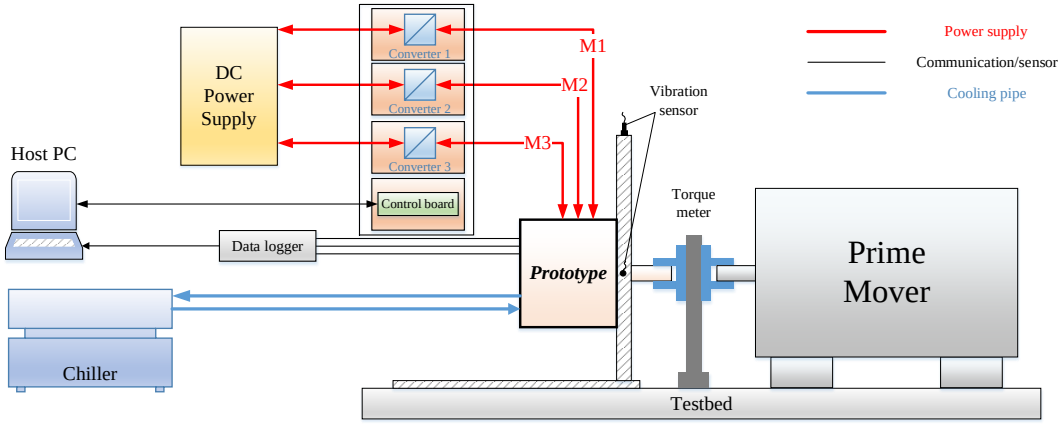


Fig. 8.16 The schematic of setup for machine test.

The electrical machine was aligned with prime mover for dynamic test. Bellows couplings and a torque meter were mounted between electrical machine and prime mover, as shown in *Fig. 8.17*. Besides, two vibration sensors were mounted on the vertical and horizontal direction to measure the vibration during the operation, as shown in *Fig. 8.18*.

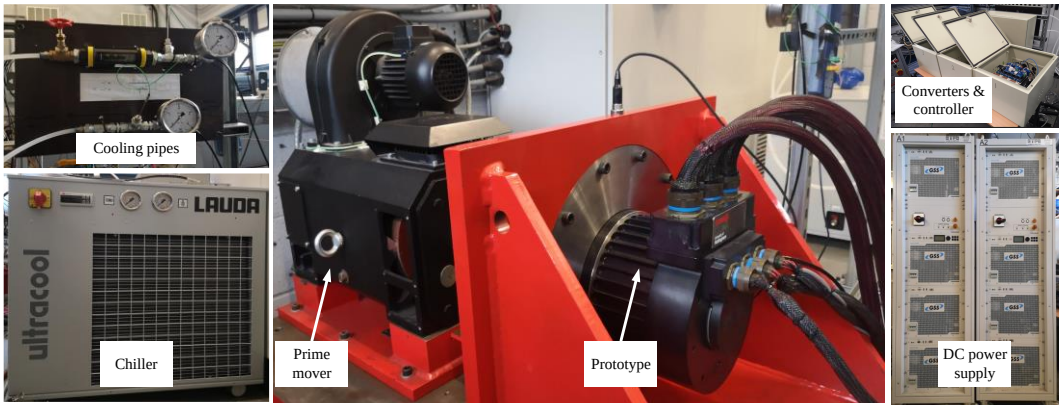


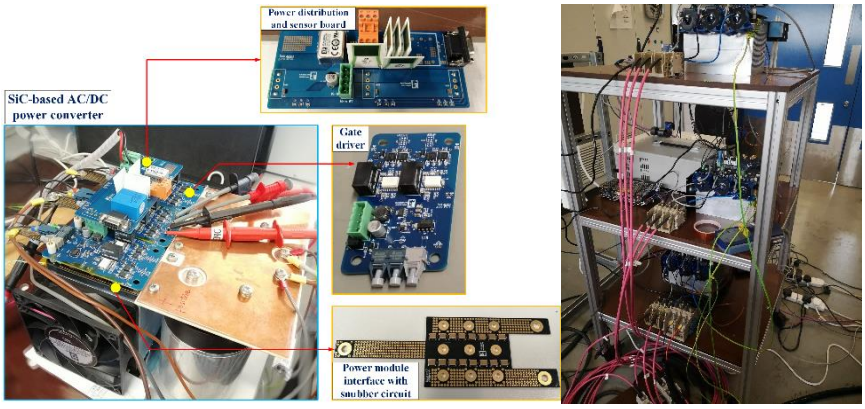
Fig. 8.17 Setup of testbed connection.



Fig. 8.18 Vibration sensors on the test rig.

Three independent power cables were used to connect three machine modules (M1,

M2 and M3) with SiC-based AC/DC power converters. These converters have been prepared for supporting the energy conversion of two operation modes, generation and motoring. For every converter, three SiC modules were adopted to pursue high power density and compact design. Single module and the whole converters are shown in *Fig. 8.19*. These converters have been tested in advance, and its efficiency at 8.07 kW is 96.51% with a power density of 7.5 kW/L.



(a) (b)

Fig. 8.19 AC/DC power converters for IGNITE machine (a) single unit. (b) three modules assembly.

This layout provides the isolation of every channel which benefits the reliability. In the case of electrical faults in one channel, the other healthy can maintain operation continuously. It is worth mentioning that all the devices and cables should be well-arranged to avoid potential issues. All the devices should be far away from the test rig, because mechanical vibration is easy to cause false output of the electronics, thus resulting in trouble of the system. Similarly, electrical devices and cables should consider the potential leakage of coolant from cooling pipe, fittings and chiller. The power converters and cables may introduce heavily EMI noise in the sensors and communications. Hence, shielded cable and backshells of connectors are necessary components for power and sensor connection.

An independent cooling system, consisted of chiller, pressure gauge, valves and flow rate meter, has been designed for machine cooling. Its layout and connection were exhibited in *Fig. 8.20*. There is a global valve near the chiller, which is used to control the pressure in the inlet pipe. Two thermal sensors were arranged in the inlet and outlet pipe to monitor the temperature of coolant. Flow meter rate in the inlet pipe can illustrate the flow rate in the whole pipe, which is crucial thermal management.

The real reading of flow rate can be used to update the thermal model of electrical machine, because the coolant is continuous in the whole cooling pipe, including the cooling path in the water jacket.

Besides, a ball valve was installed in the outlet pipe to facilitate draining the coolant before disassembling the pipes. The layout and a list of components were shown in *Fig. 8.20*. Based on this layout, the cooling system are assembled as shown in *Fig. 8.21*. Before the dynamic test with electrical machine, the cooling system can be tested independently, by connecting inlet and outlet for checking flow rate, performance of chiller and sealing issues. Besides, the flow rate meter provides an output of electrical signal for system control.

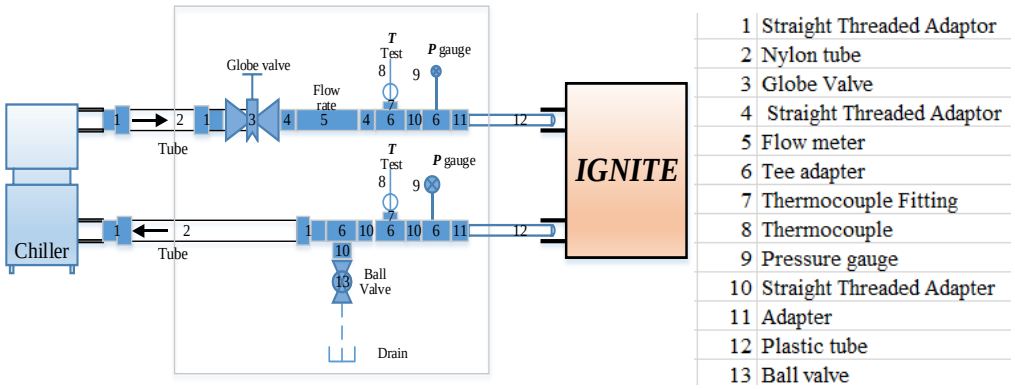


Fig. 8.20 Layout of cooling system for IGNITE machine test.



Fig. 8.21 Cooling pipe for the electrical machine test.

Above all, the components for setup are listed in Table 8.4, including their description, specification and quantity.

Table 8.4 List of setup for electrical machine test.

Device	Component	Description	Specification	Quantity
Test rig	Prime mover	Drive the motor or as load.	Oswald Test Rig motor Max speed: up to 20000 rpm. Output power: 100¬3000 kW	1
	Drive	Drive the prime mover	Inovance drive	1
Electrical device	DC power supply	Provide DC power during the on-load test or energy recovery	0 ~ 540 VDC, 0 ~ 100A.	1
	Converter	Power conversion of DC and AC	SiC modules	3
	Control unit	For communication and machine control	CAN bus, DSP+FPGA	1
	Power cable	Connection between machine and convert	Three-phase, 0 ~ 60 A.	5 m*6*3
	Sensor cable	Connection of sensor and data loggers	0 ~ 3A.	3 m * 30
Cooling system	Chiller	Pump cool coolant into machine and	Range of temperature: -5 °C ~25 °C Pump pressure Max. : 3.4 bar Pump flow max: 42 L/min	1
	Coolant	For the electrical machine cooling	75% Water + 25 % glycol	25 L
	Global valve	Adjust the pressure of coolant in the pipe	Maximum Working Pressure: 32 bar	1
	Pressure gauge	Monitor the pressure of coolant in the pipe	Monitor the pressure in the inlet and outlet pipe	2
	Flow rate meter	Monitor the flow rate of coolant in the pipe	Variable Area Flow Meter, 1~15 L/min	1
	Thermal sensors	Monitor the temperature of coolant in the pipe	Type K Thermocouple	2
Data acquisition	Oscilloscope	Sample the data of search coil, torque, back-EMF, etc.	200MHz bandwidth/ 4 GS/s sampling rate	1
	Differential voltage probe	For torque sensor, back-EMF	Bandwidth: 120MHz; Voltage Max: 1000V	3
	Clamp current probe	For phase current	0~200 A	3
	Data logger of temperature	Data acquisition of thermal sensors inside of machine	PICO, PT-104	3
	Data logger of vibration	Data acquisition of vibration of electrical machine	Data Physics, ABACUS 901	1
Extra device	Megohmmeter	For insulation test	1000V	1
	Thermal camera	Monitor the hotspot	-25°C and 300°C	1
	Vibration sensors	Monitor the vibration during dynamic test	Range: ±50 g pk (±490 m/s² pk)	2
	RLC analyser	For static measurement of resistance and inductance	0 ~1ohm, 0 to 1mH inductance at frequencies up to 20kHz	1

After setup, insulation test is necessary before any dynamic test. These tests were carried out between winding and housing, sensor and windings, cables, etc. During the test, 1000 V was applied on the probes, and the resistance between two probes should bigger than 500 MΩ.

8.4.2 Commissioning

The definition of commissioning test hereby means the rotor shaft is driven by prime mover. Besides, the connection between phase winding and converters were disconnected. Before the current input, run up is necessary to check the magnitude of vibration and possible resonance. Meantime, back-emf can be measured of all the three modules.

8.4.2.1 Vibration

ISO 10816-1 is a basic document which sets out general guidelines for the measurement and evaluation of mechanical vibration of machines. According to the ISO 10816 standard, the machine classifications is listed in Table 8.5. The prototype machine belongs to the Class II due to capacity of 35 kW.

Table 8.5 Classification of rotating machinery in ISO 10816.

Class	Power
I	< 15 kW
II	15 ~ 75 kW
III	Large prime mover
IV	> 10 MW

Two types of testing were conducted for the run-up. In the first test, the prime mover drives the prototype machine from standstill to a higher speed, with every 500 rpm more. The speed curve is stepped, and it operates more than 30 seconds at each speed point, as shown in *Fig. 8.22*. This test is a basis or guidance for following dynamic test. Once a heavy vibration occurred, then it can be stopped emergently.

Table 8.6 Velocity range limits and machine classes.

Velocity		Velocity Range Limits and Machine Classes			
				Large Machines	
mm/s RMS	In/s RMS	Small Machines Class I	Medium Machines Class II	Rigid Supports Class III	Less Rigid Supports Class IV
0.28	0.02				
0.45	0.03				
0.71	0.04	Good			
1.12	0.06				
1.80	0.10	Satisfactory			
2.80	0.16				
4.50	0.25	Unsatisfactory			
7.10	0.40				
11.20	0.62				
18.00	1.00	Unacceptable			
28.00	1.56				
45.00	2.51				

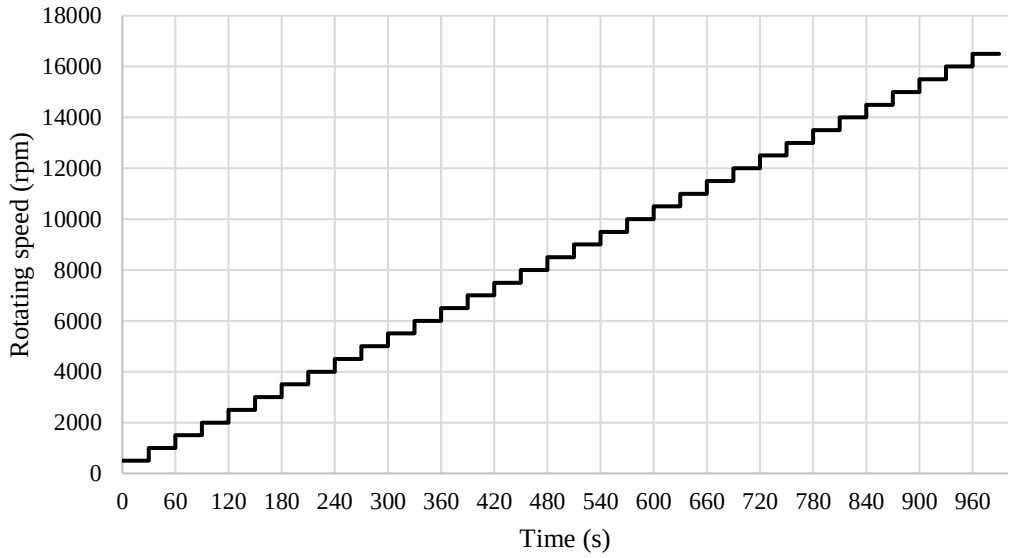


Fig. 8.22 Stepped speed curve.

The results of this test procedure are shown in *Fig. 8.23*. According to the ISO standard, there are four kinds of colour embedded as background to illustrate the

vibration severity. The RMS value of vertical and horizontal vibration were recorded, which its total vibration is calculated. There were four operation points which vibration value exceed the threshold of good zone (green area), 4500 rpm, 9000 rpm and 12000 rpm, in sequence.

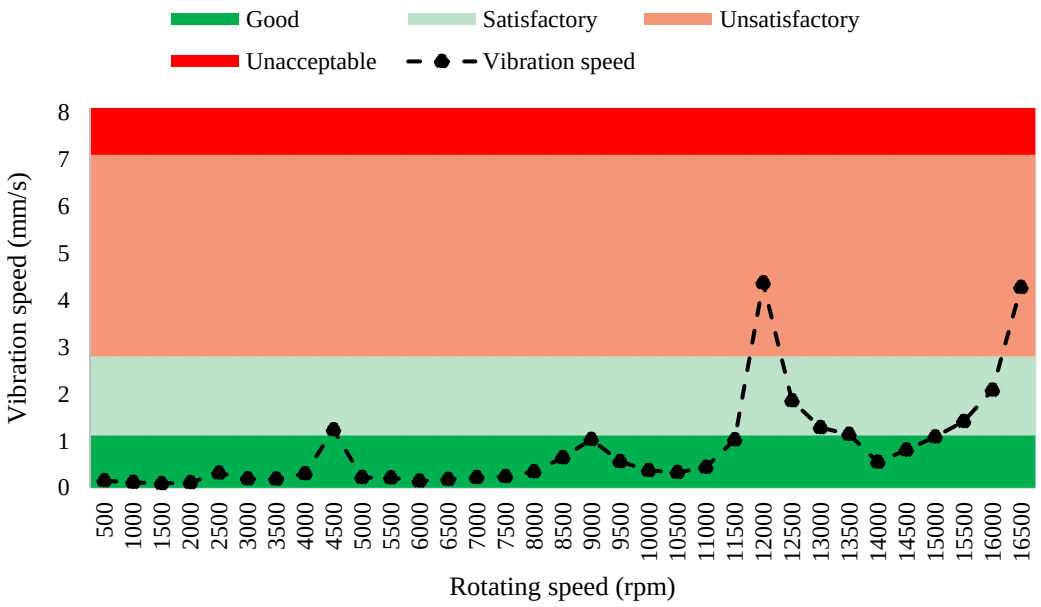


Fig. 8.23 Measured vibration of electrical machine from standstill to 16500 rpm (Stepped).

Meanwhile, the vibration acceleration of this test procedure was also recorded, as shown in *Fig. 8.24*. Additionally, the real-time acceleration value can be monitoring during the test. The FFT spectrums of evert specific operation point were analysed, which figures were plotted for finding dominant vibration source. The spectrum of operation point at 10500 rpm is shown in *Fig. 8.25*. The dominant vibration point is at 200 Hz, which magnitude value vibration acceleration is 640 mg.

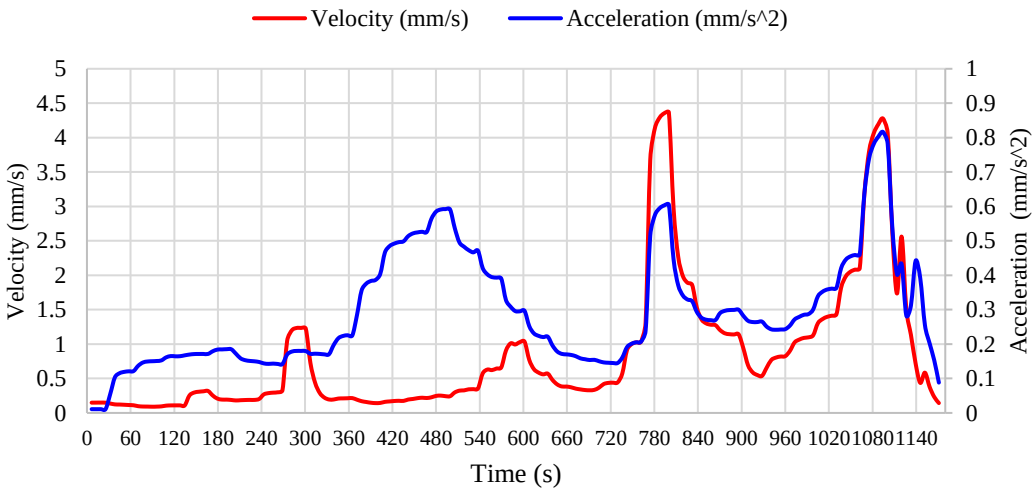


Fig. 8.24 Vibration acceleration of IGNITE machine in the stepped speed test.

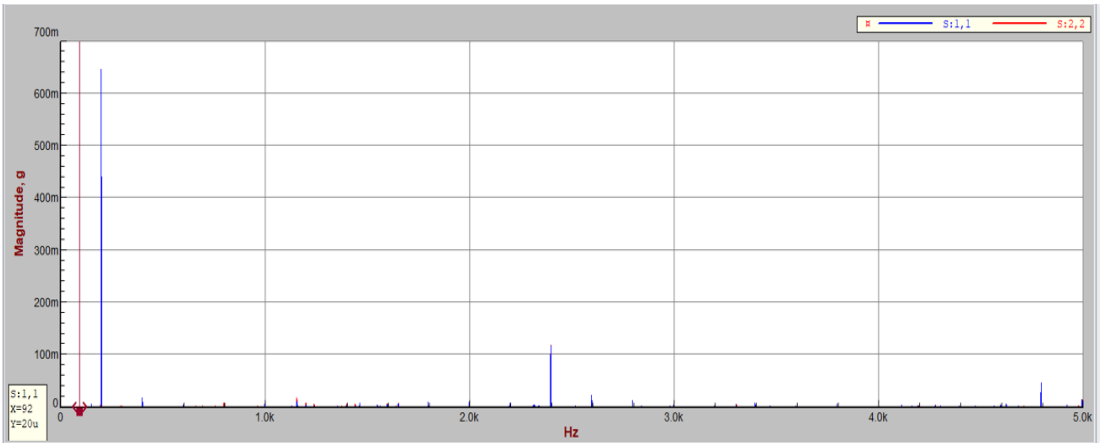


Fig. 8.25 FFT spectrum of vibration at 10500 rpm.

In the first test, the stepped speed may miss or skip potential resonance speed point, but its results can be used as a benchmark. Then the continuous test was carried out from standstill to maximum speed continuously. In this case, all the speed points can be covered. Any potential resonance point can be recognized as the operation guidance for following test.

The speed curve of this test procedure is shown in *Fig. 8.26*. The machine was driven to the maximum speed 20000 rpm in 2 min 36 s, and then the machine will operate at this speed for a while, to avoid a speed shock. The whole results were record and plotted in *Fig. 8.27*. The yellow zone represents the period of 20000 rpm. There are three peak values of vibration appeared before the electrical machine achieves the maximum speed, which speeds are around 6000 rpm, 10000 rpm and 13000 rpm, in sequence. These results prove the machine can operate safely in majority speed

range. In the deceleration zone, a higher peak value occurs due to the sudden deceleration, which can generate additional shocks.

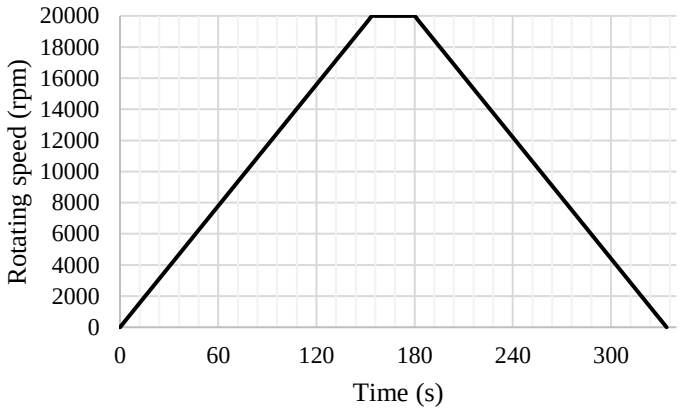


Fig. 8.26 Test procedure for continuous run-up test.

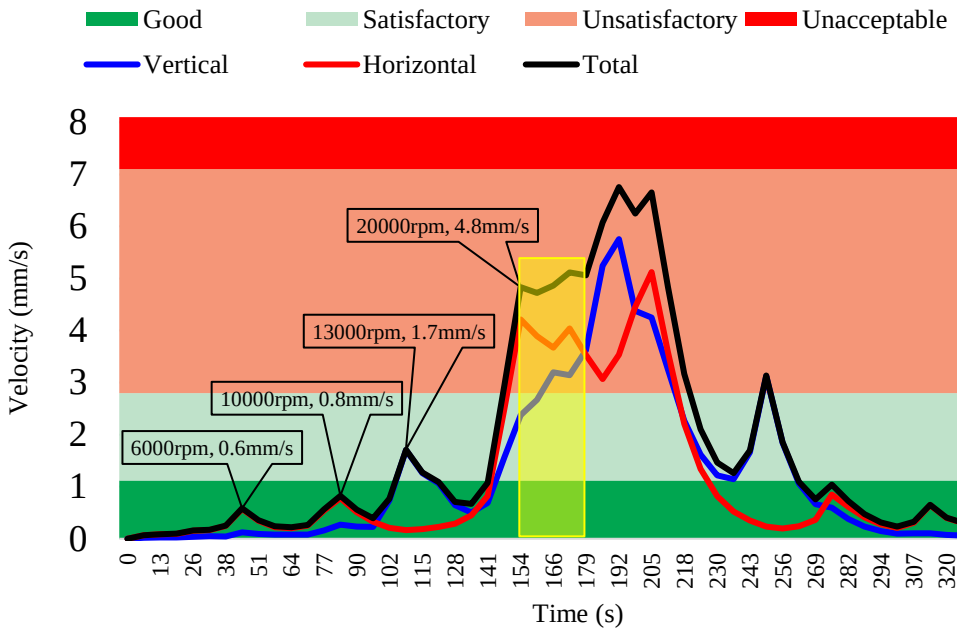


Fig. 8.27 Measured vibration of electrical machine from standstill to 20000 rpm (continuous).

These results of vibration can provide a basis for following test. In general, the vibration of electrical machine consists of electrical and mechanical source. For mechanical source, they may include the vibration from test rig, prime mover, or electrical machine itself. In the electrical side, the vibration source relates to the operation frequency. Both of these two test procedures, vibration spikes are all caused by mechanical issues. Similarly, electrical faults at these operation points can generate significant vibration rise than others.

8.4.2.2 Search coil

As introduced in the chapter 7.2.1, there were 9 search coils was embedded in the same position as phase winding, for health monitoring and detection. During the constant rotating driven by prime mover, sinusoidal induced voltage can be record (shown in *Fig. 8.28*), which can be utilized as benchmark for faults monitoring, as shown in *Fig. 8.29*. Faults in the winding or permanent magnet can have an effect on the peak value. In the healthy operation, the peak values of induced voltage in all search coils are same, and these values can form a regular radar map.

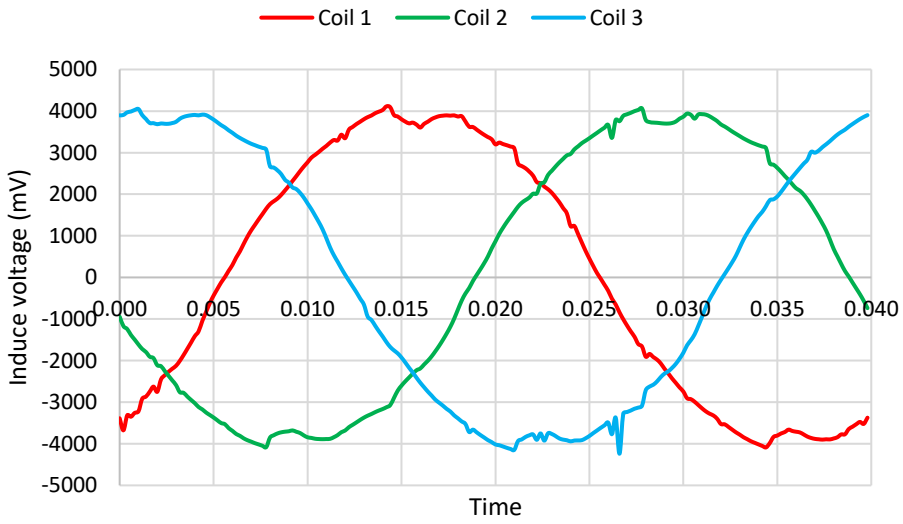


Fig. 8.28 Measured induced voltage in the search coils at 2000rpm.

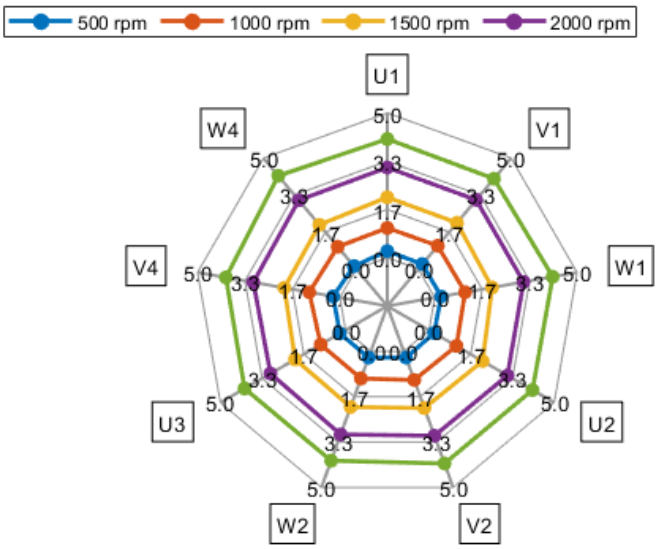


Fig. 8.29 Radar map of the measured peak values in the 9 search coils at varied speed (500 ~ 2000 rpm).

8.4.2.3 Back-EMF

As aforementioned introduction, rotating PM induces back-EMF in the windings of every module. The electrical machine was driven by prime mover at ambient temperature (20 degrees).

The results of back-EMF line-line voltage was measured and recorded, by differential voltage probe and oscilloscope. In every single module, the magnitudes of line-line voltage are almost same and their phase positions form 120-degree lead or lag. The peak-peak (pkpk) values of every channel (phase U-V, phase V-W and phase W-U) were measured, as shown in *Fig. 8.30* (a). Then, the comparison of FEA and measured results is shown in *Fig. 8.30* (b). It can be noted that the voltage waveform is highly sinusoidal, and the measured results exhibit a good match with FEA results.

Compared with FEA results, the magnitudes and shape exhibit the offsets. The reasons may derive from two aspects: vibration (deformation) and manufacturing error. For reason of the vibration, this can be observed in *Fig. 8.33*, which depicts a potential trendline showing an increasing error at higher speeds. Additionally, more reasons are listed.

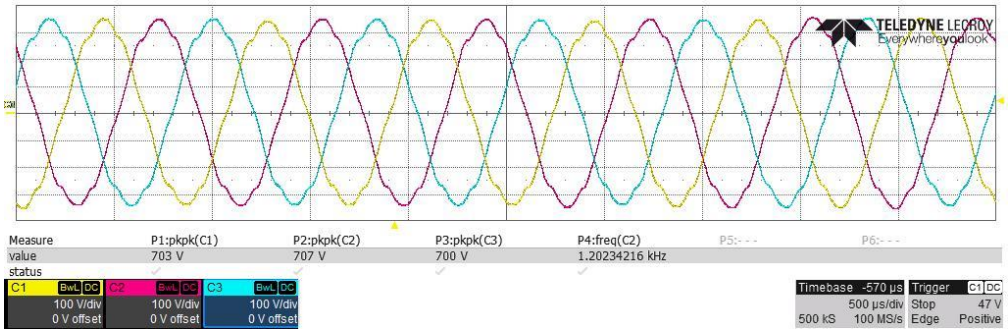
(a) In the optimal design, the width of the gap is set at 2mm, while the remaining width of the stator teeth on each side is 3 mm. These dimensions can be influenced by the manufacturing and assembly processes, as well as operational factors.

(b) The innovative stator design, with its thinner and more sensitive teeth, is susceptible to elastic deformation and increased gap width when subjected to the filling process and high vibrations during operation.

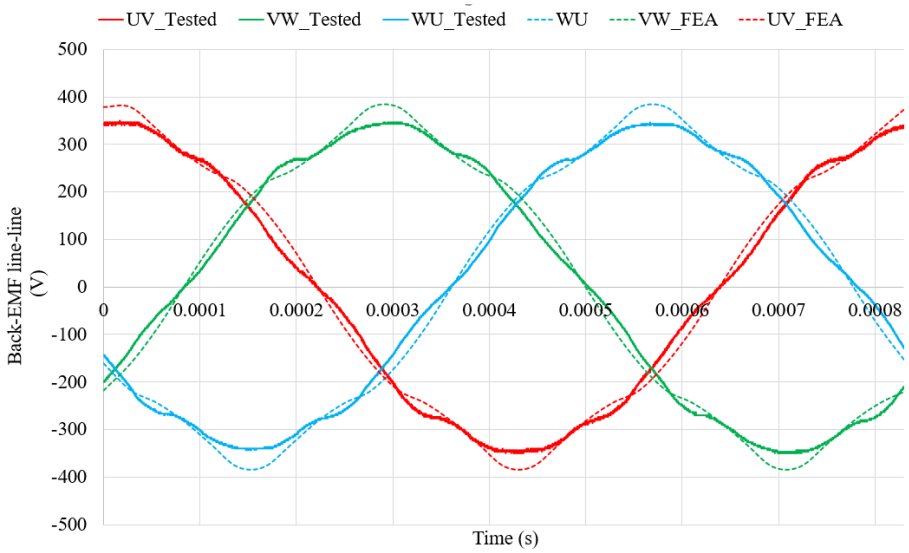
(c) Wider gaps in the stator result in reduced gap flux density and back-emf, which in turn contributes to the observed deviation from the FEA results. These conclusions have been validated in Chapter 5.4.1, where it was demonstrated that wider gaps result in a performance drop.

(d) The alteration of gap size and shape can influence the flux paths and distribution of harmonics. This, in turn, can impact the proportion of harmonics present. In the comparison between the measured results and FEA results, it is

observed that the measured results contain a higher amount of 3rd harmonic.



(a)



(b)

Fig. 8.30 Waveform of line-line back-EMF (a) at 11000 rpm (b) Comparison with FEA results.

To illustrate the linear relation between rotating speed and induced voltage, the line-line voltage was collected, started from standstill to maximum speed, as shown in *Fig. 8.31*. The line-line voltage of the back-EMF was measured for every additional 1000 rpm. The peak values of sinusoidal waveform of back-EMF with rotating speed can be utilized to check the linearity between speed and back-EMF. The slope of back-EMF (V_E) and angular velocity ω (rad/s), as known as back-EMF constant K_E, can be calculated, 0.276 $V/rad \cdot s^{-1}$. The motor's angular speed is directly proportional to the back EMF that it generates.

$$\omega = V_E / K_E \tag{8.4}$$

The repetitive test procedures were carried out in module 2 and module 3. Based on the illustration in Chapter 5, this topology with single layer 18 slot/12 pole

combination has been divided into three independent modules. The phasors of slot of every module are same. Then, the induced voltage in three modules is theoretically same, as shown in *Fig. 8.31*. The measured results based on three modules are very close which prove the consistence of modular design. The FFT spectrums will be given later for the explanation of the gap between the measured results and the FEA results.

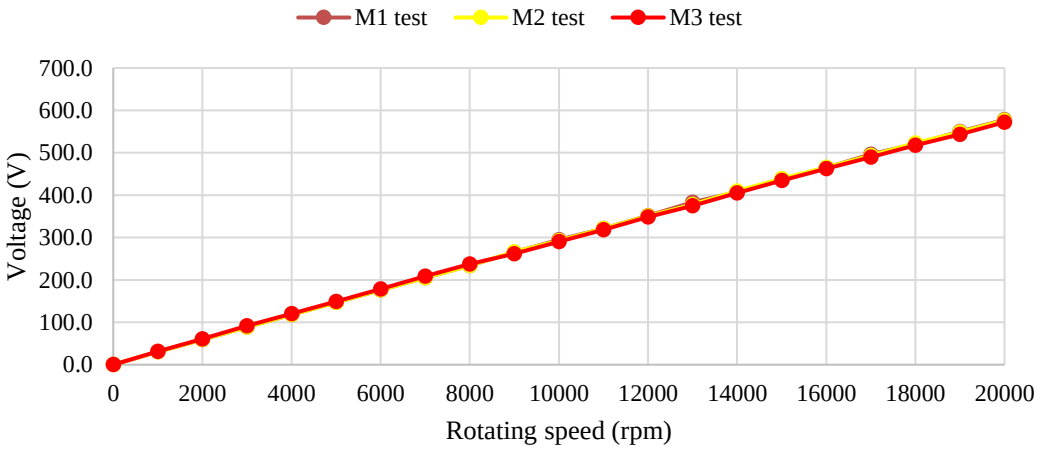


Fig. 8.31 Measured back-EMF line-line voltage results in three modules.

Furtherly, to compare the error between modules, FEA and measured results. The FFT spectrum was adopted to investigate the fundamental component of line-line back-EMF values, and the errors between FEA and measured results. *Fig. 8.32* lists the back-EMF spectra in three modules and they exhibit consistent. As shown in the *Fig. 8.33*, the comparison of fundamental line-line back-EMF between FEA and measured value in the full speed range is given, along with the error. As an example, at 12000 rpm, the error in module 1 is less than 4%. The figure displays a potential trendline of the error, showing a deviation from the FEA results at high speeds. One possible reason for this deviation is the increasing vibration response at high speeds, which can impact the output performance.

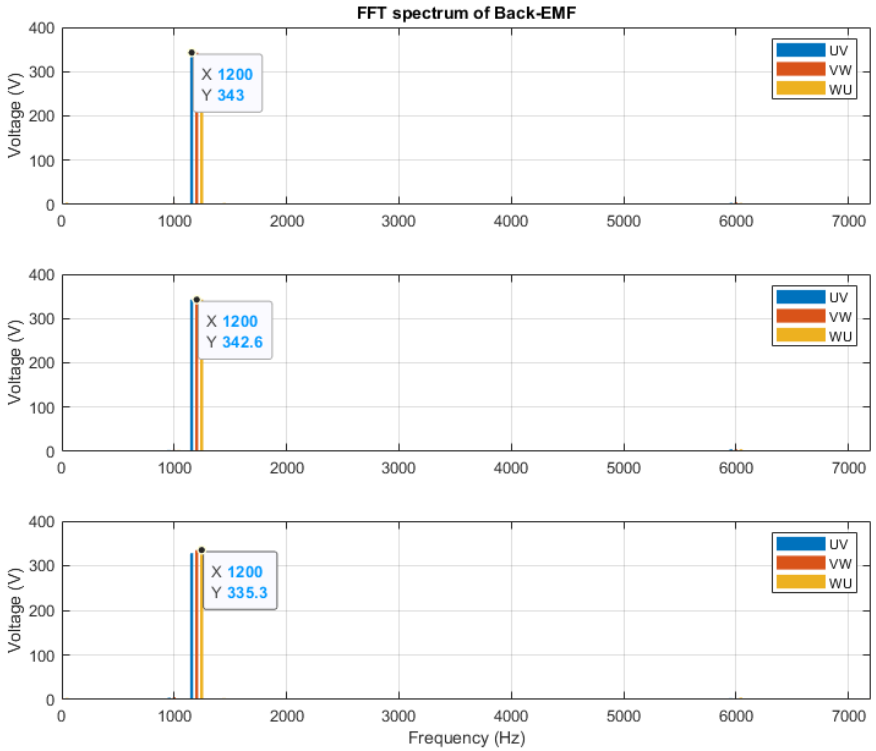


Fig. 8.32 FFT spectrum of measured line-line back-EMF in three modules (at 12000rpm).

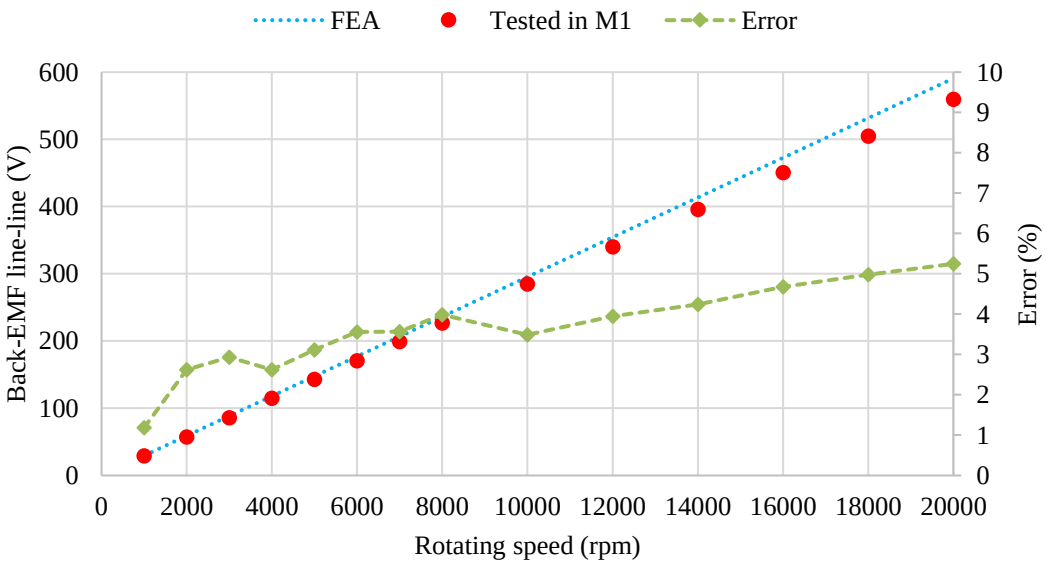


Fig. 8.33. Comparison of line-line back-EMF voltage between measured results in module 1 (M1) and FEA results (fundamental results).

8.4.2.4 Thermal management

In the commissioning test, the electrical machine was connected with prime mover. Between the electrical machine and power converters, the connection makes a

difference in temperature rise of windings.

If the cables of phase winding and power converters are not connected, it was supposed that no current in the winding, nor temperature rise in the winding. In fact, current clamp was used to measure the current in the cables. The high dv/dt can generate current in the winding, as well as temperature rise. The temperature rise in the windings was monitored.

As introduced in Chapter 8.2.1, temperature sensors were arranged in all the phase in the slot and end-winding, M1 and M2 are selected to monitor the winding temperature. During the commissioning, the temperature rises of phases increased from ambient to 100 degrees, in 43 minutes (the prototype was driven from standstill to maximum, 20 krpm). After the commissioning, the record was stopped. The record of temperature rise during the commissioning test is shown in *Fig. 8.34*. The highest hot point can be founded in M2-V, and the temperature rise in M1 were relatively low. The coolest point was in the M2-U, while their temperature difference can be recognized, about 18 degrees. This temperature difference is determined obviously by the cooling path and inlet.

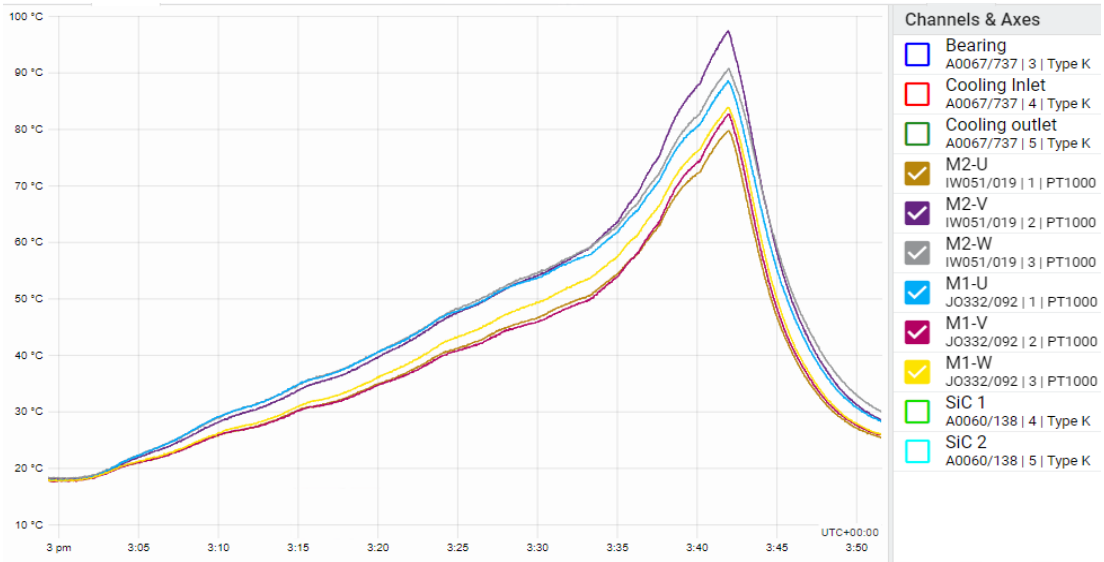


Fig. 8.34 Temperature rises during the commissioning.

8.5 On-load test

In this test procedure, three modules were connected with three converters, independently. Bidirectional DC power supply is connected with converters. As shown in *Fig. 8.35*, to avoid EMI issues, metal boxes were bespoken to contain the

converters for shielding, as well as the control box. Several holes were drilled in the metal boxes for heat emission. Thermal sensors were stick on the SiC power modules for temperature rise check.

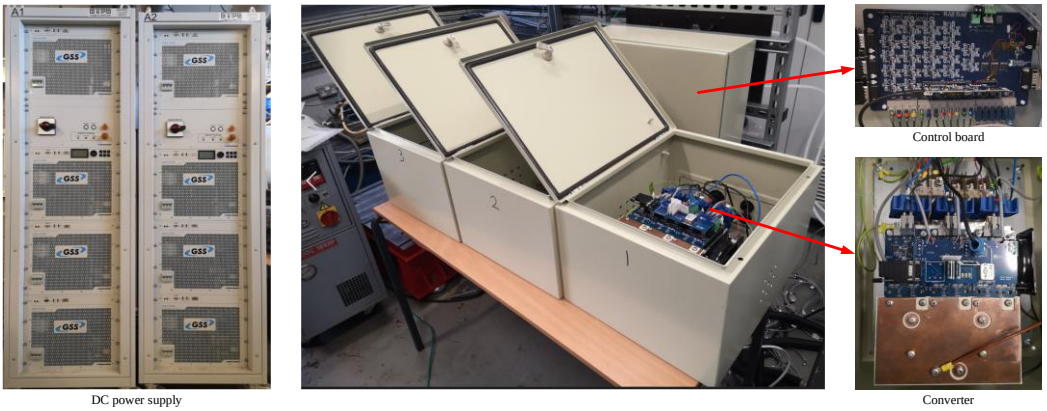


Fig. 8.35 Three converters and control box.

Although the results of commission provide a basis for following test, the on-load test was started from the combinations of low speed (started from 3000 rpm), DC voltage (started from 270 VDC) and input current (started from 5 A).

The on-load operation points were carefully selected. during on-load operation, it is important to ensure that the operating point is far away from the critical speed points, such as 4500 rpm and 12000 rpm. All the measured operation points are shown in *Fig. 8.36*. Firstly, concerning the safety of machine, initial operation points were test under 270 VDC. Then, operation points which can achieve higher output, were tested under 540 VDC.

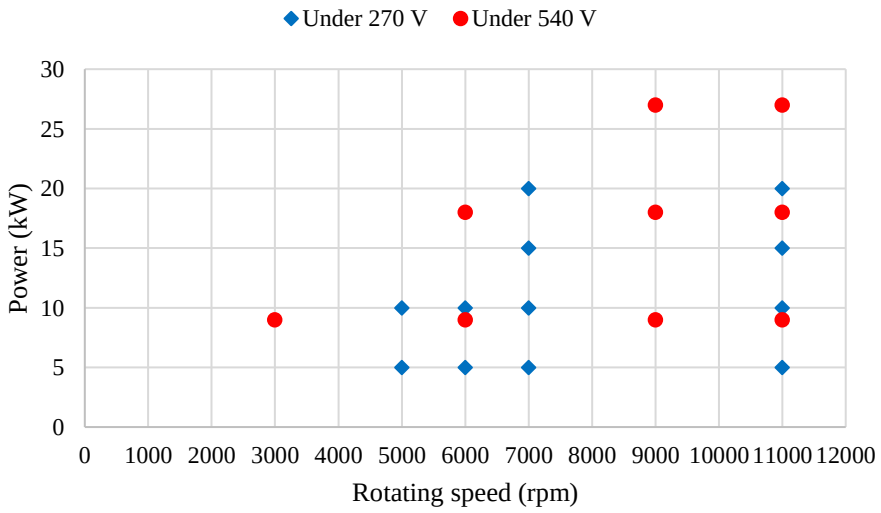


Fig. 8.36 Operation points of on-load in the test procedures.

8.5.1 On 270 VDC

To reduce the complexity of machine control and maintain a cool winding, there were two limitation was set: 1) avoid flux weakening limitation in the initial test. 2) The peak phase current is lower than 40 A. To avoid flux weakening under 270 VDC, the testing speed was started from low speed to 7000 rpm. If the speed of prime mover is higher than 8000 rpm, flux weakening is needed for machine control.

During the test, the input power, phase current, output torque, and temperature rise were measured for evaluating the machine performance. The scatter figure of current and torque is shown in *Fig. 8.37*, compared with simulated results. It can be found a linear trendline between current and torque, even at varied speed. The slope of the curve is named as torque constant, K_T (Nm/A), and it is 0.652 Nm/A of this prototype machine. The output torque T is directly proportional to the current I through the windings regardless of the rotating speed. The torque constant is specific to the topology design, including its permanent magnet property, number of wire turns, and armature length.

$$T = K_T \cdot I \tag{8.5}$$

In the conventional three-phase machine, the torque constant, K_T and the back EMF constant, K_E are equal. This can be demonstrated by applying the law of conservation of energy: input electrical power must be equal to output mechanical power plus motor electrical losses. Similarly, this relation is applicable in multiple three-phase machine, K_T and K_E are equal in every module or sector. If every module or sector are identical, then the K_T is multiple of K_E, which is determined by the amount of three-phases. The constants of K_T and K_E of this innovative topology are shown in Table 8.7. The ratio between K_T and K_E is not 3, as the errors are a combination of the vibration sensor and the asymmetry caused by the three sectors. These errors have been found in the static measurement in resistance and inductance.

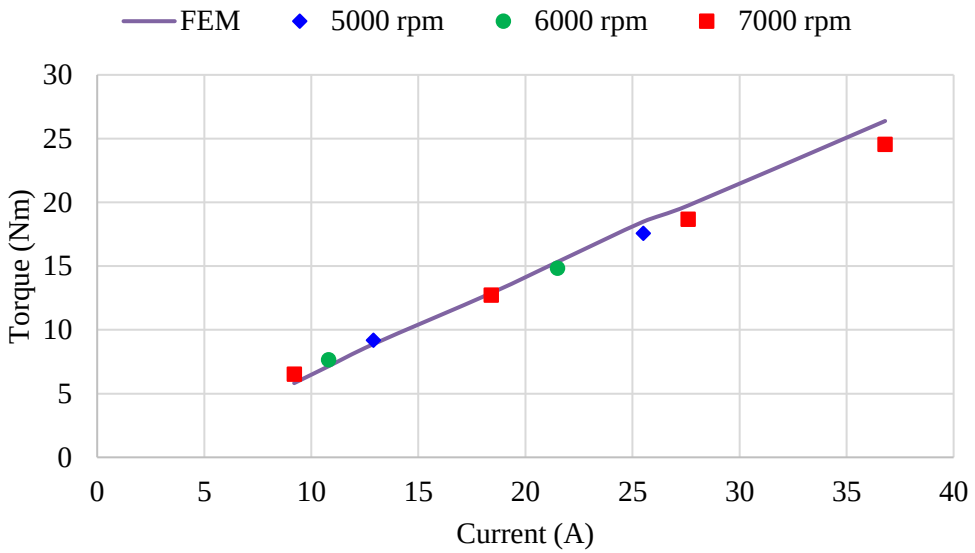


Fig. 8.37 Measured current vs. torque under 270 VDC.

Table 8.7 Measured back-EMF constant and torque constant.

Constant	Value	Unit
K_T	0.652	Nm/Amp
K_E	0.276	$V/rad \cdot s^{-1}$

The peak phase current and corresponding output power at varied speed are shown in *Fig. 8.38*. For same output, the operation points with higher speed draw low current from converter sides. Similarly, the comparison of measured and simulated current vs. efficiency under 270 VDC is shown in *Fig. 8.39*. The tested efficiency consisted of electrical machine and converters, are lower with higher load. For same operation speed, the higher load can introduce higher losses.

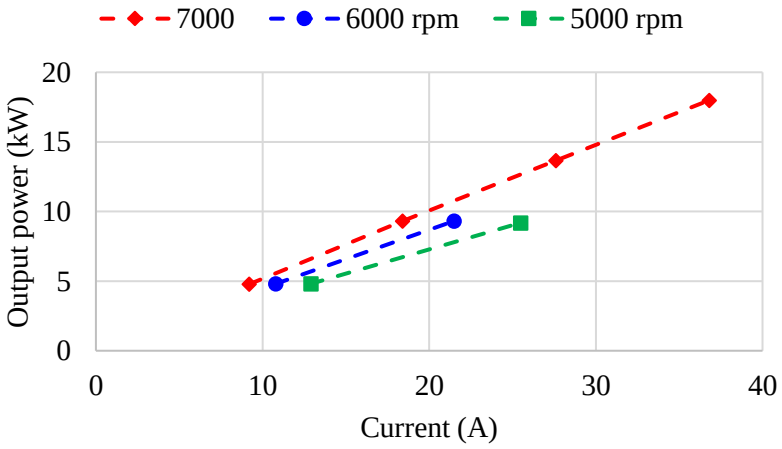


Fig. 8.38 Measured current vs. output power under 270 VDC.

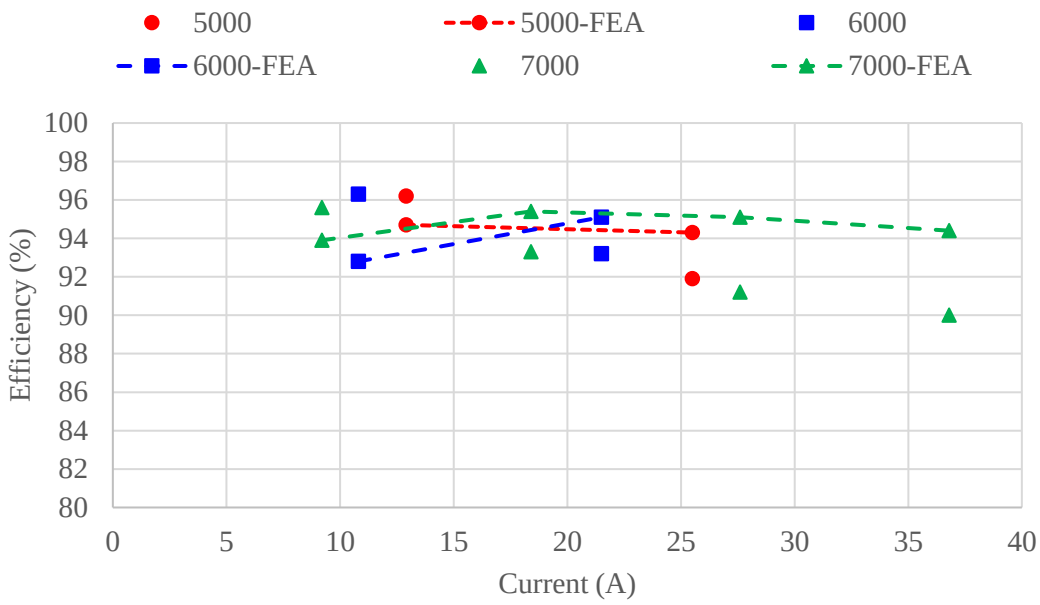
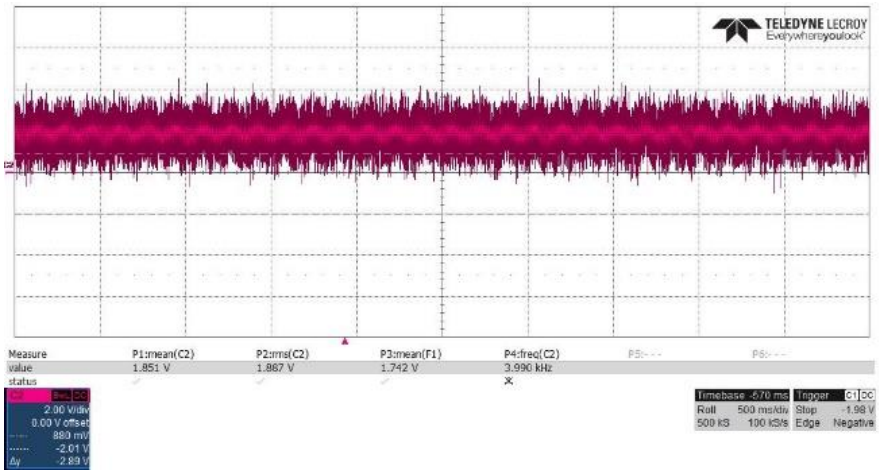


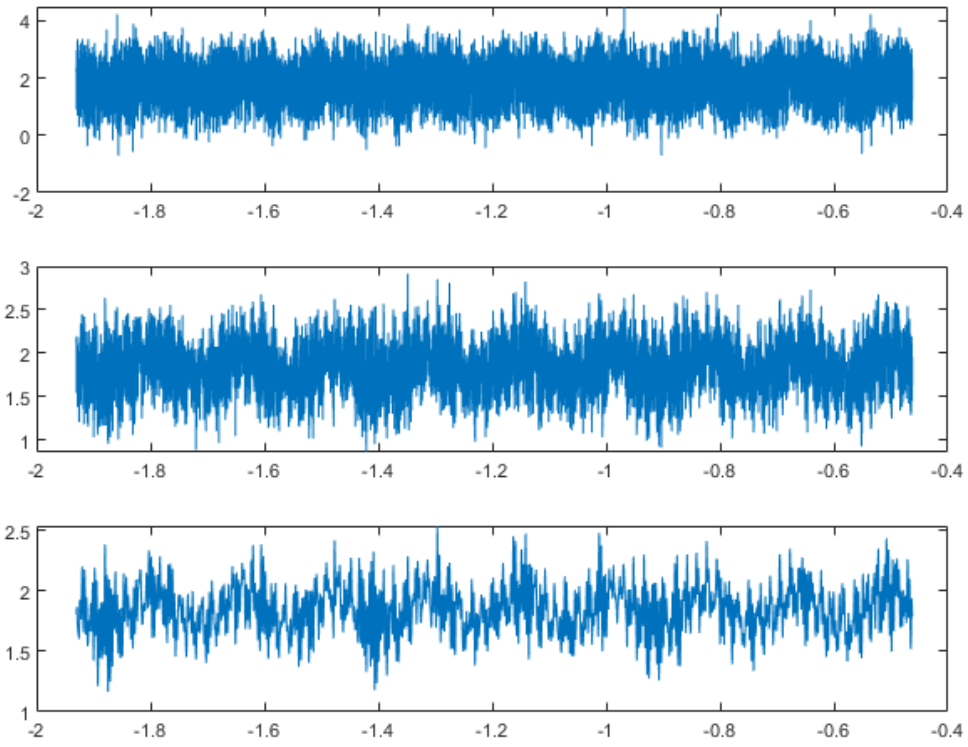
Fig. 8.39 Comparison of measured and simulated current vs. efficiency on 270 VDC under varied speeds (5000 rpm, 6000 rpm and 7000 rpm).

The operation point of 7000 rpm on 270 VDC was selected to illustrate the detailed performance. Based on the voltage signal feedback of torque sensor, the raw data of torque curve is shown in *Fig. 8.40*. Concerning the initial offset of torque sensor and filtering the raw data, the average output torque is 24.5 Nm.

The transient temperature rise was record by temperature sensors embedded in phase windings, via the software of PicoLog. The transient temperature rise vs. real time of 7000 rpm with 24.5 Nm output is shown in *Fig. 8.41*. It rises from 20 ℃ to 75 ℃, where the hot point occurred in the Phase W in module 1. There are discontinuous areas in these curves which were caused by EMI issues.



(a)



(b)

Fig. 8.40 Measured output torque curve (a) raw data. (b)Filtered data.

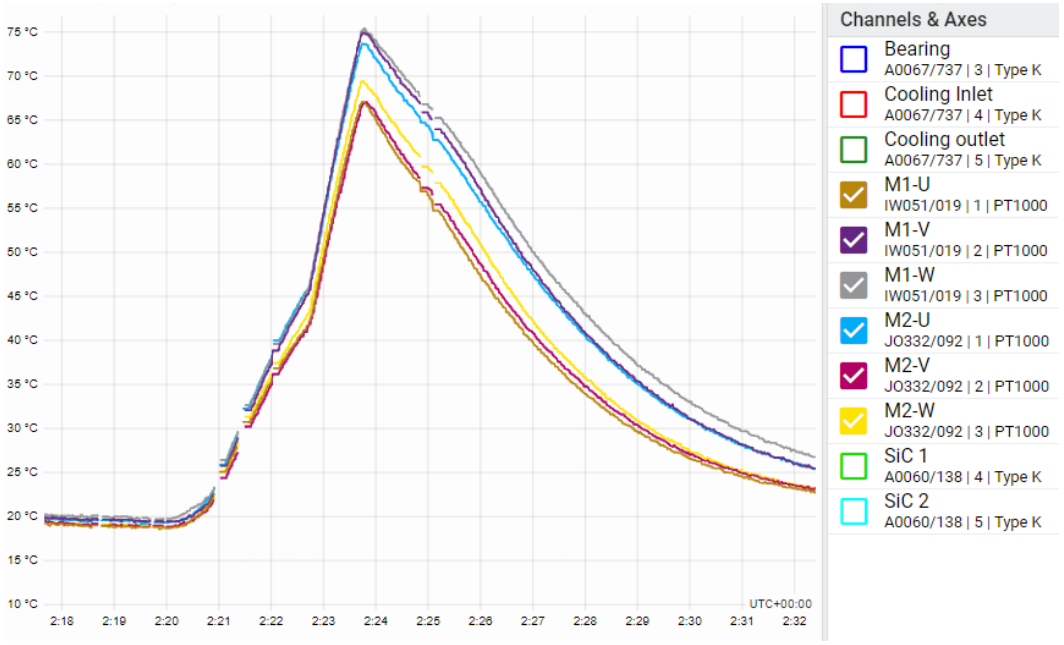


Fig. 8.41 Transient temperature rise of 7000 rpm with 24.5 Nm output.

8.5.2 On 540 VDC

Based on the results 270 VDC and same setup, similar test procedures were carried out under 540 VDC with wider speed range, from 3000 rpm to 11000 rpm (rated speed). The maximum speed reached during the on-load test was limited by the

heavily encountered EMI issues during high-speed testing.

Similar scatter figure can be plotted to illustrate the performance on higher DC voltage, such as measured current vs. torque (*Fig. 8.42*), current vs. efficiency (*Fig. 8.43*), current vs. output power (*Fig. 8.44*), output torque and transient temperature (*Fig. 8.45*). Operation points with high load exhibits bigger gap with simulated results; besides, low speed operations have lower efficiency, such as 3000 rpm and 6000 rpm, with bigger gap with simulated results.

Due to the unstable reading from power supply on high load and torque (the raw data from torque sensor shown in *Fig. 8.45*), the calculated input power has big fluctuation. Then, it results in a big error between FEA results and tested results.

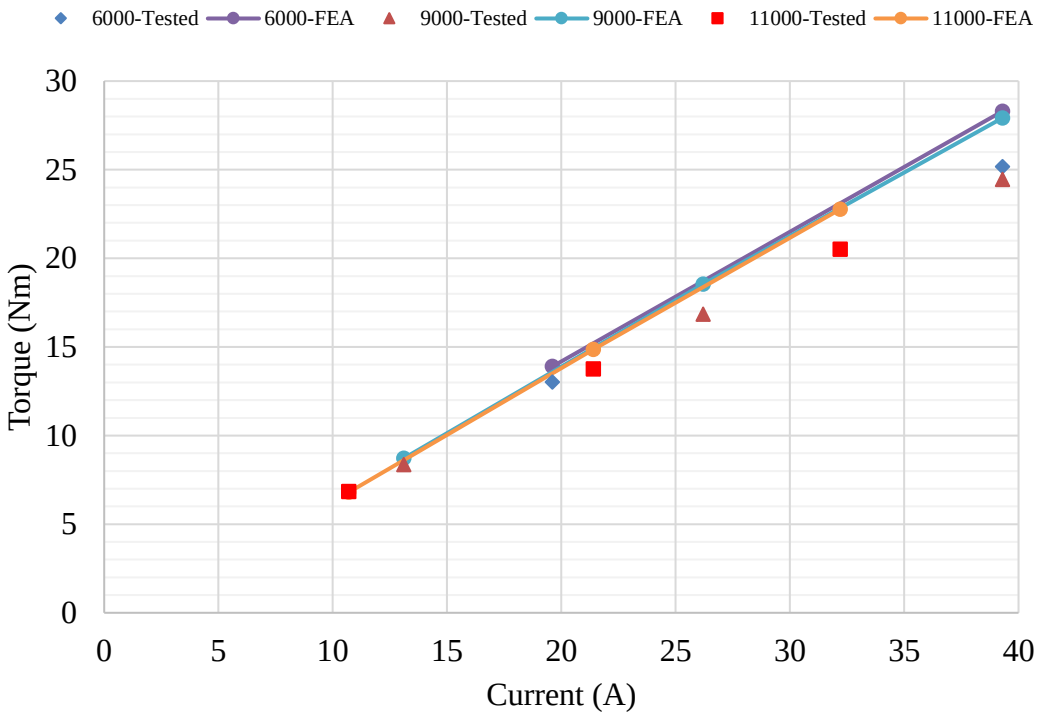


Fig. 8.42 Comparison of measured and simulated current vs. efficiency under 540 VDC.

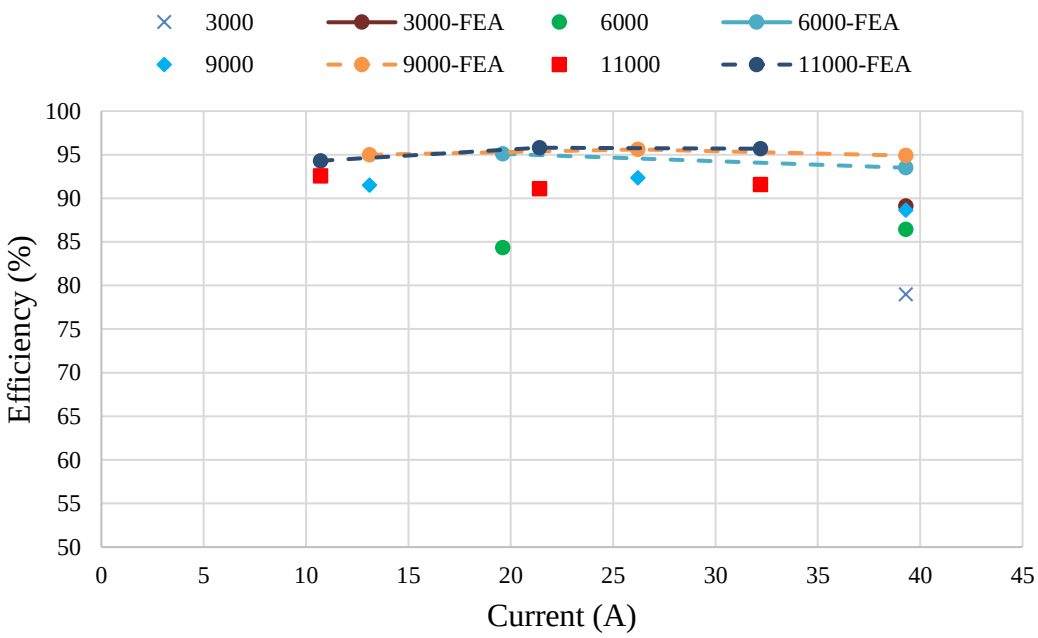


Fig. 8.43 Comparison of measured and simulated current vs. efficiency under 540 VDC.

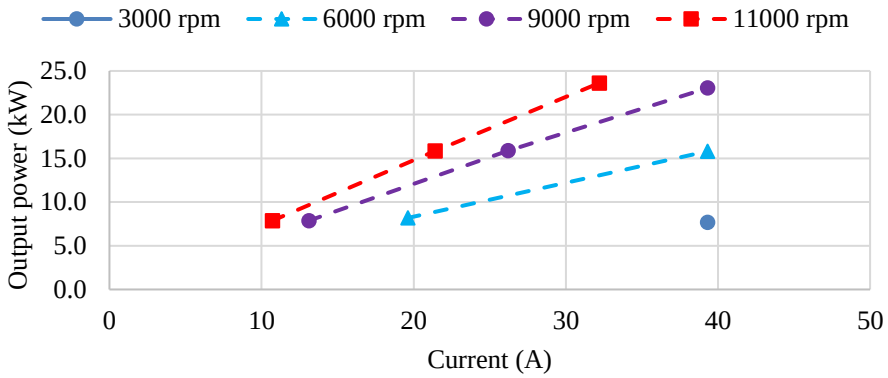


Fig. 8.44 Measured current vs. output power under 540 VDC.

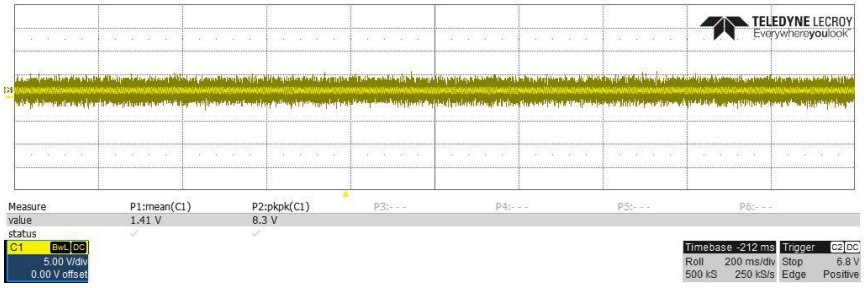


Fig. 8.45 Raw data of measured voltage output from torque sensor.

The main challenge on 540 VDC is the EMI issues. It can be found in the *Fig. 8.46*. The operation point is 11000 rpm with varied load. The signals from temperature sensors are easy to be affected due to EMI issues.

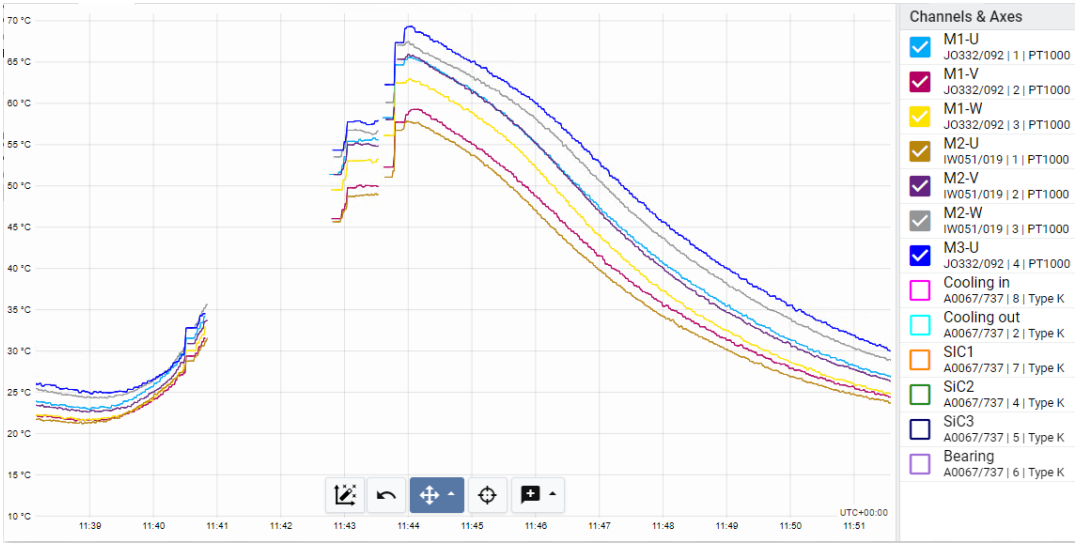


Fig. 8.46 Transient temperature rise of 11000 rpm under 540 VDC.

8.6 Faulty scenarios

8.6.1 Open-circuit (OC) fault

The tests of OC fault were carried out by inserting a circuit breaker between power converter and electrical machine, as shown in *Fig. 8.47* . To investigate the effect of OC phases to the performance of electrical machine. As shown in *Fig. 8.48*, the amount of OC phases starts from 3 to 6 phases (one to two sectors). The post-fault behaviour of OC has been investigated.

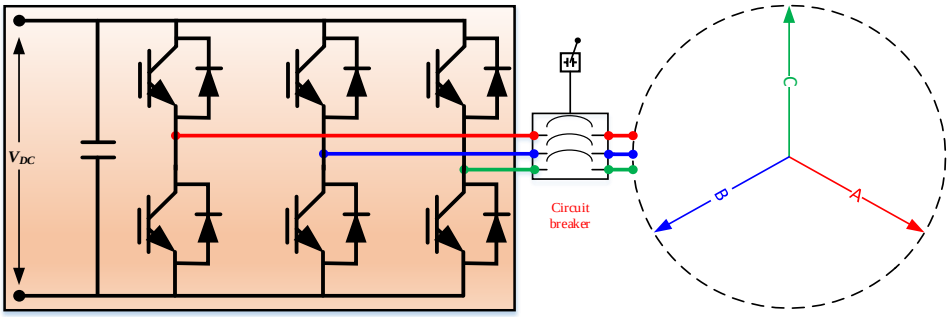
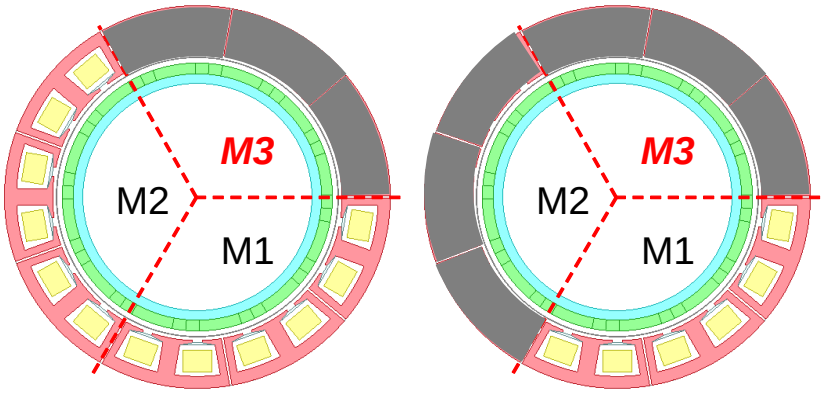


Fig. 8.47 Circuit breaker for open-circuit test.



(a) (b)

Fig. 8.48 Schematic of OC occurred in phase or sectors. (a) One sector OC. (b) Two sectors OC.

8.6.1.1 Output performance

These types of faults have been simulated in Chapter 5.3. Under the fault of OC, there are no current flow in phases, nor energy conversion. The output will decrease pro rota. The transient waveform of output torque from healthy to OC fault is shown in *Fig. 8.49*. The operation point with 6000 rpm, 20 A was carried out. The output torque in healthy status is 14.0 Nm. By introducing the OC fault in M1 or M1&M3, the torque deceases to 9.4 Nm and 5.0 Nm, respectively, and the remaining output ratio is 67.1% and 35.7%, which close to the expected ratio, 2/3 and 1/3, as listed in Table 8.8. The operation speed of 6000 rpm exhibits a noticeable vibration response, which can introduce errors in measuring the output torque and create a discrepancy between the tested results and FEA results, particularly when the M1&M3 OC fault is present.

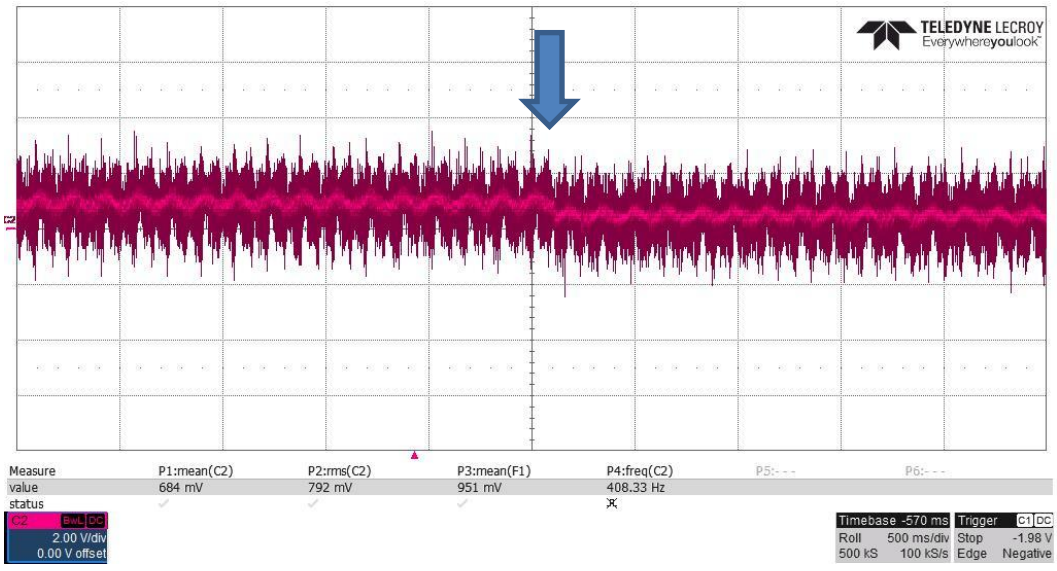


Fig. 8.49 Transient response of output torque.

Table 8.8 Comparison of measured post-fault output.

Module	Status			FEA result (Nm)		Measured value	
	M1	M2	M3	Torque (Nm)	Output Ratio	Torque (Nm)	Output Ratio
Healthy	On	On	On	15.0	100 %	14.7	100 %
M1 OC	On	On	Off	10.0	66.7%	9.4	67.1%
M1 & M3 OC	On	Off	Off	5.0	33.3%	5.7	35.7%

8.6.1.2 Response of vibration

To meet the requirement of fault tolerance, the electrical machine was expected to operate continuously in case of fault. In the post OC fault, the balance of radial force will be changed in some extent, due to the absence of OC phases. This scenario has been simulated by FEM and illustrated in Chapter 5.5.4. This unbalanced radial force will increase the vibration inevitably, while the contribution of electrical vibration will be increased. Then, acceptable vibration rise is a prerequisite for post-fault operation. This investigation was carried out and recorded, as shown in *Fig. 8.50*. This test procedure was started from low speed, 1000 rpm to higher speed; the data was distracted for analysis based on varied rotating speed. The statuses of random OC fault & varied speed are listed in the Table 8.9. These combinations consist of 3 speed points and 2 OC fault positions.

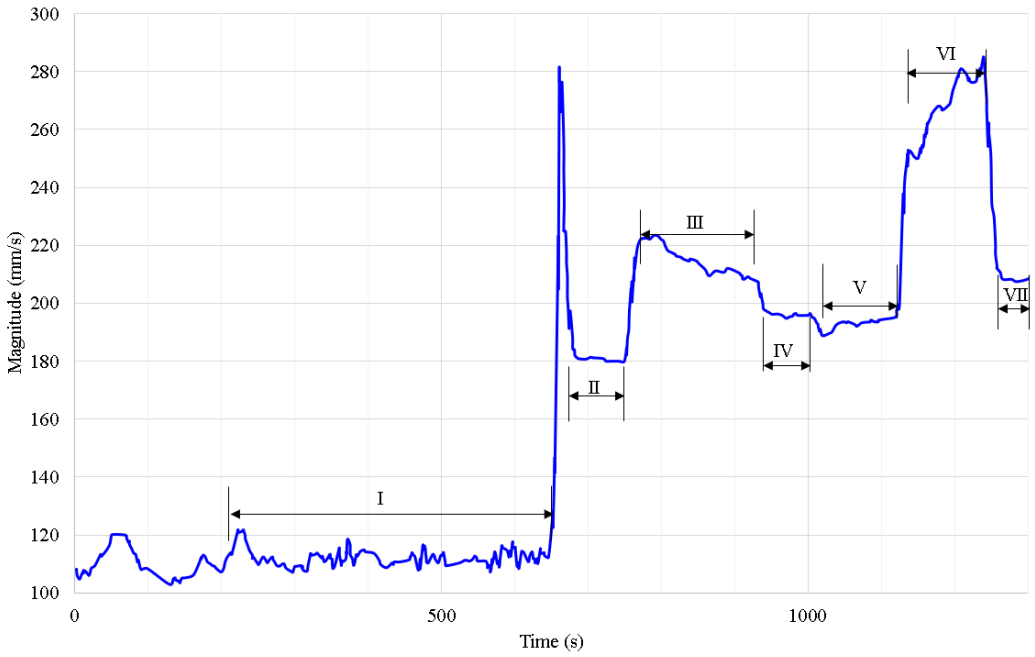


Fig. 8.50 Response of vibration speed of OC test.

Table 8.9 The status of the vibration test with random OC fault.

No.	Speed (rpm)	Status	Average vibration velocity (mm/s)
Before I	1000	Healthy	110.2
I	1000	2nd sector OC	114.5
II	5000	Healthy	181.1
III	5000	2nd sector OC	213.1
IV	5000	1st sector OC	196.0
V	6000	Healthy	192.3
VI	6000	2nd sector OC	276.4
VII	Ramp down		

The vibration response at 1000 rpm was shown in *Fig. 8.51*, because the electrical vibration is dominant contribution at this speed point. Whatever the statuses of machine, healthy, on-load (Phase current equals 5 A) or M1&M3 OC fault, the machine exhibits very low and stable vibration speed and acceleration, around 0.12 mm/s and 0.13 g, respectively. This proves that post-fault operation of OC in low speed are safe and insensitive.

The rotating speed 5000-rpm fall in between two critical speed points, 4500 rpm and 6000 rpm. Four scenarios were operated and compared, including healthy, M1 OC, M3 OC and M1&M3 OC. Compared with 1000 rpm operation point, the differences can be recognized. The vibration responses were plot by solid and dash line represented velocity and acceleration respectively in *Fig. 8.52*. Both of these two parameters are not sensitive to the statuses of phases, while one modular or two modules can not result in a vibration spike under 5000 rpm. Moreover, the position of faulty sector makes the difference increase of vibration speed. The M3 (3rd in Figure) exhibits higher effect on vibration velocity but lower vibration acceleration increase, compared with M1.

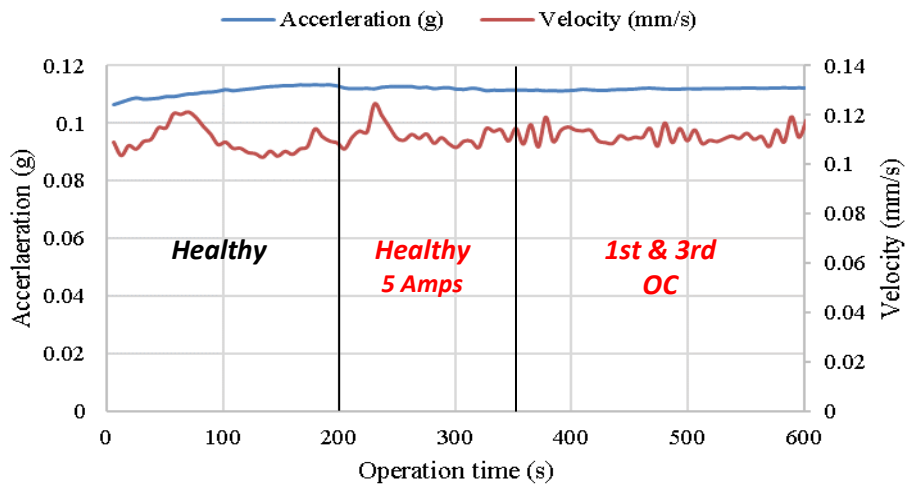
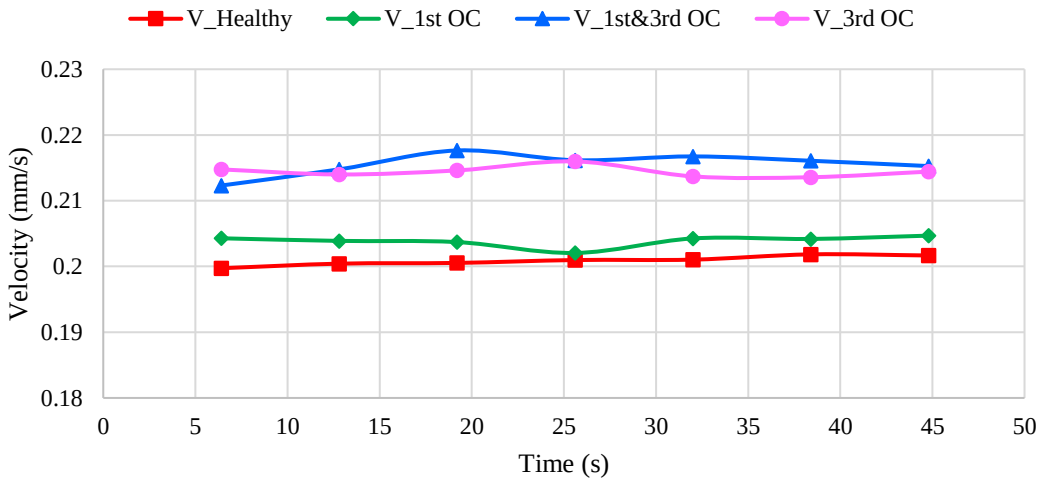
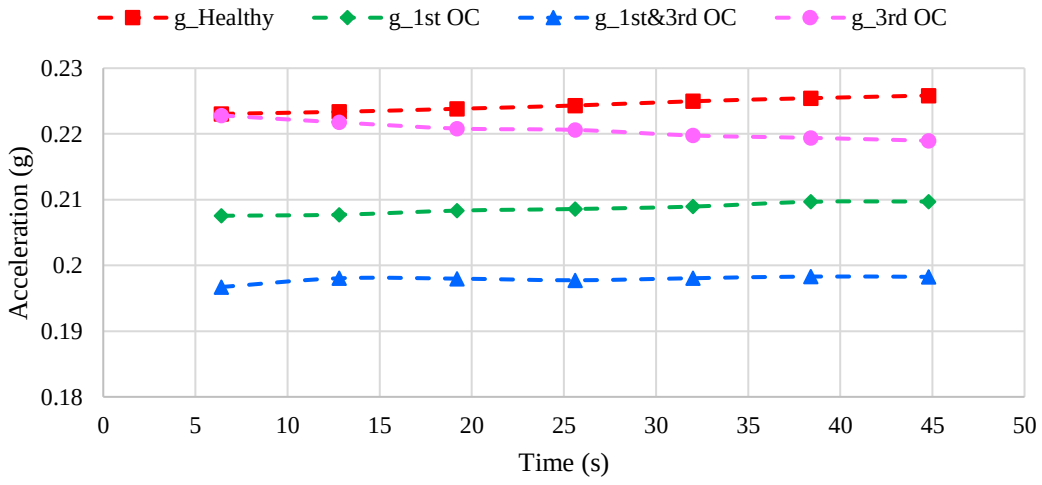


Fig. 8.51 Measured vibration response of post OC fault at varied speed at 1000 rpm.



(a)



(b)

Fig. 8.52 Measured vibration response of post OC fault at 5000 rpm (a) velocity (b) acceleration.

Based on the previous commissioning test, the rotating speed at 6000 rpm is a critical operation point which exhibits higher vibration even at healthy arrangement. Similar post-fault test procedure was carried out and the results is shown in *Fig. 8.53*. Unlike the operation point of 5000 rpm, post-fault vibration velocity and acceleration at 6000 rpm occurred obvious and predictable rise, as shown in Fig. It can be found that the M3 OC can cause a higher effect on vibration rise than M1 OC in velocity and acceleration. Although the OC fault can intensify the vibration response, the total behaviours are far below the safety threshold. It is feasible to maintain operation in the case of OC faults.

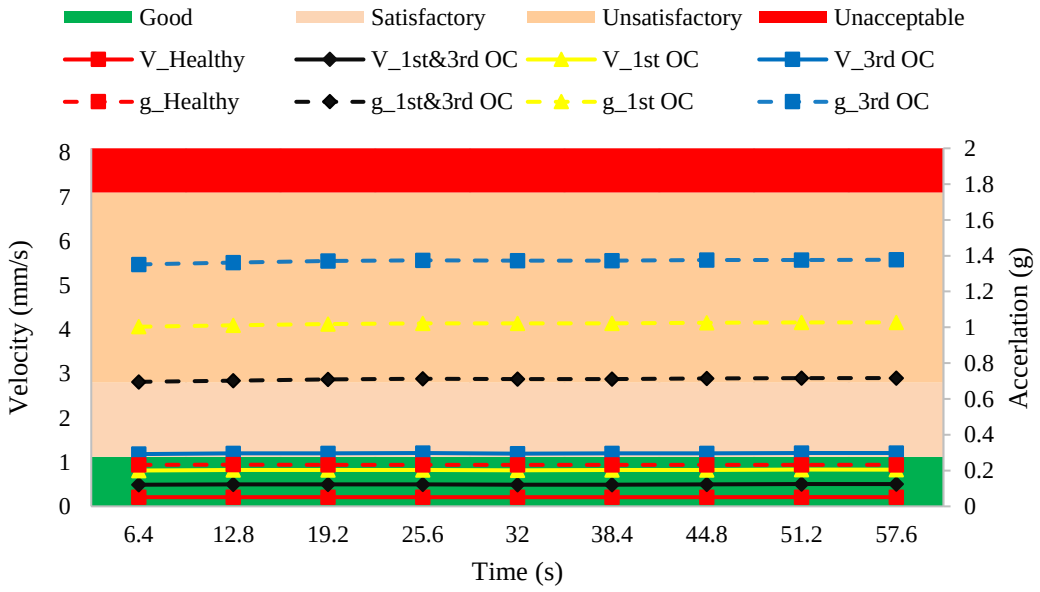


Fig. 8.53 Vibration response of post OC fault at 6000 rpm.

8.6.1.3 Current of Post fault

During the manual OC fault test, the phase current in three independent modules were tested and recorded simultaneously. Due to the fault tolerant design, these three modules are totally identical but independent, such as the phase current in every module. In healthy scenario, the waveforms of phase current in three modules are the same, as shown in *Fig. 8.54* (a). The current in three modules under the fault of one module or two modules are shown in *Fig. 8.54* (b) and (c). The phase current in healthy part is not affected at all by faulty parts.

Similarly, phases (U, V and W) temperature rises of in M1 and M2 were recorded during the test, as shown in *Fig. 8.55*. M1 was set to connect converter all the time;

a circuit breaker was inserted in the connection of M2, which was used to switch the M2 status, healthy or OC. The tests were the combinations of operation speed (1000, 5000 and 6000 rpm), load (0, 10 or 20 A) and healthy/faulty M2. With the increase of speed or load, the temperature increases continuously in phases. The OC fault can occur randomly in M2, then the temperatures (solid lines) decrease correspondingly, as the solid lines shown in *Fig. 8.56*. For a stable operation at 6000 rpm with 20 A phase current, the multiple OC occurred in M2. The temperature in M1 (dash lines) were stable and impervious. These results prove the capacity of thermal isolation between different modules.

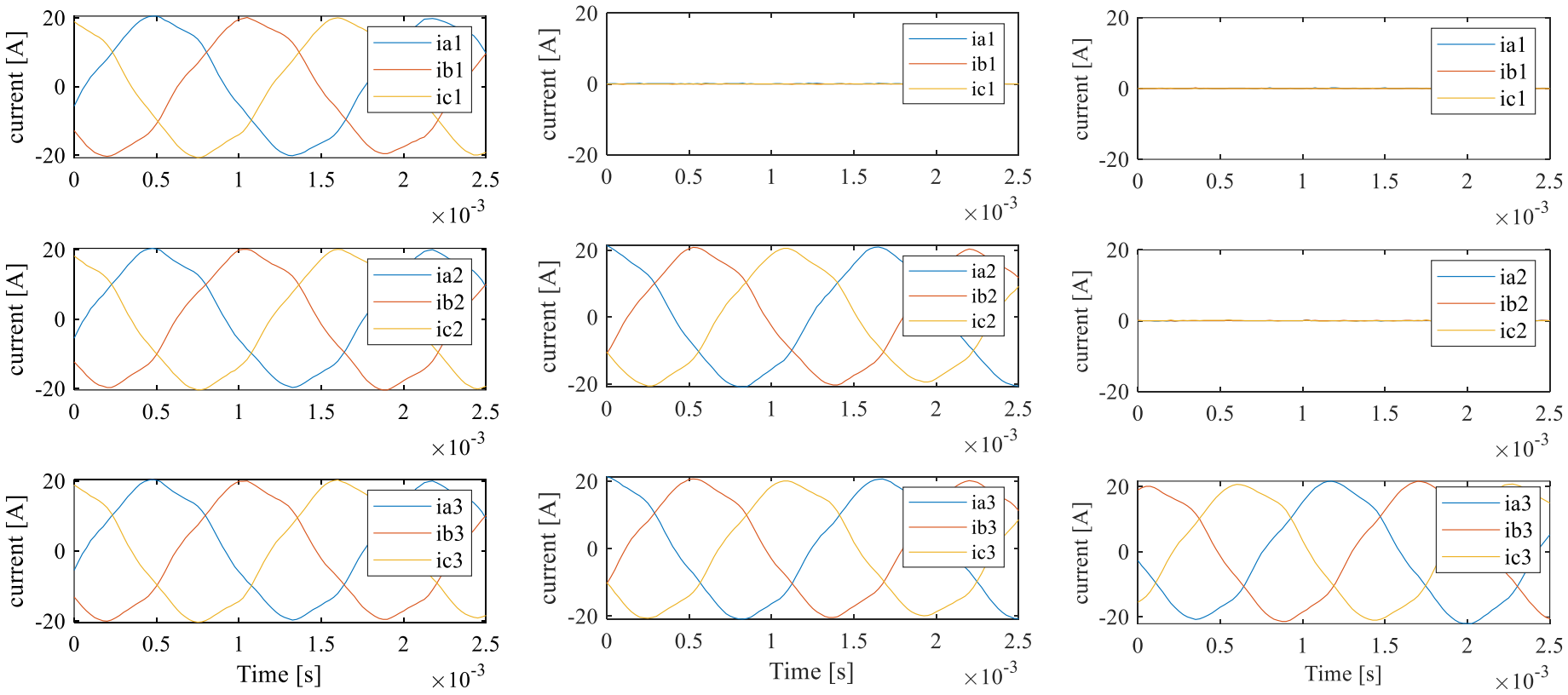


Fig. 8.54 Waveform of phase current under varied scenarios. (a) Healthy. (b) OC in one module. (c) OC in two modules.

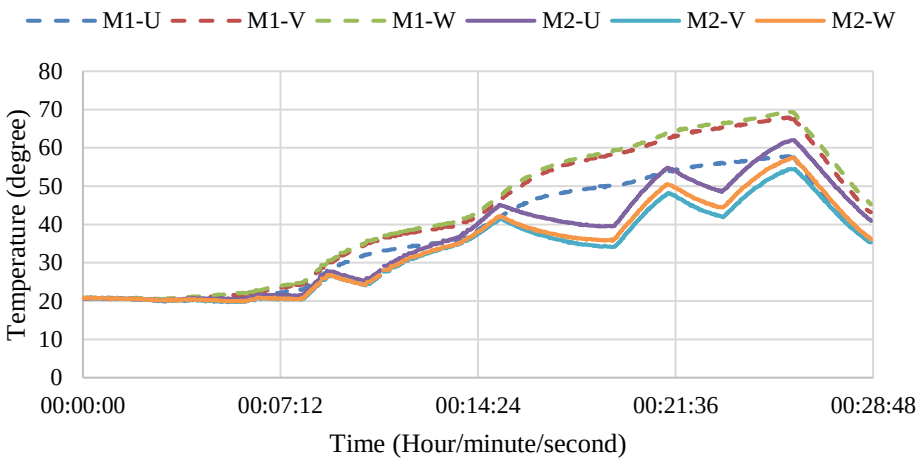


Fig. 8.55 Measure temperature curves in combined test of speed (1000, 5000 and 6000 rpm), load (0, 10 or 20 A) and healthy/faulty M2 (solid lines).

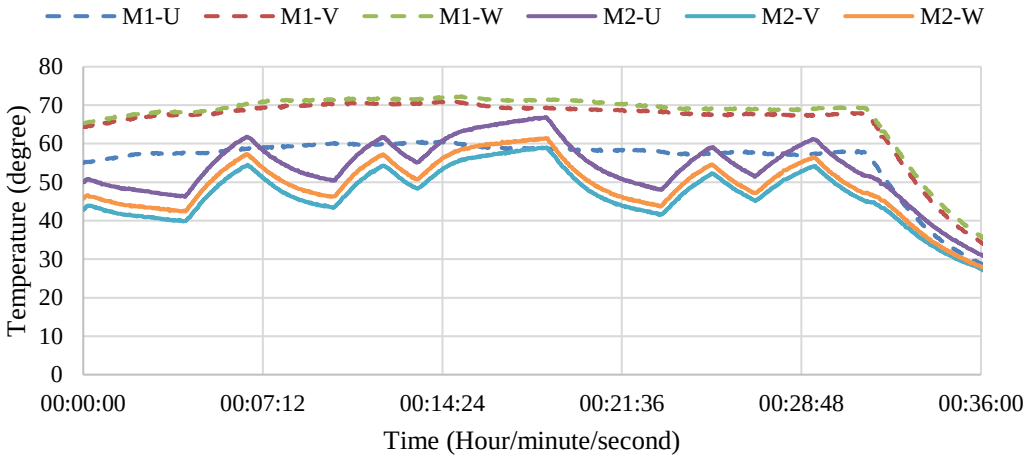


Fig. 8.56 Measured temperature fluctuation of M1 and M2 under 6000 rpm with 20 A phase current.

8.6.2 Short-circuit (SC) fault

The causes and types of short-circuit fault in windings are diverse. During the real operation, three-phase winding is connected with power converter. As introduced in Chapter 3, SC faults may be caused by multiple reasons. Generally, the electrical machine itself is robust and reliable. The winding and cooling system can be designed to withstand fault current in case of phase-phase short-circuit. Nevertheless, post-fault operation is not allowed to operate in the case of turn-to-turn short circuit. The position, amount of SC turns, and corresponding faulty current are not unknown and quantified correctly. If the machine operates in the case of turn-turn SC, the

status will get worse.

The SiC-based converters in machine control introduce frequently EMI issues. The high switching frequency combined the high dv/dt may result in interference in other electronics.

8.6.2.1 Unexpected fault

During the test, an unexpected electrical machine faults occurred which caused by power converters faults, and finally the one phase of machine was damaged. Compared with designed SC experiments, this unexpected fault is close to the reality. During the effect of EMI, the converter operates which not following the designed command.

The faulty phase currents are shown is *Fig. 8.57*, which healthy phase currents should be three-phase sinusoidal waveform. This disordered current caused unexpected temperature rises in relevant windings.

The curves of temperature and converters can explain the process of fault. As shown in *Fig. 8.58*, there were two discontinuous areas in all the curves of phase windings (M2-U/V/W and end-winding). Once the converter started operation, the signals of thermal sensor was interfered and lost in short time, which illustrates the fast switching actions makes power electronic equipment a significant source of EMI to nearby devices. Following a period of test operation, temperature spikes can be recognized in the phases of M2. The maximum temperature can reach 180 ℃, which is far beyond designed values.

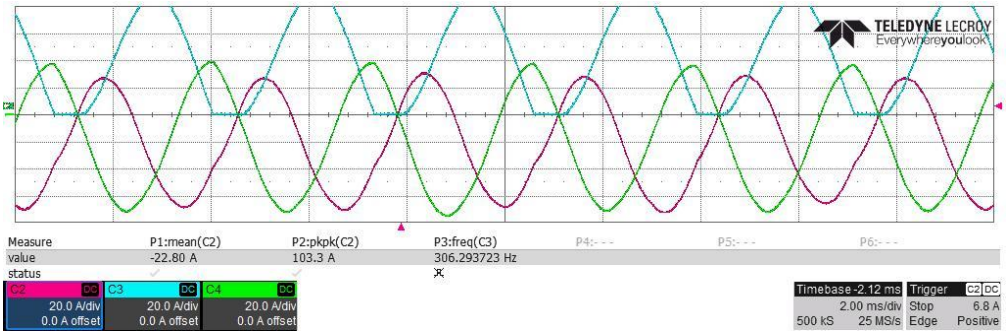


Fig. 8.57 Fault current during the EMI issue.

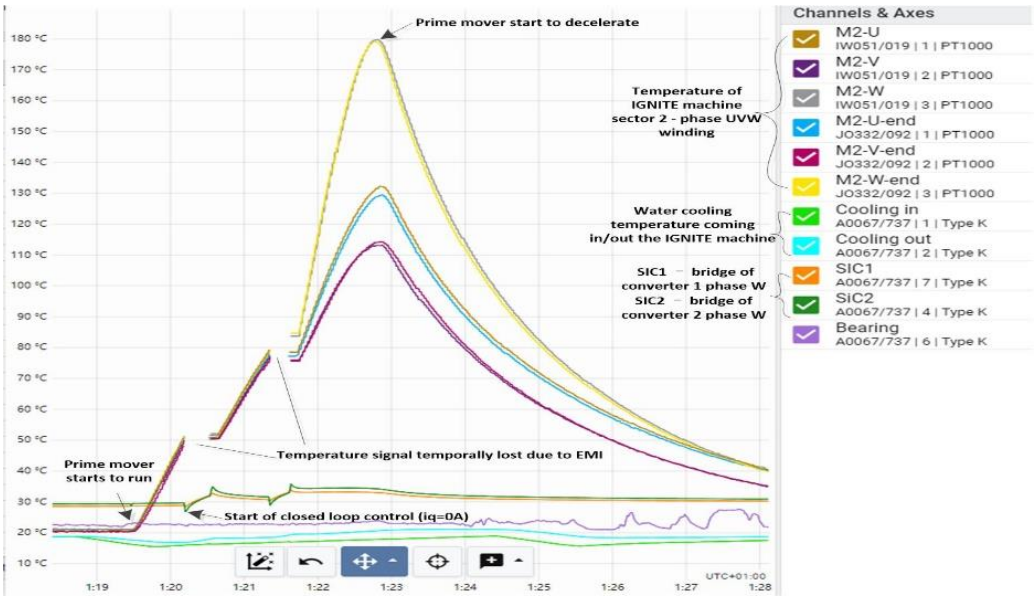


Fig. 8.58 Waveform of fault current during the EMI issue.

Similarly, this kind of faults also occurred in different modules. It was shown in the *Fig. 8.59*. During a stable test, a temperature spike can be found in Phase U of M3, which temperature increases from 38℃ to 73℃ in 12 seconds. Then, all the phases become cool after switching off the test.

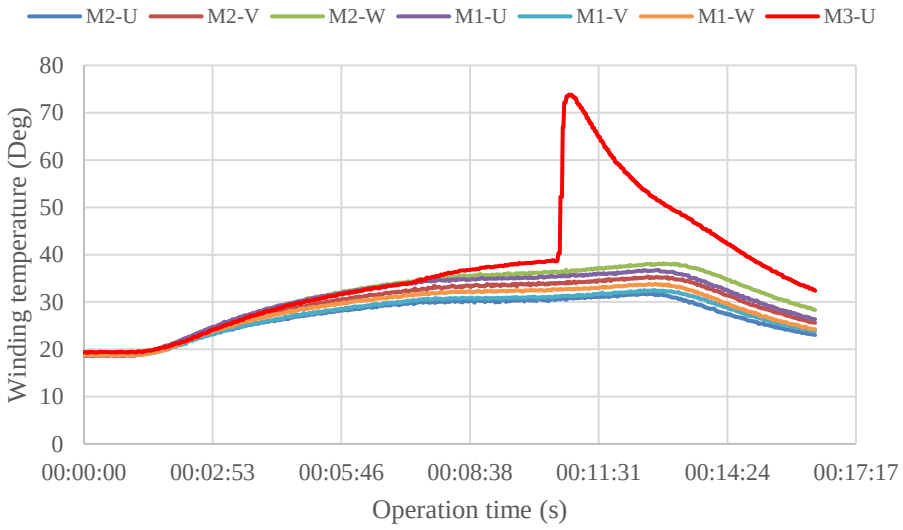


Fig. 8.59 Example of unexpected temperature rise in phase winding during the machine test.

8.6.2.2 Critical failure

After several tests of this prototype machine, its converters were blown up and relevant machine module was involved in this failure. Phase V of module 2 was damaged finally. After several explosion of capacitor in converters, the temperature

sensor of M2-V reached high reading then to an unreasonable low reading (as shown in *Fig. 8.60*), which means this sensor has damaged in this test. Extreme high transient current in this winding generated high temperature which burn the winding and sensor.

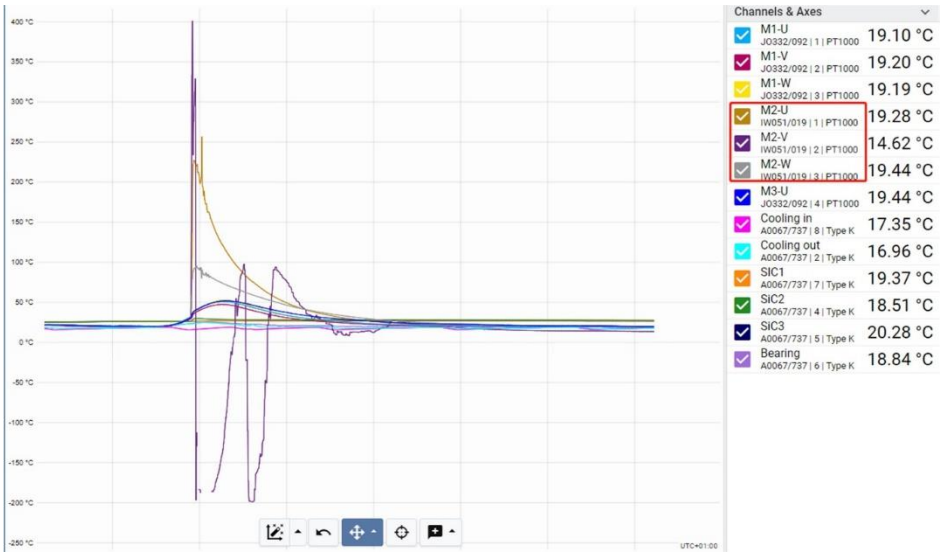


Fig. 8.60 Temperature record of critical failure.

This prediction was proved by parameter measurement. Static measurement of resistance and inductance of faulty winding was carried out, based on same test procedure as before. The tested results are shown in Table 8.10. Compared with healthy values, the results of resistance and inductance decreased sharply. This means turn-turn SC fault is existed in this winding.

Table 8.10 Static measurement after converter damaged.

Parameter test		Resistance ($m\Omega$)	Inductance (μH)
50 Hz	Healthy	71	403
	Faulty	31	32
2000 Hz	Healthy	505	350
	Faulty	2.8	2.3

8.6.2.3 Review of SC fault

One of the targets of fault tolerant design is the competence of thermal isolation. The turn-turn SC fault is a fatal but ideal scenario to verify this capacity. In this case, M2 was short-circuited finally by unexpected faults. It is clear that winding temperature spike occurred in M3 due to faulty current. However, the temperature of adjacent

windings in other modules, M1 and M2, were stable, which almost affected by the high temperature of faulty windings. This proves a better thermal isolation in this machine.

The advanced control, such as current injection, can make it feasible for continuous operation in the presence of SC fault. This kind of work focuses on machine control side, so it is not validated in this thesis.

8.7 Conclusion

The complete details of prototype and verification of performance were implemented in this chapter. To achieve feasibility of manufacture, bespoke mechanical design has been applied.

Test procedures was started from static measurement, including resistance and inductance. There are three independent modules in this machine. Some errors were founded in the test results, which were expected to identical between different modules.

Dynamic tests were begun from commissioning, while the machine was driven by prime mover to spin from standstill to the maximum speed, 20000 rpm. There were several critical speed points, such as 4500, 6000 and 12000 rpm. But, the vibration source attributes to the testbed, prime mover or machine itself. The back-emf of three modules prove their consistency.

Several operation points were selected to carry out the on-load test, based on the power supply of 270 VDC and 540 VDC, respectively. Meanwhile, the output, temperature rise was recorded. Compared with simulation results, the tested results illustrated a good match under 270 VDC.

Faulty scenarios were designed to verify the fault tolerance, including open-circuit and short-circuit. The OC tests approve the simulation results, while the machine can maintain operation under the OC faults. The sudden SC faults occurred during the test, which finally damaged one phase machine. But the results have proved the better performance in isolation, thermal, magnetic and electrical.

Chapter 9 Conclusion and future work

The main research work and contributions of the thesis are summarized in this chapter. Besides, the limitations and the potential future work are also included.

9.1 General conclusion

The continuous efforts of aircraft electrification are pushing the development of traditional aircraft towards MEA. On conventional aircraft, more and more on-board secondary system, are replacing with electrical counterparts, for energy conversion. Among aircraft electrification, the permanent magnet electrical machine plays an important role due to its many merits, such as high power density and efficiency. The electric power generation system is one of the pillar systems supporting this change among emerging systems. Currently, the PMSG has been a topic of significant research interest.

To investigate the feasibility of PM electrical machine as safety-critical application on aircraft, a comprehensive technical review of failure mode, fault tolerant topologies for PMSM in transportation electrification has been summarized. The machine faults distributed in electrical, magnet and mechanical issues have been introduced in sequence. To improve the fault tolerance and fail-safe strategy, fault tolerant machine approaches were also introduced. Multiple three-phase topologies still are the main choices for the safety-critical aircraft application..

Based on the requirements capture and initial definition, an iterate design process of permanent magnet starter/generator was carried out. The core challenges are the capacity of high power density and fault tolerance. The design process is demonstrated by the method of multiple-objective and multiple-discipline optimizations, with the objectives of light weight, high efficiency and low SC current. After optimization and selection, the 18 slot/12 pole surface mounted PM machine shows the better comprehensive performance than other topologies under the restriction of specification and space envelop. These conclusions were selected as benchmark for following FT improvement.

To pave way for the operation in the fault scenarios, fault partition designs have been done in electrical, magnetic and thermal isolation. Based on the electromagnetic performance rank, the feasibility of multiple three-phase for all candidates have been illustrated. Concerning the balance between reliability and cost, dual three-phase and triple three-phase are mainstream candidates compared with quadruple and sextuple three-phase. Triple three-phase 18 slot/12 pole, single layer concentrated winding, is determined as the initial candidate for this application. To pursue further fault tolerance, the concept of modular design was applied, by splitting the whole stator into independent segments.

Thermal management plays an important role in the operation, especially for high power electrical machine. For FT machine, thermal isolation is an essential capacity. Concerning the performance and cost, water jacket cooling was selected for thermal management of this machine. And, in this modular triple three-phase machine, the presence of segment gaps in the stator did not affect the temperature rise. To simulate short-circuit in specific windings, extra loss was added. The results illustrate few interactions between segments in thermal conduction. This kind of effect can be regarded as thermal isolation. In the post-fault operation, it is feasible to operate continuously while one segment suffering damage of high heat.

After the electromagnetic, thermal and fault tolerant design, the final design of this electrical machine was given, which make it possible in real application. Besides, fault monitoring design was completed, based on extras sensors, such as search coils and RTDs. All the sensors can provide real-time results to evaluate the potential symptom of faults. A 3D mechanical model was used to carry out mechanical analysis, which focus on rotor stress and modal analysis, due to the high speed operation. The strength of carbon fibre sleeve was checked to select an appropriate thickness. Loads on the rotor shaft have been investigate for the bearing selection. Based on these results, detailed considerations for mechanical design and assembly were carried out. To ensure the design of electrical isolation, independent electrical interfaces are highlighted. Based on these details, machine can be manufactured for prototyping.

Test procedures were started from static measurement, including resistance and inductance. There are three independent modules in this machine. Some errors was

founded in the test results, which were expected to identical between different modules. Dynamic tests were begun from commissioning, while the machine was driven by prime mover to spin from standstill to the maximum speed, 20000 rpm. There were several critical speed points, such as 4500, 6000 and 12000 rpm. But, the vibration source attributes to the testbed, prime mover or machine itself. The back-emf of three modules prove their consistency.

Several operation points were selected to carry out the on-load test, based on the power supply of 270 VDC and 540 VDC, respectively. Meanwhile, the output, temperature rise was recorded. Compared with simulation results, the tested results illustrated a good match under 270 VDC.

In general, this thesis provides a complete design progress of fault tolerant electrical machine for aircraft application, from requirements to implementation. This modular topology could be generalized for safety critical application.

9.2 Future work

Although some contributions of the research work have been verified in this thesis, various potential further research works can be investigated further.

Update cooling method. Based on current cooling method, the output power is 30 kW. Additionally, winding potting method is an available method to allow higher current density in the stator slot. Then, the output power could be improved to 50 kW.

Further Modular design. Modular concept could be extended to the whole electrical machine. The stator segment and housing can be integrated as independent unit, to pursue higher fault tolerance. Then, interchangeability can be achieved in big volume/size electrical machine in case of winding faults.

System level design. To pursue high performance and reliability, the electrical machine should be designed with power converter together rather than independent design. The prototype machine is damaged by unexpected faults caused by converter. With the application of new power modules, new requirements are increasing critical for machine design, such as breakdown voltage. High quality insulations are needed for machine windings, slots, etc.

Lightweight design. High power density was set as a core target in the multiple-objective design. But the weight of other auxiliary components were ignored. For aircraft application, the design process should do an overall consideration rather than active parts. The housing and cooling components should be optimized design, then the whole unit could be compact.

Updated test procedure. In the validation of fault tolerant performance, only open-circuit (OC) and phase-phase short-circuit (SC) faults were considered. In fact, unexpected fault scenarios are the decisive challenge of novel prototype. This novel type of faults should be considered, such as high dv/dt, bearing current, etc.

System level test Due to the limitations of time and cost, a complete powertrain including prototype machine and clutch was not built in this thesis. In the future, it is expected that the whole powertrain can be integrated, implemented and evaluated.

Bibliography

1. Han, P., et al. *Integrated Modular Motor Drives Based on Multiphase Axial-flux PM Machines with Fractional-slot Concentrated Windings*. in *2021 IEEE International Electric Machines & Drives Conference (IEMDC)*. 2021. IEEE.
2. Bennett, J.W., et al., *Fault-tolerant design considerations and control strategies for aerospace drives.* IEEE Transactions on Industrial Electronics, 2011. **59**(5): p. 2049-2058.
3. Wolmarans, J., et al. *Selecting an optimum number of system phases for an integrated, fault tolerant permanent magnet machine and drive*. in *2009 13th European Conference on Power Electronics and Applications*. 2009. IEEE.
4. Shi, Z., et al., *Robust design optimization of a five-phase PM hub motor for fault-tolerant operation based on Taguchi method.* IEEE Transactions on Energy Conversion, 2020. **35**(4): p. 2036-2044.
5. Bianchi, N., S. Bolognani, and M.D.P. Pre, *Impact of stator winding of a five-phase permanent-magnet motor on postfault operations.* IEEE Transactions on Industrial Electronics, 2008. **55**(5): p. 1978-1987.
6. Baudart, F., et al. *Control under normal and fault tolerant operation of multiphase SMPM synchronous machines with mechanically and magnetically decoupled phases*. in *2009 International Conference on Power Engineering, Energy and Electrical Drives*. 2009. IEEE.
7. Si, J., et al., *A novel high torque density six-phase axial-flux permanent magnet synchronous motor with 60 phase-belt toroidal winding configuration.* IET Electric Power Applications, 2021.
8. Cao, W., et al., *Overview of electric motor technologies used for more electric aircraft (MEA).* IEEE transactions on industrial electronics, 2012. **59**(9): p. 3523-3531.
9. Jiang, X., et al., *Electric drive system of dual-winding fault-tolerant permanent-magnet motor for aerospace applications.* IEEE Transactions on Industrial Electronics, 2015. **62**(12): p. 7322-7330.
10. Sangha, P. and T. Sawata. *Design and test results for dual-lane fault-tolerant*

PM motor for safety critical aircraft actuator. in *2015 IEEE Energy Conversion Congress and Exposition (ECCE)*. 2015. IEEE.

11. Zheng, P., et al., *Investigation of a novel 24-slot/14-pole six-phase fault-tolerant modular permanent-magnet in-wheel motor for electric vehicles.* Energies, 2013. **6**(10): p. 4980-5002.
12. Sarigiannidis, A.G., et al., *Fault tolerant design of fractional slot winding permanent magnet aerospace actuator.* IEEE Transactions on Transportation Electrification, 2016. **2**(3): p. 380-390.
13. Ifedi, C.J., et al., *Fault-tolerant in-wheel motor topologies for high-performance electric vehicles.* IEEE Transactions on Industry Applications, 2013. **49**(3): p. 1249-1257.
14. Wang, X., et al., *Design and Analysis for Multi-Disc Coreless Axial-Flux Permanent-Magnet Synchronous Machine.* IEEE Transactions on Applied Superconductivity, 2021. **31**(8): p. 1-4.
15. Chai, F., L. Geng, and Y. Pei, *A Novel Fault Tolerant Machine With Integral Slot Non-Overlapping Concentrated Winding.* IEEE Access, 2019. **7**: p. 99462-99469.
16. Zhu, X., et al., *A non-rare-earth doubly salient flux controllable motor capable of fault-tolerant control.* IEEE Transactions on Magnetics, 2015. **51**(11): p. 1-4.
17. Zhang, Z., Y. Liu, and J. Li, *A HESM-based variable frequency AC starter-generator system for aircraft applications.* IEEE Transactions on Energy Conversion, 2018. **33**(4): p. 1998-2006.
18. Chan, C.C., A. Bouscayrol, and K. Chen, *Electric, hybrid, and fuel-cell vehicles: Architectures and modeling.* IEEE transactions on vehicular technology, 2009. **59**(2): p. 589-598.
19. Polaczyk, N., et al. *A review of current technology and research in urban on-demand air mobility applications*. in *8th Biennial Autonomous VTOL Technical Meeting and 6th Annual Electric VTOL Symposium*. 2019.
20. Sarlioglu, B. and C.T. Morris, *More electric aircraft: Review, challenges, and opportunities for commercial transport aircraft.* IEEE transactions on Transportation Electrification, 2015. **1**(1): p. 54-64.
21. Thomson, R., et al., *Aircraft electrical propulsion the next chapter of aviation.* Roland Berger, 2017: p. 17.

22. Moir, I. and A. Seabridge, *Aircraft systems: mechanical, electrical, and avionics subsystems integration*. Vol. 52. 2011: John Wiley & Sons.
23. Fu, J., J.-C. Maré, and Y. Fu, *Modelling and simulation of flight control electromechanical actuators with special focus on model architecting, multidisciplinary effects and power flows.* Chinese Journal of Aeronautics, 2017. **30**(1): p. 47-65.
24. Tron, X.L. *A380 Flight Controls overview*. 2007; Available from: https://www.fzt.haw-hamburg.de/pers/Scholz/dglr/hh/text_2007_09_27_A380_Flight_Controls.pdf.
25. Wagner, H., et al., *Challenges for health monitoring of electromechanical flight control actuation systems.* SAE International Journal of Aerospace, 2011. **4**(2011-01-2701): p. 1316-1323.
26. Bennett, J., et al., *Safety-critical design of electromechanical actuation systems in commercial aircraft.* IET Electric Power Applications, 2011. **5**(1): p. 37-47.
27. Bennett, J.W., *Fault tolerant electromechanical actuators for aircraft*. 2010, Newcastle University.
28. Gerada, C., et al. *Integrated machine design for electro mechanical actuation*. in *2007 IEEE international symposium on industrial electronics*. 2007. IEEE.
29. Gerada, C. and K.J. Bradley, *Integrated PM machine design for an aircraft EMA.* IEEE Transactions on Industrial Electronics, 2008. **55**(9): p. 3300-3306.
30. Qiao, G., et al., *A review of electromechanical actuators for More/All Electric aircraft systems.* Proceedings of the Institution of Mechanical Engineers, Part C: Journal of Mechanical Engineering Science, 2018. **232**(22): p. 4128-4151.
31. Villani, M., et al., *High reliability permanent magnet brushless motor drive for aircraft application.* IEEE transactions on industrial electronics, 2012. **59**(5): p. 2073-2081.
32. Niu, S., S. Ho, and W. Fu, *A novel direct-drive dual-structure permanent magnet machine.* IEEE transactions on magnetics, 2010. **46**(6): p. 2036-2039.
33. Charrier, J.-J. and A. Kulshreshtha. *Electric actuation for flight and engine control; evolution and current trend*. in *45th AIAA Aerospace Sciences*

Meeting and Exhibit. 2007.

34. Hill, C.I., et al. *More electric aircraft electro-mechanical actuator regenerated power management*. in *2015 IEEE 24th International Symposium on Industrial Electronics (ISIE)*. 2015. IEEE.
35. Jean-Charles, M. and F. Jian, *Review on signal-by-wire and power-by-wire actuation for more electric aircraft.* Chinese Journal of Aeronautics, 2017. **30**(3): p. 857-870.
36. Linke-Diesinger, A., *Systems of commercial turbofan engines: an introduction to systems functions*. 2008: Springer Science & Business Media.
37. Nagel, N., *Actuation challenges in the more electric aircraft: Overcoming hurdles in the electrification of actuation systems.* IEEE Electrification Magazine, 2017. **5**(4): p. 38-45.
38. FAA. *Aircraft Landing Gear Systems*. Aviation Maintenance Technician Handbook–Airframe Volume 2 Chapter 13 2018; Available from: https://www.faa.gov/regulations_policies/handbooks_manuals/aircraft/media/amt_airframe_hb_vol_2.pdf.
39. Safran. *Extension/retraction system*. 2019; Available from: https://www.safran-landing-systems.com/systems-equipment/extension/retraction-system.
40. LIEBHERR. *Landing gear systems*. 2019; Available from: https://www.liebherr.com/en/are/products/aerospace-and-transportation-systems/aerospace/products-and-solutions/products-and-solutions.html.
41. Florian. *Recent advances and future electrical landing gear systems*. ICAS Workshop–Cape Town 2013; Available from: http://www.icas.org/media/pdf/Workshops/2013/ICAS%20-%20Recent%20Advances%20and%20Future%20Electrical%20Landing%20Gear%20Systems%20Publish.pdf.
42. Re, F., *Assessing environmental benefits of electric aircraft taxiing through object-oriented simulation.* SAE International Journal of Aerospace, 2012. **5**(2012-01-2218): p. 503-512.
43. Safran. *Electric taxiing*. 2019; Available from: https://www.safran-landing-systems.com/systems-equipment/electric-taxiing-0.
44. Gerada, C., M. Galea, and A. Kladas. *Electrical machines for aerospace applications*. in *2015 IEEE Workshop on Electrical Machines Design,*

Control and Diagnosis (WEMDCD). 2015. IEEE.

45. Bennett, J., et al., *Fault-tolerant electric drive for an aircraft nose wheel steering actuator.* IET electrical systems in transportation, 2011. **1**(3): p. 117-125.
46. Weimer, J.A. *The role of electric machines and drives in the more electric aircraft*. in *IEEE International Electric Machines and Drives Conference, 2003. IEMDC'03.* 2003. IEEE.
47. Mecrow, B.C., et al., *Design and testing of a four-phase fault-tolerant permanent-magnet machine for an engine fuel pump.* IEEE Transactions on Energy Conversion, 2004. **19**(4): p. 671-678.
48. Schwalm, G.K., *On-board inert gas generation system*. 2007, Google Patents.
49. Fabri, G., et al. *PM brushless motor for helicopters electric tail rotor drive system*. in *2017 IEEE International Electric Machines and Drives Conference (IEMDC)*. 2017.
50. Castellini, L., M.D. Andrea, and M. Villani. *Electric powertrain for helicopter tail rotor*. in *2016 6th International Electric Drives Production Conference (EDPC)*. 2016.
51. Madonna, V., P. Giangrande, and M. Galea, *Electrical Power Generation in Aircraft: Review, Challenges, and Opportunities.* IEEE Transactions on Transportation Electrification, 2018. **4**(3): p. 646-659.
52. Griffo, A., et al., *Design and characterization of a three-phase brushless exciter for aircraft starter/generator.* IEEE Transactions on Industry Applications, 2013. **49**(5): p. 2106-2115.
53. Wiegand, C. *F-35 Air Vehicle Technology Overview*. in *2018 Aviation Technology, Integration, and Operations Conference*. 2018.
54. El-Refaie, A. and M. Osama, *High specific power electrical machines: A system perspective.* CES Transactions on Electrical Machines and Systems, 2019. **3**(1): p. 88-93.
55. UK, A.C. *Electric Machines Roadmap 2020.* Available from: https://www.apcuk.co.uk/app/uploads/2021/09/https___www.apcuk_.co_.uk_app_uploads_2021_02_Exec-summary-Technology-Roadmap-Electric-Machines-final.pdf.
56. Sayed, E., et al., *Review of Electric Machines in More/Hybrid/Turbo Electric Aircraft.* IEEE Transactions on Transportation Electrification, 2021.

57. Wang, Y., et al., *Challenges and opportunities for wound field synchronous generators in future more electric aircraft.* IEEE Transactions on Transportation Electrification, 2020. **6**(4): p. 1466-1477.
58. Nøland, J.K., et al., *High-power machines and starter-generator topologies for more electric aircraft: A technology outlook.* IEEE Access, 2020. **8**: p. 130104-130123.
59. Masson, P.J., et al., *Design of HTS axial flux motor for aircraft propulsion.* IEEE Transactions on Applied Superconductivity, 2007. **17**(2): p. 1533-1536.
60. Cao, W., et al., *Overview of electric motor technologies used for more electric aircraft (MEA).* IEEE transactions on industrial electronics, 2011. **59**(9): p. 3523-3531.
61. Bozhko, S., et al., *Development of Aircraft Electric Starter–Generator System Based on Active Rectification Technology*. IEEE transactions on transportation electrification, 2018. **4**(4): p. 985-996.
62. El-Refaie, A. and M. Osama. *High specific power electrical machines: A system perspective*. in *2017 20th International Conference on Electrical Machines and Systems (ICEMS)*. 2017.
63. Caujolle, M. and R. Gage, *Airbus, Rolls-Royce, and Siemens team up for electric future Partnership launches E-Fan X hybrid-electric flight demonstrator.* URL: http://www. airbus. com/newsroom/press-releases/en/2017/11/airbus--rolls-royce--and-siemens-team-up-for-electric-future-par. html (retrieved 30 January 2018), 2017.
64. Golovanov, D., et al., *4MW Class High Power Density Generator for Future Hybrid-Electric Aircraft.* IEEE Transactions on Transportation Electrification, 2021.
65. Van der Geest, M., et al. *Machine selection and initial design of an aerospace starter/generator*. in *2013 International Electric Machines & Drives Conference*. 2013. IEEE.
66. Arumugam, P., et al., *Analysis of vertical strip wound fault-tolerant permanent magnet synchronous machines.* IEEE Transactions on Industrial Electronics, 2013. **61**(3): p. 1158-1168.
67. Dusek, J., et al., *Impact of slot/pole combination on inter-turn short-circuit current in fault-tolerant permanent magnet machines.* IEEE Transactions on Magnetics, 2015. **52**(4): p. 1-9.

68. Wentao Zhang, Y.X., Yingliang Huang, Jibin Zou., *Reduction of High-frequency Vibration Noise for Dual-branch Three-phase Permanent Magnet Synchronous Motors.* Chinese Journal of Electrical Engineering, 2020. **6**: p. 42-51.
69. Anton, F., *Siemens eAircraft overview*. 2019.
70. magniX, *The magni650 electric propulsion unit*. 2021.
71. Khowja, M.R., et al. *Trade-off Study of a High Power Density Starter-Generator for Turboprop Aircraft System*. in *IECON 2019-45th Annual Conference of the IEEE Industrial Electronics Society*. 2019. IEEE.
72. Ganev, E., *High-reactance permanent magnet machine for high-performance power generation systems.* SAE Transactions, 2006: p. 888-897.
73. Jiang, Y., et al., *Three-phase current injection method for mitigating turn-to-turn short-circuit fault in concentrated-winding permanent magnet aircraft starter generator*. IET Electric Power Applications, 2018. **12**(4): p. 566-574.
74. Gao, Z., C. Cecati, and S.X. Ding, *A survey of fault diagnosis and fault-tolerant techniques—Part I: Fault diagnosis with model-based and signal-based approaches.* IEEE transactions on industrial electronics, 2015. **62**(6): p. 3757-3767.
75. Gao, Z., C. Cecati, and S.X. Ding, *A survey of fault diagnosis and fault-tolerant techniques—Part II: Fault diagnosis with knowledge-based and hybrid/active approaches.* IEEE Transactions on Industrial Electronics, 2015. **62**(6): p. 3768-3774.
76. !!! INVALID CITATION !!! [36-38].
77. Papaoikonomou, D., M. van der Geest, and H. Polinder, *Comparison between induction and PM machine for high speed starter-generator applications.* 2014.
78. Van der Geest, M., et al. *Design and testing of a high-speed aerospace permanent magnet starter/generator*. in *2015 International Conference on Electrical Systems for Aircraft, Railway, Ship Propulsion and Road Vehicles (ESARS)*. 2015. IEEE.
79. Zhang, B., et al. *A comparison of the transverse, axial and radial flux PM synchronous motors for electric vehicle*. in *2014 IEEE International Electric Vehicle Conference (IEVC)*. 2014. IEEE.
80. Bonnett, A.H. and C. Yung, *Increased efficiency versus increased reliability.*

IEEE Industry Applications Magazine, 2008. **14**(1): p. 29-36.

81. Akai, H., *Maximum performance of permanent magnet materials.* Scripta Materialia, 2018. **154**: p. 300-304.
82. Peng, P., et al., *Effects of external field orientation on permanent magnet demagnetization.* IEEE Transactions on Industry Applications, 2017. **53**(4): p. 3438-3446.
83. Kim, K.T., Y.S. Lee, and J. Hur, *Transient Analysis of Irreversible Demagnetization of Permanent-Magnet Brushless DC Motor With Interturn Fault Under the Operating State.* IEEE Transactions on Industry Applications, 2014. **50**(5): p. 3357-3364.
84. Faiz, J. and E. Mazaheri-Tehrani, *Demagnetization modeling and fault diagnosing techniques in permanent magnet machines under stationary and nonstationary conditions: An overview.* IEEE Transactions on Industry Applications, 2016. **53**(3): p. 2772-2785.
85. Li, S., D. Han, and B. Sarlioglu. *Analysis of temperature effects on performance of spoke-type interior permanent magnet machines*. in *2017 IEEE Transportation Electrification Conference and Expo (ITEC)*. 2017. IEEE.
86. Xiong, H., et al., *Permanent-magnet demagnetization design and validation.* IEEE Transactions on Industry Applications, 2016. **52**(4): p. 2961-2970.
87. Seo, M.-K., et al., *Irreversible demagnetization analysis with respect to winding connection and current ripple in brushless DC motor.* IEEE Transactions on Applied Superconductivity, 2018. **28**(3): p. 1-4.
88. Tong, W., et al. *Analysis and Experimental Verification of Segmented Rotor Structure on Rotor Eddy Current Loss of High-Speed Surface-Mounted Permanent Magnet Machine*. in *2021 IEEE International Magnetic Conference (INTERMAG)*. 2021. IEEE.
89. Li, G., et al., *Demagnetization withstand capability enhancement of surface mounted PM machines using stator modularity.* IEEE Transactions on Industry Applications, 2017. **54**(2): p. 1302-1311.
90. Espinosa, A.G., et al., *Fault detection by means of Hilbert–Huang transform of the stator current in a PMSM with demagnetization.* IEEE Transactions on Energy Conversion, 2010. **25**(2): p. 312-318.
91. Technologies, A.M., *Samarium Cobalt Magnets*. 2021.

92. Borisavljevic, A., H. Polinder, and J.A. Ferreira, *On the speed limits of permanent-magnet machines.* IEEE Transactions on Industrial Electronics, 2009. **57**(1): p. 220-227.
93. Zhang, F., et al., *Rotor retaining sleeve design for a 1.12-MW high-speed PM machine.* IEEE Transactions on Industry Applications, 2015. **51**(5): p. 3675-3685.
94. Binder, A., T. Schneider, and M. Klohr, *Fixation of buried and surface-mounted magnets in high-speed permanent-magnet synchronous machines.* IEEE Transactions on Industry Applications, 2006. **42**(4): p. 1031-1037.
95. Tenconi, A., S. Vaschetto, and A. Vigliani, *Electrical machines for high-speed applications: Design considerations and tradeoffs.* IEEE Transactions on Industrial Electronics, 2013. **61**(6): p. 3022-3029.
96. Gerada, D., et al., *High-speed electrical machines: Technologies, trends, and developments.* IEEE transactions on industrial electronics, 2013. **61**(6): p. 2946-2959.
97. Lee, T.-W. and D.-K. Hong, *Electrical and Mechanical Characteristics of a High-Speed Motor for Electric Turbochargers in Relation to Eccentricity.* Energies, 2021. **14**(11): p. 3340.
98. Tong, W., et al., *Modeling and Analysis of Axial Flux Permanent Magnet Machines with Coexistence of Rotor Radial Deviation and Angular Eccentricity.* IEEE Transactions on Energy Conversion, 2020. **35**(4): p. 2181-2190.
99. Lin, F., S. Zuo, and W. Deng, *Impact of rotor eccentricity on electromagnetic vibration and noise of permanent magnet synchronous motor.* Journal of Vibroengineering, 2018. **20**(2): p. 923-935.
100. Takahata, R., et al., *Influence of rotor eccentricity on vibration characteristics of permanent magnet synchronous motor.* IEEJ Journal of Industry Applications, 2019. **8**(3): p. 558-565.
101. Polat, A., Y. Ertuğrul, and L. Ergene. *Static, dynamic and mixed eccentricity of induction motor*. in *2015 IEEE 10th international symposium on diagnostics for electrical machines, power electronics and drives (SDEMPED)*. 2015. IEEE.
102. Li, B., et al., *Neural-network-based motor rolling bearing fault diagnosis.* IEEE transactions on industrial electronics, 2000. **47**(5): p. 1060-1069.

103. von Jouanne, A., et al. *Motor Bearing Current Characterization in SiC-based Variable Frequency Drive Applications*. in *2020 IEEE Energy Conversion Congress and Exposition (ECCE)*. 2020. IEEE.
104. Liu, Y., et al. *Research on Bearing Current Detection Method of High-speed Motor Driven by PWM Inverter*. in *2019 22nd International Conference on Electrical Machines and Systems (ICEMS)*. 2019. IEEE.
105. Plazenet, T., et al., *A comprehensive study on shaft voltages and bearing currents in rotating machines.* IEEE Transactions on Industry Applications, 2018. **54**(4): p. 3749-3759.
106. Valente, G., et al., *Performance improvement of bearingless multisector PMSM with optimal robust position control.* IEEE Transactions on Power Electronics, 2018. **34**(4): p. 3575-3585.
107. Jiang, X., et al., *Design and optimization of dual-winding fault-tolerant permanent magnet motor.* CES Transactions on Electrical Machines and Systems, 2019. **3**(1): p. 45-53.
108. Dusek, J., et al., *Impact of slot/pole combination on inter-turn short-circuit current in fault-tolerant permanent magnet machines.* IEEE Transactions on Magnetics, 2016. **52**(4): p. 1-9.
109. Xu, Y., et al., *Numerical Analysis of Turn-to-Turn Short Circuit Current Mitigation for Concentrated Winding Permanent Magnet Machines With Series and Parallel Connected Windings.* IEEE Transactions on Industrial Electronics, 2019. **67**(11): p. 9101-9111.
110. Ishak, D., Z. Zhu, and D. Howe, *Comparison of PM brushless motors, having either all teeth or alternate teeth wound.* IEEE Transactions on Energy Conversion, 2006. **21**(1): p. 95-103.
111. Li, G., et al., *Influence of flux gaps on electromagnetic performance of novel modular PM machines.* IEEE Transactions on Energy Conversion, 2014. **29**(3): p. 716-726.
112. Li, G.-J., et al., *Modular permanent-magnet machines with alternate teeth having tooth tips.* IEEE Transactions on Industrial Electronics, 2015. **62**(10): p. 6120-6130.
113. Zhu, Z., Z. Azar, and G. Ombach, *Influence of additional air gaps between stator segments on cogging torque of permanent-magnet machines having modular stators.* IEEE Transactions on Magnetics, 2011. **48**(6): p. 2049-

2055.

114. Barcaro, M., N. Bianchi, and F. Magnussen, *Analysis and Tests of a Dual Three-Phase 12-Slot 10-Pole Permanent-Magnet Motor.* IEEE Transactions on Industry Applications, 2010. **46**(6): p. 2355-2362.
115. Hemeida, A., et al., *Applicability of fractional slot axial flux permanent magnet synchronous machines in the field weakening region.* IEEE Transactions on Energy Conversion, 2016. **32**(1): p. 111-121.
116. Capponi, F.G., et al., *Fractional-slot concentrated-winding axial-flux permanent-magnet machine with tooth-wound coils.* IEEE Transactions on Industry Applications, 2014. **50**(4): p. 2446-2457.
117. Golovanov, D., et al., *4-MW Class High-Power-Density Generator for Future Hybrid-Electric Aircraft.* IEEE Transactions on Transportation Electrification, 2021. **7**(4): p. 2952-2964.
118. Krishnan, R., *Permanent magnet synchronous and brushless DC motor drives*. 2017: CRC press.
119. Zhu, Z. *Recent development of Halbach permanent magnet machines and applications*. in *2007 Power Conversion Conference-Nagoya*. 2007. IEEE.
120. Lipo, T.A., *Introduction to AC machine design*. 2017: John Wiley & Sons.
121. Al-Timimy, A., et al., *Design and losses analysis of a high power density machine for flooded pump applications.* IEEE Transactions on Industry Applications, 2018. **54**(4): p. 3260-3270.
122. Mellor, P., R. Wrobel, and N. Simpson. *AC losses in high frequency electrical machine windings formed from large section conductors*. in *2014 IEEE Energy Conversion Congress and Exposition (ECCE)*. 2014. IEEE.
123. Bardalai, A., et al., *Reduction of winding AC losses by accurate conductor placement in high frequency electrical machines.* IEEE Transactions on Industry Applications, 2019. **56**(1): p. 183-193.
124. Nategh, S., et al. *A Study on Thermal Effects of Different Potting Strategies in Traction Motors*. in *2018 IEEE International Conference on Electrical Systems for Aircraft, Railway, Ship Propulsion and Road Vehicles & International Transportation Electrification Conference (ESARS-ITEC)*. 2018.
125. Boglietti, A., et al., *Evolution and modern approaches for thermal analysis of electrical machines.* IEEE Transactions on industrial electronics, 2009. **56**(3):

p. 871-882.

126. Boglietti, A., A. Cavagnino, and D. Staton, *Determination of critical parameters in electrical machine thermal models.* IEEE transactions on Industry Applications, 2008. **44**(4): p. 1150-1159.
127. Sciascera, C., et al., *Analytical thermal model for fast stator winding temperature prediction.* IEEE Transactions on Industrial Electronics, 2017. **64**(8): p. 6116-6126.
128. Popescu, M., et al., *Thermal analysis of duplex three-phase induction motor under fault operating conditions.* IEEE Transactions on Industry Applications, 2013. **49**(4): p. 1523-1530.
129. Zhang, H., et al., *Comparative study on two modular spoke-type PM machines for in-wheel traction applications.* IEEE Transactions on Energy Conversion, 2019. **34**(4): p. 2137-2147.
130. Zhang, F., et al., *Back-iron extension thermal benefits for electrical machines with concentrated windings.* IEEE Transactions on Industrial Electronics, 2019. **67**(3): p. 1728-1738.
131. Madonna, V., et al., *Improved thermal management and analysis for stator end-windings of electrical machines.* IEEE Transactions on Industrial Electronics, 2018. **66**(7): p. 5057-5069.
132. Gronwald, P.-O. and T.A. Kern, *Traction motor cooling systems, a literature review and comparative study.* IEEE transactions on transportation electrification, 2021.
133. Bobek, V., *PMSM electrical parameters measurement.* Freescale Semiconductor, 2013. **7**(8): p. 13.
134. Bardalai, A., et al. *AC loss Analysis in Winding of Electrical Machines with varying Strands-in-hand and Bundle Shapes*. in *2020 23rd International Conference on Electrical Machines and Systems (ICEMS)*. 2020.
135. Bardalai, A., et al., *Reduction of Winding AC Losses by Accurate Conductor Placement in High Frequency Electrical Machines.* IEEE Transactions on Industry Applications, 2020. **56**(1): p. 183-193.
136. Wang, Z., et al., *Initial Rotor Position Detection for Permanent Magnet Synchronous Motor Based on High-Frequency Voltage Injection without Filter.* World Electric Vehicle Journal, 2020. **11**(4): p. 71.
137. Bobek, V., *PMSM electrical parameters measurement*, in *Freescale*

Semiconductor. 2013. p. 13.

138. Fitzgerald, A.E., et al., *Electric machinery*. Vol. 5. 2003: McGRAW-hill New York.